


Chemical and physical effects of interaction between oilfield chemicals and formation rocks and integration with sand failure prediction models.

WUYEP, E.O.

2018

The author of this thesis retains the right to be identified as such on any occasion in which content from this thesis is referenced or re-used. The licence under which this thesis is distributed applies to the text and any original images only – re-use of any third-party content must still be cleared with the original copyright holder.



CHEMICAL AND PHYSICAL EFFECTS
OF INTERACTION BETWEEN
OILFIELD CHEMICALS AND
FORMATION ROCKS AND
INTEGRATION WITH SAND FAILURE
PREDICTION MODELS

Elizabeth Olive Wuyep (1409868)

ROBERT GORDON UNIVERSITY ABERDEEN





CHEMICAL AND PHYSICAL EFFECTS OF INTERACTION BETWEEN OILFIELD
CHEMICALS AND FORMATION ROCKS AND INTEGRATION WITH SAND FAILURE
PREDICTION MODELS

ELIZABETH OLIVE **WUYEP**

A thesis submitted in partial fulfilment of the requirements of

The Robert Gordon University

For the degree of Doctor of Philosophy

(School of Engineering)

This research is funded by



Petroleum Technology Development Funds (PTDF), Abuja, Nigeria

October 2018



**CHEMICAL AND PHYSICAL EFFECTS OF INTERACTION BETWEEN OILFIELD
CHEMICALS AND FORMATION ROCKS AND INTEGRATION WITH SAND
FAILURE PREDICTION MODELS**

PhD Candidate

Elizabeth Olive Wuyep

Supervisory Team

¹Dr Gbenga F. Oluyemi (Principal supervisor)

²Dr Kyari Yates

³Prof Alfred R. Akisanya

¹School of Engineering, Robert Gordon University, Sir Ian Wood Building, Riverside East, Garthdee Road, Aberdeen, AB10 7GJ, United Kingdom

²School of Pharmacy and Life Sciences, Robert Gordon University, Sir Ian Wood Building, Riverside East, Garthdee Road, Aberdeen, AB10 7GJ, United Kingdom

³School of Engineering, University of Aberdeen, Aberdeen. AB24 3UE, United Kingdom

Dedication

This work is dedicated to God Almighty to whom I owe this achievement; and to the memory of my late father, Elder Egidi Jacob Akubo who deprived himself of so many privileges to ensure I had a firm education foundation that guaranteed this continuous search for knowledge.

The work is also dedicated to: my wonderful and prayerful mother, Enegbani Janet Akubo; my loving & dedicated husband, Sunday Wuyep; and our four lovely children, Manchang, Nanna, Selnan and Selpon.

Acknowledgment

O' Lord "*For You formed my inward parts; You covered me in my mother's womb. I will praise You, for I am fearfully and wonderfully made, marvellous are Your works, and that my soul knows very well* (Psalm 139:13-14)". I give glory to God Almighty for counting me worthy to embark on the PhD journey and brought it to an expected end. All that I am and all that I have belong Him.

I wish to express my sincere gratitude to my wonderful and amazing supervisory team, Dr Gbenga Oluyemi, Dr Kyari Yates and Prof. Alfred Akisanya. I thank God to have blessed me with very understanding academic giants, who have worked assiduously to provide the much valued guidance and encouragement that saw me to the successful completion of my PhD programme. I could not have had a better combination of sound academic personalities like this team who made studentship so easy for me. I always looked forward to our monthly interactive meeting to share from their wealth.

My special thanks go to the Petroleum Technology Development Funds (PTDF) for funding my PhD programme. I am also grateful to Aberdeen Formation Evaluation Society (AFES) for supporting my research twice with grants. My profound appreciation goes to three amazing people, Mrs Ifeoma Nwokike, Hon. Beni Lar and Mr Ibifubara Wariso who were extremely supportive throughout the PhD journey. Special thanks to Dr Rosslyn Shanks (Admin Manager, School of Engineering) for her excellent and gentle administrative guidance, Dr Draco Iyi for his professional guidance. To my colleague in the School of Engineering research hub, RGU, I say thank you for the spirit of oneness shown.

I also acknowledge the encouragement and prayer support of my siblings; Mr Pius Yusufu, Mrs Pauline Ajanya, Mrs Ruth Maha, Mrs Rose Ugbane, Mr Ben Akubo, Mr Amos Akubo and Mr Natha Akubo and their spouses; and my cousin, Mr James Odiba and his wife for their prayers and encouragement. I also extend my gratitude to my 'Kaka' (father in-law), Mr Ali Banfa Wuyep for his constant prayers and my brother in-laws Pharmacist Nimnan Wuyep, his wife Deborah Wuyep and Mr Titus Wuyep for their encouragement.

My heartfelt gratitude goes to Prof. Nuhu Obaje, Prof. Peter Onwualu and Dr Moses Omojola for their mentorship and believing in my capability; my friends Mrs Eunice Yakusak, Mr & Mrs David Millaham, Mrs Nana Veronica Ocheja, Dr (Barr) Ilesanmi, Mrs Talatu Nweke, and Mrs Mercy Emmanuel for their moral and prayer support. My gratitude goes to technical staff, Helen Love (Gray School of Arts, RGU); Mark Gourlay (School of Engineering, University of Aberdeen); Stephen Williamson and Stuart Craig (School of Pharmacy and Life Sciences, RGU); Andy Ross, David Smith, Alan Macpherson and Benjamin Bird (School of Engineering, RGU), other technical staff and the janitors for their support. Thanks to Andrew Lamb for granting Research Students 24 hours access into the building. I thank many other people whose names are not mentioned but have contributed one way or the other.

This acknowledgement fails to complete without thanking my wonderful husband, Dr Sunday Wuyep, for his understanding, prayer support and keeping the family together throughout the research period; my adorable children, Manchang, Nanna, Selnan and Selpon for their endurance and being very supportive; and my dedicated niece, Ojochogwu Nuhu for holding forth for me on the home front.

God bless you all!

Abstract

Sand failure may result in the production of formation sand at the same time the formation fluids are being produced. Sand failure occurs when the formation stress exceeds the strength of the formation which is derived majorly from the natural material that cements the sand grain and cohesive forces. The sand failure and production is a serious challenge that if not properly handled can have a drastic effect on oil and gas production rate, cause downhole and subsea equipment damage and also increase the risk of catastrophic failure.

Several models are in existence for the prediction of sand failure in the oil and gas wells, but none of these models account for the failure effects of oilfield chemicals on the reservoir rock that has experienced significant use of these chemicals. Oilfield chemicals have many applications in the oil and gas industry and have been used extensively as inhibitor, surfactant, biocide, stabilizer, depressant, retarder, scavenger, defoamer, demulsifier and stimulant etc. However, the weakening effect that the chemical – formation interaction may pose on the grain fabrics has not been given attention by the current industry approach to geomechanical evaluation of reservoir rock for sand failure and production forecast.

This work investigates the failure effects of some oilfield chemicals (corrosion inhibitor, scale inhibitor and biocide) on the geomechanical strength of reservoir rocks, the mechanisms of interaction as well as the mechanism of such failure. A combination of rock mechanical testing, grain size distribution analysis, analytical techniques and numerical modelling was used to establish and define the geomechanical and mechanical failure effects of these chemicals and the mechanisms of failure. The failure effects of the oilfield chemicals on sandstone

and carbonates may be integrated within any suitable and relevant existing sand failure prediction models.

Results clearly show that dissolution/precipitation reaction took place leading to weakening of the reservoir grain fabrics and reduction of the geomechanical strength which in turn causes sand failure/production. This work has established that volume fraction and porosity change are functions of dissolution and precipitation reactions; and the dissolution/precipitation reaction is a function of the type of minerals in the rock.

Key words: Sand failure, Geomechanical strength, Oilfield chemicals, Grain fabrics, Prediction models, Dissolution, Precipitation, Sandstone, Carbonates, Reservoir rocks.

Table of Contents

List of Figures.....	xiii
List of Tables	xx
Nomenclature	xxii
List of Publications	xxviii
Chapter One.....	1
1 Introduction	1
1.1 Background.....	1
1.2 Research gaps.....	6
1.3 Aim and Objectives	6
1.4 Methodology	7
1.5 Contributions to knowledge	7
1.6 Order of thesis presentation	8
References	11
Chapter Two.....	15
2 Literature Review	15
2.1 Introduction	15
2.2 Key petrophysical and geomechanical properties	16
2.2.1 Pore volume, Porosity and Permeability.....	17
2.2.2 Particle size distribution and sorting.....	19
2.3 Geomechanical properties	21
2.3.1 Unconfined compressive strength (UCS) and Young’s modulus	21

2.3.2	Confined compressive strength (CCS)	24
2.4	Mechanisms of Chemical-rock interaction.....	26
2.5	Numerical studies of oilfield chemicals interaction with formation rock..	27
2.5.1	Geochemical interaction	28
2.5.1.1	Fluid flow.....	31
2.5.1.2	Chemical reaction	32
2.5.1.3	Transport.....	38
2.6	Sand failure	41
2.6.1	Causes of sand failure.....	42
2.6.2	Mechanisms of sand failure.....	43
2.7	Sand failure prediction.....	44
2.8	Summary.....	51
	References	53
	Chapter Three	71
3	Research Methodology/Approach.....	71
3.1	Introduction	71
3.2	Materials and equipment.....	73
3.3	Pre and post-chemical treatment test programme.....	77
3.3.1	Mechanical testing	77
3.3.1.1	Uniaxial compression test	78
3.3.1.2	Triaxial test.....	80
3.3.2	Analytical characterisation	83

3.3.2.1	Elemental analysis using SEM/EDXA.....	84
3.3.2.2	Mineralogical analysis using XRPD.....	84
3.3.3	Preparation of brine and injection chemicals	85
3.3.4	Static saturation.....	86
3.3.5	Dynamic saturation test	88
3.3.5.1	Material preparation for core flooding	88
3.3.5.3	Injection of Li tracer for porosity measurement	91
3.3.5.4	Sample analysis by ICP-OES	92
3.3.6	Particle size distribution analysis	93
	References	95
	Chapter Four	98
4	Geomechanical effects of oilfield chemicals on sand failure under static condition	98
4.1	Introduction	98
4.2	Materials, Pre and Post chemical treatment tests	99
4.2.1	Mechanical test	99
4.2.2	SEM, EDXA and XRPD analysis	100
4.2.3	Static saturation.....	100
4.2.4	Particle size distribution	101
4.3	Results and Discussion of the effects of chemicals on Real Reservoir core samples	101
4.3.1	Characterisation of real reservoir sandstone and limestone samples	

4.3.2	Effect of chemicals on geomechanical strength.....	107
4.3.3	Failure effects on sandstone	110
4.3.4	Failure effects on limestone	115
4.3.5	Grain size distribution	121
4.4	Results and Discussion of the effects of chemicals on Outcrop core samples	124
4.4.1	Characterisation of outcrop sandstone and carbonate samples	125
4.4.2	Grain size distribution analysis	130
4.4.3	Effect of chemicals on strength and Young’s Modulus	133
4.4.4	Effect of chemicals on mineralogy.....	137
4.5	Summary.....	146
	References	148
	Chapter five	152
5	Evaluation of the Interactions between oilfield chemicals and reservoir rocks under dynamic condition (Core flooding)	152
5.1	Introduction	152
5.2	Materials & Methods.....	153
5.2.1	Data Analysis.....	154
5.2.1.1	Porosity	154
5.2.1.2	Permeability measurement.....	154
5.2.1.3	Chemical injection.....	155
5.3	Results and Discussion	156

5.3.1	Effect of chemicals on porosity/permeability of sandstone and carbonates.	156
5.4	Particle/grain detachment.....	159
5.5	Effect of chemical treatment on the mineralogy	162
5.5.1	Sandstone.....	162
5.5.2	Carbonate	168
5.6	Effect of chemicals on Unconfined Compressive Strength and Young's modulus.....	175
5.7	Effect of chemicals on Confined Compressive Strength and Young's modulus.....	183
5.7.1	Sandstone	188
5.7.2	Carbonate	192
5.8	Summary.....	196
	References	198
	Chapter Six	203
6	Numerical modelling of oilfield chemical interaction with the porous medium	203
6.1	Introduction	203
6.2	Geochemical modelling Approach.....	204
6.2.1	Fluid flow modelling.....	204
6.2.2	Model definition.....	205
6.2.3	Mass Transport	206
6.2.4	Modelling Reacting flow in porous media	207

6.2.5	Chemical Reaction	208
6.2.6	Modelling dissolution/precipitation	208
6.3	Results and Discussion	209
6.3.1	Chemical interaction with the porous media.....	209
6.3.2	Reaction mechanisms	209
6.3.3	Model formulation	210
6.3.4	Fluid and Matrix	212
6.3.5	Mass Transfer in porous media.....	214
6.3.6	Reactions and Rate laws.....	217
6.3.7	Dissolution/Precipitation reaction.....	220
6.4	Summary.....	224
	References	225
	Chapter Seven.....	227
7	Conclusion and Recommendations for Future work	227
7.1	Conclusion	227
7.2	Recommendations for future work	229
	Appendices.....	232
	Appendix A: Linear variable differential transformer (LVDT) calibration	233
	Appendix B: Design and Engineering drawing for Perspex core holder.....	235
	Appendix C: Procedure for determination of pore volume, dead volume and porosity	241

List of Figures

Figure 1.1: Loose sand particles from unconsolidated reservoir rock flow into wells along with oil and gas damaging hardware and impending or stopping production (Energy future 2015).....	5
Figure 2.1: A sketch of shear failure as pressure is exerted axially (shown by the arrows) to the rock sample.....	26
Figure 2.2: Derivation of rates from concentration/time data (Appelo and Postma 2005)	34
Figure 2.3: Order of reaction: (a) Zeroth order; (b) First order; (c) Second order (Appelo and Postma 2005)	34
Figure 2.4: Kinetic dissolution of quartz based on equation (2.19) for a quartz soil (Appelo and Postma 2005)	36
Figure 2.5: Dissolved sulfate versus time for marine sediment incubated in the laboratory (Appelo and Postma 2005).....	37
Figure 3.1: Schematic diagram of the methodology	72
Figure 3.2: Structures of the selected oilfield chemicals	74
Figure 3.3: Unconfined compressive strength determination using uniaxial compression test device: (a) Sandstone and limestone samples with strain gauge; (b) Instron 3382; (c) Core sample positioned between the loading platen before test; and (d) Test device calibration	80
Figure 3.4: Rock triaxial equipment.....	82
Figure 3.5: Static saturation calibration for both sandstone and limestone	87
Figure 3.6 Sketch of Perspex core holder	89
Figure 3.7: Designed Perspex core holder showing: (a)–(b) component.	89
Figure 3.8: ICP-OES calibration	93

Figure 4.1: Characterisation of untreated sandstone: (a) SEM micrograph, (b) EDX scan, (c) XRPD bulk mineralogy, and (d) XRPD clay fraction identification. 103

Figure 4.2: Characterisation of untreated limestone: (a) SEM micrograph, (b) EDX scan, (c) XRPD bulk mineralogy and (d) XRPD clay fraction identification. 106

Figure 4.3: Uniaxial compression response pre-treatment and post chemical treatment of (a) sandstone and (b) limestone..... 107

Figure 4.4: Damaged limestone due to treatment with ATMP 110

Figure 4.5: The SEM micrograph and EDX scan of sandstone post saturation showing: (a) pitting with betaine treated sample indicated by red arrows; (b) the spread of altered minerals on unaltered grain in ATMP treated sample; (c) pitting with glutaraldehyde treated sample indicated by red ellipsoid and elemental composition of samples treated with: (d) betaine; (e) ATMP; (f) glutaraldehyde. 112

Figure 4.6: XRPD whole rock mineralogy and clay fraction identification of chemically treated sandstone: (a) betaine; (b) ATMP; (c) glutaraldehyde; (d) betaine (clay); ATMP (clay); (f) glutaraldehyde (clay)..... 114

Figure 4.7: The SEM micrograph and EDX scan of limestone post saturation with: (a) betaine treated limestone showing the spreading of altered minerals on unaltered grain; (b) precipitation of halite in ATMP treated limestone; (c) spreading of altered grains in the glutaraldehyde treated limestone; (d) betaine, EDX scan, (e) ATMP, EDX scan; (f) glutaraldehyde, EDX scan..... 117

Figure 4.8: XRPD whole rock mineralogy and clay fraction identification of chemically treated limestone: (a) betaine; (b) ATMP; (c) glutaraldehyde; (d) betaine (clay); (e) ATMP (clay); (f) glutaraldehyde (clay). 118

Figure 4.9: Comparison of the particle size distribution of the original brine and of (a) the effluent of sandstone and limestone in the brine; (b) the original brine and effluents from sandstone in betaine, ATMP and glutaraldehyde; (c) the original brine and effluents from limestone in glutaraldehyde, ATMP and betaine. 123

Figure 4.10: SEM micrograph and EDX scan of untreated sandstone: (a) orthorhombic detrital quartz coated with illite and interconnected pores (P); (b) quartz grains coated with clay minerals and a pronounced mixed-layer illite/smectite honeycomb morphology (white rectangle); (c) quartz overgrowth forming a distinct boundary contact with detrital quartz grains (d) EDX scan magnification: (a) 250 X; (b) 500 X; (c) 2.00 KX. 126

Figure 4.11: Mineralogical characterisation of untreated sandstone: (a) XRPD whole rock; (b) clay fraction. 127

Figure 4.12: SEM micrograph showing the pore spaces at various magnifications and EDX spectrum of untreated Edward Brown carbonate: (a) XRPD, 250X; (b) XRPD, 500X; (c) XRPD, 2.00KX; and (d) EDX spectrum. 128

Figure 4.13: Mineralogical analysis of untreated carbonate: (a) XRPD whole rock; (b) clay fraction. 129

Figure 4.14: SEM micrograph at various magnifications and EDX spectrum of untreated carbonate: (a) XRPD, 1.00KX; (XRPD), 500X; (c) XRPD, 2.50KX; and (d) EDX spectrum. 130

Figure 4.15: Grain size distribution profiles of: (a) original brine and brine effluents from sandstone and carbonate; (b) chemical effluents from sandstone; (c) chemical effluents from carbonate. 132

Figure 4.16: Stress-strain relationship and chemically treated: (a) sandstone with complete response to failure; (b) carbonate with complete response to failure; (c)

sandstone with stress-small strain response; (d) carbonate with stress-small strain response..... 136

Figure 4.17: SEM micrograph and EDX scan of brine treated leopard sandstone using different magnification: (a) SEM, 250X; (b) SEM, 500X; (c) SEM, 2.00KX; (d) EDX spectrum. 138

Figure 4.18: Mineralogical characterization of chemically treated leopard sandstone: (a) ATMP, SEM (Mag. 250X); (b) ATMP, EDX; (c) betaine, SEM (Mag. 250X); (d) betaine, EDX; (e) glutaraldehyde 1, SEM (Mag, 250X), (f) glutaraldehyde 1, EDX; (g) glutaraldehyde 2, SEM (Mag. 250X); (h) glutaraldehyde 2, EDX. 141

Figure 4.19: Characterisation of brine treated Edward Brown carbonate under magnification: (a) 200X; (b) 500X; (c) 2.00KX; (d) EDX scan 143

Figure 4.20: Mineralogical characterisation of chemically treated carbonates: (a) betaine-desert pink, SEM (Mag.250X, EDX; (b) betaine-desert pink, EDX; (c) ATMP-desert pink, SEM (Mag. 250X); (d) ATMP-desert pink, EDX; (e) glut-Edward brown 5, SEM (Mag. 250X); (f) glut- Edward brown 5, EDX; (g) glut-Edward brown 3, SEM (Mag.250X); (h) glut-Edward brown 3, EDX..... 145

Figure 5.1: Pre and post injection petrophysical characterisation: (a) lithium tracer profile for sandstone; (b) lithium tracer profile for carbonate, where Co and C represent initial and final lithium concentrations; (c) differential pressure profile during sandstone permeability measurement; (d) differentials pressure profile during carbonate permeability measurement; (e) average porosity and permeability of sandstone; (f) average porosity and permeability of carbonate. 159

Figure 5.2: Grain size distribution profiles of original brine, brine and chemical uptake and flow back effluents under dynamic condition [(a) sandstone, and (b) carbonate]. 161

Figure 5.3: SEM micrographs and EDX spectrum of the sandstone after exposure to (a1) brine showing pitting within the white ellipse, SEM; (a2) brine, EDX; (b1) betaine showing pitting with the white ellipse, SEM; (b2) betaine; EDX, (c1) ATMP showing pitting with the white square, SEM; (c2) ATMP, EDX; (d1) glutaraldehyde showing spreading of altered clay and calcite grains on the surface of the larger unaltered quartz grains locations identified by the arrows, SEM; and (d2) glutaraldehyde, EDX..... 163

Figure 5.4: Bulk mineralogy of clay fraction characterisation of treated sandstone with: (a1) Brine, XRPD; (a2) Brine, Clay fraction; (b1) Betaine, XRPD; (b2) Betaine, Clay fraction; (c1) ATMP, XRPD; (c2) ATMP, Clay fraction; (d1) Glutaraldehyde, XRPD; (d2) Glutaraldehyde, Clay fraction. 166

Figure 5.5: Carbonate post chemical treatment SEM micrograph showing filled pore spaces and EDX: (a1) brine, SEM; (a2) Brine, EDX; (b1) betaine SEM; (b2) Betaine, EDX;(c1) ATMP, SEM; (c2) ATMP, EDX; (d1) glutaraldehyde, SEM and (d) glutaraldehyde, EDX..... 170

Figure 5.6: Bulk mineralogy (weight %) and clay fraction characterisation of treated carbonate: (a1) Brine, XRPD; (a2) Brine, clay fraction; (b1) Betaine, XRPD; (b2) Betaine, clay fraction; (c1) ATMP, XRPD; (c2) ATMP, Clay fraction; (d1) Glutaraldehyde (XRPD); (d2) Glutaraldehyde, Clay fraction. 174

Figure 5.7: Stress-strain curve for untreated and chemically treated samples under dynamic condition: (a) sandstone and (b) carbonate. 177

Figure 5.8: Stress-small strain response for untreated and chemically treated samples under dynamic condition: (c) sandstone, and (d) carbonate..... 177

Figure 5.9: Relationship between porosity, UCS and Young’s Modulus of: (a) Sandstone; (b) Carbonate. The dot-dot line is the second order polynomial best fit to the experimental data.....	180
Figure 5.10: Comparison of the porosity – unconstrained compressive strength (UCS) relationship with existing correlations for (a) sandstone; and (b) carbonates ..	181
Figure 5.11: Stress-strain response during multiple failures at different confining pressure for: (a) Sandstone; (b) Carbonate.	184
Figure 5.12: Sandstone samples before test: (a, c & e) and after test (b, d & f).	188
Figure 5.13: Failure envelope for untreated, brine treated and betaine treated sandstone.....	190
Figure 5.14: q-p curves indicating shear failure mode devoid of compaction for sandstone	191
Figure 5.15: Comparison between the UCS at zero confining pressure and non-zero confining pressure.....	192
Figure 5.16: Bilinear yield surface of carbonate at peak states.....	193
Figure 5.17: q-p curves indicating various failure modes for carbonate	194
Figure 5.18: Carbonate samples before test: (a, c & e) and after test (b, d & f).	195
Figure 6.1: Model geometry and mesh arrangements	204
Figure 6.2: Sketch of Modelled domain and boundary notations	206
Figure 6.3: Model domain with (a) Velocity profile; and (b) Pressure distribution contour.....	213

Figure 6.4: Change in concentrations of reactant and product (a) ATMP (reactant); (b) consumed ATMP (reactant) (c) ATMP-Ca complex (product); and (c) produced ATMP-Ca complex (product) during chemical-rock interaction. 217

Figure 6.5: Precipitation of calcite (a) and reduction of porosity (b) over 24 hours. 222

Figure 6.6: Time dependent change in (a) Calcite content; and (b) Porosity. . 222

List of Tables

Table 2.1: Sorting classification (Folk 1968)	20
Table 3.1: Geometrical parameters and location of real reservoir and outcrop core samples used for static saturation	74
Table 3.2: Geometrical parameters and location of outcrop core samples used for dynamic saturation.....	76
Table 3.3: Geometrical parameters and location of outcrop core samples used for dynamic saturation and triaxial test.....	77
Table 3.4: Classification of deformability	83
Table 3.5: Brine composition	86
Table 3.6: Operating Conditions for ICP-OES in Axial View	92
Table 4.1: Elemental composition of sandstone using SEM-EDX pre and post treatment	104
Table 4.2: XRPD Bulk Mineralogy (wt %) based on reference intensity ratio (RIR) Method	104
Table 4.3: Relative percentage of clay minerals in the < 2 μ m clay size fraction	105
Table 4.4: Elemental composition of limestone using SEM-EDX pre and post treatment.	107
Table 4.5: Summary of mechanical test results for sandstone and limestone .	109
Table 4.6: Interaction between oilfield chemicals and formation rocks	119
Table 4.7: Key parameters of the grain size distributions of the original brine and the effluents from real core samples.....	124
Table 4.8: Key parameters of the grain size distributions of the original brine and the effluents from outcrop samples.	133

Table 4.9: UCS and Young's modulus of sandstone and limestone with recommended correction factors (ASTM C42-90) and BS (1881) under static condition.....	137
Table 5.1: D10, D50, D90 and sorting of brine, brine and chemical uptake and flowback effluents under dynamic condition (sandstone and carbonate).....	161
Table 5.2: Elemental composition of sandstone and carbonate cores pre and post chemical treatment.	167
Table 5.3: XRPD Bulk Mineralogy (wt %) based on reference intensity ratio (RIR) Method.	168
Table 5.4: Relative percentage of clay minerals in the <2 μ m clay size fraction.	168
Table 5.6: Summary of different models used to describe UCS-porosity relationship	181
Table 5.7: Summary of the effects of chemicals on particle size distribution, porosity, mineralogy and UCS of sandstone and carbonates.	183
Table 5.8: The dimensions and densities of sandstone and carbonate	185
Table 5.9: Summary of triaxial test results for sandstone and carbonate.....	187
Table 5.10: Summary of the models obtained at the two peaks to describe shear strength.....	187
Table 6.1: Model Parameters	211
Table 6.2: Variables for Reaction Rate	211
Table 6.3: Variables for Porous Matrix	212
Table 6.4: Mesh statistics.....	214

Nomenclature

Symbol	Description
A	Pre-exponential factor
A	Cross sectional area of sample
a	Borehole length
[A], [B], [C], [D]	Effective concentrations of reactants
a, b, c, d	Stoichiometry
A_0	Initial surface area
ATMP	Aminotrimethylphosphonic acid
b	Borehole diameter
c	Function of borehole diameters
CCS	Confined compressive strength
C_K	Total concentration of component K
C^5	Concentration of the 5 th solute
C/C_h	Normalised concentration values
C_i	Concentration of the species
C_0	Mean compressive strength
D	Diameter of the core sample
D	Diffusion coefficient
D_D	Tensor
D_F	Effective diffusion
DT_c	Acoustic travel time
D_K	Diffusion coefficient of component K
d_a, e_a	Mass transfer coefficients
d_m	Mean grain size
E	Young's modulus
E_a	Activation energy

EDXA	Energy-dispersive X-ray Spectrometry
EPS	Equivalent plastic strain
exp	Exponential
F	Force that accounts for the influence of small compressibility effects
g	Acceleration due to gravity
$G_i(j)$	Dissolution/Precipitation
$g(C)$	Function that comprises the effects of the solution composition
HECS	High Effective Confining Stress
IAP	Ionic Activity Product
IAEG	International Aerospace Environmental Group
i	Mineral
j	Mineral reaction
K	Permeability
K_b	Permeability to brine
K	Rate constant
K_{eq}	Equilibrium constant
K_r	Relative permeability
L	Length of core sample
LECS	Low Effective Confining Stress
LVDT	Linear variable differential transformer
m	Moles of solid at a given time
m_0	Initial moles of solid
m_s	Specific mass flux
N	Number of mineral reactions
N_i	Flux vector
p	Pressure at a given time

p	Effective stress that represents the normal compressive stress
p_0	Pressure at zero
p^0	Function of initial grain size and log-normal size distribution
P_{\max}	Maximum load
PSD	Particle size distribution
Q	Reaction quotient
q	Effective differential stress that represents the shear stress
q_u	Specific discharge normal to the boundary
q_{cr}	Critical value of specific discharge
q^5	Source term associated with chemical reaction in bulk fluids
Q_b	Flow rate
R	Gas constant
R	Overall rate
S_v	Sample volume
S_0	Apparent cohesion
S_i	Source/sink term
SSA	Specific surface area
SSA_0	Initial specific surface area
T	Absolute temperature
T_s	Relaxation time
u	Velocity
u_0	Initial velocity
UCT	Uniaxial compression test
UCS	Unconfined compressive strength
V	Rate of sand production per unit length of the wellbore

V	Solution volume
V	Kinematic viscosity
V_b	Bulk volume
V_d	Dead volume
V_p	Pore volume
V_p	P-wave velocity
V_T	Total volume
x_1, x_2	Material parameters
XRPD	X-Ray powder diffraction
z	Upward pointing vector
Φ	Porosity
φ	Phi
σ_{tn}	Tension
σ_{cn}	Compression
σ_u	Uniaxial strength
σ_0	To be calculated strength
Φ_c	Critical Porosity
Φ_{ct}	Critical Porosity in tension
Φ_{cc}	Critical Porosity in compression
$\langle y \rangle$	MacCauley brackets
Δt	Interval transit time
ρ	Density
\vec{u}	Velocity vector
η	Dynamic viscosity
μ	Viscosity
$\vec{\nabla} p$	Vector that points to the direction of the largest pressure

τ	Tortuosity
Ω	Saturation state
g_{α}^5	Distribution function of the concentration of the 5 th solute
$g_{\alpha}^{5,eq}$	Corresponding equilibrium distribution
e_{α}	Discrete velocity
ω_{α}	Weight coefficient
∇p	Pressure gradient
r_K	Rate contribution of mineral dissolution-precipitation reactions to component K per unit volume of fluid
λ	Erosion rate coefficient
ρ_s	Grain density
e^p	Plastic strain shear strain
e_{peak}^p	Shear strain at peak strength
λ_1, λ_2	Calibration constants
$\Delta\sigma$	Change in stress
$\Delta\varepsilon$	Change in strain
ΔP	Differential pressure
σ_1	Major principal stress
σ_2	Intermediate
σ_3	Minor principal stress
φ	Angle of internal friction
Γ_i	Diffusive flux
Θ	Volume fraction
ρ_b	Bulk density
ϵ_p	Maximum porosity
Ω	Saturation state

σ_n

Normal stress

σ_s

Shear stress

List of Publications

Journal Articles

1. **Wuyep, E.O.**, Oluyemi, G.F., Yates, K. and Akisanya, A.R. (2018). Geochemical effects of oilfield chemicals on sand failure in reservoir rocks. *Journal of Petroleum Science and Engineering*, 165, 347-357.
2. **Wuyep, E.O.**, Oluyemi, G.F., Yates, K. and Akisanya, A.R. (2018). Evaluation of the interaction between oilfield chemicals and reservoir rocks. Submitted to *Natural Resource Research Journal* - Springer.
3. **Wuyep, E.O.**, Oluyemi, G.F., Yates, K. and Akisanya, A.R. (2018). Numerical modelling of oilfield chemicals interaction with Porous Medium. Prepared for publication in: *Environmental and Engineering Geoscience*.

Conference Proceedings Paper and Abstracts

1. **Wuyep, E.O.**, Oluyemi, G.F., Yates, K. and Akisanya, A.R. (2018). Numerical Modelling of Oilfield Chemical Interaction with the Porous Medium. Geological Society of America (GSA) Annual meeting and Exposition, 4 – 7 Nov. 2018. Indianapolis, Indiana, USA
2. **Wuyep, E.O.**, Oluyemi, G.F., Yates, K. and Akisanya, A.R. (2018). Sand failure: Effect of Biocide on the geomechanical properties of outcrop carbonate rock under static condition. Recent Advances in Geo-Environmental Engineering, Geomechanics and Geotechnics, and Geohazard. Proceedings of the 1st Springer Conference of the Arabian Journal of Geosciences (CAJG-1), Tunisia, 182 - 185.
3. **Wuyep, E.O.**, Oluyemi, G.F., Yates, K. and Akisanya, A.R. (2016). Sand failure Prediction: Effects of oilfield chemicals on the Geomechanical Strength of the reservoir rocks. SPE SMN Euro forum Aberdeen Exhibition and Conference Centre (AECC) 30 – 31 March, 2016, UK.

4. **Wuyep, E.O.**, Oluyemi, G.F., Yates, K. and Akisanya, A.R. (2015). Geomechanical effects of oilfield chemicals on sand failure in reservoir rocks. Geological Society of America (GSA) Annual meeting and Exposition, 1 – 4 Nov. 2015, Baltimore Convention Centre, Mary Land, USA.

Poster Presentations

1. **Wuyep, E.O.**, Oluyemi, G.F., Yates, K. and Akisanya, A.R. (2015). Geomechanical effects of oilfield chemicals on sand failure in reservoir rocks. IDEAS Research Students Symposium on Innovation, Design and Sustainability, December 2015, IDEAS Research Institute, RGU, Aberdeen.
2. **Wuyep, E.O.** and Oluyemi, G.F., (2014). Hydrocarbon systems and integrated exploration risk reduction in the Southern Bida Basin of North Central Nigeria. IDEAS Research Students Symposium on Innovation, Design and Sustainability, December 2014, IDEAS Research Institute, RGU, Aberdeen.

Chapter One

1 Introduction

1.1 Background

Sand failure is a serious challenge in the oil and gas industry which if not properly handled can have a drastic effect on oil and gas production rate, cause downhole and subsea equipment damage and also increase the risk of catastrophic failure. Sand failure occurs when the formation stress exceeds the strength of the formation (Oyeneyin et al. 2005) which is derived majorly from the natural material that cements the sand grain and cohesive forces. The factors that induce the stress on the sand grains include pore-pressure (since the strength and stiffness of the rock depend on the stresses within the sand granular fabric), drag forces by producing fluids, over-burden pressure loading and tectonic actions. Danielson (2007) and Salama (2000) observed that sand, as a consequence of sand failure, is produced at the same time as the reservoir fluids (oil and gas) are produced (Figure 1.1). Sand production (Figure 1.1) costs the oil and gas industry tens of billions of dollars annually (Acock et al. 2004, Al_Awad 2001) to control, yet this produced sand is of no economic value. Several factors cause reservoir rocks to produce sand amongst which is the effect of the oilfield chemicals on the geomechanical strength of the rock. Oilfield chemicals have a wide range of applications in the petroleum industry and have been used extensively for decades as scale inhibitor, surfactant, biocide, stabilizer, friction reducer, gelling agent, depressant, retarder,

corrosion inhibitor, scavenger, defoamer, demulsifier and stimulant (Fink 2003). However, the potential deleterious geomechanical effects of these chemicals on the reservoir formation rocks are often not considered by the existing industry approach to geomechanical evaluation and sand failure/production prediction of the reservoir formation that have experienced substantial application of these chemicals. Geomechanical evaluation of the effects of these oilfield chemicals on the properties of the reservoir rock is required in the development of accurate sand failure models (Oluyemi et al. 2010). When a chemical is injected into the reservoir rock, it is thought to be adsorbed via electrostatic and Van der Waals interactions between the inhibitor and formation minerals (Jordan, et al. 1994a). The level of the chemicals adsorption into the formation is determined by such factors as temperature, pH, mineral substrate, chemical concentration and cations like Ca^{2+} . Adsorption is faster and higher with the minerals like clay that have large surface area (Jordan et al. 1994b). The dissolution and precipitation of minerals that takes place as a result of chemical-reservoir rock interaction is capable of altering porosity and permeability of the reservoir rock. The alteration which could be a decrease or an increase depending on the mineral composition of the rock, particle size distribution, shape of the particle and the pore space can also affect the stability of the reservoir rock (Lamy-Chappuis et al. 2014).

A number of studies (Wilson 2016, Oluyemi 2014, Mohamed and Nasr-El-Din 2013, Denney 2013, Bybee 2010, Egermann et al. 2011, Tomson et al. 2008, Metcalf and Devine 2004, Kan et al. 2005, 2004, Ramachandran et al. 1999) have been undertaken to evaluate the effects of the interaction

between chemicals like hydrochloric acid (HCl), carbon dioxide (CO₂), brine, water (H₂O), diethylenetriamine penta (methylene phosphonic acid) (DETPMP), 2,2 bis(4-hydroxyphenyl)-4-methylpentane (BHPMP), corrosion inhibitor and reservoir rocks (limestone, sandstone and chalk) on the reservoir strength and properties. The purpose of these studies were to: (i) predict evolution of petrophysical properties of sandstone during diagenesis (Yang et al. 2017); (ii) determine the mechanisms involved in the chemistry of water flowback in a water/shale interaction (Wilson 2016); (iii) establish fundamental knowledge on the behaviour of clastic and carbonate rocks in the presence of a scale inhibitor (Oluyemi 2014, Tomson et al. 2008); (iv) investigate the effect of CO₂-carbonate rock interaction on the strength and petrophysical properties of the rock (Mohamed and Nasr-El-Din 2013, Denney 2013, Egermann et al. 2011); (v) investigate wellbore integrity as it relates to CO₂ migration during CO₂/cement/brine interactions (Bybee 2010); and (vi) assess rock strength after acid fracture treatment using HCl (Metcalf 2004). However, the chemicals used in some of the works (Yang et al. 2017, Wilson 2016, Mohamed and Nasr-El-Din 2013, Denney 2013, Egermann et al. 2011, Bybee 2010; Metcalf and Devine, 2004) do not have the same chemistry as the chemical inhibitors used in the oil and gas reservoirs and the investigations were not conducted on both clastic and carbonate rocks simultaneously. Different chemicals have different properties/chemistries and each of them may exert different geochemical effects on the reservoir rocks on application. As such, the corresponding results from these prior studies cannot be extrapolated to predict the effects of commonly used oilfield chemicals on failure tendency of reservoir rocks. Other works (Oluyemi 2014, Tomson et al. 2008), did not integrate

mechanical testing and mineral characterisation to define failure mechanisms in their studies and furthermore only investigated the interaction of the inhibitors with sandstone. It is therefore, difficult and limiting to use such results to predict the failure effects of oilfields chemicals on the geomechanical strength of other conventional reservoir rocks.

The formation properties that may be affected by the chemical-formation interaction include: grain size distribution, porosity, hardness, permeability, Young's Modulus, Unconfined Compressive Strength (UCS), shear strength and tensile strength. The interaction between the oilfield chemicals and the formation rock may give rise to the weakening of rock grain fabrics which often cause reservoir rock instability. This impact can cause serious field challenges like alteration in reservoir permeability, compaction and subsidence which can lead to sand failure and eventual sanding. Ability to predict the geomechanical and geochemical responses of the formation in the presence of the oilfield chemicals plays a key role in avoiding borehole vulnerability which in most cases can lead to sand failure during production.

Predicting sand failure prior to drilling and production will enable evaluation of sand control options. The goal of Engineers and researchers has always been to have the ability to develop models that can predict if a well can produce the desired fluid without producing sand or predict that some type of sand control will be required before drilling or production take place. Different methods have been developed over the past decades (Veeken et al. 1991, Van den Hoek et al. 2000) to predict the onset of sand failure as a function of formation strength, drawdown and reservoir pressure. Wilson et al. (2002) focussed on establishing methodologies to predict the rate at

which sand is produced if the threshold for sanding is exceeded. Nevertheless, none of the methods accounted for the effect of oilfield chemicals.

This current work investigates the effects of biocide, scale and corrosion inhibitors (oilfield chemicals) on the geomechanical strength of reservoir rocks and mechanisms of failure of rock in contact with the chemicals by integrating a wide range of laboratory testing and numerical modelling. These tests include: mechanical testing (uniaxial compression test and triaxial test), grain size distribution analysis and analytical techniques such as scanning electron microscope (SEM), energy dispersive X-ray analysis (EDXA) and X-ray powder diffraction (XRPD).



Figure 1.1: Loose sand particles from unconsolidated reservoir rock flow into wells along with oil and gas damaging hardware and impending or stopping production (Energy future 2015).

1.2 Research gaps

Following the review of previous works as presented in section 1.1, there is currently lack of comprehensive technical knowledge and understanding on the failure effects of the oilfield chemicals on the geomechanical strength of reservoir rocks and mechanisms of this failure. Several models exist to predict sand production in the reservoir rock. However, none of these existing prediction models accounts for the effect of oilfield chemical-formation rock interactions.

1.3 Aim and Objectives

The aim of this research is to investigate the effects of oilfield chemicals on the geomechanical strength of reservoir rock numerically and experimentally and integrate these effects with an existing sand production prediction model.

The objectives of this research are as follows:

- i. To establish the mechanism of the interaction between the chemicals and the formation.
- ii. To investigate and establish the impact of inhibitors' injection on the mechanical, physical and petrophysical properties of the formation rock.
- iii. To evaluate the transformation/changes in the reservoir rocks due to geochemical reaction in space and time.

- iv. To develop models of oilfield chemicals' interaction with the various reservoir rocks suitable for integration with existing sand prediction model.

1.4 Methodology

This section gives a brief overview of the type of analysis and the parameters considered in this study. Mechanical testing, particle size distribution analysis and analytical (SEM, SEM/EDXA and XRPD) tests were conducted on sandstone and carbonate under static and dynamic conditions prior to and after treatment with the oilfield chemicals to determine the effect of scale inhibitor, corrosion inhibitor and biocide on the mechanical strength, Young's Modulus, grain size distribution, elemental and mineral composition, pore volume, mineralogy, porosity and permeability of sandstone and carbonate.

Numerical study was conducted using COMSOL multiphysics to evaluate the transformation/changes that took place due to oilfield chemical-formation interaction and establish the mechanism of interaction. The three-physics involved in the modelling are: fluid flow in porous medium solving Brinkman equation, chemical reaction solving Mass balance equation and rate laws to model the dissolution/precipitation of materials and transport of diluted species solving advection-diffusion equation.

1.5 Contributions to knowledge

The purpose for which this research was conducted is to contribute to the body of knowledge by providing a better understanding on the role the commonly used oilfield chemicals play in sand failure and production in the

oil and gas industry. Specifically, the research adds another dimension to our understanding of chemical-rock interaction and establishes failure mechanisms due to this interaction. The established failure mechanisms include:

- Adsorption of oilfield chemicals to the mineral surface;
- Dissolution of rock cementing materials thereby, increasing the porosity, leading to weakening of the grain-to-grain binding;
- Precipitation of new materials that emanated from the continuous interaction of the de-bonded materials with other particles, and increase in concentration of calcium cation (Ca^{2+}), pH leading to porosity reduction, strength increase and formation damage;
- Ionic substitution between the oilfield chemicals and the minerals;
- Expansion of the clay minerals in the presence of the chemicals leading to constriction of the pore throats.

Furthermore, the failure effects of the oilfield chemicals on the formation rocks have been evaluated, established and quantified. These failure effects can be integrated with existing sand failure prediction models in order to make them more robust and accurate. Specifically the model developed by Liu et al. (1997), Appelo and Postma (2005) and Andersen et al. (2012) will be candidate models for this integration.

1.6 Order of thesis presentation

This section gives a general overview of the thesis layout as represented by the following three broad sections: chapters, references and appendices. There are seven (7) chapters in the thesis.

Chapter one: This chapter presents the background to the research problem of this thesis including aim and objectives, methodology, research gap and contributions to knowledge.

Chapter two: This chapter presents a critical and systematic review of the previous works on the effects of chemical-rock interaction on key petrophysical and geomechanical properties (particle size distribution, porosity, permeability, mineralogy, Young's modulus, confined and unconfined compressive strength-CCS and UCS), mechanisms of interaction, numerical modelling of the interaction between the chemicals and the reservoir rocks, sand failure, causes of sand failure, failure mechanism and sand failure/production prediction. The chapter discusses the limitations of the existing models, which forms the basis upon which the current research was carried out.

Chapter three: This chapter presents a detailed discussion of methodology/approaches employed in this research to achieve the objectives of the thesis. The approaches include static saturation, analytical tests, mechanical test and particle size distribution analysis.

Chapter four: This chapter presents results of the experimental work carried out to investigate the interaction between oilfield chemicals and formation rock. It further discusses the effects of the interaction on a range of geomechanical, petrophysical and mineralogical properties of formation rock such as the UCS and Young's Modulus, particle size distribution, elemental and mineralogical composition of the rock under static condition using reservoir and outcrop samples.

Chapter five: This chapter presents results of the experimental work carried out to investigate the interaction between oilfield chemicals and formation rock. It further discusses the effects of the interaction on a range of geomechanical, petrophysical and mineralogical properties of formation rock such as the UCS, CCS and Young's Modulus, particle size distribution, elemental and mineralogical composition of the rock under dynamic condition using only outcrop samples.

Chapter six: This chapter presents the results of the numerical modelling carried out to validate the experimental results. It also discusses the procedure for the numerical modelling.

Chapter seven: This chapter presents the overall conclusions drawn from the research findings and recommendations for further work.

References

ACOCK, A., O'ROURKE, T., SHIRMBOH, D., ALEXANDER, J., ANDERSEN, G., KANEKO, T., VENKITARAMAN, A., LÓPEZ-DE CÁRDENAS, J., NISHI, M., NUMASAWA, M., 2004. Practical approaches to sand management. In: *Oilfield Review*, 10–27.

AL-AWAD, M.N. 2001. The mechanism of sand production caused by pore pressure fluctuations. *Oil & Gas Science and Technology – Rev. IFP* 56 (4): 339-345.

BYBEE, K., 2010. Two-Phase Cement/CO₂/Brine Interaction in Wellbore Environments. *Journal of Petroleum Technology*, 62(05), 78-80.

DANIELSON, T.J., 2007. Sand transport modeling in multiphase pipelines. *Offshore Technology Conference*. Offshore Technology Conference. Houston, TX: Offshore Technology Conference, April 30 – May 3, 1–11.

DENNEY, D., 2013. Simulating the Chemical Interaction of Injected CO₂ and Carbonic Acid. *Journal of Petroleum Technology*, 65(07), 125-127

EGERMANN, P., BEKRI, S. and VIZIKA, O., 2011. An integrated approach to assess the petrophysical properties of rocks altered by rock-fluid interactions (CO₂ injection). *International Journal Of Greenhouse Gas Control*. 5(3), 579-588.

FINK, J., 2003. *Oil field chemicals*. Gulf Professional Publishing. Burlington, 68 – 107

FUTURE ENERGY 2015. Connecting to the reservoir [online]. Available from: <http://energy-future.org/connecting-to-the-reservoir/> [Accessed 24 July 2015]

JORDAN, M., SORBIE, K., JIANG, P., YUAN, M. AND TODD, A., 1994a. TK" Mineralogical controls on inhibitor adsorption/desorption in Brent Group sandstone and their importance in predicting and extending field squeeze lifetimes. *Proceedings, European Production Operations Conference and Exhibition, Aberdeen, UK.*

JORDAN, M., SORBIE, K., PING, J., YUAN, M.D., TODD, A. AND HOURSTON, K., 1994b. Phosphonate Scale Inhibitor Adsorption/Desorption and the Potential for Formation Damage in Reconditioned Field Core. *SPE Formation Damage Control Symposium. Society of Petroleum Engineers.*

KAN, A.T., FU, G., TOMSON, M.B., AL-THUBAITI, M., XIAO, A. J. 2004. Factors affecting scale inhibitor retention in carbonate-rich formation during squeeze treatment, *SPE Journal* 9(3), 280–289. SPE80230-PA.

KAN, A.T., FU, G.M., TOMSON, M.B. 2005. Adsorption and precipitation of an aminoalkylphosphonate onto calcite. *Journal of Colloid and Interface Science*, 281(2), 275–284

LAMY-CHAPPUIS, B. ANGUS, D., FISHER, Q., GRATTONI, C. and YARDLEY, B.W., 2014. Rapid porosity and permeability changes of calcareous sandstone due to CO₂-enriched brine injection. *Geophysical Research Letters*, 41(2), 399-406.

METCALF, A. AND DEVINE, C., 2004. Evaluation of interaction of acid systems and formation samples improves production response. *Journal of Canadian Petroleum Technology*, 43(05).

MOHAMED, I. AND NASR-EL-DIN, H.A., 2013. Fluid/rock interactions during CO₂ sequestration in deep saline carbonate aquifers: laboratory and modeling studies. *SPE Journal*, 18(03), 468-485.

OLUYEMI, G., 2014. Conceptual Physicochemical Models for Scale Inhibitor-Formation Rock Interaction. *Petroleum Science and Technology*, 32(3), pp. 253-260.

OLUYEMI, G.F., OYENEYIN, B.M. and MACLEOD, C., 2010. UCS neural network model for real time sand prediction. *International Journal of Engineering Research in Africa*. 2 (01) 1-13.

OYENEYIN, M.B., MACLEOD, C., OLUYEMI, G. and ONUKWU, A., 2005. Intelligent Sand Management. Proceedings of *Nigeria Annual International Conference and Exhibition, Abuja, Nigeria*.

SALAMA, M.M., 2000. Influence of sand production on design and operations of piping systems. *Corrosion 2000*. NACE International.

TOMSON, M.B., KAN, A.T., FU, G., SHEN, D., NASR-EL-DIN, H.A., SAIARI, H.A. and AL THUBAITI, M.M., 2008. Mechanistic Understanding of Rock/Phosphonate Interactions and Effect of Metal Ions on Inhibitor Retention. *SPE Journal*, 13(03), 325-336.

VAN DEN HOEK, P. HERT, G.M., KOOIJMAN, A.P., DE BREE, P.H., KENTER, C.J. and PAPAMICHOS, E., 2000. A new concept of sand production

prediction: theory and laboratory experiments. *SPE Drilling & Completion*, 15(04), 261-273

VEEKEN, C., DAVIES, D., KENTER, C. and KOOIJMAN, A., 1991. Sand production prediction review: developing an integrated approach. *SPE annual technical conference and exhibition*. Society of Petroleum Engineers.

WILSON, A., 2016. Chemical Analysis of Flowback Water and Downhole Gas-Shale Samples. *Journal of Petroleum Technology*, 68(09), 114-115.

WILSON, S., MOSCHOVIDIS, Z., CAMERON, J. and PALMER, I., 2002. New model for predicting the rate of sand production. SPE/ISRM Rock Mechanics Conference, Irving Texas, 20-23 October 2002.

YANG, L., XU, T., LIU, K., PENG, B., YU, Z. and XU, X., 2017. Fluid-rock interactions during continuous diagenesis of sandstone reservoirs and their effects on reservoir porosity. *Sedimentology*, 64 (5), 1303-1321.

Chapter Two

2 Literature Review

2.1 Introduction

Chemical injection/squeeze has been a common operation in the oil and gas field primarily to either enhance productivity or inhibit scale formation and deposition and corrosion. Corrosion inhibitor is injected alongside acid to prevent corroding effect of acid on the pipelines and well casing. Scale inhibitor on the other hand is squeezed into the formation rock to prevent scale formation; whilst biocide is injected to control the activities of undesirable bacteria and microorganisms that cause corrosion of the pipelines and produce substances like H₂S, organic acids, etc. that affect the yield and quality of oil and gas negatively. However, the negative effects that arise from the interaction between these chemicals and reservoir on the reservoir geomechanical properties and strength has not been investigated and quantified. Therefore, it is imperative to evaluate the geomechanical effects of these oilfield chemicals on the properties of the reservoir rock to be able to develop accurate sand failure prediction models (Oluyemi et al. 2010).

This chapter reviews the relevant literature on the interaction between chemicals including oilfield chemicals and formation rock. Also reviewed are the mechanisms of chemical-rock interaction, the key petrophysical and

geomechanical properties of formation rock. The chapter also attempts to review the literature on sand failure, causes and mechanisms of sand failure as well as sand failure prediction models.

Chemicals are injected into the reservoir rocks every moment for different purposes, such as stimulating oil production, inhibiting scale formation, preventing corrosion, enhancing oil recovery, etc. It is noteworthy that some of these chemicals are adsorbed to the mineral surface of the formation rock enabling interaction. A number of experimental studies have been conducted (Khather et al. 2017, Yang et al. 2017, Wilson 2016, Tarkowski et al. 2015, Oluyemi 2014, Zemke et al. 2010, Gaus 2010, Egermann 2011, Seto et al. 1997) to investigate the interaction between chemicals and the formation rock and how it affects petrophysical and geomechanical properties of the rock.

2.2 Key petrophysical and geomechanical properties

The purpose of this section is to review effects of chemical-rock interaction on the key petrophysical properties such as pore volume, particle size distribution, mineralogy, porosity and permeability; and geomechanical properties like UCS, CCS and Young's modulus. The works of Zemke et al. (2010), Kaszuba et al. (2013), Oluyemi (2014), Tarkowski et al. (2015), Smirnov et al. (2016) and Khather et al. (2017) discussed alterations and changes of petrophysical properties (specific surface area, porosity, permeability, pore size and pore distribution) of reservoir rock due to dissolution/precipitation of minerals during rock-chemical interaction. However, the chemistries of the chemicals used in the studies by these authors do not have the same chemistries as those commonly used in the

oil field; therefore, the results cannot be extrapolated to interpret the behaviours of the commonly used oilfield chemicals.

2.2.1 Pore volume, Porosity and Permeability

Porosity is one of the key rock properties that is used to characterise porous media. Evaluating the effects of interaction between the oilfield chemicals and the reservoir rock on the reservoir properties is important to prevent the risk of rock strength weakening and sand failure and production potential that is associated with this interaction. Although some progress has been made to establish a relationship between porosity, permeability and rock strength, there is still lack of knowledge on how to factor the effect of oilfield chemicals into such a relationship. Experimental studies (Sarda et al, 1993; Palchik 1999) established that rock strength diminishes in tension and in compression when the volume fraction of voids increases. However, the rocks used for their investigation did not have contact with any fluid, hence the result cannot be used to interpret behaviour of reservoir rocks in contact with fluids. Further study by Zou et al. (2000) revealed that dolomite dissolution at the injection of brine has little effect on porosity and permeability. Li and Aubertin (2003), used the knowledge of existing relationships between porosity and uniaxial strength to appraise the influence of porosity on uniaxial strength in compression (σ_c) and tension (σ_t). The work proposed a general model that is applicable to various materials over a wide range of porosities. Unfortunately, the chemicals used in the study (water, moisture content and carbon dioxide) are quite different in composition from the oilfield chemicals being investigated in the current work, thus the results cannot be extrapolated to account for the effect of

the oilfield chemicals on the strength of the reservoir rock. Egermann et al. (2011) evaluated the petrophysical properties of carbonate rocks altered by fluid-rock interaction using CO₂. The work revealed that permeability evolution as a function of the degree of dissolution is highly dependent on the pore structure. Recent work by Oluyemi (2014) reported sand failure due to scale inhibitor-rock interaction and proposed conceptual physicochemical failure models to analyse and explain the inhibitor-formation interaction.

Some limitations are identified in this work:

- The models are theoretical and have not been completely proven.
- Mechanical test and mineral characterisation were not performed;
- Only scale inhibitor and sandstone were used, hence, results cannot to be used to predict the sanding potential of other reservoir rocks when interacted with other oilfield chemicals.

Tarkowski et al. (2015), Smirnov et al. (2016) observed no substantial change in the reservoir properties after the partial dissolution of the rock matrix and cements of sandstone and carbonates on exposure to CO₂. Zemke (2010) and Khather et al. (2017) reported a slight increase in porosity and permeability of dolostone and sandstone respectively on exposure to CO₂. A more recent study by Yang et al. (2017) investigated fluid-rock interaction during continuous diagenesis of sandstone reservoirs and their effects on reservoir porosity and found that calcite and feldspar dissolved due to the first organic acid incursion, resulting in the visual porosity increase. The result also showed that some minerals were precipitated at the last stage in an alkaline environment. It was concluded

that combination of petrographic observations, laboratory experiments and numerical simulations can, in addition to the ability to reconstruct the diagenetic process, also provide a quantitative evaluation and prediction of reservoir petrophysical properties.

2.2.2 Particle size distribution and sorting

The particle size distribution (PSD) of either powder, or granular material or particles dispersed in fluid can be defined as the mathematical function that indicates the sizes of particles (typically by mass) present and the proportions in which they are present. In determining the PSD, what comes to mind is the measurement of width or breadth of the distribution. Dvorkin and Gutierrez (2002) described particle size and particle size distribution as basic characteristics of sediment texture that has a direct effect on the quality of reservoir through porosity and permeability. PSD have influence on the reactivity of solids in chemical reactions and the mechanical properties (strength) of rock and soils. Oluyemi et al. (2006) postulated that a change in grain size distribution in a sand producing reservoir during oil and gas production can lead to a change in the UCS.

Rahmati et al. (2013) attributed particle detachment with high pressure gradient due to fluid flow. Prasad et al. (2009) and Silva et al. (2015) conducted an experiment on room-dry carbonate and sandstone rocks respectively to improve the method for estimating the strength and found that particle size distribution is key in the prediction of uniaxial compressive strength. They presented the following correlations in Equations 2.1 and 2.2 respectively, which account for the impact of PSD on the UCS of the reservoir rock:

$$UCS = 31,031/(DT_c^{1.5} d_m^{0.25}) \quad [2.1]$$

$$UCS = 9.42E^{0.25} / \phi^{0.45} d_m^{0.5} \quad [2.2]$$

where DT_c = acoustic travel time ($\mu\text{sec}/\text{ft}$), d_m = mean grain size (mm), E = Young's modulus, ϕ = Porosity.

However, the experiments were performed on untreated samples and in their natural form, hence cannot account for the effect of any fluids including the oilfield chemicals.

Sorting measures the variation in the grain size of a sample encompassing the largest parts of the size distribution measured from the cumulative curve. The best approach for quantifying grain sorting globally is the use of graphic standard deviation suggested by Folk (1968) which is calculated as:

$$\sigma_1 = \frac{\phi_{84} - \phi_{16}}{4} + \frac{\phi_{95} - \phi_5}{6.6} \quad [2.3]$$

Where ϕ_{84} , ϕ_{16} , ϕ_{95} and ϕ_5 are the percentile values. The grain size distribution in this case was assumed to follow a log-normal distribution (Andrew 2014). Folk (1968) used a classification scale for grain sorting (Table 2.1).

$$\phi = -\text{Log}_2 d \quad [2.4]$$

Table 2.1: Sorting classification (Folk 1968)

Logarithmic Standard Deviation	Sorting Classification
0.00 - 0.35	Very well sorted
0.35 - 0.50	Well sorted
0.50 - 0.71	Moderately well sorted
0.71 - 1.00	Moderately sorted
1.00 - 2.00	Poorly sorted
2.00 - 4.00	Very poorly sorted
> 4.00	Extremely poorly sorted

2.3 Geomechanical properties

Formation rock evaluation which is based on two major factors (internal and external) that govern rock strength is usually carried out prior to execution of any major oilfield development activity such as drilling to ascertain the strength of the rock. The interconnectivity that exists between the effects of these internal (porosity, particle size distribution, compressive strength, mineralogy, cementation and type of cementation) and external (stresses that act on the reservoir rock) factors often time influence sand production (Oluyemi 2007). In this section, the effect of chemical-rocks interaction on the UCS, CCS and the Young's modulus are reviewed.

2.3.1 Unconfined compressive strength (UCS) and Young's modulus

Strength is a key property used for reservoir characterisation, as such it is relevant to investigate how this rock property is influenced by changes in other factors like porosity, grain size distribution, permeability, mineralogical and elemental composition of rock matrix. Compression is the most commonly used mechanical test in rock strength determination. Uniaxial compressive strength from this test is an intrinsic property introduced as a specific parameter in failure criterion for rocks (Li and Aubertin 2003). Previous works have shown that rock fabric and petrography play an important role in controlling mechanical properties of rocks (Török and Vásárhelyi 2010). Experimental modelling to investigate the effect of CO₂-fluid-rock interaction on the strength of reservoir rock has been conducted by a number of researchers (Madland et al. 2011, Zangiabadi 2011, Shogenov et al. 2015, Lyu et al. 2016, Feng 2017,). They

found that the dissolution of minerals arising from the interaction between fluid and rock diminishes strength and stiffness. The results presented by these authors have provided vital information about rock properties/strength response to fluids invasion, but the substrate used for the studies was chalk which is naturally weaker than sandstone and carbonate. To establish a general relationship between porosity and UCS, Li and Aubertin (2003) used Equations 2.5 and 2.6 to formulate a general unified equation (Equation 2.7) that can be applied to both uniaxial tensile strength and uniaxial compressive strength of any material, but the model being developed for a variety of materials including rocks and soils may have some set back in that it is not developed specifically for the rocks, thus it may be difficult to delineate the cause of changes in rock strength.

$$\sigma_{tn} = \sigma_{t0}(1 - \phi)^m \quad [2.5]$$

$$\sigma_{cn} = \sigma_{c0}(1 - f\phi)^2 \quad [2.6]$$

$$\sigma_{un} = \left\{ \sigma_{u0} \left[1 - \sin^{x_1} \left(\frac{\pi \phi}{2 \phi_c} \right) \right] + \langle \sigma_{u0} \rangle \cos^{x_2} \left(\frac{\pi \phi}{2 \phi_c} \right) \right\} X \left\{ 1 - \frac{\langle \sigma_{u0} \rangle}{2\sigma_{u0}} \right\} \quad [2.7]$$

where σ_u is the uniaxial strength, which can be used for compression ($\sigma_u = \sigma_c$) and tension ($\sigma_u = \sigma_t$), σ_{tn} is the uniaxial tensile strength of the material with porosity ϕ , σ_{t0} is a parameter representing the calculated strength of a similar nonporous material and m is an empirical constant, f is a pore space structure parameter, ϕ_c is the critical porosity of material when σ_u is zero, in tension (ϕ_{ct}) or in compression (ϕ_{cc}), σ_{un} is expressed

for porosity ϕ ($\leq \phi_c$), with σ_{u0} corresponding to $n = 0$; x_1 and x_2 are material parameters, and MacCauley brackets $\langle y \rangle = 0.5(y + |y|)$.

The influence of porosity and permeability on the rock strength has been reported by a number of researchers (Reyer and Philipp 2014, Palchik and Hatzor 2004, Palchik 1999, Sabatakakis et al. 2008; Chang et al. 2006). Other works (Hagan et al. 2012, Bastos et al. 2007, Kahraman et al. 2008) studied the effect of saturation on the strength. Evaluation of the influence of chemical (HCl, detergent, KOH and distilled water) attack on physical and mechanical properties of some rock from Brazil was carried out by Bastos et al. (2007); it was found that the interaction between the chemicals and the rock led to 25%, 24%, 27% and 13% strength reduction owing to treatment with HCl, detergent, KOH and distilled water, respectively. Kahraman et al. (2008) reported a range of 5.0% to 25.3% strength reduction in marbles under uniaxial compression test (UCT), Brazilian tensile test (BTS) and point load index test (Is) due to water saturation. Hagan et al. (2011) investigated the effect of potassium chloride (KCl) and copper sulphate (CuSO_4) on coal and discovered an increase in strength. A study of chemical-rock interaction by Han et al. (2016) shows a weakening tendency of granite when treated with Na_2SO_4 , NaOH and NaHCO_3 and established that based on changes in porosities the relationships between the fracture toughness, splitting tensile strength, compressive strength of the specimens, and damage variable showed an exponential function, whilst the relations between the P-wave velocity of the granite specimens and the damage variable were linear.

Young's modulus measures the ability of materials to resist elastic deformation under load. In other words, it measures the stiffness of any material. The stiffness of a component reflects the deflection capacity under a given load which depends on the Young modulus of the material, the loading style, the shape and size of the component. A stiff material has a high Young modulus and changes its shape only slightly under elastic load. Han and Dusseault (2002) reported increase in rock deformability due to the reduction effect of water-sand interaction on the Young's modulus.

In spite of the progress made to report the influence of chemical-rock interaction on rock strength and stiffness by these scholars, there are some limitations:

- The fluids used in the studies have different chemistry from the commonly used oilfield chemicals.
- Non-integrated approach was used to determine the effect of the interaction on the strength.

2.3.2 Confined compressive strength (CCS)

Chang et al. (2006) empirically related UCS and internal friction angle of sandstone, shale, limestone and dolomite to rock physical properties such as interval transit time, Young's modulus and porosity (derived from geophysical well logs). The work revealed that a reasonable fit to the strength of weak sand was obtained when interval transit time (Δt) was used with equations 2.8 and 2.9. Furthermore, Equation 2.10 allows one to use porosity measurements to estimate weak sand UCS when porosity is relatively high ($\Phi > 0.1$). It was also pointed out that equation 2.11 fits some

of the weaker rocks with high interval transit time of sonic wave ($\Delta t < 80$) and equation 2.12 allows estimation of UCS from porosity data over a narrow range of porosities ($0.1 < \Phi < 0.25$). However, empirical equations are specific to a particular problem and do not have wide application.

$$1.4138 \times 10^7 \Delta t^{-3} \quad [2.8]$$

$$1.745 \times 10^{-9} \rho V_p^2 - 21 \quad [2.9]$$

$$277 \exp(-10\Phi) \quad [2.10]$$

$$(7682/\Delta t)^{1.82}/145 \quad [2.11]$$

$$143.8 \exp(-6.95\Phi) \quad [2.12]$$

Where Δt is the interval transit time ($\mu\text{s}/\text{ft}$), Φ is porosity, ρ is density (kg/m^3) and V_p is P-wave velocity (m/s).

Zoback (2007) defined strength as the value of the maximum principal stress at which a sample loses its ability to support the applied stress. The confined compressive strength simulates the strength of the reservoir at depth and it is determined using triaxial compression test (Figure 2.1). In an attempt to study the confined compressive strength model of rock for drilling optimization, Shi et al. (2015) proposed a new confined compressive strength model incorporating the effect of porosity and nonlinear characteristics with increasing confining pressure. The work found that the proposed model can be used to identify changes in UCS, in addition to identifying inefficient drilling situations of underbalanced and overbalanced drillings. However, the experiment was conducted on intact dry rock hence the results cannot be extrapolated to account for rock behaviour in the

presence of fluids. It is worthy of note that shear strength can be determined from either multi-stage triaxial test or conventional single-stage triaxial test.

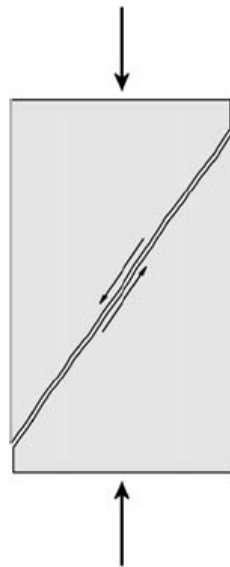


Figure 2.1: A sketch of shear failure as pressure is exerted axially (shown by the arrows) to the rock sample.

2.4 Mechanisms of Chemical-rock interaction

Understanding the mechanisms of interaction between the formation rock and the injected fluid plays a vital role in the determination of the effects the interaction would have on the strength of the formation rock. Zangiabadi et al. (2009, 2011) investigated the interaction between chalk and water and recognised dissolution of chalk grains and precipitation reaction as the cause of the water weakening in chalk. In a similar manner, Gutierrez et al. (2000) investigated the effect of fluid (water and synthetic oil) content on the mechanical behaviour of fractures in chalk to provide better understanding of the mechanisms of chalk-fluid interaction. It was found that capillary pressure and dissolution reaction are responsible for the chalk-water interaction. Again, water activity such as adsorption was

suggested by Risnes et al. (2003) as the mechanism governing the chalk-water interaction. According to Anderson et al. (2012) advection, diffusion, dissolution/precipitation, ion exchange, aqueous equilibrium of carbon species, and charge balance are mechanisms of interaction between water and chalk. Han and Dusseault (2002) identified quartz hydrolysis, dissolution/precipitation as well as clay swelling in addition to capillary force as the mechanisms responsible for the formation water-weakening activity with sand that leads to instability and strength reduction in sandstone reservoir.

2.5 Numerical studies of oilfield chemicals interaction with formation rock

Interactions between chemicals and rock formation has great influence on several geological and geomechanical processes like hydrocarbon migration, mineralisation, diagenesis, ground water evolution as well as sand production in earth sciences. Understanding of processes like flow, heat transfer, multi-species transport and chemical reactions is required to predict the amount of precipitation, or dissolution over the entire period of fluid-rock interaction (Bartels et al. 2002). It is worthwhile to develop numerical schemes that will accurately model the effects of these chemicals on the reservoir rocks. The use of numerical simulation has been on the increase for the past decades for geochemical studies. It is used to predict geochemical behaviour over time scales as well as for setting up and interpreting experiments to understand natural processes (Marty et al. 2015). In numerical modelling of fluid-rock interaction it is appropriate to consider heterogeneous chemical reactions that take place at the interface

between the aqueous reactive species in the pore-fluid and mineral in fluid-saturated porous rock masses (Reitner et al. 2013). Numerical modelling has been used by a number of researchers (Beyer, et al. 2012, Mohamed and Nasr-El-Din 2013, Kang et al. 2014, Marty et al. 2015) to investigate fluid-rock interaction. Several other authors (Tartakovsky et al. 2007, Molins et al. 2012, Noiriél et al. 2013, Ovaysi and Piri 2014, Kang et al. 2014, Chen et al. 2014, Liu et al. 1997) have discussed the complexity of the transport of a reactive fluid through a porous medium with dissolution as it embraces such processes as fluid flow, species transport, chemical reaction, and alternations of solid and porous structures. Coupling between advection, diffusion and reaction as well as the mineralogical heterogeneity that leads to complex reactive transport behaviours has also been discussed (Min et al. 2016).

The numerical approach adopted in this work is based on solving the equations of fully coupled fluid flow, species transport and chemical/rock reactions.

2.5.1 Geochemical interaction

O'Brien et al. (2000) stressed the need to consider heterogeneous porosity, mineral dissolution and precipitation and the feedback between the reactions and porosity in any realistic model. However, the focus of their work was on deionized water and calcite. Several works have modelled the interaction between CO₂ (Mohamed and Nasr-El-Din 2013, Bybee 2010, Xu et al. 2008, Kang et al. 2003), brine, water, acid (Metcalf 2004, Liu et al. 1997,) and reservoir rocks numerically. Similarly, Wang and Zhang (2015) developed a numerical framework to model and simulate gas-liquid-solid

three phase interaction. The framework was discovered capable of treating the complicated problem associated with three phase (gas-liquid-solid) simulation. Minton et al (2015) modelled migration-diffusion-reaction process numerically in an idealized Lithium-Sulphur cell and observed precipitation of species produced at the discharge end. Saldña et al. (2016) numerically simulated mixed-brine-CO₂/H₂S-rock interaction during the reinjection of non-condensable gases (NCG) to quantify the fluid-rock interaction for better understanding of NCG reinjection on the reservoir. An increase in porosity/permeability was discovered which diminishes further away from the injection point.

Kan et al. (2004) studied the factors affecting scale inhibitor retention in carbonate-rich formation during squeeze treatment to provide mechanistic understanding of how inhibitors react with core material and develop a methodology that predict and control inhibitor/core reactions. The author discovered that the extent of inhibitor retention by carbonate-rich formation rock was limited by the amount of calcite that can dissolve prior to inhibitor-induced surface poisoning. In a further study Kan et al. (2005) investigated adsorption and precipitation of an aminoalkylphosphonate onto calcite to quantify the interaction of phosphonates with calcite and relate phosphonate retention/release from formation material. It was found that after multiple layers of phosphonate are formed on the calcite surface, the solution is no longer at equilibrium with calcite.

Baraka-Lokmane and Sorbie (2010) conducted a coreflooding experiment to study the effect of scale inhibitor (SI) concentration and pH on the inhibitor adsorption and on the evolution of the inhibitor and cation (calcium

and magnesium); as well as study the transport and inhibitor/carbonate rock interactions when less than 1 pore volume of inhibitor solution is injected. It was found that the higher the concentration of SI and the lower the pH, the more calcium dissolution is observed in the effluent.

Kan et al. (1991) and Veloso et al. (2014) reported adsorption of scale inhibitor on sandstone formation. Yan et al. (2015) studied the interaction between scale inhibitors and shale and sandstone at an elevated temperature of 70°C to provide a mechanistic understanding on the effect of repeated squeeze treatment, temperature and flow rates on inhibitor return. It was observed that the sorption between phosphonate and Berea sandstones consists of fast and slow reactions which are kinetically controlled.

Ramachandran et al. (1999) in another study, applied the molecular modelling technique to investigate the binding, adsorption, and film formation of imidazoline to iron carbonate during the interaction between corrosion inhibitors and iron carbonate. The study revealed that inhibitor film formation to nonconductive material like iron carbonate (FeCO_3) may strengthen the corrosion product film, reducing its porosity and retarding transport of reactants to the corroding surface.

However, certain questions regarding the effect of the interaction between the scale inhibitor, corrosion inhibitor, biocide and the formation rock on the geomechanical strength of the rocks; and their mechanism of interaction still remained unanswered.

2.5.1.1 Fluid flow

The laws of flow of fluid through porous media are essential in the calculation of fluids (natural gas, underground water, petroleum) movement through sand and rocks. Pore-fluid flow is the main driving force that causes the heterogeneous chemical reactions at the interface between the pore-fluid and minerals. Fluid motion through the porous media is often described by Darcy law which is used as a momentum equation. In a single-phase flow, Darcy law modified from Liu et al. (1997) is given as:

$$\vec{u} = \frac{KK_r}{\mu} (\vec{\nabla}p + \rho\vec{g}\vec{z}) \quad [2.13]$$

Where K is the rock permeability; K_r and μ are the relative permeability and viscosity respectively; $\vec{\nabla}p$ is the vector that points to the direction of the largest pressure variation, g is acceleration due to gravity and the vector z is the unit upward pointing vector. However, a situation where the interaction leads to dissolution of mineral grains and precipitation of another mineral, the transport of species in the fluid cannot be accounted for by Darcy equation. This is because Darcy's law cannot handle the viscous effects that arise from the free fluid flow (Liu et al. 1997). Hence, the need for Brinkman equation (Equation 2.14) which is an extension of Navier Stokes equation. The boundary conditions are the inflow ($u \cdot n = u_0$) and outflow ($p = p_0$) with no slip ($u = 0$) wall. The general Brinkman equation is presented in Equation 2.14:

$$\rho \frac{\partial u}{\partial t} - \nabla \cdot \eta (\vec{u} + (\vec{u})^T) - \left(\frac{\eta}{K} u + \nabla p - F \right) = 0 \quad [2.14]$$

$$\nabla \cdot u = 0$$

Where ρ denotes density of the fluid (kg/m^3), η the dynamic viscosity (pa.s), u the velocity vector (m/s), p the pressure (Pa), k the permeability of the porous media (m^2) and F the force that accounts for the influence of small compressibility effects (N/m^2) and τ is tortuosity. The Brinkman equation interpolates between the Darcy's law and Stokes equation.

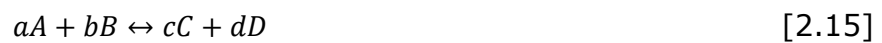
Fluid flow problem can be laminar or turbulent and has been solved by a number of studies using Darcy equation (Richardson et al. 2002), Navier Stokes equation (Strumendo 2016, Venetis 2015, Gupta and Kalita 2005, Assa et al. 2007) and Brinkman equation (Kobera 2008, Liu et al. 1997) depending on the nature of the problem. Bhatnagar-Gross-Krook (BGK) method which is a discrete approach for modelling fluid flow has also been used to model fluid-rock interactions with heterogeneous porosity (O'Brien et al. 2000). The current work models the flow of reactive oilfield chemicals through the porous media using the Brinkman equation which permits description of single-phase fluid motion in porous media and free fluid domains. The reason being that particles are expected to be released into the flow stream as the chemicals react with the porous media.

2.5.1.2 Chemical reaction

Chemical-rock interactions modelling include dissolution and precipitation of materials. When reactive fluids such as the inhibitor species are injected into the porous media, depending on such factors as temperature, pH, mineral substrate, chemical concentration and cations like Ca^{2+} they are adsorbed into the mineral surface via electrostatic and Van der Waal forces. The adsorbed chemical reacts with the mineral with which it is out of

equilibrium and begins to dissolve to produce new fluid composition at the interface which is supersaturated with respect to some other mineral phase (Putnis 2015). Most often the outcome of the chemical reaction with the rock is the dissolution and precipitation of mineral constituents of the rock which have been discussed extensively by several authors under various conditions as mentioned in section 2.5.1. The amount of mineral that dissolves or precipitates in a closed system is described in terms of chemical thermodynamics and kinetics as influenced by the superficial morphologies of the dissolving and precipitating species (Ritchie 1994). While thermodynamics stipulates the possible reactions, kinetics indicates the required time for the transformations and the reaction pathways.

In modelling the dissolution/precipitation due to chemical reaction, the law of mass action and rate law play key roles. Appelo and Postma (2005) defined both laws respectively for mineral dissolution and precipitation as:



$$K_{eq} = \frac{[C]^c [D]^d}{[A]^a [B]^b} \quad [2.16]$$

where K is the equilibrium constant and the [A], [B], [C] and [D] denote effective concentrations and a,b,c,d are the stoichiometry.

In a simple reaction where compound A is converted to B by the reaction:



Reaction rate is the change in concentration with time (Figure 2.2).

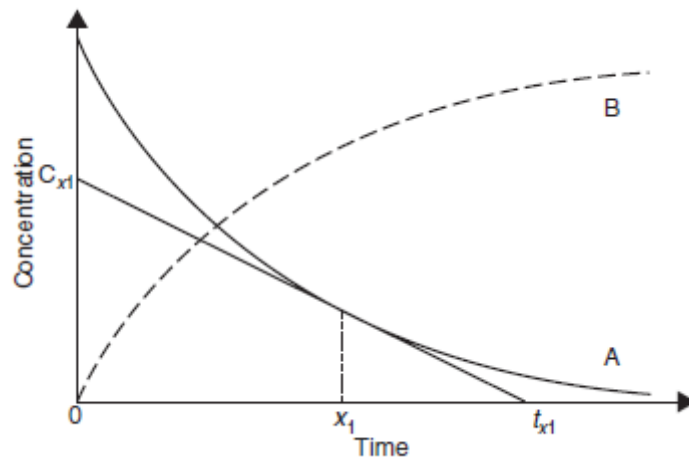


Figure 2.2: Derivation of rates from concentration/time data (Appelo and Postma 2005)

The rate (Equation 2.17) is given a negative sign for concentration decrease of a reactant, while rate is positive with product increase, hence the order of reaction can be zero, first or second (Figure 2.3).

$$rate = -dc_A/dt = dc_B/dt \quad [2.17]$$

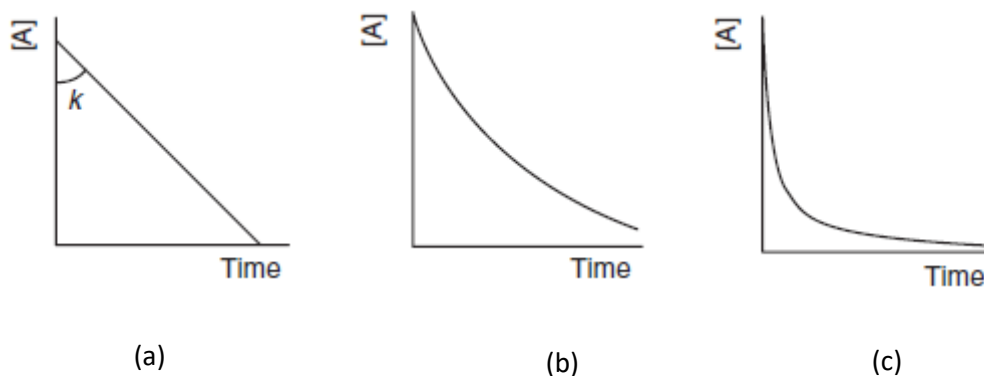


Figure 2.3: Order of reaction: (a) Zeroth order; (b) First order; (c) Second order (Appelo and Postma 2005)

Appelo and Postma (2005) gave a general rate law (Equation 2.18) for the change in solute concentration due to mineral dissolution/precipitation as:

$$R = k \frac{A_0}{V} \left(\frac{m}{m_0} \right)^{p^0} g(C) \quad [2.18]$$

where R is the overall rate (mol/L/s), k is the specific rate (mol/m²/s), A_0 is the initial surface area of the solid (m²), V is the volume of solution (m³), m_0 is the initial moles of solid, and m is the moles of solid at a given time. The overall rate in this case depends first on the specific rate k and the ratio of surface area, A_0 to the solution volume, V ; while, the factor $(m/m_0)^{p^0}$ is responsible for the changes in the surface area (reactive surface site). $P^0 = 2/3$ for a monodispersed population of uniformly dissolving or growing spheres and cubes, since m is proportional to the volume, or r^3 which is the radius of a sphere or the side of a cube, while the surface area is proportional to r^2 . However, for a polydisperse crystal populations, P^0 becomes a function of the initial grain size distribution and log-normal size distribution values of up to $P^0 = 3.4$ because the finest crystals dissolve selectively leading to modification of the size distribution (Dixon and Hendrix 1993). Larsen and Postma (2001) pointed out that the disintegration of the crystal during dissolution may also modify P^0 . $g(C)$ is a function that comprises the effects of the solution composition on the rate, like the pH, the distance from equilibrium, and the effects of the catalysis and inhibition (Lasaga 1998). The mentioned authors modelled dissolution/precipitation rate of quartz and calcite during the interaction between water and sandstone as well as water and carbonate. Realising that the rate must slow down as equilibrium is approached, Rimstidt and Barnes (1980) introduced saturation state (Ω) into the rate equation (Equation 2.19) to change it from a zero order rate equation (Figure 2.4).

$\Omega = IAP/K$, where IAP is the Ionic Activity Product and K is the solubility product and the reaction rate for sandstone becomes:

$$r = k * \left(1 - \frac{IAP}{K_{eq}}\right) \quad [2.19]$$

where k is the rate constant and is equal to $10^{-13.7}$ mol/m²/s at 25°C. Equation 2.19 defines the rate as positive at subsaturation, zero at equilibrium and negative at supersaturation (Figure 2.4).

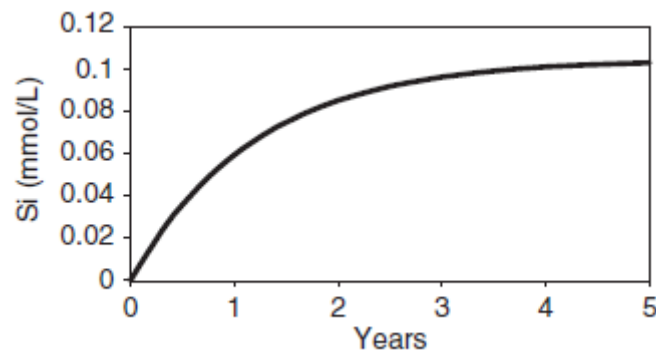


Figure 2.4: Kinetic dissolution of quartz based on equation (2.19) for a quartz soil (Appelo and Postma 2005)

The rate is independent of the reactant concentration in zeroth order kinetics which is an implication that the rate is being controlled by the reactants or other unknown factors. This is exemplified by the dissolution of sulfate in water (Figure 2.5). The straight line obtained in Figure 2.5 is an indication of zeroth order dependence on the sulfate concentration.

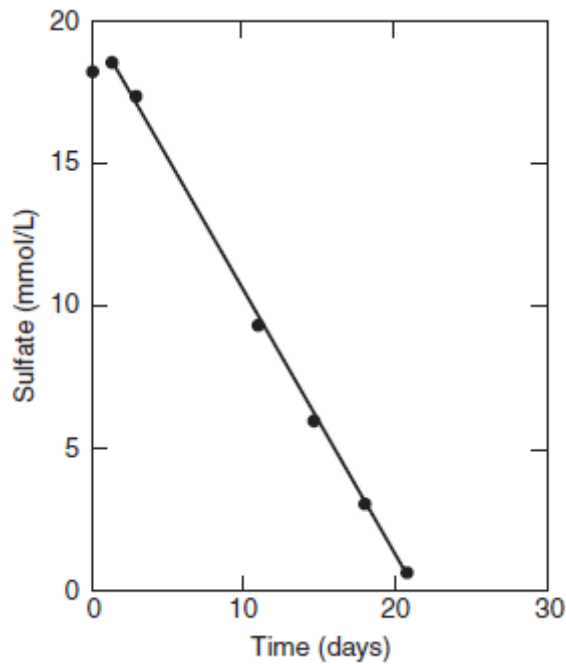


Figure 2.5: Dissolved sulfate versus time for marine sediment incubated in the laboratory (Appelo and Postma 2005).

Berner (1980) related the solubility of minerals to the dissolution mechanism and concluded that the dissolution of sparingly soluble minerals was controlled by surface processes while that of soluble minerals was controlled by transport processes predominantly.

Liu et al. (1997) reported that geochemical modelling and computer simulation provide understanding on the damage caused by precipitation during the reactions of acids with formation minerals. A two-dimensional simulator was used by the author; which fully couple fluid flow, species transport, rock/fluid reactions including effects of grain growth/dissolution and the alteration of porosity and permeability to mineral reactions. The simulator was based on a model that consists of a set of mass and momentum conservation equations. The mass conservation equation was however, supplemented with reaction rates and sink/source terms which represent injection/production wells. In order to complete the model

formulation, the author included grain texture-porosity-permeability relations.

Equations [2.18] and [2.19] were combined to model the dissolution and precipitation in the form:

$$R = k * \left(1 - \frac{IAP}{K}\right) * \frac{A_0}{V} * \left(\frac{m}{m_0}\right)^{p_0} \quad [2.20]$$

Equation 2.20 is adopted in the current work and it will be described extensively in section 6.3.6 of Chapter Six.

2.5.1.3 Transport

Transport of reactive fluid in heterogeneous porous media with dissolution of solid phase is a common phenomenon in rock formation and industrial application. The heterogeneity of porous media in geological formations is embodied by the heterogeneous porous structure (Min et al. 2016). Reactive transport modelling is an important tool used for the analysis of chemical, physical and biological processes in earth systems. Often time convection and diffusion play a key role in the transport of materials in air, water or soil. Several numerical methods have been implemented to model the fluid flow and transport with chemical reactions. Lattice Boltzmann (LB) method (Equation 2.21) was adopted by Kang et al. (2002), Kang, et al. (2006), Chen et al. (2013), Chen et al. (2014), Kang et al. (2014), Yoon et al. (2015).

$$g_{\alpha}^5(X + e_{\alpha}\delta_t, t + \delta_t) - g_{\alpha}^5(X, t) = -\frac{g_{\alpha}^5(X, t) - g_{\alpha}^{5,eq}(C^5, u)}{T_s} + \omega_{\alpha}q^5 \quad [2.21]$$

where g_{α}^5 is the distribution function of the concentration of the 5th solute, T_s is the relaxation time, q^5 is the source term associated with chemical

reaction in bulk fluids, $g_{\alpha}^{5,eq}$ is the corresponding equilibrium distribution, e_{α} and ω_{α} are the discrete velocity and associated weight coefficient, respectively, C^5 is the concentration of the 5th solute.

In an earlier study, Kang et al. (2002) developed a LB model that coupled flow and chemical dissolution for a system of two aqueous species in porous media. The study considered the dynamic processes of advection, diffusion, reaction, and the complex geometry of natural porous media as well as evolution caused by chemical reaction.

In a further study, Kang et al. (2006) extended the model to account for advection, diffusion, homogeneous reaction within multiple aqueous species using Lattice Boltzmann's method; the model also considers heterogeneous reactions between the aqueous solution and minerals, as well as changes in solid and pore geometry.

Molins et al. (2012) observed that despite the fact that Lattice Boltzmann models are efficient and scalable for flow and transport problems, they do not have ability to incorporate the wide range of geochemical reactions available in many geochemical models. Again, the author reported that particle methods such as smoothed particle hydrodynamics that appear robust, are not suitable for large systems. The author used a direct numerical simulation method to characterise transport and structural parameter changes during CO₂-rich brine injection. The injection of CO₂-rich brine through carbonate rock was seen to have induced different dissolution features depending on the CO₂ concentration. The model considered flow, transport and geochemical reactions at the pore scale

using Navier-Stokes and Advection-diffusion-reaction as governing equations:

$$\frac{\partial u}{\partial t} + (u \cdot \nabla)u + \nabla p = v\Delta u \quad [2.22]$$

$$\nabla \cdot u = 0$$

$$\frac{\partial \rho c_k}{\partial t} + \nabla \cdot \rho u c_k = \nabla \cdot \rho D_k \nabla c_k + \rho r_k \quad [2.23]$$

where u is the fluid velocity, ∇p the pressure gradient, c_k the total concentration of component k , ρ the fluid density, v the kinematic viscosity, D_k the diffusion coefficient of component k in the fluid, and r_k the rate contribution of mineral precipitation-dissolution reactions to component k per unit volume of fluid.

In a more recent study, Kang et al. (2014) further introduced a term that describes changes induced by dissolution of materials in porous media at the pore scale. The Lattice Boltzmann technique was applied by the author to coupled flow, transport, and reaction in a simple fracture medium and a more complex porous medium. It was found that the permeability-porosity relationship depends strongly on both different dissolution regimes characterized by Pe/Da and specific porous medium structure.

Cementation of porosity due to carbonate precipitation was observed during the interaction of CO_2 with minerals in fractured rocks, confined aquifer or fault (Yoon et al. 2015) using Lattice Boltzmann-based approaches for pore-scale reactive transport. According to Min et al. (2016) the transport of a reactive fluid through a porous medium with dissolution is a complicated

process as it embraces multiple physicochemical sub-processes including fluid flow, species transport, chemical reactions, and alternations of solid and porous structures.

Smooth particle hydrodynamic (SPH) method was used by Tartakovsky et al. (2007) to simulate reactive transport and mineral precipitation in porous and fractured porous media. The work demonstrated that SPH, Lagrangian particle method is an effective tool for studying pore-scale flow and transport and the reduction in the fluid flux increases with increasing Damkohler number for any reduction in porosity. The author claimed that precipitation in porous media occurs uniformly for large Peclet and small Damkohler numbers, and that complex processes like diffusion, reaction, and mineral precipitation were also modelled with ease.

2.6 Sand failure

Sand failure and production have been a serious challenge associated with unconsolidated or poorly consolidated formation rock. The effects of sand failure are detrimental to short or long term productivity of the well. The sand failure phenomenon is experienced severely in areas like Nigeria, Malaysia, Egypt, Venezuela, Indonesia, Trinidad, Canada and Gulf of Mexico which have their reservoirs at depths between 3,500 and 10,000 ft (Aborisade 2011). Several researchers and experts including Tronvoll et al. (2004), Fjar et al. (2008), Isehunwa and Farotade (2010), Richard (2013) have discussed sand failure taking into account different techniques used in the industry to control and alleviate the problem. The sand failure happens when formation stress exceeds the strength of the formation as the produced fluids ease the migration of the loose grains into the wellbore.

These stresses are shear, tensile, compressive and cohesive stresses. Khomehchi and Reisi (2015) described three types of sand production as:

- Transient - the concentration of sand that declines with time under constant well production condition;
- Continuous - a situation where the produced sand settles inside the wellbore and increases the hold-up depth;
- Catastrophic sand production which is referred to events where the well is suddenly blocked and/or die due to a high influx sand rate.

2.6.1 Causes of sand failure

Aborisade (2011) recognised that such factors as degree of consolidation, reduction of pore pressure, production rate, reservoir fluid viscosity and increasing water production throughout the life of a well influence the tendency of a producing well to fail at certain point. Rahmati et al. (2013) indirectly linked drilling operations, cyclic effects of shut-in and start-up, operational conditions, reservoir pressure depletion and strength-weakening effect of water to the cause of sand failure. Ability of any formation rock to withstand perforation depends solely and strongly on the grain-to-grain bonding. Yet, the degradation of the grain fabrics due to the interaction between oilfield chemical-reservoir rocks that leads to sand failure has not been properly accounted for. The degree of sand failure varies from reservoir to another. The mechanical characteristic that is considered when discussing the issue of consolidation is the compressive strength. However, the matrix material of well consolidated formation rock can also be degraded and produce sand when exposed to certain chemical attack.

2.6.2 Mechanisms of sand failure

Three types of failure mechanisms have been reported by Santarelli et al. (1989) as: (1) excess deviatoric stress governed by the pressure drawdown which is the difference between formation and bottom-hole pressures; (2) excess tensile effective stress that takes place when the pore pressure gradient at the wall is larger than the total radial stress gradient and the total radial stress turns to tensile; and (3) fine migration which can cause cyclic but stable sand production as it reduces the permeability of the formation rock. Sarda et al. (1993) proposed tensile rupture and compressive rupture as mechanisms of sand failure. The tensile rupture is said to be possible if the fluid pressure gradient at the production face is larger than the gradient of the radial stress. It is also possible when the tangential effective stress does not exceed the level of compressive failure. Sarda et al. (1993) also reported that the compressive rupture is possible if the pressure gradient remains smaller than the gradient of the radial stress, and the effective tangential stress reaches the unconfined compressive strength critical level under symmetrical conditions.

Seto et al. (1997) demonstrated the failure due to chemical effect [dodecyl trimethyl ammonium bromide ($C_{15}H_{34}NBr$), polyethylene Oxide (PEO), and aluminium chloride ($AlCl_3$)] on the strength of sandstone in an attempt to evaluate the effect of chemical solutions on the rock strength to provide an understanding of underlying mechanism of the chemically assisted fracturing. Han and Dusseault (2002) reported that variations of capillary force with water saturation have more influence on sand failure than

chemical reactions in weakly consolidated sandstone at the onset of water breakthrough.

An earlier study (Abass et al. 2002) observed that most existing mathematical models for predicting sand failure are based on failure mechanisms as pressure drawdown/compressive strength, Mohr Coulomb, cohesive strength failure, elastoplastic failure around perforation, viscoplastic modelling and empirical correlations. The author reports that there are no guidelines on how these models can be applied based on the characteristics of the formation rock, and proposed tensile, shear, cohesive and pore collapse as well as failure due to chemical effects that occur when the cementation materials are weakened due to chemical interactions as the mechanisms of failure. Khomehchi and Reisi (2015) associated sand failure mechanisms with formation strength, flow stability, viscous drag forces, and pressure drop in the wellbore; however, they identified formation strength, in-situ stress and production rate as the most critical factors. The mechanisms of failure such as tensile failure, shear failure, cohesive failure, pore collapse and failure due to the effects of chemical activities of water, gas and acid on the carbonate cementing materials are well discussed (Pinkert and Grozic 2014, Abass et al. 2002). Rahmati et al. (2013) reported that shear and tensile failure, critical pressure gradient, critical plastic strain and erosion are based on pressure drawdown.

2.7 Sand failure prediction

It is imperative to have good knowledge of sand failure behaviour as a function of oilfield chemical-rock interaction to provide information necessary for the establishment of wellbore stability during chemical

injections. This information is critical in the planning of offshore/onshore well and successful production. Sand production in formation rocks which are known to be relatively young in geologic age poses a big challenge to the oil and gas producing companies. Most of the offshore oilfields worldwide are domiciled in unconsolidated sand reservoir that are prone to various degrees of sand production.

Ability to predict reservoir failure prior to formation fluids production is vital in the decision of what control measures to put in place. Yet, the industry lacks enough predictable tools for this phenomenon due to insufficient knowledge on the conditions under which it takes place. For accurate prediction of sanding potential, such factors as formation strength, in-situ stress and production rate are usually critically considered. Other factors usually considered include mechanical properties, formation cementation, porosity, permeability, compressibility, pressure drawdown, and reservoir pressure. Several models exist to predict sand failure/production, however these models focused on the aforementioned factors without looking into the cause of changes in those factors; in addition, the models are specific to the type of the reservoir being studied. Earlier prediction techniques included statistical models, numerical models, mechanical logs, sand strength logs as well as core studies (Moore 1994). Completion engineers in newer offshore areas are often confronted with the challenge of sand production forecast, especially those without analogous reservoir performance that can serve as a guide. A combination of two or more of the existing categories are often used for prediction.

The first technique relating the formation shear strength to sand production in well was initiated by Stein and Hilchie (1972). Data from sonic and density logs were used to relate production of sand-producing well to that of the well under study. The limitation with this method is that a completed well that can produce large quantity of sand is required to obtain accurate and reliable results.

Tixier et al. (1975) developed a log-derived model that focused on the rock mechanical properties. It was found that a threshold for sand existed at $G/C_b = 0.8 \times 10^{12} \text{ Psi}^2$; where G is the Shear modulus and C_b is the bulk compressibility.

Coates and Denoo (1981) related sand production to the stress levels existing around the near-wellbore reservoir rock using Mohr's circle stress analysis technique. Although the technique is well accepted, it can only be used in a well that does not produce significant volume of water.

Weissenburger et al. (1987) developed an engineering system for sand production prediction. The system integrated geology, rock mechanics, logging and reservoir management information to forecast perforation cavity stability. Morita et al. (1989a, 1989b) presented numerical model and parametric studies on sand production prediction. The model considered well pressure, normalised pressure gradients at cavity surface, in-situ stresses, loading history, deformation and failure characteristics of rocks, perforation geometry and density, borehole inclination capillary pressure and rock-weakening effect by chemical reaction. However, their techniques are rarely used because they require extensive data.

In a different study, Liu et al. (1997) developed a two-dimensional geochemical simulator and its application to matrix analysis and design. The author observed that both laboratory and simulation results indicate that an acidizing treatment may induce formation damage due to the precipitation of by-products from the reactions of acids with the mineral component of rock. The simulator was also reported to be capable of predicting permeability and productivity improvements for typical acid treatments of both damaged and undamaged wells in sandstone formations whilst in carbonate formation it was capable of capturing the fingering and wormholing phenomena. The author provided a model that describes the dissolution rate as:

$$\frac{\partial R_i}{\partial t} = \sum_{j=1}^{N_s} G_{i(j)} \quad [2.24]$$

where i is the mineral, j is the mineral reaction, N is the number of mineral reactions (kinetic reactions) and a positive value of $G_{i(j)}$ stands for dissolution, whilst a negative value means mineral precipitation.

Van den Hoek et al. (2000) combined theory and laboratory experiment to predict sand failure around cylindrical and hemispherical cavities in weak sandstones under a variety of in-situ stress and dynamic conditions. Contrary to previous sand failure concepts, it was found that whether a cavity failed in compression or in tension for most cases depends only on cavity size, and not on near-wellbore stress or drawdown.

Wu et al. (2002) developed a model that was based on poroelasticity and brittle plasticity with a critical equivalent plastic strain on cavity surface as the sanding criterion. The model was applied in a gas field to predict sand production. The result shows that the calculated drawdown pressure was

higher than that based on linear elasticity, but lower than those based on plasticity model; depletion of reservoir pressure significantly decreased the critical drawdown pressure; and sand was produced when the fractures were visible on the cavity surface. Other works (Nouri et al. 2006, Vardoulaski et al. 1996, Scheuermann et al. 1998, Papamichos and Vardoulakis 2005, Nouri et al. 2003) used continuum models based on elasto-plastic constitutive models to model laboratory and field-based data. The models, besides lacking details of the underlying mechanics of sand production process, do not account for the effects of oilfield-rock interaction on the geomechanical strength. Most of the existing sand production prediction models have been extensively reviewed by Rahmati et al. (2013). The reviewed models were found to have fundamental deficiencies that need to be addressed. Some recommendations that cover many aspects were made by the study, however the aspect of the sand production due to the weakening effect of the oilfield chemicals was not given a consideration. Experimental study of the effect of water-cut on sand production by Wu et al. (2005) shows that effect of water-cut on the perforation strength and sand production is dependent on the mineralogical composition of the sandstone and the degree of residual water saturation are the determinant factors of the water-cut effect. The result also shows that the effect is most significant for sandstone that has high content of clay and low residual water saturation.

Boutt et al. (2011) presented a two-dimensional fluid-solid model that quantifies the micro-mechanisms responsible for sand production. The model was used to capture initial sand production due to early-time drawdown and later-time results show episodic sand production rate

associated with formation stability and instabilities. It was observed that high confining pressure inhibits the production of sand through elevated interparticle contact forces.

A volumetric sand production prediction model is presented by Azadbakht et al. (2012). The work associated sanding in injector well with the back-flow and cross-flow created during shut-in as well as waterhammer pressure pulsing in the wellbore resulting from the changes in flow rate. The model captures stress-dependent elasticity, hardening, softening and dilatancy of sandstone. The model states that the rate of sand mass produced is proportional to the specific flow rate:

$$\frac{dm_s}{dt} = \lambda \rho_s (1 - \phi) (q_u - q_{cr}) \quad [2.25]$$

where m_s is the specific mass flux, q_u = specific discharge normal to the boundary, q_{cr} = critical value of specific discharge, λ = erosion rate coefficient, ϕ = rock porosity and ρ_s = grain density.

In order to improve the sanding rate prediction, Papamichos, et al. (2001) suggested introduction of an erosion coefficient λ as a function of equivalent plastic strain (EPS) since using it as a constant could lead to physically unrealistic behaviour. As such sand is produced at the rate given by Equation 2.16 until the porosity of the element reaches a critical value. The model accounts for the water weakening effect.

Recent study by Suez and Subbiah (2014) produced a sand failure prediction model that quantified the fundamental properties that govern deformation and failure - Young modulus, UCS, poisson's ratio, internal friction angle, grain size, tensile strength, pore and overburden pressure as well as the magnitude and direction of the horizontal stresses. It was found

that sand failure occurs when the draw down pressure exceeds a critical limit. A more recent work by Khomehchi and Reisi (2015) presented a sand failure model that was developed using a ratio of Shear modulus to bulk compressibility technique; thus empirically relating the ratio of Shear modulus to bulk compressibility to sand influx.

Gholami et al. (2016) developed an analytical model to predict the volume of sand shear failure during drilling and production using a carbonate reservoir. The model determines the shape factor based on different failure criteria taking into account the effect of the intermediate principal stress.

The model is presented in Equation 2.26:

$$V = \frac{\pi}{4}ab - \frac{\pi}{4}b^2 = \frac{\pi}{4} \frac{1-c}{c} b^2 \quad [2.26]$$

Where V is the rate of sand production per unit length of the wellbore (m^3/m), a and b are the borehole length and diameter, respectively, c is a function of borehole diameters which is defined as:

$$c = b/a \quad [2.27]$$

The reliability of this model, however, is dependent on the accurate determination of the geomechanical parameters prior to the production stage when using wells and field data.

Li et al. (2018) presented a finite element based approach for simulating the realistic sanding process, putting into consideration the coupling between mechanical failure and hydrodynamic erosion of the rock. Results revealed that plastic strain and flow velocity around the wellbore majorly control sand production. The author further reported from the experimental point of view that initial sanding occurs only after the strength of the rock is outweighed and the material enters a strain softening phase. The models

developed for the prediction of sand production are presented in Equation 2.28 and 2.29:

$$\frac{\dot{m}}{\rho_s} \lambda (1 - \phi) \sqrt{q_i q_i} \quad [2.28]$$

$$\lambda(\gamma^p) = \begin{cases} 0 \\ \lambda_1 (e^p - e_{peak}^p) & \text{if } e^p < e_{peak}^p \\ \lambda_2 & \text{if } e_{peak}^p \leq e^p \leq e_{peak}^p + \lambda_2/\lambda_1 \\ & \text{if } e^p > e_{peak}^p + \lambda_2/\lambda_1 \end{cases} \quad [2.29]$$

where e^p is the plastic strain shear strain; e_{peak}^p is the shear strain at peak strength; and λ_1 and λ_2 are calibration constant which can be obtained through calibrations with experimental sand production data (Papamichos and Malmager 2001; Papamichos et al. 2001). This implies that sand erosion cannot occur until after the critical strength of the rock is exceeded as presented in equation 2.28.

2.8 Summary

An attempt has been made to present a general review of the effects of interaction between the reservoir rocks and CO₂, brine and a range of chemicals including oilfield chemicals on rock properties using experimental and numerical approaches. The review covers the key petrophysical (particle size distribution, pore volume, porosity and permeability), geomechanical (unconfined and confined compressive strength and Young's modulus) and geochemical (fluid flow, transport and chemical reaction) properties, relating them to sand failure/production potential in the reservoir rock. An extensive review of mechanism of fluid-rock interaction, sand failure, causes of sand failure, mechanism of sand failure and sand

failure prediction was also carried out. Again, attempts were made to identify and present the existing gap in knowledge on the effect of interaction between the oilfield chemicals and the reservoir rocks in this chapter.

References

ABASS, H., NASR-EL-DIN, H. and BATAWEEL, M., 2002. Sand control: sand characterization, failure mechanisms, and completion methods. SPE Annual Technical Conference and Exhibition. Society of Petroleum Engineers, San Antonio, TX, 29 September – 2 October.

ABORISADE, O.M., 2011. Practical Approach to Effective Sand Prediction, Control and Management Master's Thesis. African University of Science and Technology, Abuja. [online].

ANDERSEN, P.Ø., EVJE, S., MADLAND, M.V., HIORTH, A., 2012 A geochemical model for interpretation of chalk core flooding experiments. *Chemical Engineering Science*. 84, 218–241

ANDREW, M.G., 2014. Reservoir-Condition pore-scale imaging of multiphase flow. Imperial University, PhD thesis. Held OpenAIR [online].

APPELO, C., POSTMA, D., 2005. *Geochemistry, Groundwater and Pollution* Second edition. AA Balkema, Rotterdam.

ASSA, H., GUILBAUD, M and BA, M., 2007. Direct resolution of navier-stokes equations for a two-dimensional Numerical Wave Tank. Proceedings of the Sixteenth (2007) International Offshore and Polar Engineering Conference. Lisbon, Portugal, 1-6 July.

AZADBAKHT, S., JAFARPOUR, M., RAHMATI, H., NOURI, A., VAZIRI, H., and CHAN, D., 2012. A numerical model for predicting the rate of sand production in injector wells,” in *Proceedings of the SPE Deep Water and*

Completions Conference and Exhibition, 20-21, Galveston, Texas, USA, June 2012.

BARAKA-LOKMANE, S., SORBIE, K.S. 2010. Effect of pH and scale inhibitor concentration on phosphonate-carbonate interaction. *Journal of Petroleum Science Engineering* 70, 10–27.

BARTELS, J., KÜHN, M., SCHNEIDER, W., CLAUSER, C., PAPE, H., MEYN, V. and LAJCSAK, I., 2002. Core flooding laboratory experiment validates numerical simulation of induced permeability change in reservoir sandstone. *Geophysical Research Letters*, 29 (9), 1320.

BASTOS, M.D.P., MARQUES, E.G. and MOREIRA SOSSAI, F.J., 2007. Influence of Chemical Attack on Physical and Mechanical Properties of Some Dimension Stones from Brazil. In: *11th ISRM Congress* – Ribeiro e Sousa, Olalla and Grossmann (editors) Taylor & Francis Group, London.

BERNER, R.A., 1980. *Early diagenesis - a theoretical approach*. Princeton Univ. Press, 241 pp.

BEYER, C., LI, D., DE LUCIA, M., KÜHN, M. and BAUER, S., 2012. Modelling CO₂- induced fluid-rock interactions in the Altensalzwedel gas reservoir. Part II—coupled reactive transport simulation. *Environmental Earth Science* 67(2), 573–588.

BYBEE, K., 2010. Two-Phase Cement/CO₂/Brine Interaction in Wellbore Environments. *Journal of Petroleum Technology*, 62(05), 78-80.

BOUTT, D.F., COOK, B.K., WILLIAMS, J.R., 2011. A coupled fluid-solid model for problems in geomechanics: application to sand production.

International Journal for Numerical and Analytical Methods in Geomechanics (35), 997–1018.

CHANG, C., ZOBACK, M.D., KHAKSAR, A., 2006. Empirical relations between rock strength and physical properties in sedimentary rocks. *Journal of Petroleum Technology*, 51, 223-237.

CHEN, L., KANG Q., ROBINSON B., HE, Y-L., TAO, W-Q., 2013. Pore-scale modelling of multiphase reactive transport with phase transitions and dissolution/precipitation processes in closed systems. *Physical Review E* 87.

CHEN, L., KANG, Q., VISWANATHAN, H., TAO, W-Q., 2014. Pore-scale study of dissolution induced changes in hydrologic properties of rocks with binary minerals. *Water Resources*; 50:9343–65.

COATES, G.R., DENOO, S.A., 1981. Mechanical properties program using borehole analysis and Mohr's circle, in: Proc, SPW1A 22nd Annual Logging Symposium, Mexico City, 23–26 June.

DIXON, D.G. AND HENDRIX, J.L., 1993. Theoretical basis for variable order assumption in the kinetics of leaching of discrete grains. *AIChE Journal* 39, 904–907.

DVORKIN, J. and GUTIERREZ, M. 2002. Grain sorting, porosity and elasticity. *Petrophysics* 43, 185–196.

EGERMANN, P., BEKRI, S. and VIZIKA, O., 2011. An integrated approach to assess the petrophysical properties of rocks altered by rock-fluid interactions (CO₂ injection). *International Journal Of Greenhouse Gas Control*. 5(3) 579-588.

FENG X.T., 2017. *Rock Mechanics and engineering Volume 3: Analysing, Modelling & Design (Book)*. Technology & Engineering, Taylor & Francis Group, London.

FJAR, E., Holt, R., RAAEN, A., RISNESS, R, HORSRUD, P., 2008. Petroleum Related Rock Mechanics, *Development in Petroleum Science (33)*, Elsevier, Amsterdam, Netherlands.

FOLK, R.L., 1968. A review of grain-size parameters. *Sedimentology*, 6(2) 73-93.

GAUS, I., 2010. Role and impact of CO₂—rock interactions during CO₂ storage in sedimentary rocks. *International Journal of Greenhouse Gas Control* 4, 73–89.

GHOLAMI, R., AADNOY, B., RASOULI, V., and FAKHARI, N., 2016. An analytical model to predict the volume of sand during drilling and production. *Journal of Rock Mechanic and Geotechnical Engineering* 8 (4) 521-532.

GUTIERREZ, M., ØINO, L.E. and HØEG, K., 2000. The effect of fluid content on the mechanical behaviour of fractures in chalk. *Rock Mechanic and Rock Engineering* 33 (2) 93-117.

GUPTA, M. and KALITA, J., 2005. A new paradigm for solving Navier–Stokes equations: stream function-velocity formulation, *Journal of Computational Physics* 207 (1) 52–68.

HAGAN, P., SAYDAM, S., ELIAS, E., DENVER, L.D. and HEBBLEWHITE, B., 2012. The effect of certain chemical solutions on some material properties

of clay bearing rocks. In: Harmonizing Rock Engineering and Environment - *Proceedings of 12th ISRM Congress on Rock Mechanics*, Beijing, China 18 - 21 October.

HAN, T., SHI, Y., CHEN, J. and LI, Z., 2016. Effect of Chemical Corrosion on the Mechanical Characteristics of Parent Rocks for Nuclear Waste Storage. *Science and Technology of Nuclear Installations*, 1-11.

HAN, G. and DUSSEAULT, M., 2002. Quantitative analysis of mechanisms for water-related sand production. *International Symposium and Exhibition on Formation Damage Control*. Society of Petroleum Engineers.

ISEHUNWA, S. and FAROTADE, A., 2010. Sand Failure Mechanism and Sanding Parameters in Niger Delta Oil Reservoirs. *International Journal of Engineering Science and Technology*, 2(5) 777-782.

KAHRAMAN, S., GUNAYDIN, O. and FENER, M., 2008. The effect of water saturation on the strength of marbles. *ISRM International Symposium-5th Asian Rock Mechanics Symposium*. Tehran, Iran, 24-26 November 2008.

KANG, Q., CHEN, L., VALOCCHI, A. and VISWANATHAN, H., 2014. Pore-scale study of dissolution-induced changes in permeability and porosity of porous media. *Journal of Hydrology*. 517, 1049-1055.

KANG, Q., LICHTNER, P. and ZHANG, P. 2006. Lattice Boltzmann pore-scale model for multicomponent reactive transport in porous media. *Journal of Geophysical Research: Solid Earth* (1978–2012). 111(B5).

KANG, Q., ZHANG, D. and CHEN, S., 2003. Simulation of dissolution and precipitation in porous media, *Journal of Geophysical Research*, 108, 2505.

KANG, Q., ZHANG, D., CHEN, S. and HE, X., 2002. Lattice Boltzmann simulations of chemical dissolution in porous media, *Physical Review*, E 65: 036318.

KAN, A.T., YAN, L., BEDIENT, P. B., ODDO, J. E. and TOMSON, M. B. 1991. Sorption and Fate of Phosphonate Scale Inhibitors in the Sandstone Reservoir: Studied by laboratory apparatus with core material. SPE Production Operations Symposium, 7-9 April, Oklahoma City, Oklahoma.

KAN, A.T., FU, G., TOMSON, M.B., AL-THUBAITI, M., XIAO, A. J. 2004. Factors affecting scale inhibitor retention in carbonate-rich formation during squeeze treatment, *SPE Journal* 9(3), 280–289. SPE80230-PA.

KAN, A.T., FU, G.M., TOMSON, M.B. 2005. Adsorption and precipitation of an aminoalkylphosphonate onto calcite. *Journal of Colloid and Interface Science*, 281(2), 275–284

KASZUBA J., YARDLEY B. and ANDREANI M., 2013. Experimental perspectives of mineral dissolution and precipitation due to carbon dioxide-water-rock interactions. *Reviews in Mineralogy and Geochemistry*, 77(1) 153-188.

KHAMEHCHI, E. and REISI, E., 2015. Sand production prediction using ratio of shear modulus to bulk compressibility (case study). *Egyptian Journal of Petroleum*, 24(2), 113-118.

KHATHER, M., SAEEDI, A., REZAEI, R., NOBLE, R., and GRAY, D., 2017. Experimental investigation of changes in petrophysical properties during

CO₂ injection into dolomite-rich rocks. *International Journal of Greenhouse Gas Control*, 59, 74-90.

KOBERA, M., 2008. Brinkman equations as a model for flows in porous media, in WDS'08 Proceedings of Contributed Papers, Part III, 38-43.

LARSEN, O. and POSTMA, D., 2001. Kinetics of bulk dissolution of lepidocrocite, ferrihydrite, and goethite. *Geochim. Cosmochim. Acta* 65, 1367–1379.

LASAGA, A.C., 1998. *Kinetic theory in the earth sciences*. Princeton Univ. Press, 811.

LI L. and AUBERTIN M., 2003. A general relationship between porosity and uniaxial strength of engineering materials. *Canadian Journal of Civil Engineering*, 30(4), 644–58.

LI, X., FENG, Y., GRAY, K.E. 2018. A hydro-mechanical sand erosion model for sand production simulation. *Journal Petroleum Science and Engineering*, 166, 208-224.

LIU, X., ORMOND, A., BARTKO, K., LI, Y. and ORTOLEVA, P., 1997. A geochemical reaction-transport simulator for matrix acidizing analysis and design. *Journal of Petroleum Science and Engineering*, 17(1-2), 181-196.

LYU, Q., RANJITH, P.G., LONG, X.P. and LI, B., 2016. Experimental Investigation of Mechanical Properties of Black Shales after CO₂-water-rock Interaction. *Materials* 9, 663.

MADLAND M. V., HIORTH A., OMDAL E., MEGAWATI M., HILDEBRAND-HABEL T., KORSNES R. I., EVJE S. and CATHLES L. M., 2011. Chemical

alterations induced by rock–fluid interactions when injecting brines in high porosity chalks. *Transport in Porous Media*, 87(3), 679–702.

MARTY N., CLARET F., LASSIN A., TREMOSA J. and BLANC P., 2015. A database of dissolution and precipitation rates for clay-rocks minerals. *Applied Geochemistry*, 55, 108–118.

METCALF, A. AND DEVINE, C., 2004. Evaluation of interaction of acid systems and formation samples improves production response. *Journal of Canadian Petroleum Technology*, 4(05), 49-56.

MIN, T., GAO, Y., CHEN, L. KANG, Q., and TAO, W.Q., 2016. Changes in porosity, permeability and surface area during rock dissolution: Effects of mineralogical heterogeneity. *International Journal of Heat and Mass Transfer*, 103, 900-913.

MINTON, G. PURKAYASTHA, R., WALUS, S., MARINESCU, M., ZHANG, T. and OFFER, G., 2015. Modelling migration-diffusion reaction processes in an idealised lithium-sulfur cell. [online]. Available from: https://www.comsol.com/paper/download/358031/minton_presentation.pdf [Accessed 13 October 2016].

MOHAMED, I. and NASR-EL-DIN, H.A., 2013. Fluid/rock interactions during CO₂ sequestration in deep saline carbonate aquifers: laboratory and modelling studies. *SPE Journal*, 18(03), 468-485.

MOLINS, S., TREBOTICH, D., STEEFEL, C. and SHEN, C., 2012. An investigation of the effect of pore scale flow on average geochemical

reaction rates using direct numerical simulation. *Water Resources Research* 48(3).

MOORE, W.R. 1994. Sand Production Prediction. *Journal of Petroleum Technology*, 955. SPE 29331-PA.

MORITA, N., WHITFILL, D.L., MASSIE, I. and KNUDSEN, T.W., 1989a. Realistic Sand Production Prediction: Numerical Approach. *SPE production engineering*, 4(01), 15-24.

MORITA, N., WHITFILL, D.L., FEDDE, O.P. and LEVIK, T.H., 1989b. Parametric study of sand-production prediction: analytical approach. *SPE production engineering*, 4(01), 25-33.

NOURI, A. VAZIRI, H., BELHAI, H. and ISLAM, M., 2006. Sand-production prediction: a new set of criteria for modeling based on large-scale transient experiments and numerical investigation. *SPE Journal*, 11(02), 227-237.

NOURI, A., VAZIRI, H., BELHAI, H. and ISLAM, R., 2003, Comprehensive approach to modelling sanding during oil Production," SPE 81032, Presented at the SPE Latin American and Caribbean Petroleum Engineering Conference held in Port-of-Spain, Trinidad, West Indies, 27 - 30 April 2003.

NOIRIEL, C., GOUZE, P. and MADÉ, B., 2013. 3D analysis of geometry and flow changes in a limestone fracture during dissolution. *Journal of hydrology*, 486, 211-223.

O'BRIEN, G., BEAN, C. and MCDERMOTT, F., 2000. Numerical and experimental modelling of fluid-rock interactions with heterogeneous porosity. *Journal of Geochemical Exploration*, 69, 119-125.

OLUYEMI, G., 2014. Conceptual Physicochemical Models for Scale Inhibitor-Formation Rock Interaction. *Petroleum Science and Technology*, 32(3), 253-260.

OLUYEMI, G.F., OYENEYIN, B.M. and MACLEOD, C., 2010. UCS neural network model for real time sand prediction. *International Journal of Engineering Research in Africa*, 2, 1-13.

OLUYEMI, G.F., 2007. Intelligent grain size profiling using neural network and application to sanding potential prediction in real time. Robert Gordon University, PhD thesis. Held on OpenAiR [online].

OLUYEMI, G., OYENEYIN, B. and MACLEOD, C., 2006. Prediction of directional grain size distribution: An integrated approach. *Nigeria Annual International Conference and Exhibition*. Society of Petroleum Engineers. Abuja, Nigeria, July 31 – Aug. 2.

OVAYSI, S. and PIRI, M., 2014. Pore-space alteration induced by brine acidification in subsurface geologic formations. *Water Resources Research*, 50(1), 440-452.

PALCHIK, V., HATZOR, Y., 2004. The Influence of Porosity on Tensile and Compressive Strength of Porous Chalks. *Rock Mechanics and Rock Engineering* 37 (4), 331-341.

PALCHIK, V., 1999. Influence of porosity and elastic modulus on uniaxial compressive strength in soft brittle porous sandstones. *Rock Mechanics and Rock Engineering*, 32(4), 303-309.

PAPAMICHOS, E. and I. VARDOULAKIS, I., 2005. Sand erosion with a porosity diffusion law. *Computers and Geotechnics*, 2(1), 47-58.

PAPAMICHOS, E. and MALMANGER, E.M., 2001. A sand-erosion model for volumetric sand predictions in a North Sea reservoir. *SPE Reservoir Evaluation Engineering* 4, 44-50.

PAPAMICHOS, E., VARDOULAKIS, I., TRONVOLL, J. and SKJAERSTEIN, A., 2001. Volumetric sand production model and experiment. *International Journal for Numerical and Analytical Methods in Geomechanics* 25, 789-808.

PINKERT, S. and GROZIC, J., (2014). Failure mechanisms in cemented hydrate-bearing sands. *Journal of Chemical and Engineering Data* 60(2), 376-382.

PRASAD, U., CURRY, D.A., MOHANTY, B. and NASSERI, F., 2009. Improved Method for Estimating the Strength of Carbonate Rocks. *International Petroleum Technology Conference*. Salt Lake City, Utah, 27 - 30 June.

PUTNIS, A., 2015. Transient Porosity Resulting from Fluid-Mineral Interaction and its Consequences. *Reviews in Mineralogy and Geochemistry* 80(1), 1-23.

RAHMATI, H., JAFARPOUR, M., AZADBAKHT, S., NOURI, A., VAZIRI, H., CHAN, D. and XIAO, Y., 2013. Review of sand production prediction models. *Journal of Petroleum Engineering*, 1-16.

RAMACHANDRAN, S., JOVANCICEVIC, V. and WARD, M.B., 1999. Understanding interactions between corrosion inhibitors & iron carbonate

films using molecular modelling, Houston, NACE International, paper no. 7).

REITNER, J., STUWE, K. and TRAUTH, M.H., 2013. Lecture Notes in Earth system Sciences. Vol. 110-144, 73-93.

REYER, D., PHILIPP, S. 2014. Empirical relations of rock properties of outcrop and core samples from the Northwest German Basin for geothermal drilling. *Geothermal Energy Science*, 2, 21-37.

RICHARD, U.R., 2013. Sand & fines in multiphase oil and gas production. Master's thesis, Norwegian University of Science and Technology, Trondheim.

RICHARDSON, J. F., HARKER, J. H., and BACKHURST, J. R., 2002. Flow of fluids through granular beds and packed columns. In: *Chemical Engineering, Particle Technology and Separation Processes*, vol. 2, 5th ed. Butterworth-Heinemann, Oxford. 191-236.

RIMSTIDT, J.D. and BARNES, H.L., 1980. The kinetics of silica water reactions. *Geochim. Cosmochim. Acta* 44, 1683-1699.

RISNES, R., HAGHIGHI, H., KORSNES, R.I. and NATVIK, O., 2003. Chalk-fluid interactions with glycol and brines. *Tectonophysics* 370, 213-226.

RITCHIE, G., 1994. Role of dissolution and precipitation of minerals in controlling soluble aluminium in acidic soils. *Advances in Agronomy*, 53, 47-83.

SABATAKAKIS, N., KOUKIS, G., TSIAMBAOS, G. and PAPANAKLI, S., 2008. Index properties and strength variations controlled by microstructure for sedimentary rocks. *Engineering Geology* 97, 80–90.

SALDAÑA, A.G.M., KAYA, E., ZARROUK, S.J., CALLOS, V. and MOUNTAIN, B.W., 2016. Numerical simulation of mixed brine-CO₂/H₂S-Rock interaction during the reinjection of non-condensable gases. In: 41st Workshop on Geothermal Reservoir Engineering Stanford University. Stanford, California SGP-TR-209.

SANTARELLI, F., DETIENNE, J. and ZUNDEL, J., 1989. Determination of the mechanical properties of deep reservoir sandstones to assess the likelihood of sand production. In: Maury, V., Fourmaintraux, D., (Eds), *Rock at Great Depth*. A.A. Balkema, Brookfield, VT, 779-787.

SARDA, J., KESSLER, N., WICQUART, E., HANNAFORD, K. and DEFLANDRE, J., 1993. Use of porosity as a strength indicator for sand production evaluation. *SPE 47196*. In: Proceedings of SPE Annual Technical Conference and Exhibition. *Society of Petroleum Engineers*, Richardson, Texas, 381–388.

SCHEUERMANN, A., STAVROPOULOU, M., VARDOULAKIS, I., PAPANASTASIOU, P., 1998. A sand erosion problem in axial flow conditions on the example of contact erosion due to horizontal groundwater flow. *IUTAW, Kluwer Academic Publishers, Dordrecht*, 169-175.

SHOGENOV, K., SHOGENOVA, A., VIZIKA-KAVVADIAS, O. and NAUROY, J.F., 2015. Experimental Modelling of CO₂-fluid-rock interaction: the

evolution of the composition and properties of host rocks in the Baltic Region. *Earth Space Science* 2, 262–284.

SETO, M. NAG, D.K., VUTUKURI, V.S. and KATSUYAMA, K., 1997. Effect of chemical additives on the strength of sandstone. *International Journal of Rock Mechanics and Mineral Science* 34, 3-4.

SHI, X., MENG, Y., LI, G., LI, J., TAO, Z. and WEI, S., 2015. Confined compressive strength model of rock for drilling optimization. *Petroleum*, 1(2015), 40-45.

SILVA, G., RABE, C., NUNES, A., GARCIA, J. and PRASAD, U., 2015. Development of a new Correlation Based on Grain Size Distribution to Estimate Sandstone Reservoir Uniaxial Compressive Strength. *13th ISRM*, Montreal, Canada, 237.

SMIRNOV, N., TORRES, M., VALENTE, L., TADZHIBAYEV, R., VLADIMIROVICH, R, VITALIEVICH, K. and PAVLOVICH, K., 2016. Geomechanics based completion strategy optimization for the chemical interaction effect with mechanical properties. SPE Annual Technical Conference and Exhibition. Moscow, Russia, 24 – 26 October.

STEIN, N. and HILCHIE, D.W., 1972. Estimating the maximum production rate possible from friable sandstones without using sand Control. *Journal of Petroleum Technology*, 1157-1160.

STRUMENDO, M., 2016. Solution of the incompressible Navier–Stokes equations by the method of lines. *International journal for Numerical methods in fluids*, 80 (5), 317-339.

SUEZ, G., SUBBIAH, S., 2014. Innovative sand failure analysis and prediction modelling restore lost production in North Sea field. *World Oil* August Issue, 71-76.

TARKOWSKI, R., WDOWIN, M. and MANECKI, M., 2015. Petrophysical examination of CO₂-brine-rock interactions-results of the first stage of long-term experiments in the potential Zaosie anticline reservoir (central Poland) for CO₂ storage. *Environmental Monitoring Assessment* 187, 4215.

TARTAKOVSKY, A., MEAKIN, P., SCHEIBE, T. and WOOD, B., 2007. A smoothed particle hydrodynamics model for reactive transport and mineral precipitation in porous and fractured porous media, *Water Resources Research*, 43(5), 1-18.

TIXIER, M., LOVELESS, G. and ANDERSON, R., 1975. Estimation of Formation Strength from the Mechanical-Properties Log (includes associated paper 6400). *Journal of Petroleum Technology*, 27(3), 283-293.

TÖRÖK, Á and VÁSÁRHELYI, B., 2010. The influence of fabric and water content on selected rock mechanical parameters of travertine, examples from Hungary. *Engineering Geology*, 115(3), 237-245.

TRONVOLL, J., LARSEN, I., LI, L., SKJETNE, T. and GUSTAVSEN, Ø., 2004. Rock mechanics aspects of well productivity in marginal sandstone reservoirs: Problems, analysis methods, and remedial actions. In: *Proceeding of SPE International Symposium and Exhibition on Formation Damage Control*, Louisiana, 18 – 20 February.

VAN DEN HOEK, P. HERTOOGH, G., KOOIJMAN, A., DE BREE, P., KENTER, C. and PAPAMICHOS, E., 2000. A new concept of sand production prediction: theory and laboratory experiments. *SPE Drilling & Completion*, 15(04), 261-273.

VARDOULAKIS, I., STAVROPOULOU, M. and PAPANASTASIOU, P., 1996. Hydromechanical aspects of the sand production problem. *Transport in Porous Media*, 22(2), 225-244.

VELOSO, C.B., SILVA, N. A., WATANABE T. G., PAES, B. C., DE LUNA, F.T. and CAVALCANTE, Jr, C.L. 2014. Scale inhibitor adsorption studies in rock sandstone type. *Adsorption*, 20(8), 977-985.

WANG C., and ZHANG LT., 2015. Numerical modelling of gas-liquid-solid interactions: gas-liquid free surfaces interacting with deformable solids. *Computer Methods in Applied Mechanics and Engineering*, 286, 123-146.

WEISSENBURGER, K., MORITA, N., MARTIN, A. and WHITFILL, D., 1987. The engineering approach to sand production prediction. *SPE Annual Technical Conference and Exhibition*. Society of Petroleum Engineers.

WILSON, A., 2016. Chemical Analysis of flowback water and downhole gas-shale samples. *Journal of Petroleum Technology*, 68(9), 114-115.

WU, B., TAN, C., OIL, S. and RICHARDSON, T., 2002. Sand production prediction of gas field: methodology and laboratory verification. SPE Paper no. 77841. *SPE Asia Pacific Oil & Gas Conference and Exhibition*. Irving, Texas, 20-23 October.

XU T., PRUESS K. and APPS, J., 2008. Numerical studies of fluid-rock interactions in enhanced geothermal systems (EGS) with CO₂ as a working fluid. Proceedings of the thirty-third workshop on Geothermal Reservoir Engineering, Stanford University, 28-30 January.

YANG, L., XU, T., LIU, K., PENG, B., YU, Z. and XU, X., 2017. Fluid-rock interactions during continuous diagenesis of sandstone reservoirs and their effects on reservoir porosity. *Sedimentology*. 64(5), 1303-1321.

YAN, F., BHANDRI, N., WANG, L., DAI, Z., ZHANG, Z., BOLANOS, V., KAN, A. and TOMSON, M., 2015. Interaction between scale inhibitors and shale and sandstone formations. Presented at International symposium on oilfield chemistry, The Woodlands, TX, USA, 13 – 15 April.

YOON, H., KANG, Q. and VALOCCHI, A., (2015). Lattice Boltzmann-based approaches for pore-scale reactive transport. *Reviews in Mineralogy & Geochemistry*, 80, 393-431.

ZANGIABADI, B., KULATHILAGON, P., and MIDTUN, B., 2011. Evaluation of Rock-Fluid Interactions in an Outcrop Chalk: Experimental Study with MgCl₂ solution. 45th US Rock Mech. Sym., 4th U.S.-Canada Rock Mech. Symposium., San Francisco, CA, 26-29 June.

ZANGIABADI, B., KORSNES, R.I., HILDEBRAND-HABEL, T., HIORTH, A., SUTARJANA, I.K., LIAN, A. and MADLAND, M.V., 2009. Chemical water weakening of various outcrop chalks at elevated temperature. In: H.I. Ling, Smyth, A., and Betti, R. (Editor), *4th Biot conference on poromechanics*. DEStech Publication Inc. Columbia University, New York, 543-548.

ZEMKE, K., LIEBSCHER, A. and WANDREY, M., 2010. Petrophysical analysis to investigate the effects of carbon dioxide storage in a subsurface saline aquifer at Ketzin, Germany (CO2SINK), *International Journal of Greenhouse Gas Control*, 4(6), 990–999.

ZOBACK, M.D., 2007. Reservoir Geomechanics. Cambridge University Press, New York, NY, USA, 84-94.

ZOU, B., MCCOOL, C., GREEN, D. and WILLHITE, G., 2000. A study of the chemical interactions between brine solutions and dolomite. *SPE Reservoir Evaluation & Engineering* 3 (3), 209–212 June.

Chapter Three

3 Research Methodology/Approach

3.1 Introduction

In this Chapter the methodology and approach including materials and equipment used for the work reported in chapters 4 and 5 are discussed extensively. Two approaches, experimental and numerical were used to determine the effect of interaction between selected oilfield chemicals and the formation rock as indicated in the schematic diagram (Figure 3.1)

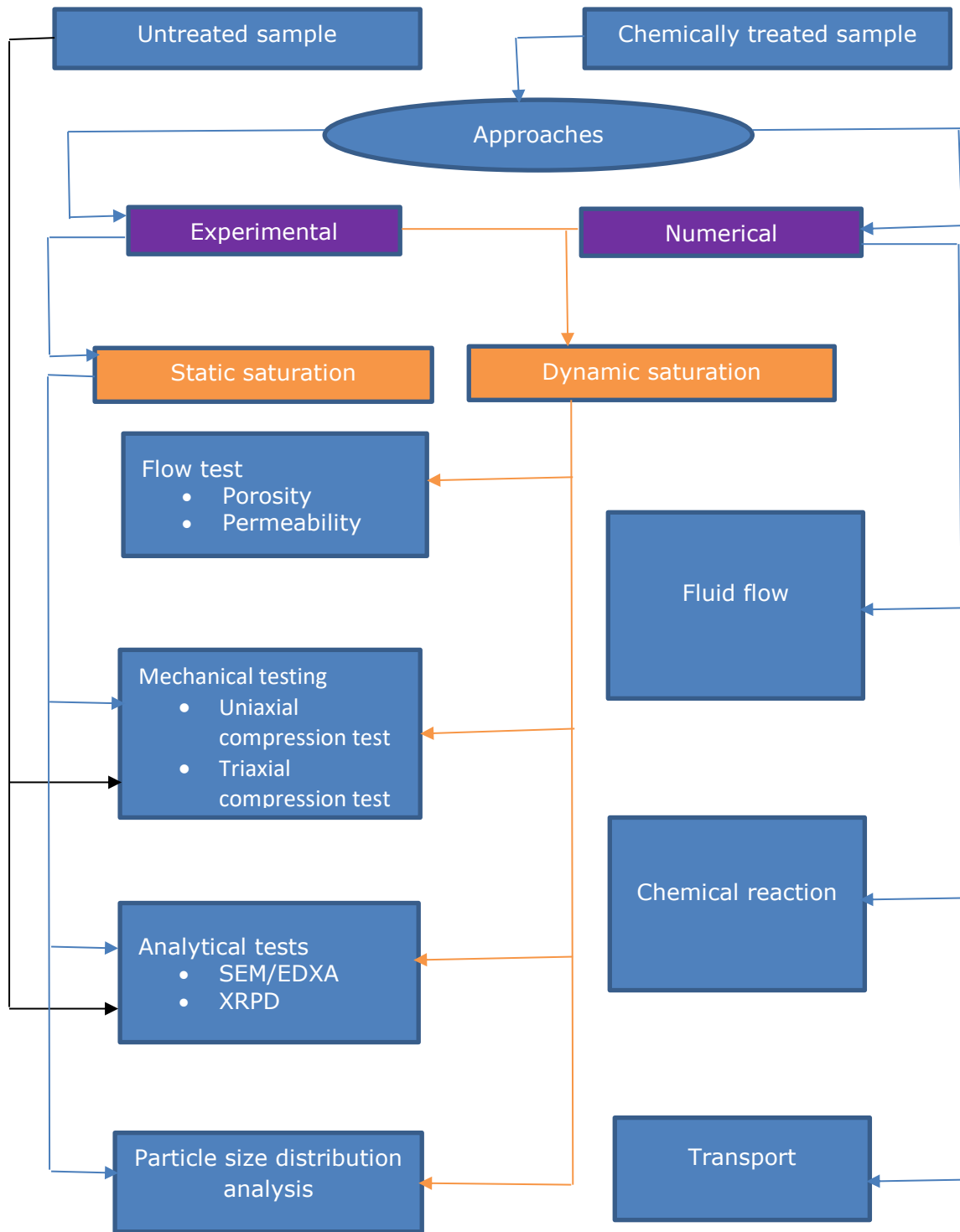


Figure 3.1: Schematic diagram of the methodology

The untreated samples were tested for strength, morphology, texture, elemental and mineralogical composition prior to chemical saturation using mechanical testing, Scanning Electron Microscopy (SEM)/Energy Dispersive

X-ray analysis (EDXA) and X-Ray Powder diffraction (XRPD) test. The purpose of these tests was to identify and quantify the changes the interaction between the chemicals (biocide, scale inhibitor and corrosion inhibitor) and the formation rocks have made to these properties.

3.2 Materials and equipment

Two sets of core samples, real reservoirs and outcrop core samples were used in this study. The samples include four (4) cylindrical real reservoir sandstone core samples obtained from Egoli 1 well in Niger Delta (Nigeria), five (5) cylindrical limestone core samples obtained from Sokoto and Anambra Basins, Nigeria; twenty-seven (27) sandstone outcrop and twenty-seven (27) carbonate outcrop core samples obtained from Kocurek Industries Ltd, believed to have their origin from Texas, USA. The geometrical parameters of the real core samples and outcrop samples used for the static saturation are presented in Table 3.1; whilst the geometrical parameters of the outcrop samples used for the dynamic saturation and triaxial test, respectively are presented in Tables 3.2 and 3.3. The oilfield chemicals considered in this work are the commonly used ones obtained from REDA Oilfield UK Ltd; they include corrosion inhibitor (glycine betaine - $C_5H_{11}NO_2$), biocide (glutaraldehyde - $C_5H_8O_2$), scale inhibitor Aminotri (methylenephosphonic acid) - ATMP ($C_3H_{12}NO_9P_3$), see chemical structures in Figure 3.2. The choice of these chemicals is based purely on the fact that they are commonly used in the oil and gas field.

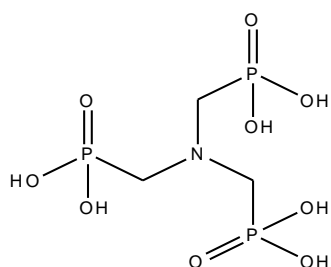
Table 3.1: Geometrical parameters and location of real reservoir and outcrop core samples used for static saturation

Sample identifiers	Mean L (mm)	Mean D (mm)	L/D	Depth (ft)	Location
SST-1	31	57	0.5	1946-1966	Niger Delta
SST-2	39	56	0.7	1946-1966	Niger Delta
SST-3	27	59	0.5	4009-4022	Niger Delta
SST-4	22	62	0.4	1580-1583	Niger Delta
LST-0	29	57	0.5	34-39	Sokoto Basin
LST-3	50	47	1.1	131	Anambra Basin
LST-4	35	54	0.6	22-25	Sokoto Basin
LST-5	46	46	1.0	53	Anambra Basin
LST-6	41	58	0.7	88-101	Sokoto Basin

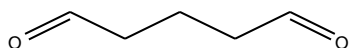
SST = Sandstone; LST = Limestone; L = Length; D = Diameter

LP	50	38	1.3	600	Millsap
LP	51	38	1.3	600	Millsap
LP	51	38	1.3	600	Millsap
LP	51	38	1.3	600	Millsap
LP	50	38	1.3	600	Millsap
ED	50	38	1.3	600	Austine
ED	50	38	1.3	600	Austine
ED	50	38	1.3	600	Austine
DP	51	38	1.3	600	Austine
DP	50	38	1.3	600	Austine

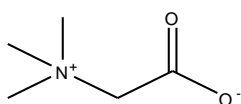
LP = Leopard (sandstone); ED = Edward brown (carbonate); DP = Desert Pink (carbonate)



Aminotris(methylenephosphonic acid) - ATMP



Glutaraldehyde



Betaine

Figure 3.2: Structures of the selected oilfield chemicals

ATMP is a colourless aliphatic amine acid with a strong oxidizing properties. Its log octanol-water partition coefficient (log Kow = -3.53 hence possess low bioaccumulation potential), it is soluble in both acids and bases

including most brine and can disperse available solids; it is water soluble at 1000mg/L. Three active phosphate groups can be identified with ATMP. This attribute makes three potential reacting sites with calcium cations possible (Pairat and Sumeath 1997). ATMP is adsorbed to formation mineral surface via Van der Waals interactions as a function of pH, temperature, mineral substrates, and involves cations like Ca^{2+} . Nevertheless, interaction of low pH ATMP with formation rock can cause deleterious dissolution of minerals (pitting) leading to sand production (Jordan et al. 1994).

Glutaraldehyde otherwise called 1,5-pentane dial belong to the aldehyde family. It is a colourless liquid with pungent odour. Its log octanol-water partition coefficient, log Kow is -0.18, thus bioaccumulation potential, water solubility is 16720mg/L. The functional group of glutaraldehyde reacts with basic constituents of proteins (Videla 2002). Glutaraldehyde is pH sensitive and work well in neutral to alkaline water (Karnovsky 1965).

Betaine is a neutral organic compound with a positively charged cationic (quaternary ammonium) and a negatively charged carboxylate group. Its log octanol-water partition coefficient, log Kow is 4.93, hence low bioaccumulation potential and water solubility is 1000g/L. Betaine has significantly lower adsorption levels on limestone than it has on sandstone and adsorption increases by divalent ions (Mannhardt et al. 1993).

Table 2.2: Geometrical parameters and location of outcrop core samples used for dynamic saturation

Sample Identifiers	Mean L (mm)	Mean D (mm)	L/D	Depth (ft)	Location
LP 1	51	38	1.3	600	Millsap
LP 2	50	38	1.3	600	Millsap
LP 3	51	38	1.3	600	Millsap
LP 4	50	38	1.3	600	Millsap
LP 5	51	38	1.3	600	Millsap
LP 6	51	38	1.3	600	Millsap
LP 7	50	38	1.3	600	Millsap
LP 8	50	38	1.3	600	Millsap
LP 9	51	38	1.3	600	Millsap
LP 10	51	38	1.3	600	Millsap
LP 11	51	38	1.3	600	Millsap
LP 12	50	38	1.3	600	Millsap
LP 13	51	38	1.3	600	Millsap
LP 14	51	38	1.3	600	Millsap
LP 15	51	38	1.3	600	Millsap
ED 1	51	38	1.3	600	Austine
ED 2	50	38	1.3	600	Austine
ED 3	50	38	1.3	600	Austine
ED 4	51	38	1.3	600	Austine
ED 5	51	38	1.3	600	Austine
ED 6	51	38	1.3	600	Austine
ED 7	50	38	1.3	600	Austine
ED 8	51	38	1.3	600	Austine
ED 9	50	38	1.3	600	Austine
ED 10	50	38	1.3	600	Austine
ED 11	51	38	1.3	600	Austine
ED 12	51	38	1.3	600	Austine
ED 13	51	38	1.3	600	Austine
ED 14	50	38	1.3	600	Austine
ED 15	51	38	1.3	600	Austine

LP = Leopard; ED = Edward brown; L = Length; D = Diameter

Table 3.3: Geometrical parameters and location of outcrop core samples used for dynamic saturation and triaxial test

Sandstone					
Sample identifiers	Mean L (mm)	Mean D (mm)	L/D	Depth (ft)	Location
LP 4	102	51	2	600	Millsap
LP 7	102	51	2	600	Millsap
LP10	102	51	2	600	Millsap
LP 13	102	51	2	600	Millsap
LP 29	102	51	2	600	Millsap
LP 34	102	51	2	600	Millsap
Carbonate					
ED 7	102	51	2	600	Millsap
ED 8	102	51	2	600	Millsap
ED 10	102	51	2	600	Millsap
ED 14	102	51	2	600	Millsap
ED 33	102	51	2	600	Millsap
ED 36	102	51	2	600	Millsap

3.3 Pre and post-chemical treatment test programme

The pre and post-static and dynamic chemical saturation (treatment) tests were conducted on the cores to establish changes that have taken place in the rock petrophysical and geomechanical properties (UCS, particle size distribution/sorting, mineralogical and elemental composition, porosity and permeability) as a result of interaction between the core samples and the selected oilfield chemicals.

3.3.1 Mechanical testing

Uniaxial compression and triaxial tests were carried out on the core samples in accordance with the recommended international standard for Rock Mechanics (ISRM), (Bieniawski and Bernede 1979) and ASTM D2166-80 to determine their unconfined compressive strength, confined compressive strength and Young's modulus.

3.3.1.1 Uniaxial compression test

Uniaxial compression test (UCT) was conducted on untreated and oven dried chemically treated cylindrical core samples (Figure 3.3a) to measure the uniaxial compressive strength (UCS) of the rock. The test was performed using a screw-driven mechanical test machine Instron® 3382 that has a load capacity of 150kN. The weight, length, and diameter of the cores were measured and recorded prior to the tests. The length and the diameter were measured using digital Vernier calliper. The core samples were loaded in the displacement control (Figures 3.3b,c) at a rate of 0.5mm/min and 1 point/sec data rate until failure occurred. The load and the corresponding displacement were continuously recorded using the test machine in-built data logger and the linear variable differential transformer (LVDT) at 73 °F. The stress (σ)-strain (ϵ) curve was plotted and the UCS was determined from the maximum load and the average diameter of the core sample using equation 3.1.

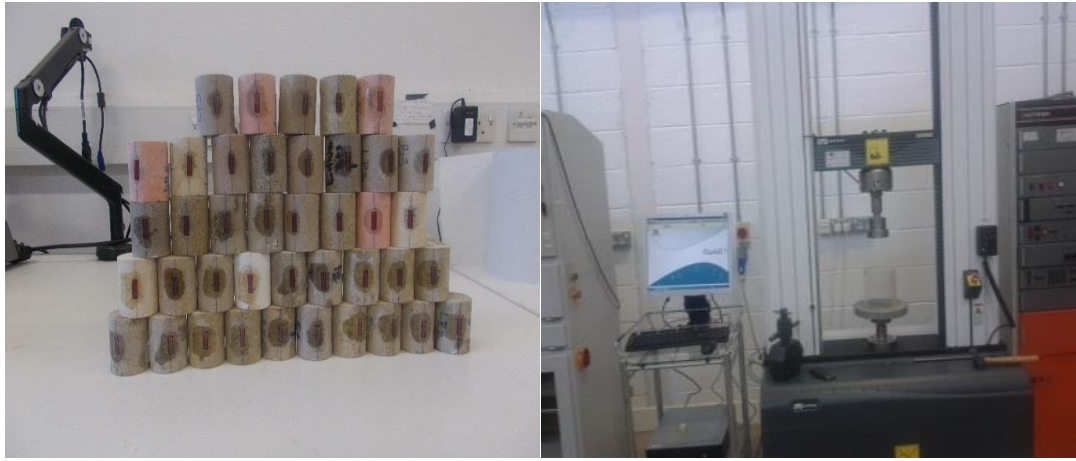
$$UCS = \frac{P_{max}}{\pi * \left(\frac{D}{2}\right)^2} \quad [3.1]$$

where P_{max} = Maximum load (N), D (m) = diameter of the core sample and UCS expressed in MPa.

The crosshead displacement was used to obtain the strain values used to plot the stress-strain curve for the UCS. The Young's modulus was measured using strain gauge and half (1/2) Wheatstone bridge. Prior to the test, the LVDT and the Instron 3382 were calibrated (Figure 3.3d); using the procedure in appendix D. A dummy sample was available as a control.

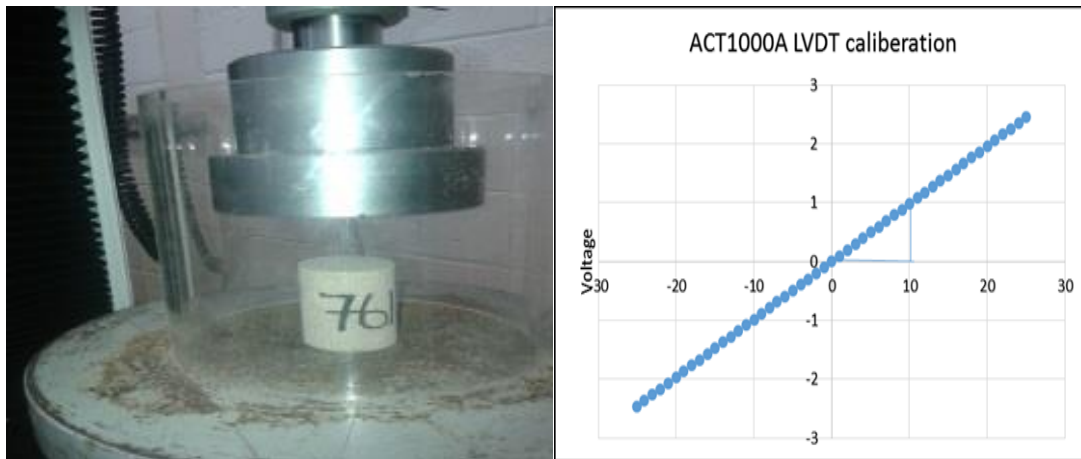
The stress-small strain slope was used to calculate the Young's Modulus (E) using equation 3.2.

$$E = \frac{\text{Change in stress}}{\text{Change in strain}} = \frac{\Delta\sigma}{\Delta\varepsilon} \quad [3.2]$$



(a)

(b)



(c)

(d)

Figure 3.3: Unconfined compressive strength determination using uniaxial compression test device: (a) Sandstone and limestone samples with strain gauge; (b) Instron 3382; (c) Core sample positioned between the loading platen before test; and (d) Test device calibration

3.3.1.2 Triaxial test

Fourteen (14) outcrop core samples (seven sandstone and seven carbonate), prepared to a nominal size of 50 mm diameter and 100 mm long were used to perform the multiple failure triaxial test. The geometrical parameters of the outcrop samples used for pre- and post- chemical treatment triaxial test are presented in Table 3.3.

The pre- and post- chemical treatment triaxial tests were carried out using Hoek cell (Figure 3.4) in accordance with the method proposed by the International Society for Rock Mechanics (ISRM). The test was conducted to determine the peak strength envelope, the residual strength envelope, the angle of internal friction, the apparent cohesion or shear strength, and Young's Modulus under compression. The multiple failure type of test was performed due to the limited amount of sample available for chemical treatment and cost consideration. As such, only betaine which was observed to have produced the most impact on other parameters and brine which serves as control were injected (dynamic saturation) into the samples for the triaxial test. The confining pressure was applied using a hydraulic pump and was monitored by a calibrated diaphragm type pressure transducer (Figure 3.4).

The provided unconfined compressive strength of carbonate and sandstone by the supplier (Kocurek Industries Ltd) were 4,000 psi (27.6 MPa) and 3,000 psi (20.7 MPa) respectively. Based upon these strength values, the confining pressure applied to fully characterise the rocks both in brittle zone and beyond the brittle-ductile transition are: 3, 6, 9, 12, 15, 20, 30, 40, 50 and 60 MPa.

To allow the multiple failure test to be carried out, the axial load was applied in displacement control to a nominal axial strain rate of 10^{-5} s^{-1} . This was regulated by two diametrically opposite axial LVDT's which were connected to the ram of the testing machine to provide feedback to the control system. The axial load was applied by a calibrated Denison-Mayes compression testing machine.

The axial load, axial displacement and the confining pressure were logged in real-time on a computer at a sampling rate of 1 Hz.

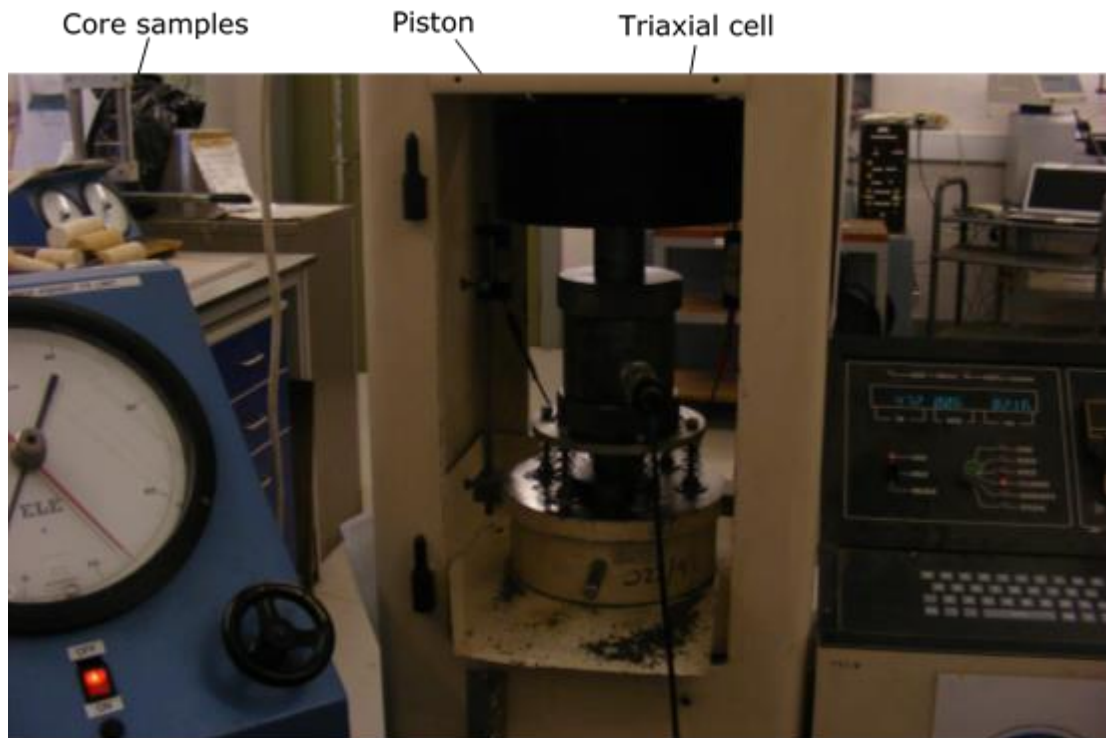


Figure 3.4: Rock triaxial equipment

Rock sample was placed in a rubber sleeve to prevent ingress of pressuring fluid (hydraulic). Confining pressure was applied, and held constant. Axial load was slowly applied at the above stated strain rate, until the peak axial load was attained. The confining pressure was increased, and the axial load was further increased until the peak load was attained. The process was repeated until the peak failure load for the chosen confining pressure has been determined.

The straight line Mohr-Coulomb failure envelope was fitted to the peak failure data. The residual strength envelope was obtained by slowly reducing the confining pressure after the maximum residual load was stabilised, and monitoring the resulting axial load.

The Young's modulus for each sample was calculated from its strain-stress plot, however, these are moduli at a given confining pressure rather than unconstrained uniaxial compression. This shows how the elastic modulus is affected by triaxial stress. In order to do this, the load was cycled once and the average Young's modulus calculated as the load increased. The description of the deformation from the measured modulus was based on the proposed classification of deformity by International Aerospace Environmental Group (IAEG) (1979) as presented in Table 3.4.

Table 3.4: Classification of deformability

Class	Young modulus (GPa)	Deformation Description
1	< 5	Very high
2	5 – 15	High
3	15 – 30	Moderate
4	30 – 60	Low
5	> 60	Very low

3.3.2 Analytical characterisation

Analytical characterisation of the untreated and chemically treated core samples was carried out using scanning electron microscopy (SEM), energy dispersive X-Ray (EDXA) and X-Ray powder diffraction (XRPD) to identify and quantify the chemical changes that occurred within the rock fabric which provides evidence of potential damage to the rock fabric. The effluents from the saturation tests were also subjected to inductively coupled plasma optical emission spectrometry (ICP-OES) and particle size distribution analysis.

3.3.2.1 Elemental analysis using SEM/EDXA

Both untreated and oven dried chemically treated core samples were cut into nuggets, degreased with acetone before mounting on a stub. Rock being a non-conductive material was coated with carbon at a thickness of about 20 nm, ensuring the sample was well covered. The choice of the carbon coating thickness was informed by the fact that it is too small or thin to influence the elemental analysis. With the help of carbon putty the conductive material is brought as far up the sides of the sample as possible. Zeiss EVO LS10 variable pressure scanning electron microscope with a smart camera for controlling the microscope and capturing images was used to conduct the analysis. The system was set to chamber pressure of 100 Pa, a working distance of 8.5 mm, accelerating potential of 20kV and varying magnifications (250X – 2.00 KX). EDX analysis system operates as an integrated feature of an SEM. It is not capable of operating on its own. Specimen is bombarded with an electron beam inside the scanning electron microscope during EDX analysis.

3.3.2.2 Mineralogical analysis using XRPD

Both whole rock and clay fraction analyses were carried out by means of X-Ray powder diffraction (XRPD) using identification and quantification of polycrystalline materials.

In the whole rock analysis, bulk samples were wet ground for twelve (12) minutes (in ethanol) in a McCrone mill and sprayed dried with an air brush to produce random powder specimens as described in Hillier (1999). The XRPD patterns were recorded from $2 - 75^{\circ} 2\theta$ using cobalt K α radiation, counting for 2 seconds per 0.02° step. Quantitative analysis was made by

a normalised full pattern reference intensity ratio (RIR) method as described by Omotoso et al. (2006). Expanded uncertainty using a coverage factor of 2, i.e. 95% confidence, was given by $X \pm 0.35$, where X = concentration in wt.% (Hillier 2003). The analysis was performed bearing in mind that for phases present at trace level (<1%) there may also be uncertainty as to whether or not the phase is truly present in the sample, since this is both phase and sample dependent.

In clay fraction analysis, <2 μ m portion of clay obtained by timed sedimentation was prepared as an oriented mount using the filter peel transfer technique. The fraction was scanned from 2-45° (2 θ) in the air-dried state, after glycolation, following heating at 300°C for one hour. Clay minerals identified were quantified using a mineral intensity factor approach based on calculated XRPD patterns. Unless otherwise stated, for clay minerals present in amounts >10wt.% uncertainty is estimated as better than ± 5 wt.% at the 95% confidence level.

3.3.3 Preparation of brine and injection chemicals

Synthetic formation brine was prepared from corresponding salts in deionised water (18 m Ω) by weighing the salts as detailed in Table 3.5. The set up was stirred using magnetic stirrer and allowed to stand for 24 hours before filtering through a 40 μ m sintered glass filter to remove any extraneous fines that may be present before use and degassed under vacuum. The saturating brine was prepared in concentrations that simulate typical formation water.

Individual stock solution of 1 wt. % betaine and glutaraldehyde oilfield chemicals which are corrosion inhibitor and biocide, respectively, were

prepared by diluting 2.5 g of each of the chemicals in 250 ml of the prepared brine. Also, a stock solution of 5 wt. % scale inhibitor–(ATMP) was prepared by diluting 12.50 g of the scale inhibitor in 250 L of the brine.

Table 3.5: Brine composition

Source (salt)	Ions	Actual weight (g) of salt used	Concentration (ppm)
NaCl	Na ⁺	60.7001	24870
KCl	K ⁺	1.6948	887
CaCl ₂ .2H ₂ O	Ca ²⁺	2.8956	785
MgCl ₂ .6H ₂ O	Mg ²⁺	1.0872	136
MgSO ₄ .7H ₂ O	SO ₄ ²⁻	0.0772	35
BaCl ₂ .2H ₂ O	Ba ²⁺	1.0002	561
SrCl ₂ .6H ₂ O	Sr ²⁺	0.3287	108
FeSO ₄ .7H ₂ O	Fe ²⁺	0.0149	3
NaHCO ₃	HCO ₃ ⁻	2.7728	2014
NaCl, CaCl ₂ .2H ₂ O, MgCl ₂ .6H ₂ O, BaCl ₂ .H ₂ O, SrCl ₂ .6H ₂ O, KCl	Cl ⁻		39800

3.3.4 Static saturation

Out of the nine (9) downhole samples, four (4) are sandstone and five (5) are limestone. Whereas, the outcrop samples contain five (5) sandstone and five (5) limestone samples. Each of the nineteen samples was weighed

and placed in separate 600 mL beakers. Each beaker was filled with one of the four different fluids (brine, betaine, ATMP and glutaraldehyde) to fully cover the core. The saturation was replicated for glutaraldehyde only. The cores were allowed to remain in the fluids for one week to ensure complete saturation in line with earlier calibration (Figure 3.5) and the procedure detailed in Oluyemi (2014). The cores were then removed from the fluids at the end of one week and rinsed with deionized water to prevent recrystallization of salt on the surface of the samples. The cores were aired and oven dried at 135°C until constant weights were obtained (for three days) with the weights checked on a daily basis by bringing them out of the oven, cooled, weighed and returned to the oven. The choice of the drying temperature was based on the recommendation by Tufail et al. (2017) and Lang et al. (2017) which suggested higher temperature than the standard temperature (110±50C) to avoid under estimation of cation exchange capacity and specific surface area. Quartz and limestone, the dominant minerals in the samples can withstand higher temperature (Tufail et al. 2017). Due to limited sample sandstone was not tested with brine.

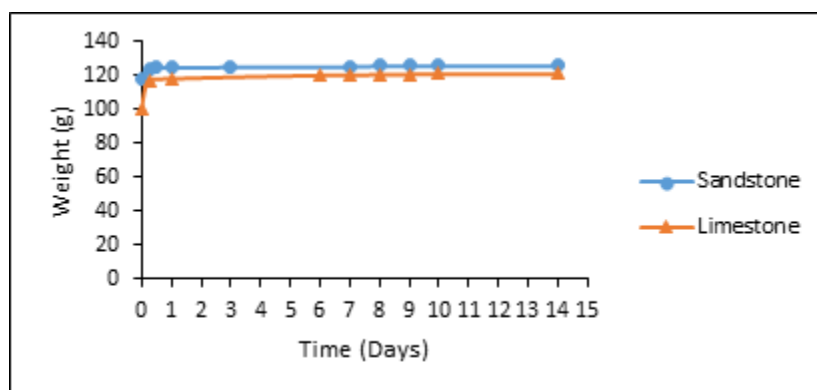


Figure 3.5: Static saturation calibration for both sandstone and limestone

3.3.5 Dynamic saturation test

Saturation under dynamic condition gives an opportunity to demonstrate flow of reacting fluid to and through the rock surface by diffusion and convection. The process involves collection of uptake and flowback effluents. The flowback effluents were analysed to investigate the release of cations/particles and mechanisms controlling the flowback chemistry. The flow experiment involved saturation of the rocks in synthetic formation brine prior to exposing the core samples to the test chemicals. The saturating brine and chemicals were prepared as detailed in section 3.3.3 and the salts used are presented in Table 3.5.

3.3.5.1 Material preparation for core flooding

Two different core holders were used in the entire work: (1) stainless steel that accommodates core sample with a dimension of 51 mm (length) x 38 mm (diameter); and (2) Perspex core holder with aluminium capping that accommodates core dimension of 102 mm (length) x 51 mm (diameter). The latter was designed using Solid works (Figures 3.6 and 3.7) and fabricated in-house. Other Perspex core holder components and engineering drawing are in Appendix B.

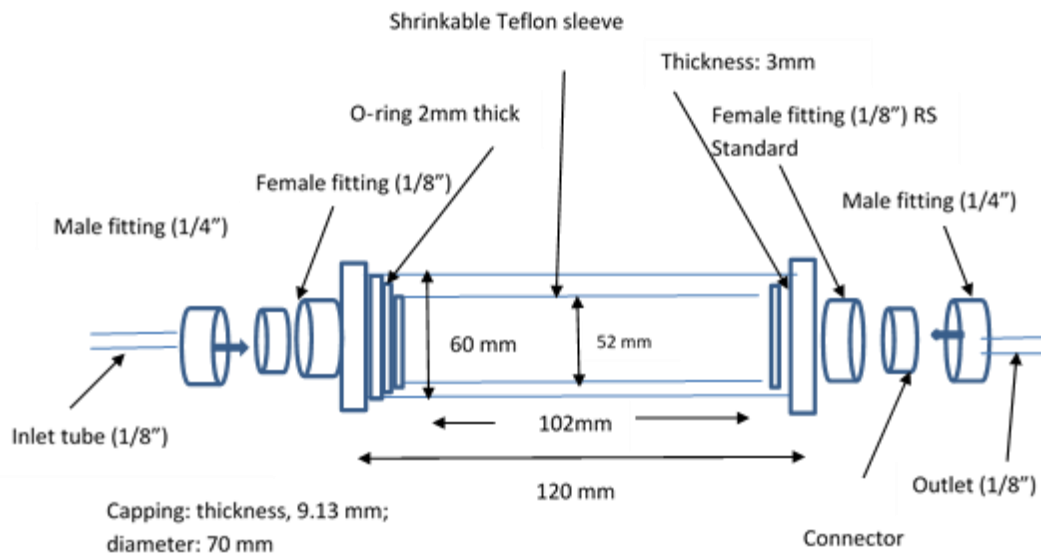


Figure 3.6 Sketch of Perspex core holder

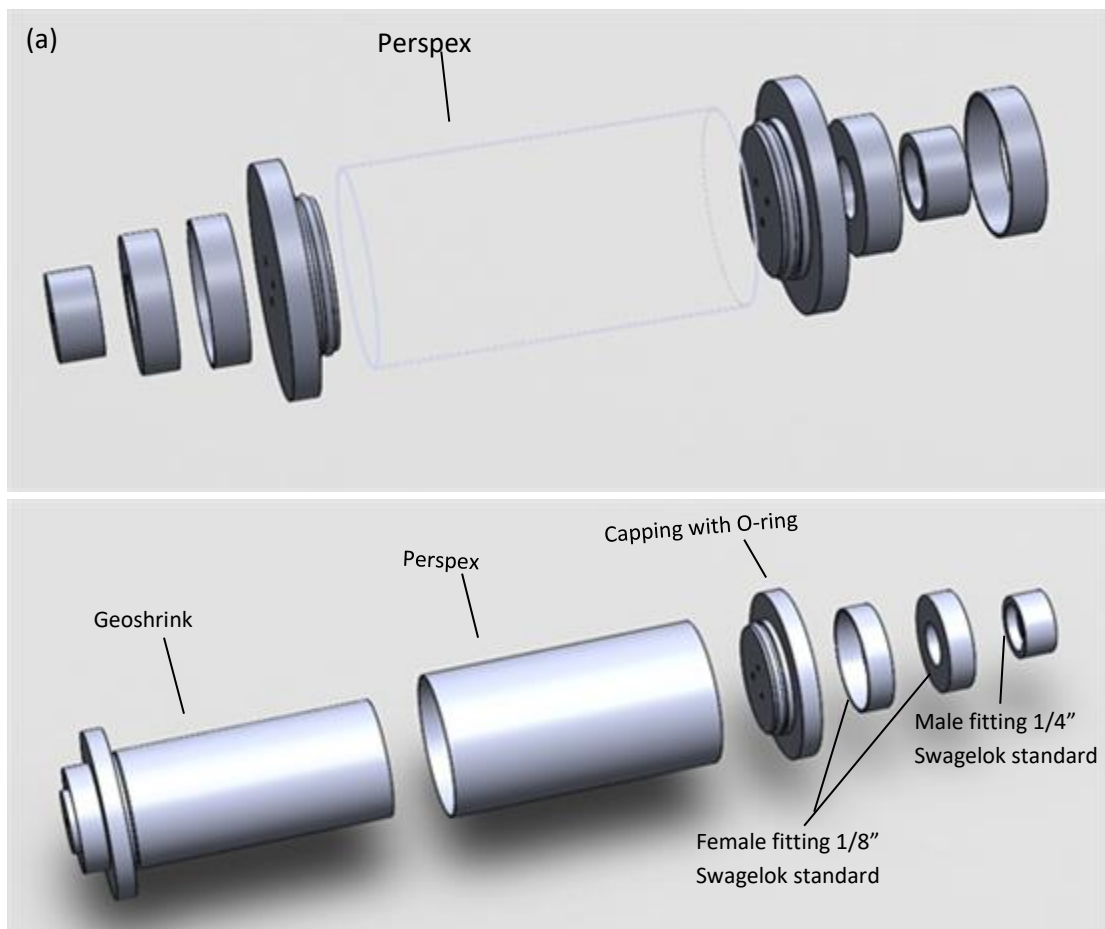


Figure 3.7: Designed Perspex core holder showing: (a)-(b) component.

3.3.5.2 Dynamic core saturation with synthetic formation brine

The core sample was held in place in the core holder with the aid of Geo-Shrink® sleeving. The Geo-Shrink® was attached to the core sample with the aid of “hot air gun” and inserted in the core holder (Figure 3.7). Injection of fluids into the core was achieved by setting up a core flood system to which the core holder was attached. With the help of the high performance syringe pump (model HPLC 1500 Scientific Systems, Inc. - SSI), the saturating brine was injected into the core sample. The pump has a maximum pressure rating of 6000 psi and the capacity to deliver at rates of up to 12.000 mL/min. The core porosity using lithium tracer and permeability using Darcy equation were measured as discussed in sections 5.2.2.3 and 5.2.3.2 (Chapter 5). All measurements and monitoring were carried out electronically using the National Instruments data acquisition system (NIDAQ) through Validyne differential pressure transducers of varying capacities mounted across the core and computer to which the reading of pressure was automated. Throughout the flooding experiment, low capacity transducer (0-12.5) was utilized. Calibration of the Pressure Transducers was carried out using Druck DPI model 615 IS. This device was also used to check any leakage prior to the commencement of experiment. This was conducted by applying an air pressure of 100 psi while the device was held in place for 5 minutes.

To ensure laminar flow that will stabilize the fines in the clay minerals, each core sample was saturated with the brine at 1 mL/min for 6 hours and effluent collected for particle size distribution analysis. The choice of the 6 hours was to ensure complete saturation and cleaning of the core sample

prior to chemical injection. Analysis of particle size distribution in brine effluent was carried out as a control measure. The establishment of the saturation time and flowrate was based on calibration and previous work by Oluyemi (2014). The calibration was done by flowing a known volume of the brine through the core and measuring the outflow/return.

3.3.5.3 Injection of Li tracer for porosity measurement

Lithium (Li) tracer technique was used in the determination of porosity of the cores before and after chemical treatment. Lithium has been used extensively by other researchers (Richards et al. 2015; Oluyemi 2014; Oluyemi et al. 2009; Wright and Moore 2003; Jordan et al. 1994; Bunny et al. 1997) because it is an inert metal and does not interact with the cores. The lithium tracer was prepared at a concentration of 2.5 ppm by dilution in deionised water from a stock 10,000 ppm lithium ICP standard in nitric acid. A total volume of 40 mL of the 2.5 ppm lithium was used for this test. 4mL of the 2.5 ppm lithium standard was injected into the core at 2 mL/min and the eluate collected in ten (10) separate 15 mL sterile centrifuge tubes at the beginning of the injection at 2 minute intervals. The rate and the time interval ensured full saturation of the core with lithium. The procedure was repeated with brine only injection to evaluate the returns. All the effluent samples were subsequently analysed for lithium using an ICP-OES as detailed in section 3.3.5.4. The Normalised concentration values (C/Ch) were plotted against the cumulative volume. The Li tracer procedure was repeated after each chemical injection. The dead volume, pore volume, bulk volume and porosity were calculated from the Li tracer profile data generated as detailed in Appendix C.

3.3.5.4 Sample analysis by ICP-OES

ICP-OES analysis was carried out using a Perkin Elmer Optical Emission Spectrometer Optima 7000DV instrument, equipped with WinLab 32 version 4.0 software. The operating conditions for the ICP-OES are given in Table 3.6.

Table 3.6: Operating Conditions for ICP-OES in Axial View

Parameter	Setting/Value
Spectral purge gas flow	Normal
Radio Frequency (RF) incident power (W)	1300
Spray chamber	Scott-Type (cyclonic)
Nebulizer	Gem-Cone
Plasma gas flow rate (L/min)	15
Auxiliary gas flow rate (L/min)	0.2
Nebulizer argon gas flow rate (L/min)	0.8
Li wavelength (nm)	670.784
Ca wavelength (nm)	317.933
Mg wavelength (nm)	285.213
Fe wavelength (nm)	238.204
Na wavelength (nm)	588.995

Calibration standards were prepared in deionised water at five different concentrations and 2.5 ppm from a stock 10000 ppm Li standard in nitric acid. A calibration blank of deionized water was also run with the calibration standards (Figure 3.8). The Li tracer effluent samples were subsequently analysed as described for the standards.

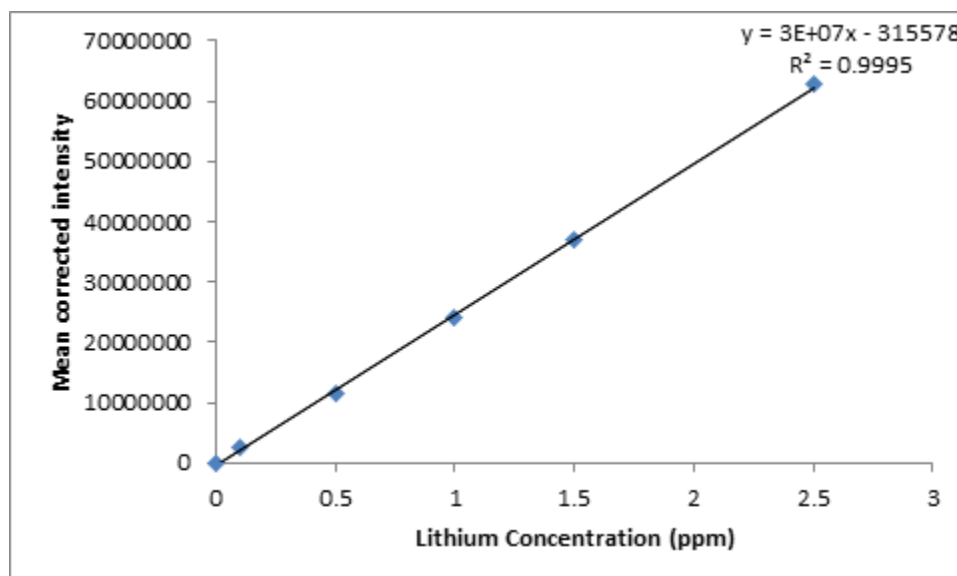


Figure 3.8: ICP-OES calibration

3.3.6 Particle size distribution analysis

The particle size distributions of the original brine and effluent samples that resulted from the static (uptake) and dynamic (uptake and flowback) saturations were measured using a Malvern Laser Mastersizer S. Prior to sample measurement the equipment was calibrated with deionised water. The effluents were stirred with magnetic stirrer into the Malvern Laser Mastersizer using 20 mL dropper to ensure the entire range of particle sizes in the original brine and the effluents was adequately captured by the equipment. The sampling compartment was regularly rinsed (at least thrice)

after each measurement using deionized water to ensure the compartment was free of any contaminant.

References

ASTM, 1992. Standard Test Method for Obtaining and Testing Method for obtaining and Testing Drilled cores and Sawed Beams of Concrete. 1991 Annual Book of ASTM Standards, *Concrete and Aggregates*, vol 4, C 42-90.

ASTM, 1995. Standard Test Method for Unconfined Compressive Strength of Intact Rock Core Specimens, D 2166-80.

BIENIAWSKI, Z. and BERNEDE, M., 1979. Suggested methods for determining the uniaxial compressive strength and deformability of rock materials: Part 1. Suggested method for determining deformability of rock materials in uniaxial compression. *International Journal of Rock Mechanics and Mineral Science & Geomechanics Abstracts*. Elsevier. 138-140.

BUNNY, JR., JORDAN, MM., SORBIE, KS., 1997. The prediction and avoidance of formation damage induced by scale inhibitor squeeze treatments. SPE European Formation Damage conference, The Hague, 2-3 June.

HILLIER, S., 2003. Quantitative analysis of clay and other minerals in sandstones by X-ray powder diffraction (XRPD). *Clay Mineral Cements in Sandstones: Special Publication*, 34, 213-251.

HILLIER, S., 1999. Use of an air brush to spray dry samples for X-ray powder diffraction: *Clay Minerals*, 34(1), 127-135.

IAEG 1979. Classification of rocks and soils for engineering geological mapping, Part 1-Rock and soil materials. Report of the Commission of

Engineering Geological Mapping, Bulletin of the International Association of Engineering Geology, 19, 364-371.

ISRM 1978. Suggested methods for determining the strength of rock materials in triaxial compression. *International Journal of Rock mechanics and Mineral Science & Geomechanics Abstracts*, 15, 47-51

JORDAN, M., SORBIE, K., PING, J., YUAN, M.D., TODD, A. and HOURSTON, K., 1994b. Phosphonate Scale Inhibitor Adsorption/Desorption and the Potential for Formation Damage in Reconditioned Field Core. *SPE Formation Damage Control Symposium*. Society of Petroleum Engineers.

KARNOVSKY, M. 1965. A formaldehyde-glutaraldehyde fixative of high osmolality for use in electron microscopy. *Journal of Cell Biology*, 27, 137A-138A.

LANG, L. XIANG, W., HUANG, W. and SCHANZ, T., 2017. An Experimental study on oven-drying methods for laboratory determination of water content of a carbon-rich bentonite. *Applied Clay Science*, 150, 153-162.

MANNHARDT, K., SCHRAMM, I. and NOVOSAD, J. 1993. Effect of Rock type and brine composition on adsorption of two foam-forming surfactants. *SPE Advances Technology Series 1 (1)*, 212-218.

OLUYEMI, G., 2014. Conceptual Physicochemical Models for Scale Inhibitor-Formation Rock Interaction. *Petroleum Science and Technology*, 32(3), 253-260.

OLUYEMI, G., STALKER, R. and GRAHAM, G. M. 2009. Chemical placement in fractured systems: laboratory characterisation and evaluation of

fractured cores. *20th International Oilfield Chemistry Symposium*, Geilo, Norway, March 22–25.

OMOTOSO, O., D. K. MCCARTY, S. HILLIER, and R. KLEEBERG, 2006. Some successful approaches to quantitative mineral analysis as revealed by the 3rd Reynolds Cup contest: *Clays and Clay Minerals*. 54 (6), 748-760.

PAIRAT, R., SUMEATH, C., BROWNING, F.H. and FOGLER, H.S., 1997. Precipitation and dissolution of calcium-ATMP precipitates for the inhibition of scale formation in porous media. *Langmuir*, 13(1), 791–1798.

RICHARDS, L., MAGNONE, D., DONGEN, B., BALLENTINE, C. and POLYA, D., 2015. Use of lithium tracers to quantify drilling fluid contamination for groundwater monitoring in Southeast Asia. *Applied Geochemistry* 63, 190-202.

TUFAIL, M., SHAHZADA, K. and GENCTURK, B., 2107. Effect of elevated Temperature on mechanical properties of limestone, quartzite and granite concrete. *International Journal of Concrete Structures and Materials*, 11.

VIDELA, H. 2002. Prevention and control of biocorrosion. *International Biodeterioration & Biodegradation* 49, 259 – 270.

WRIGHT, W.G. and MOORE, B., 2003. Application of tracer-injection techniques to demonstrate surface-water and ground-water interactions between an alpine stream and the North Star Mine, Upper Animas River Watershed, southwestern Colorado, U.S.G.S. *Water-Resources Investigation Report* 03-4172, 36.

Chapter Four

4 Geomechanical effects of oilfield chemicals on sand failure under static condition

4.1 Introduction

Interaction between chemicals and rock can be evaluated under static or dynamic condition. Saturation of rocks with chemicals under static condition establishes the transport of reacting fluid from bulk liquid to the rock surface by diffusion (Rijnaarts et al. 1993).

A previous work (Seto et al. 1997) investigated the effect of chemicals, including aluminium chloride (AlCl_3), dodecyltrimethyl ammonium bromide (DTAB), and polyethylene oxide (PEO) on the strength of sandstone under static condition to establish fundamental knowledge, that can be used in the optimization of chemically assisted fracturing. Nonetheless, the chemistries of the chemicals used in the study is absolutely different from the chemistries of the commonly used oilfield chemicals.

In this chapter, the effects of interaction between oilfield chemicals (corrosion inhibitor, scale inhibitor and biocide) and formation rock on rock properties (strength, mineralogy and elemental composition) as well as particle size distribution under static condition are presented and evaluated. Both real reservoir and outcrop core samples were used in this study. The interaction was investigated by integrating a number of laboratory tests (mechanical testing, grain size distribution analysis and analytical tests) discussed in detail in Section 3.3 of Chapter 3.

This chapter is divided into three main sections: In section 4.2 the materials and pre- and post- chemical treatment tests are presented. In section 4.3 the effects of the chemicals on real reservoir core samples are discussed; while in section 4.4 the effects of the chemicals on the outcrop core samples are discussed.

4.2 Materials, Pre and Post chemical treatment tests

Nine (9) real reservoir cores from Nigeria and ten (10) outcrop core samples from USA were used as detailed in Sections 3.2 and 3.3 of Chapter 3. The length, diameter, depth and locations of where the samples were obtained are presented in Table 3.1 (Chapter 3).

4.2.1 Mechanical test

Uniaxial compression test (UCT) was conducted on the cylindrical core samples to measure the uniaxial compressive strength (UCS) of the intact rock. The procedure involved in the test is detailed in Section 3.3.1 (Chapter 3).

The uniaxial compression test was carried out on both untreated and chemically treated samples. The samples were chemically treated as described in Section 3.3.1.1 (Chapter 3). Oven dried chemically treated cores were used for the post treatment mechanical testing. The purpose of conducting mechanical testing on the chemically treated core samples was to evaluate any mechanical damage that may have taken place as a result of exposure of the rock samples to the chemicals.

Due to difficulty in obtaining rock samples from the Niger Delta (Nigeria), only one core sample was tested for each of the chemicals and rock types.

However, to enhance reliability of results and remove effects of heterogeneity, fractures and other geological uncertainties, it was ensured that the rock/cores used were homogeneous. This was achieved by conducting XRPD test on the samples which confirmed that quartz and calcite are the predominant minerals in sandstone and limestone respectively. In a separate study, core samples taken from the same reservoir and approximately same depth as those used in this thesis have been shown to have porosity and permeability in the range of 24 - 29.5% and 379 – 613 mD respectively for sandstone (Odoh et al. 2012) and the range of 10 - 21% and 20 – 1400 mD respectively for limestone (Uroro and Igharo 2015).

4.2.2 SEM, EDXA and XRPD analysis

Combined scanning electron microscope (SEM), electron dispersive X-Ray (EDX) and X-Ray powder diffraction (XRPD) analyses of the treated and untreated rock core samples was carried out to identify and quantify the chemical changes that have taken place within the rock fabric which may form the basis for the potential mechanical damage to the rock fabric. Oven dried core samples were used for the SEM, EDX and XRPD analyses of the samples after the chemical treatment. The procedure is discussed in Section 3.3.1 (Chapter 3).

4.2.3 Static saturation

The saturating fluids were prepared and the saturation conducted as detailed in Section 3.3.4 (Chapter 3).

4.2.4 Particle size distribution

The particle size distributions of the original brine and effluent samples that resulted from the static saturation were measured using a Malvern Laser Mastersizer 2000s using the procedure discussed in Section 3.3.6 (Chapter 3).

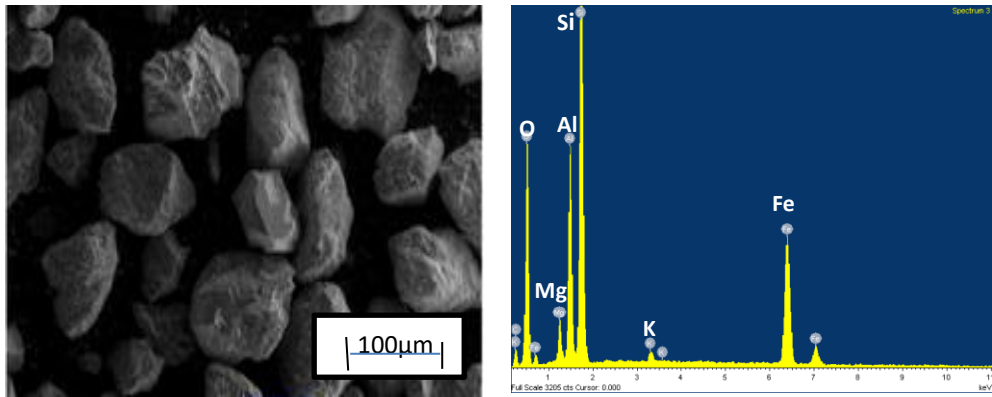
4.3 Results and Discussion of the effects of chemicals on Real Reservoir core samples

4.3.1 Characterisation of real reservoir sandstone and limestone samples

The core samples were characterized using SEM, EDX and XRPD prior to chemical treatment to determine the morphology, elemental and mineralogical composition.

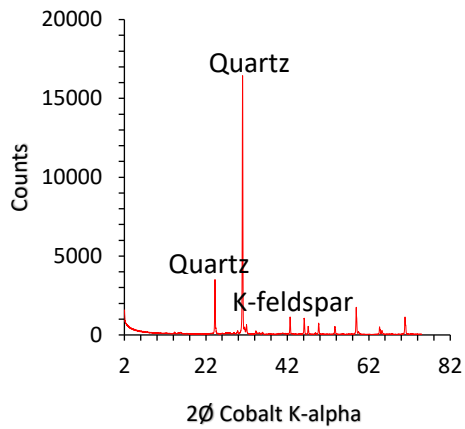
Sandstone was found to have well-sorted, sub-rounded quartz grains (Figure 4.1a). The quartz content was confirmed by EDX scan showing high traces of silicon and oxygen (Figure 4.1b and Table 4.1). The presence of Al (0.7 wt.%), K (0.1 wt.%) and Fe (0.1 wt.%) was an indication that the sandstone contains very low amount of feldspar, although unusually very low. The mean of four (4) different areas on the core surface (Table 4.1) with variability were found to be $\leq 91\%$ for untreated sandstone and $\leq 86, 44$ and 82% for betaine, ATMP and glutaraldehyde treated sandstone respectively. This could be due to the heterogenous nature of the core or the impact of the fluids used for the treatment. The presence of quartz mineral was further confirmed by the bulk mineralogy analysis using XRPD (Figure 4.1c and Table 4.2) with high proportion of quartz (83.3 wt.%) and

16.7 wt.% of other minerals, such as K-feldspar, calcite, pyrite, halite, illite plus illite/smectite mixed layer (I+I/S-ML) and kaolinite. Similar mineral composition of sandstone has been reported by Etimita (2015) from a well within the Niger Delta. Clay fraction identification shows the presence of chlorite (6 wt.%) in untreated sandstone (Figure 4.1d and Table 4.3).

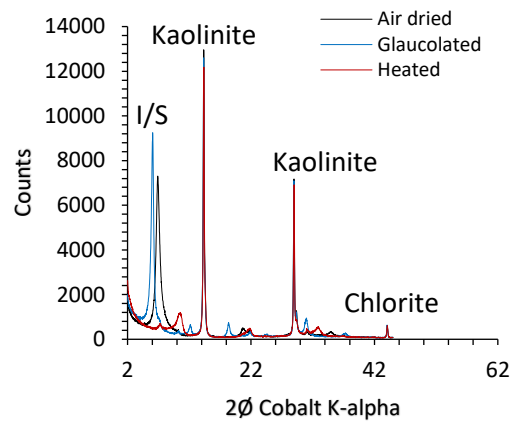


(a)

(b)



(c)



(d)

Figure 4.1: Characterisation of untreated sandstone: (a) SEM micrograph, (b) EDX scan, (c) XRPD bulk mineralogy, and (d) XRPD clay fraction identification.

Table 4.1: Elemental composition of sandstone using SEM-EDX pre and post treatment

Sandstone (n = 4)				
Elements	Pre-treatment (wt%)	Betaine (wt%)	ATMP (wt%)	Glutaraldehyde (wt%)
Na	ND	ND	ND	0.4±0.1
Mg	0.9±0.4	1.0±0.8	0.5±0.1	0.4±0.2
O	56.6±10.4	50.6±4.1	50.0±10	54.6±6.8
Al	4.5±4.1	3.9±2.6	1.6±0.6	1.1±0.9
K	0.7±0.6	0.2±0.05	0.2±0.01	0.2
Ca	0.4±0.3	ND	0.3±0.1	ND
Fe	0.5±0.5	3.9±3.3	1.0±0.4	0.6±0.4
Ti	0.1±0.02	ND	ND	ND
C	17.9±20.1	22.6±13	29.1±11.7	15.7±1.8
Si	18.4±7.6	17.8±7	17.1±7.1	27±1.1
S	ND	ND	0.2	ND
Total	100	100	100	100

ND = NOT DETECTED

Table 4.2: XRPD Bulk Mineralogy (wt %) based on reference intensity ratio (RIR) Method

Sample ID	Quartz	Plagioclase	K-feldspar	Calcite	Dolomite	Pyrite	Anatase	Halite	Apatite	**I+/S-ML	*Chlorite(Tri)	Kaolinite	Palygorskite	Total
SST-Untreated	83.3	0.0	12.1	1.3	0.0	0.1	0.0	0.2	0.0	1.0	0.0	2.0	0.0	100.0
SST-Betaine	62.9	0.3	14.8	13.2	0.0	0.4	0.1	0.1	0.0	2.5	1.5	4.2	0.0	100.0
SST-ATMP	96.4	0.0	1.3	0.2	0.1	0.1	0.0	0.9	0.0	trace	0.4	0.6	0.0	100.0
SST-Glut	96.8	0.5	1.2	0.1	0.6	0.0	0.0	0.1	0.0	trace	0.3	0.4	0.0	100.0
LST-Untreated	3.9	0.0	0.0	78.6	2.4	0.0	0.0	0.0	trace	6.1	0.0	3.5	5.5	100.0
LST-Brine	3.6	0.0	0.0	79.3	3.1	0.0	0.0	0.2	trace	4.9	0.0	3.2	5.7	100.0
LST-Betaine	0.8	0.0	0.0	95.5	0.5	0.4	0.0	0.0	0.4	2.4	0.0	0.0	0.0	100.0
LST-ATMP	1.6	0.0	0.0	79.5	0.0	0.1	0.0	0.5	0.0	5.1	0.0	0.0	13.2	100.0
LST-Glut	2.1	0.0	0.0	91.1	0.9	0.3	0.0	0.0	0.0	4.4	0.0	1.2	0.0	100.0

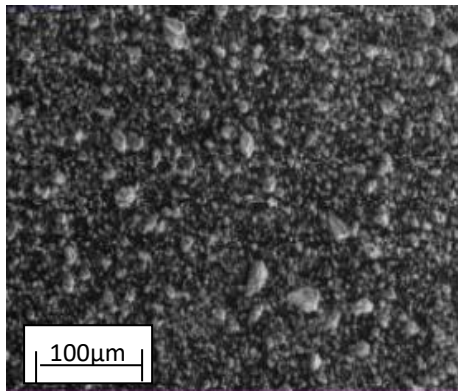
SST = Sandstone; LST = Limestone; ATMP = Aminotri (methylphosphonic acid); Glut = Glutaraldehyde
 *Chlorite (Tri) = Trioctahedral Chlorite; **I+/S-ML = Illite+Illite/Smectite - Mixed Layers

Table 4.3: Relative percentage of clay minerals in the < 2 μ m clay size fraction

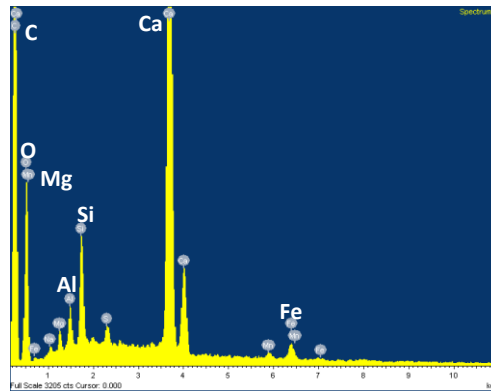
Sample ID	Chlorite	Kaolinite	Illite	I/S_ML	Palygorskite	%Expandability
SST-Untreated	6	45	2	47	0	100
SST-betaine	7	33	2	58	0	100
SST-ATMP	27	40	4	29	0	indeterminate
SST-Glut	24	44	5	27	0	indeterminate
LST-Untreated	1	18	0	44	37	85
LST-brine	0	11	0	45	44	85
LST-betaine	0	4	0	96	0	indeterminate
LST-ATMP	0	tr	0	48	52	85
LST-Glut	0	11	0	89	0	85

% Expandability is an estimate of the expandability of the mixed-layer illite/smectite clay

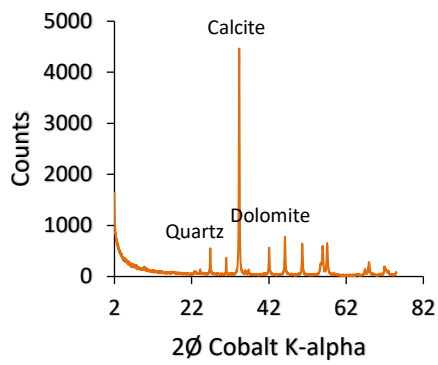
Similarly, the SEM micrograph of the limestone reveals poorly sorted, rhombohedral calcite minerals (Figure 4.2a) as confirmed by EDX scan showing high traces of calcium (Ca), oxygen (O) and carbon (C), see Figure 4.2b and Table 4.4. XRPD result further confirms the limestone consists of high proportion of calcite (78.6 wt%) and 21.4 wt% of other minerals like dolomite, quartz, I+I/S-ML, kaolinite and palygorskite (Figure 4.2c and Table 4.2). Palygorskite was found in the limestone samples from Sokoto Basin, which is consistent with previous findings (Nton and Elueze 2005). The presence of palygorskite (44%), kaolinite (18%), I/S-ML (37%) and chlorite (1%) in untreated limestone is revealed by clay fraction identification (Figure 4.2d and Table 4.3).



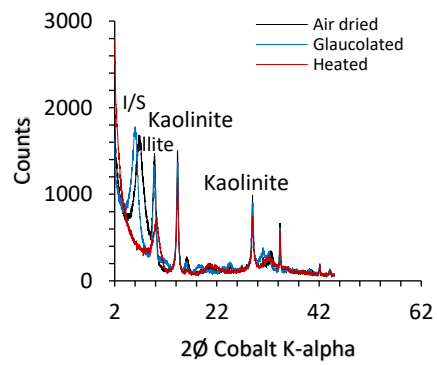
(a)



(b)



(c)



(d)

Figure 4.2: Characterisation of untreated limestone: (a) SEM micrograph, (b) EDX scan, (c) XRPD bulk mineralogy and (d) XRPD clay fraction identification.

Table 4.4: Elemental composition of limestone using SEM-EDX pre and post treatment.

Limestone (n=4)					
Elements	Pre-treatment (wt%)	Brine (Wt%)	Betaine (wt%)	ATMP (wt%)	Glutaraldehyde (wt%)
Na	0.9±0.1	ND	ND	29.1±3.1	ND
C	18.8±1.0	46.8±15	34.7±7.7	4.6±0.2	27.5±9.6
O	57.5±9.2	41.6±13	49.2±5.3	7.1±1.2	53.5±3.3
Mg	1.8±0.01	0.4±0.2	0.3±0.1	0.5±0.02	1.2±0.4
Al	4.9±0.3	0.8±0.7	0.1	1±0.1	2.0±1.0
Si	0.1	1.9±1.6	0.4±0.1	4.2±1.1	5.4±3.4
S	0.2	trace	0.1±0.1	ND	ND
Mn	0.1	ND	ND	ND	0.1±0.0
Fe	0.1	0.3±0.2	0.2±0.1	0.7±0.01	1.1±0.9
Cl	ND	trace	ND	48.1±5.2	ND
Ca	13.9±3.5	7.7±3.0	15.0±4.2	4.7±0.3	15±4.2
K	ND	trace	ND	ND	ND
Ti	ND	trace	ND	ND	0.1
Total	98.4	99.5	100	100	100

ND = NOT DETECTED.

4.3.2 Effect of chemicals on geomechanical strength

The pre and post chemical treatment uniaxial stress-strain responses in compression for the sandstone and limestone are shown in Figure 4.3. For both chemically treated (post) and untreated (pre) samples, the applied load was increased linearly with increasing axial displacement (or strain) until failure of the sample or the load limit of the test machine was reached.

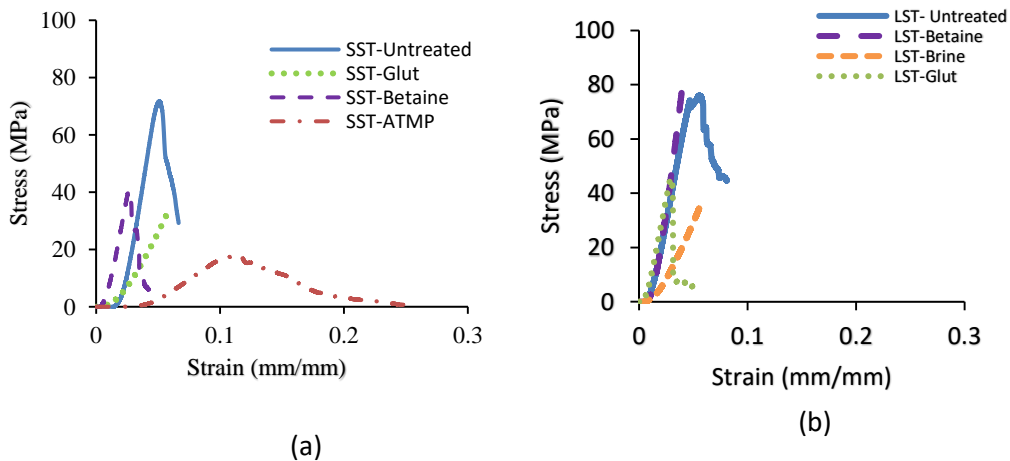


Figure 4.3: Uniaxial compression response pre-treatment and post chemical treatment of (a) sandstone and (b) limestone.

Acknowledging that the sample dimensions have influence on the strength, the measured strength of core samples with length/diameter (L/D) ratio less than 2 was corrected using the ASTM standard correction factor of 0.87 (ASTM, 1992). Table 4.5 shows the measured and corrected uniaxial compressive strength of untreated and treated sandstone. The strength of untreated sandstone reduced from 63 MPa to 16, 35 and 28 MPa following treatment with scale inhibitor (ATMP), corrosion inhibitor (betaine), and biocide (glutaraldehyde) respectively (Figure 4.3a). For the limestone, the pre-treatment strength reduced from 66 MPa to approximately 39 MPa as a result of treatment with glutaraldehyde (Figure 4.3b and Table 4.5). There was no failure in the limestone treated with corrosion inhibitor (betaine) and brine when a load of 90 kN was applied; this is equivalent to an axial stress of 54 MPa and 80 MPa respectively. Noting that the maximum load capacity of the test machine was 100 kN, the test was stopped just before the limit was attained. It is worth noting that the limestone sample treated with the scale inhibitor (ATMP) cracked and split before the mechanical test possibly as a result of the interaction between the chemical and the sample (Figure 4.4). As the sample was obtained from a relatively shallow depth (22-25 ft), see Table 3.1, it is expected to have a relatively low initial compressive strength. Consequently, no further compression tests were conducted on the sample. A summary of the uniaxial compressive strength is given in Table 4.5. These results showed a 55% and 41% reduction in strength for sandstone treated with ATMP and limestone treated with glutaraldehyde respectively, when compared with the corresponding untreated samples.

Table 4.5: Summary of mechanical test results for sandstone and limestone

Sandstone	Pre-Treatment	*Brine	ATMP	Betaine	**Glutaraldehyde
Max. load (N)	80,382	N/A	54,618	45,307	90,000
UCS (MPa)	72	N/A	18	40	32
L/D ratio	0.7	N/A	0.4	0.5	0.5
UCS (MPa) using ASTM (0.87)	63	N/A	16	35	28

Limestone	Pre-Treatment	**Brine	***ATMP	**Betaine	Glutaraldehyde
Max. load (N)	85,176	90,000	N/A	90,000	78,922
UCS (MPa)	76	≥80	N/A	≥54	45
L/D ratio	0.7	0.5	N/A	1	1
UCS (MPa) using ASTM (0.87)	66	70	N/A	47	39

* Insufficient sample
** No failure at maximum load of 90 kN
*** Specimen cracked after chemical exposure and before compression test

For the sandstone samples exposed to betaine and ATMP, failure occurred below the load capacity of the machine and it was therefore not possible to compare the relative impact of the chemicals on the geomechanical strength of the formation rock. The limestone exposed to ATMP split before mechanical testing indicating significant damage to the fabric due to the exposure to the chemical, however the core exposed to glutaraldehyde was tested to failure. Ideally it would be preferable to have been able to test all the cores to failure; nonetheless, it is believed that the number of sandstone and limestone core samples tested to failure after exposure to different chemicals were sufficient to provide adequate results for relevant comparison and meaningful conclusions.



Figure 4.4: Damaged limestone due to treatment with ATMP

The significant effect of the chemical treatment on the limestone, especially with ATMP treatment, compared to the sandstone is attributed to a more rapid deterioration of grain to grain binding in the limestone. Sandstone due to its high porosity in nature absorbs fluids more and faster, however, it does not retain the fluids compared to limestone. As such the interaction between the chemicals and the limestone as made possible by adsorption would have resulted in the weakening of the materials that bind the grains together leading to significant reduction in the compressive strength.

4.3.3 Failure effects on sandstone

Changes in the mineralogical and elemental composition of sandstone as a result of interaction with the chemicals were investigated.

The SEM micrographs, EDX and XRPD analysis of a sandstone sample post exposure to betaine are shown in Figure 4.5. The post treatment (betaine and ATMP) SEM micrographs for the sandstone sample (Figure 4.5a,b) reveals the spreading of the altered mineral constituents on the surface of the larger unaltered quartz grains as indicated by the arrow in contrast to the untreated samples which consists primarily of unaltered quartz grains

(Figure 4.1a). This observation was consistent with that of chalk when exposed to brine as reported by Madland et al. (2011). Also noted was a clear evidence of loose grain assemblages which resulted from the disintegration of the mineral constituents of the cores. Figure 4.5c shows pitting on the glutaraldehyde treated sandstone. The interaction of the chemicals with the rock materials contributed to the weakening of the grain fabrics of the rock, resulting in the disintegration of the grain-to-grain binding and eventual loosening and migration of the sand grain. This result agrees with earlier work by Oluyemi (2014). Additionally, the presence of pitting in the SEM micrograph circled in Figure 4.5c which would have been made possible by the reaction of the chemicals with the feldspar content of the rock and production of new materials is an evidence that dissolution/precipitation of certain minerals took place. Similar observation was earlier reported by Allen and Conca (1991) and Jordan et al. (1994).

The elemental composition of sandstone samples after chemical treatment as obtained from the EDX analysis (Table 4.1) reveals the presence of Na (0.6, 1.3 and 0.7) wt.%, Cl (0.6, 2.1 and 0.7) wt.% and Mg (0.3, 0.5 and 1.0) wt.% in betaine, ATMP and glutaraldehyde treated sandstone respectively (Figure 4.5d,e,f). These elements were not found in the untreated sandstone, see Table 4.1. This signifies precipitation of halite and dolomite in the presence of these chemicals. It was observed that carbon (C) decreased from 13.2 wt.% to 6.3 wt.% and 2.1 wt.% in betaine and ATMP treated sandstone respectively. Ca increased from 0.1 wt.% to 9.3 wt.% with betaine treated sandstone and is unchanged with ATMP treated sample. Little or no change in Si content was observed with betaine and

glutaraldehyde (4% decrease). However, ATMP treated sandstone showed a slight decrease which constitutes about 18% reduction in Si content. The increase in content of Na, Al, K, Ca, Fe in betaine, ATMP and glutaraldehyde treated sandstone suggests dissolution and precipitation of feldspar (K-feldspar and plagioclase) as well as clay minerals which also serve as cementing material (Table 4.1). Phosphorus was released into the ATMP treated sandstone effluents due to dissolution reaction.

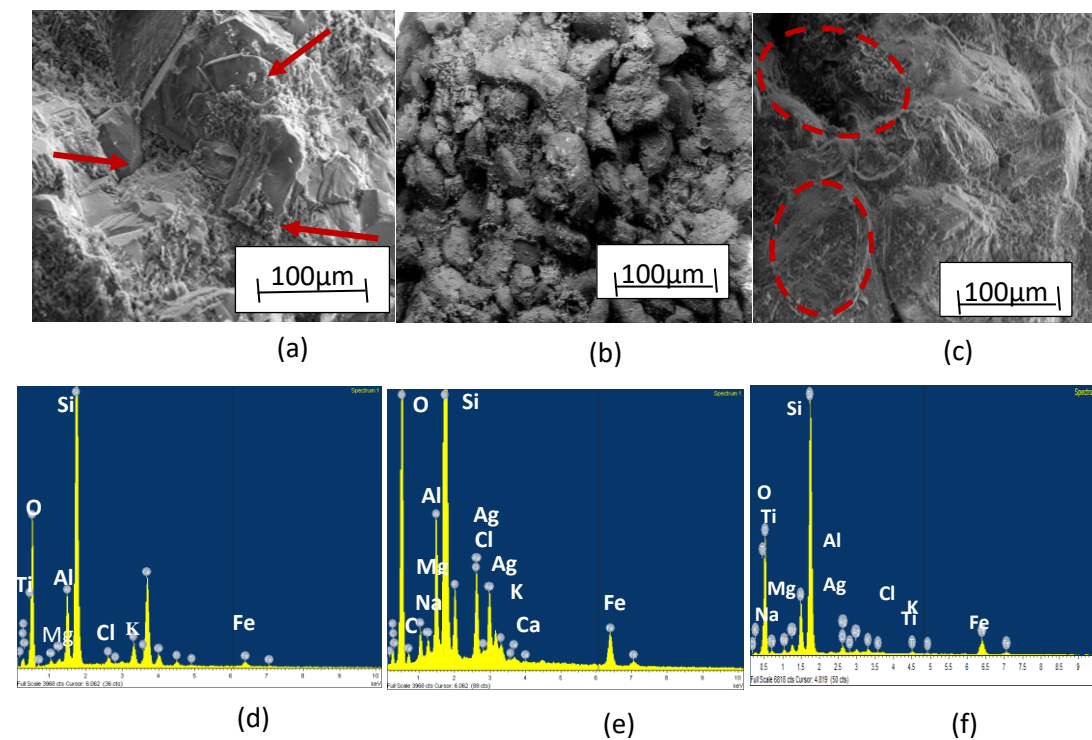


Figure 4.5: The SEM micrograph and EDX scan of sandstone post saturation showing: (a) pitting with betaine treated sample indicated by red arrows; (b) the spread of altered minerals on unaltered grain in ATMP treated sample; (c) pitting with glutaraldehyde treated sample indicated by red ellipsoid and elemental composition of samples treated with: (d) betaine; (e) ATMP; (f) glutaraldehyde.

On the other hand, the X-ray powder diffraction (XRPD) results for bulk mineralogical (whole rock) analysis, (Table 4.2 and Figure 4.6a,b,c), reveal quartz, plagioclase (albite), K-feldspar, pyrite, I+I/S-ML, chlorite, calcite and kaolinite in the sandstone treated with betaine; quartz, K-feldspar, calcite, dolomite, halite, chlorite and kaolinite in the sandstone treated with

ATMP; and quartz, plagioclase, K-feldspar, calcite, dolomite, halite, chlorite and kaolinite in sandstone treated with glutaraldehyde. Quartz which is the dominant mineral in the sandstone core sample is believed to be non-reactive in the presence of acidic inhibitor species with the exception of hydrofluoric acid, hence, may not undergo dissolution (Jordan et al. 1994). However, in this study, quartz was observed to have reduced from 83.3 wt.% to 62.9 wt.% in the presence of betaine and yet increased slightly to 96.4 wt.% and 96.8 wt.% in the presence of ATMP and glutaraldehyde respectively. The change would have been made possible by the reaction that occurs by the separate, parallel, removal of oxygen and silicon units that are dependent on the potential difference across the stern layer (Crundwell 2017). Clay fraction analysis (Table 4.3) reveals various compositions of clay minerals in untreated and chemically treated sandstone. The betaine treated sandstone shows 7% chlorite, 33% kaolinite, 2% illite and 58% mixed-layer illite+illite/smectite contents (Figure 4.6d). The result represents 27% decrease in kaolinite content and 19% increase in mixed-layer illite+illite/smectite relative to untreated sandstone. Figure 4.6e shows that ATMP treated sandstone contains 27% chlorite, 40% kaolinite, 4% illite and 29% mixed-layer illite+illite/smectite. Comparing this result with that of untreated sandstone, it represents 78% increase in chlorite, 11% decrease in kaolinite, 50% increase in illite and 38% decrease in mixed-layer illite+illite/smectite. Glutaraldehyde treated sandstone is shown in Figure 4.6f to contain 24% chlorite, 44% kaolinite, 5% illite and 27% mixed-layer illite+illite/smectite. Relating the result to that of untreated sandstone, it represents 75% increase in chlorite, 60%

increase in illite and 43% decrease in mixed-layer illite+illite/smectite contents.

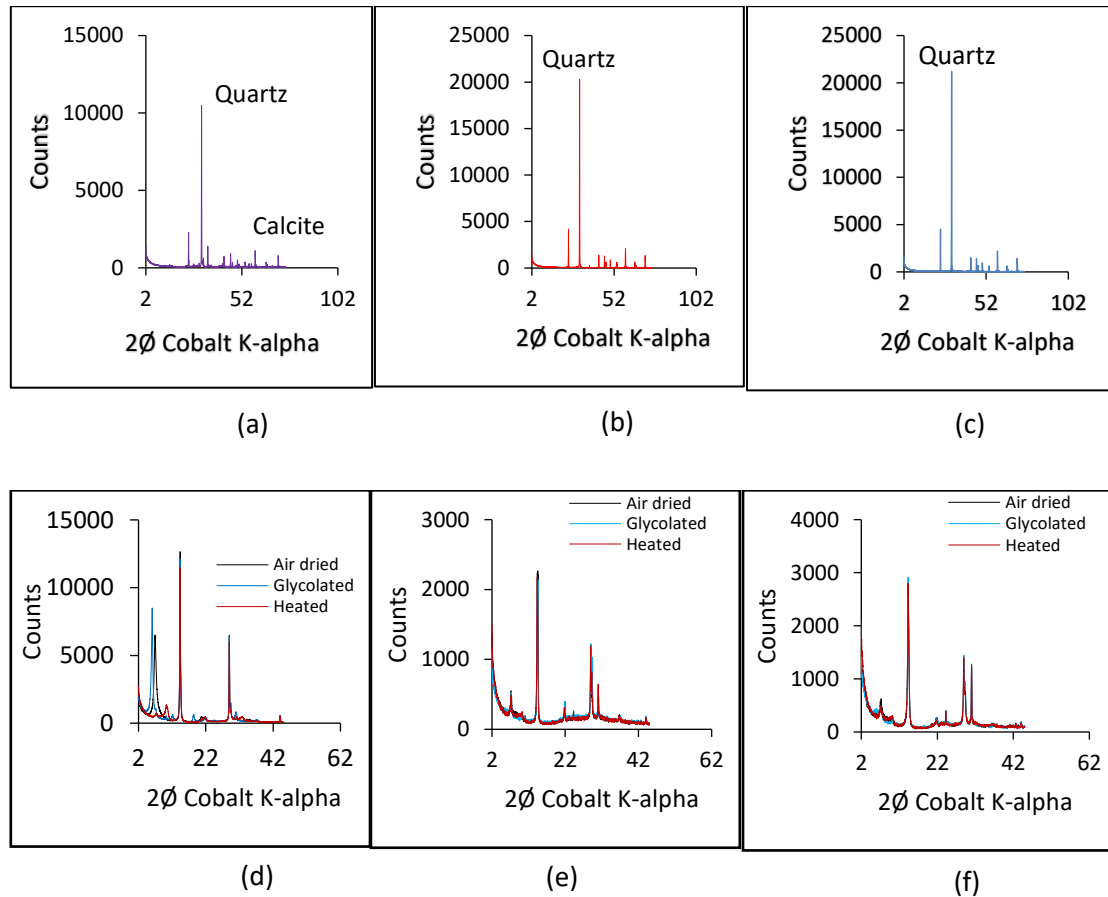
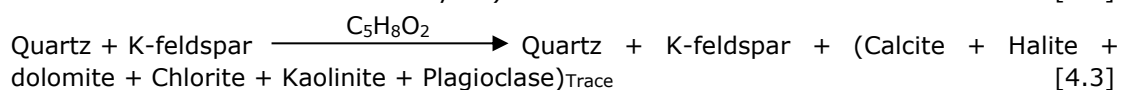
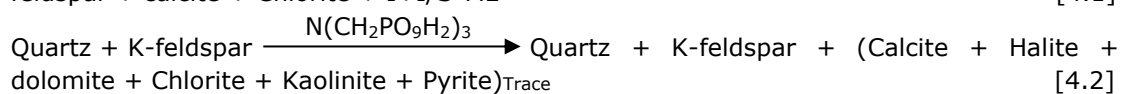
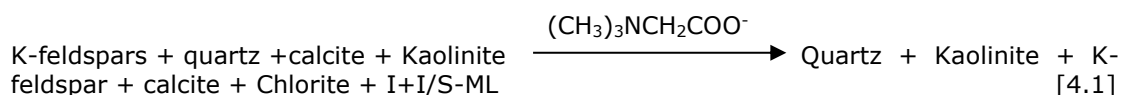


Figure 4.6: XRPD whole rock mineralogy and clay fraction identification of chemically treated sandstone: (a) betaine; (b) ATMP; (c) glutaraldehyde; (d) betaine (clay); ATMP (clay); (f) glutaraldehyde (clay).

It is believed that the changes observed in the sandstone due to exposure to betaine, ATMP and glutaraldehyde was orchestrated by dissolution, precipitation and ion exchange reactions. These likely reactions are presented in equations 4.1 to 4.3:



It is worthy of note that the absence of brine exposure due to insufficient number of core samples, which could have served as control makes it difficult to confirm that the changes observed in sandstone were entirely due to the chemical interaction with the rock and not an effect of the combined interaction of the chemical and the brine with the rock.

The studied sandstone core sample is identified to have high content of clay minerals (Table 4.3). Clay minerals in their nature are very reactive due to their large surface area and negative charge. The dissolution of feldspar and the clay minerals (kaolinite, chlorite, illite and illite/smectite) can lead to precipitation of other clay minerals as evidenced by clay fraction results (Marty et al. 2015; Shao et al. 2010); and the hydrolysis of quartz due to chemical-formation rock interaction can cause reduction of the geomechanical strength of the reservoir rock (Han and Dusseault, 2002). The weakening effect of the chemical on the rock cement was more evident in betaine treated sandstone.

4.3.4 Failure effects on limestone

Figure 4.8 shows the SEM micrograph and EDX scans of the limestone post chemical treatment. Pitting was observed on the SEM micrograph of the betaine treated limestone (Figure 4.7a). This suggests that dissolution reaction of certain minerals took place leading to precipitation of other minerals. The SEM results in Figure 4.5b shows precipitation of mineral believed to be halite owing to treatment with ATMP with the precipitates spread over the unaltered grains. Figure 4.7c shows flaking and spreading of detached mineral grains following treatment with glutaraldehyde. EDX spectrum (Figure 4.7d) confirms the dissolution/precipitation reaction with

a decrease in carbon and oxygen from 18.8 wt.% and 57.5 wt.% in untreated limestone to 7.2 wt.% and 37.6 wt.% respectively; and an increase in calcium from 13.9 wt.% to 51.4 wt.% in betaine treated limestone. Other elements that experienced a decrease on exposure to betaine were aluminium (4.9 to 2.38 wt.%), sulphur (0.2 to 0 wt.%) and manganese (0.1 to 0 wt.%). Iron and silicon increased from 0.1 to 0.6, 0.42 wt.% respectively. The changes observed in the element contents of the limestone were due to dissolution, precipitation and ionic substitution reactions. Interestingly, EDX spectrum (Figure 4.7e) shows a high content of sodium (Na), 29.1 wt% and chloride (Cl), 48.1 wt% in ATMP treated limestone with no presence of chloride in the untreated and other chemically treated limestone samples, despite that all the chemicals were prepared with brine that contains sodium chloride. The untreated limestone contains only 0.93 wt% of sodium. This could be a consequence of a new compound, for example halite (sodium chloride), being formed in the presence of ATMP and a clear evidence of elemental/ionic exchange between the limestone and the chemicals (especially betaine) to varying degrees (Table 4.4). Other elements that exhibited changes that confirms precipitation reaction are silicon (4.2 wt.%) and iron (0.7 wt.%). Evidence of dissolution reaction in ATMP treated sample is shown by decrease in content of: carbon, 18.8 to 4.6 wt.%; oxygen, 57.5 to 7.1 wt.%; magnesium, 1.8 to 0.5 wt.%; aluminium, 4.9 to 1.0 wt.%; sulphur, 0.2 to 0 wt.%; and calcium 13.9 to 4.7 wt.%. Figure 4.5f shows abundance of calcium (45.1 wt.%), oxygen (45.0 wt.%) and carbon (7.7 wt.%) that typifies calcite precipitation. Increase of Ca^{2+} in the fluid stream is a confirmation that the samples underwent dissolution reaction. The appreciable reduction of calcium in

ATMP treated sample is an indication that calcium was consumed in the reaction after dissolution to precipitate a new compound. The brine treated sample also experienced slight change in the elemental content (Table 4.4). However, the change was minimal compared to the changes observed in other chemically treated samples.

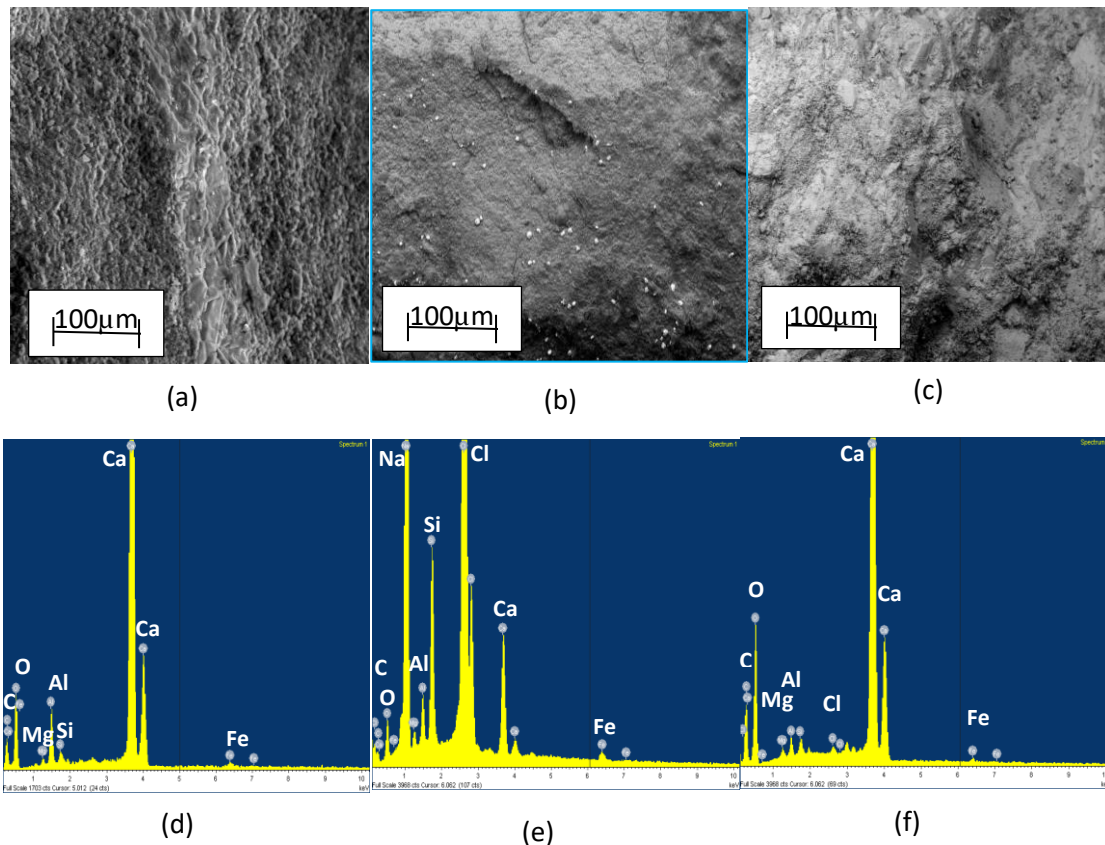


Figure 4.7: The SEM micrograph and EDX scan of limestone post saturation with: (a) betaine treated limestone showing the spreading of altered minerals on unaltered grain; (b) precipitation of halite in ATMP treated limestone; (c) spreading of altered grains in the glutaraldehyde treated limestone; (d) betaine, EDX scan, (e) ATMP, EDX scan; (f) glutaraldehyde, EDX scan.

The X-ray powder diffraction (XRPD) result for bulk mineralogical (whole rock) analysis shown in Figure 4.8a,b,c and Table 4.2 further confirms the exchange of elements between the rock cores and the chemicals to precipitate new minerals (Equations 4.4-4.7). Calcite increased from 78.6 wt% to 95.5 wt% and 91.1 wt% in the presence of betaine and

glutaraldehyde respectively, with little or no change in the presence of brine and ATMP. However, palygorskite $[(Mg,Al)2Si_4O_{10}(OH).4(H_2O)]$ increased significantly from 5.5 wt% (untreated) to 13.2 wt% with ATMP treated, and it is completely absent in the betaine and glutaraldehyde treated limestone. Precipitation of halite in ATMP treated limestone is further confirmed by XRPD (Figure 4.8b).

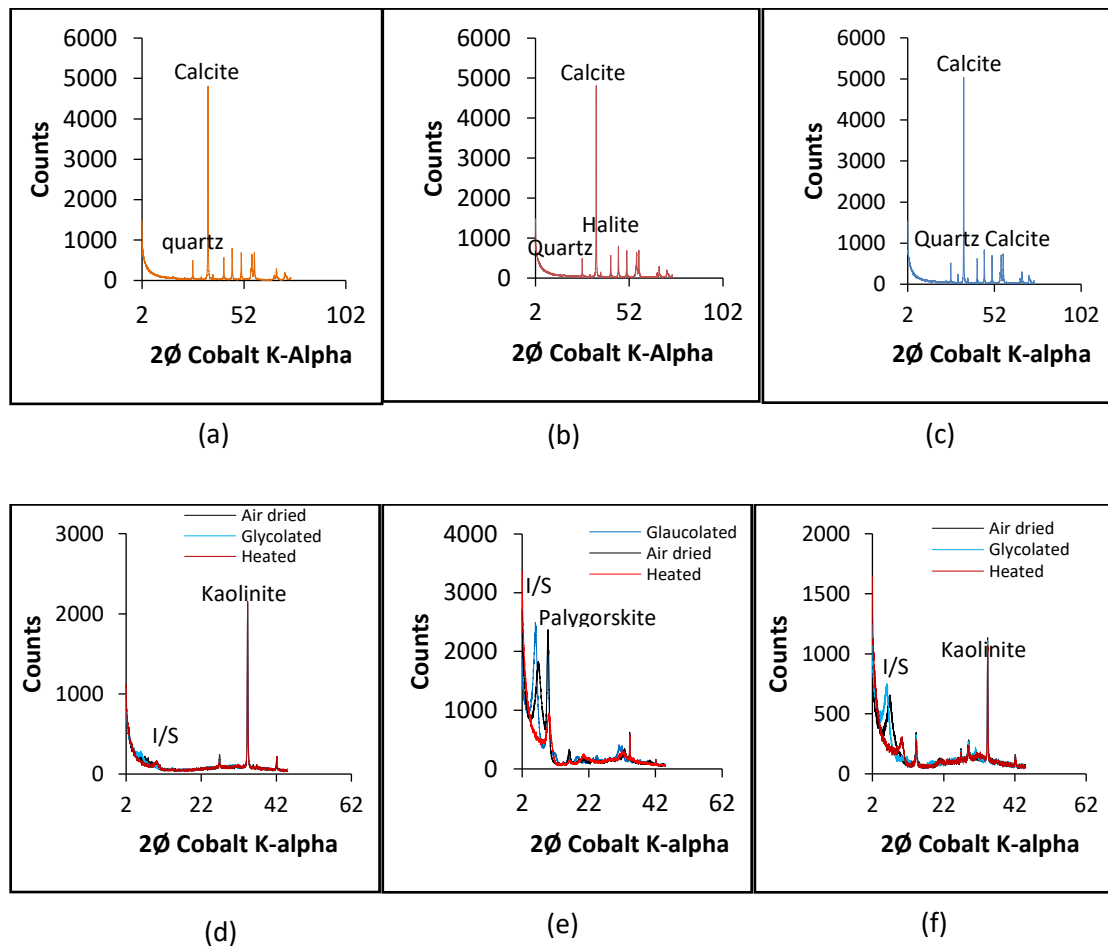


Figure 4.8: XRPD whole rock mineralogy and clay fraction identification of chemically treated limestone: (a) betaine; (b) ATMP; (c) glutaraldehyde; (d) betaine (clay); (e) ATMP (clay); (f) glutaraldehyde (clay).

The observed changes in the mineralogical composition including increase in the concentration of calcite and palygorskite can be explained by the likely chemical reactions between the two samples (limestone) and the chemical inhibitors. This is based on the high percentage of observed

elements in Tables 4.4. The chemical reactions are summarised in Table 4.6.

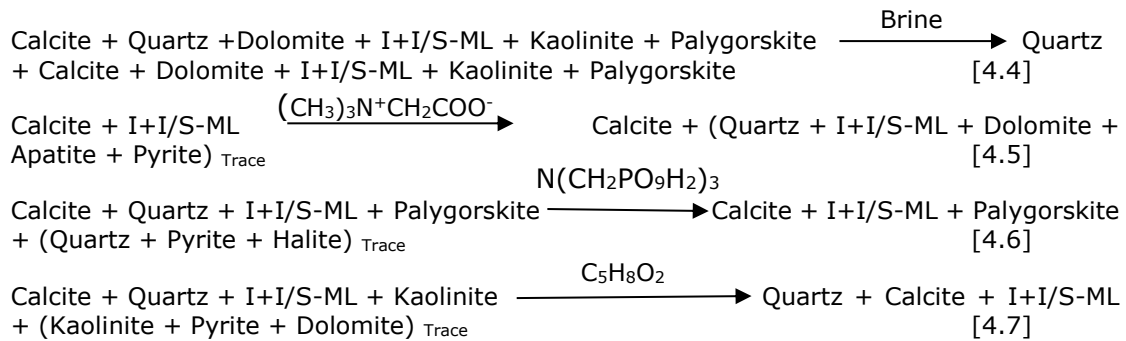


Table 4.6: Interaction between oilfield chemicals and formation rocks

Reactions	Products
Betaine (C ₅ H ₁₁ NO ₂) and sandstone (SiO ₂)	Chlorite Quartz K-Feldspar Calcite I + I/S-ML
ATMP (N(CH ₂ PO ₉ H ₂) ₃) and sandstone (SiO ₂)	Quartz
Glutaraldehyde (C ₅ H ₈ O ₂) and sandstone (SiO ₂)	Quartz
ATMP (N(CH ₂ PO ₉ H ₂) ₃) and limestone (CaCO ₃)	Calcite Palygorskite I + I/S-ML
Betaine (C ₅ H ₁₁ NO ₂) and limestone (CaCO ₃)	Calcite I+I/S-ML (quartz, dolomite, apatite, pyrite) - trace
Glutaraldehyde (C ₅ H ₁₁ NO ₂) and limestone (CaCO ₃)	Calcite I + I/S-ML (Kaolinite, dolomite, apatite, pyrite) - trace

The XRPD for clay fraction identification (Figures 4.8d) shows the peak of kaolinite and mixed-layer illite + illite/smectite in betaine treated limestone. Figure 4.9e confirms the presence of palygorskite and mixed-layer illite + illite/smectite in ATMP treated limestone. Apart from kaolinite whose amount in the untreated limestone decreased from 18% to 11%, 4%, trace and 11% in brine, betaine, ATMP and glutaraldehyde treated limestone

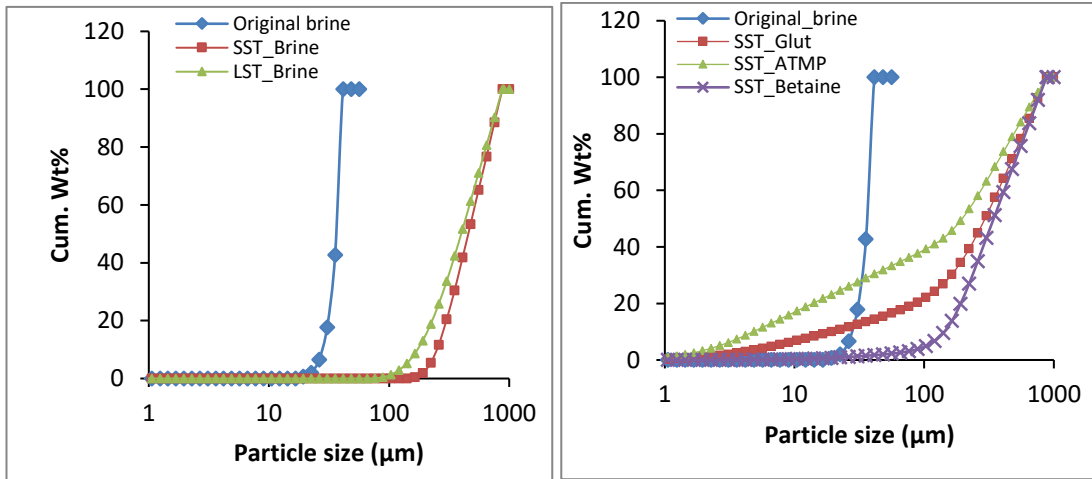
respectively, the concentration of other clay minerals increased. For example, I/S-ML increased from 44% in untreated limestone to 98%, 48% and 89% with betaine, ATMP and glutaraldehyde treated limestone respectively; and palygorskite increased from 37% to 44% and 52% in the presence of brine and ATMP respectively. The result suggests that more calcite and clay were precipitated into the fluid stream. The precipitates can settle in the pore throat and cause constriction resulting in formation damage. However, no change of I/S content was observed with brine treated limestone. This is evidence that the changes observed in the two rock types were brought about primarily by the interaction with the chemicals, and that brine has little or no effect on the rock. However, this points to new evidence with regards to brine-rock interaction which is contrary to the evidence provided from Bybee (2010) and Madland et al. (2011).

The results clearly indicate moderate to high content of clay minerals in both sandstone and limestone samples whose expansion as demonstrated by the increase in expandability (Table 4.3) might have negatively impacted the rock strength owing to clay mechanical strength being generally weaker than a typical sandstone (Balog et al. 2014). It has been shown that amphoteric betaine adsorption in the presence of divalent ions is significantly higher on sandstone, in contrast to the adsorption on limestone (Mannhardt et al., 1993). The results obtained in the current study indicate adsorption, dissolution/precipitation and ionic substitution reaction of the oilfield chemicals with both sandstone and limestone.

4.3.5 Grain size distribution

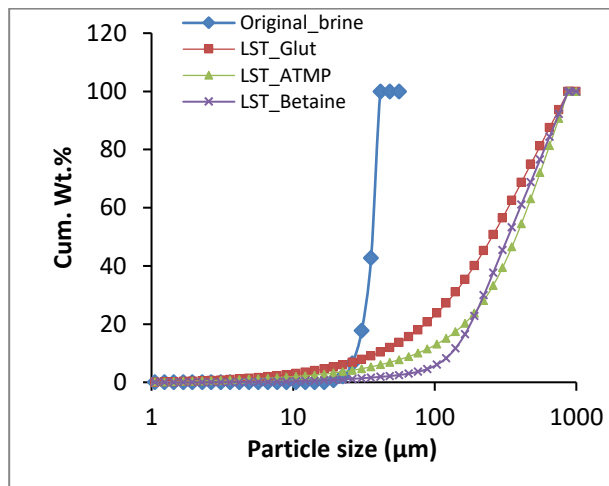
The grain size distribution profiles of the original brine and brine effluent as well as the effluents from the various chemical solutions are presented in Figure 4.9. Figure 4.9a shows that there was a notable difference in the key grain size parameters of D_{10} , D_{50} , D_{90} and sorting (also see Table 4.7) between the grain size distribution profiles of the original brine and the brine effluents from the two cores (sandstone and limestone). This is consistent with the visual observation of the presence of some particles in the effluents. The values of the key grain size parameters for the brine effluents suggest the particles originated either from the existing fines (D_{10}) in the cores prior to saturation in the brine or from the fines that were less than the glass filter could trap. Integration of these results with the mechanical and analytical test results shows that there was no failure in the brine-treated cores and, therefore, no significant release of particles into the brine during the test. However, the difference in the grain size parameters between the original brine and all the chemical effluents was much more significant (see Figures 4.9b, c; and Table 4.7). In particular, the chemical effluents appear to exhibit a broader grain distribution profile with poorer sorting in comparison to the original brine (Folk 1968). Figures 4.9b,c show that there was a release of some particles into the various chemical solutions during the tests. Similarly, integration of these results with the mechanical and analytical test results indicates failure of the chemically treated cores, which led to release of a wide range of particles into the chemical solutions. Increased proportion of particles in the effluent is implicitly caused by weakening of the rocks with a consequential reduction of their uniaxial compressive strength and release of failed materials into

the fluid streams. It is however, worthy of note, that it is possible for weakening of the bonding to occur without fine particles being released. In addition, the presence of fines in effluent does not necessarily mean the fines are from inside the core as they could be from the near outer surface of the core. This is likely to occur from low porosity and low permeability cores. Based on the SEM micrographs, it is confirmed that the fines obtained in this study were primarily from the inside of the cores. Aside from the risk of the sand production that is associated with the interaction between the oilfield chemicals and the rock, there is also the risk of low reservoir performance and formation damage near wellbore due to pore space clogging by the particles released into the fluid stream.



(a)

(b)



(c)

Figure 4.9: Comparison of the particle size distribution of the original brine and of (a) the effluent of sandstone and limestone in the brine; (b) the original brine and effluents from sandstone in betaine, ATMP and glutaraldehyde; (c) the original brine and effluents from limestone in glutaraldehyde, ATMP and betaine.

Table 4.7: Key parameters of the grain size distributions of the original brine and the effluents from real core samples.

Effluents	Particle Size			Classification (Folk 1968)	
	D10 (μm)	D50 (μm)	D90 (μm)	Sorting (σ_1)	Description
Original brine	26	40	41	0.36	Well sorted
Sandstone in brine	4.5	74	409	0.83	Moderately sorted
Limestone in brine	4.5	74	4.9	0.64	Moderately well sorted
Sandstone in glutaraldehyde	21	340	650	2.75	Poorly sorted
Limestone in glutaraldehyde	76	258	659	0.90	Very poorly sorted
Sandstone in ATMP	5	349	700	2.10	Very poorly sorted
Limestone in ATMP	76	350	800	1.23	Poorly sorted
Sandstone in betaine	141	350	750	0.94	Moderately sorted
Limestone in betaine	120	350	754	1.43	Moderately sorted

There was clear evidence that a substantial amount of sand particles was introduced into the fluids that contain the chemicals during the static saturation as a result of the weakening of the cores grain fabrics causing disintegration of the existing grain-to-grain binding which could lead to eventual failure.

4.4 Results and Discussion of the effects of chemicals on Outcrop core samples

Ten (10) cylindrical outcrop core samples, five (5) sandstone (leopard) and five (5) carbonate (Edward brown and desert pink) were saturated under static condition to determine changes in the particle size distribution, strength, elastic properties, mineralogical, elemental composition and uniaxial compressive strength. The same experimental procedures used for the investigation presented in Section 4.1 were also used for this investigation. However for this investigation, only glutaraldehyde was used

to saturate the two core types twice for repeatability purpose while brine saturation was used as control.

4.4.1 Characterisation of outcrop sandstone and carbonate samples

Characterization of the core samples was done with SEM, EDX and XRPD prior to chemical treatment to study the morphology, elemental and mineralogical composition.

SEM micrograph in Figure 4.10 shows a cross section of sandstone (leopard) to contain well-sorted, rhombic to orthorhombic detrital quartz grain coated with clay minerals. Figure 4.10a shows authigenic illite (dotted sphere), smooth mat illite (I) and mixed-layer illite/smectite (dotted square). Also revealed are developed interconnected pores (P) that describe the porous nature of sandstone and a developed authigenic quartz overgrowth (Qo) in close proximity to detrital quartz grains. Figure 4.10b further reveals the spread of clay minerals over the quartz grains, the rhombic to orthorhombic shape of the quartz grains, the honeycomb mixed-layer illite/smectite and smooth mat illite (I). A pronounced contact of the quartz overgrowth with the detrital quartz is revealed in Figure 4.10c.

EDX scan result (Figure 4.10d) confirms the presence of quartz in sandstone with high content of Si (30.38 wt. %) and O (64.23 wt. %). Whilst, the clay mineral and feldspar contents are indicated by the presence of Al (3.0 wt. %), Na (0.43 wt. %), K (0.87 wt. %), and Fe (0.50 wt. %). Also present in the sample is Ag (0.29wt.%).

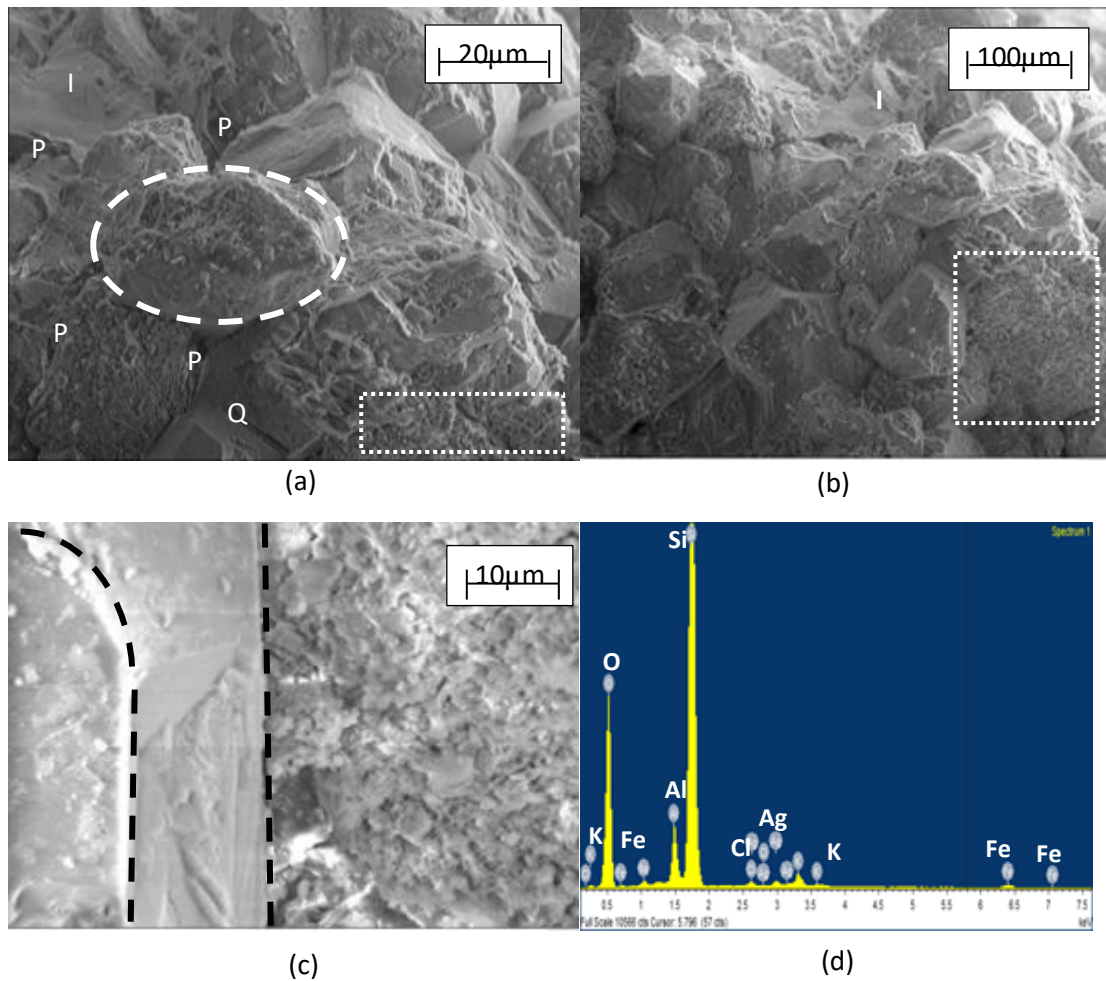


Figure 4.10: SEM micrograph and EDX scan of untreated sandstone: (a) orthorhombic detrital quartz coated with illite and interconnected pores (P); (b) quartz grains coated with clay minerals and a pronounced mixed-layer illite/smectite honeycomb morphology (white rectangle); (c) quartz overgrowth forming a distinct boundary contact with detrital quartz grains (d) EDX scan magnification: (a) 250 X; (b) 500 X; (c) 2.00 KX.

The XRPD bulk mineralogy result (Figure 4.11a) further confirms the presence of quartz (98.4 wt.%), plagioclase (0.2 wt.%), calcite (0.4 wt.%), anatase (0.2 wt.%), mixed-layer illite/smectite (0.8 wt.%) and kaolinite (trace) in untreated sandstone. Whilst, clay fraction result (Figure 4.11b) further confirms the presence of clay minerals in form of kaolinite (14%), illite (35%) and mixed-layer illite/smectite (51%) in the rock sample.

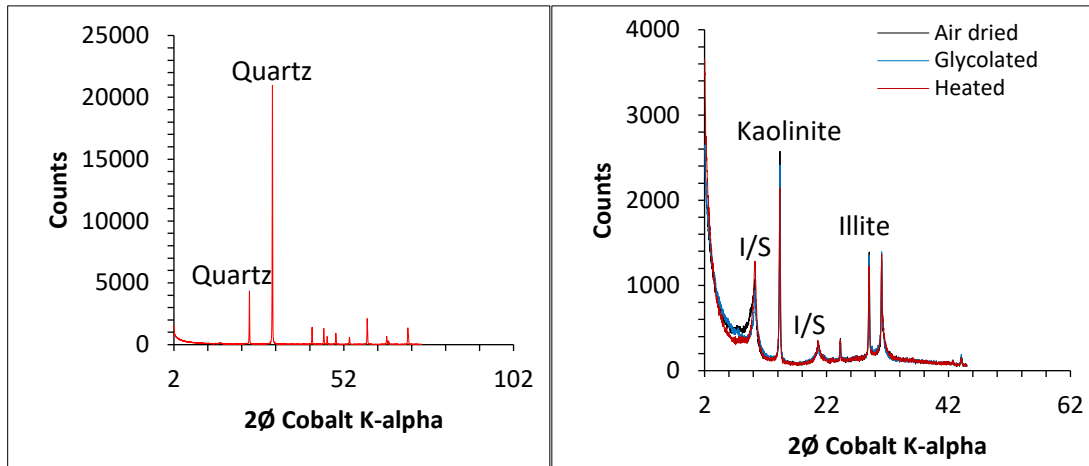


Figure 4.11: Mineralogical characterisation of untreated sandstone: (a) XRPD whole rock; (b) clay fraction.

Similarly, a cross-section of untreated carbonate (Edward brown) under SEM reveals dolomitized limestone with moderately sorted euhedral-subhedral dolomite ($\text{CaMg}(\text{CO}_3)_2$) mineral with sucrosic texture i.e recrystallized limestone with coarse texture (Figure 4.12a). Observed in the SEM micrograph are cloudy centres and light rims which are typical of dolomites (dotted spheres in Figure 4.12a). The dolomite grains are coated with pore filling calcite and authigenic clay minerals (Figure 4.12a,b,c). Several interconnected pore spaces (P) are observed in the sample. Figure 4.12c shows the typical dolomite morphology lightly coated by some authigenic grains under magnification 2.00KX. EDX spectrum (Figure 4.12d) indicates the presence of elements Si (4.30 wt.%) and O (70.20 wt.%) typical of quartz. The EDX confirms the dolomite content of the carbonate with the presence of Mg (5.79 wt.%) and Ca and that of calcite with the presence of Ca (10.88 wt.%). C (5.16 wt.%) and O are common to both dolomite and calcite. Other elements observed in the sample are Al (2.20 wt.%) K (0.65 wt.%), Cl (0.44 wt.%) and Fe (0.38 wt.%). The Al, K, Si, Ca and Mg content typifies illite, kaolinite and mixed-layer illite/smectite

content. The presence of Cl is an indication that the sample contains halite, while the Fe content indicates the presence of pyrite in the sample.

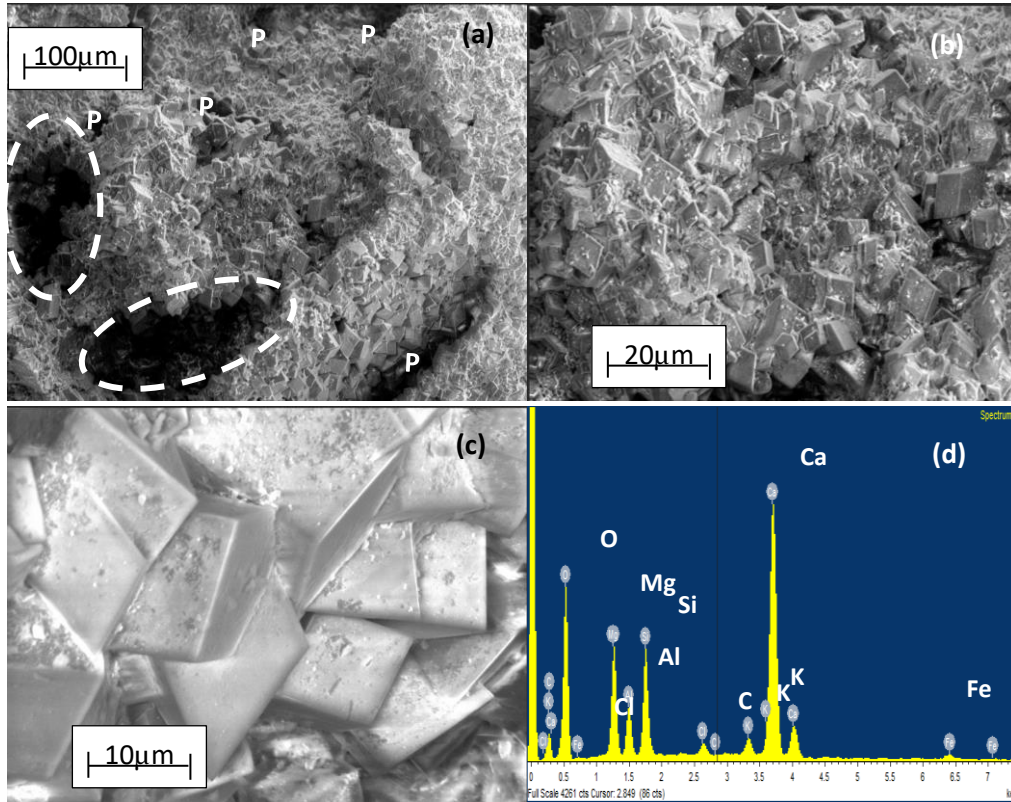


Figure 4.12: SEM micrograph showing the pore spaces at various magnifications and EDX spectrum of untreated Edward Brown carbonate: (a) XRPD, 250X; (b) XRPD, 500X; (c) XRPD, 2.00KX; and (d) EDX spectrum.

XRPD whole rock analysis (Figure 4.13a) further confirm the presence of dolomite (73.8 wt.%), calcite (21.2 wt.%), quartz (3.7 wt.%), pyrite (0.2 wt.%), halite (0.2 wt.%) and multi-layer illite/smectite (0.9 wt.%). Clay fraction analysis with XRPD (4.13b) confirms the presence of kaolinite (7%), illite (7%) and multi-layer illite/smectite (86%).

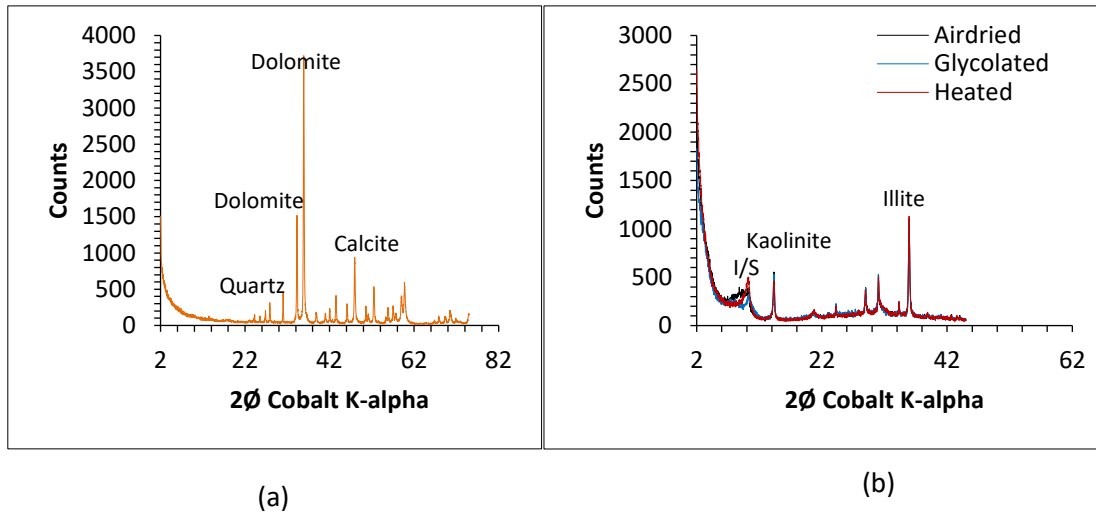


Figure 4.13: Mineralogical analysis of untreated carbonate: (a) XRPD whole rock; (b) clay fraction.

SEM analysis of untreated desert pink (carbonate) shows large, detrital calcite grains covered by authigenic pore-filling calcite (Figure 4.14a,b) under different magnifications. Also shown in Figure 4.14c are flakes of moderately sorted calcite. Based on EDX distinctive spectrum (Figure 4.14d) and analysis, desert pink is identified to contain only calcite hence, it is limestone. The elements identified are Ca (42.33 wt.%), C (9.95 wt.%) and O (47.72 wt.%). Due to time and resource constraints analysis with XRPD to further confirm the mineralogical composition of desert pink was not conducted.

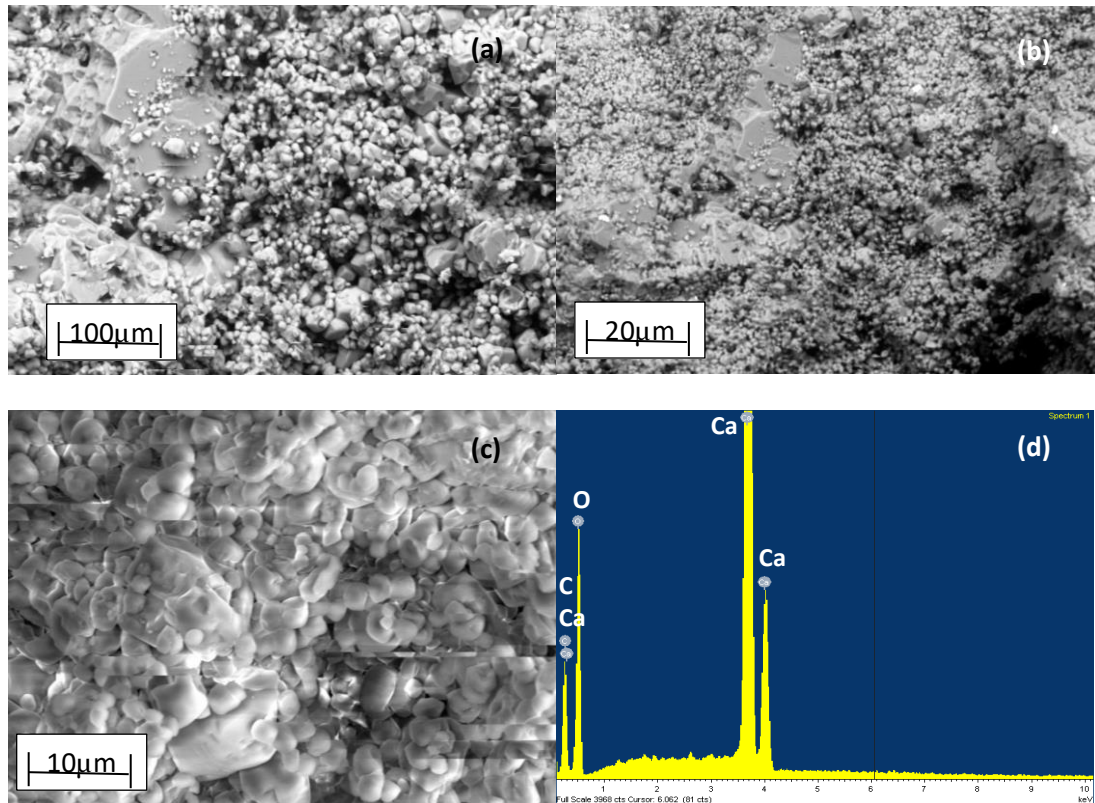
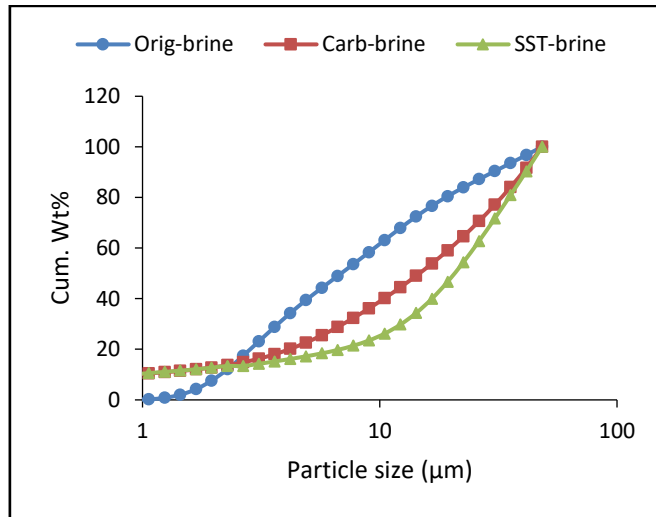


Figure 4.14: SEM micrograph at various magnifications and EDX spectrum of untreated carbonate: (a) XRPD, 1.00KX; (b) XRPD, 500X; (c) XRPD, 2.50KX; and (d) EDX spectrum.

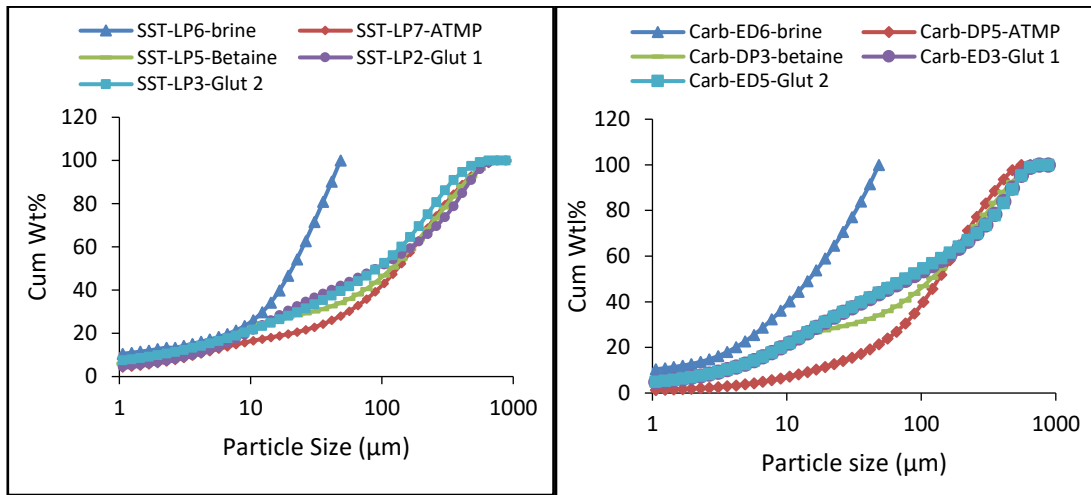
4.4.2 Grain size distribution analysis

The results of particle size distribution analysis for brine effluents and original brine produced a close range values for D_{10} , D_{50} and D_{90} (Table 4.8). Figure 4.16a shows a slight difference in shape and values between the grain size distribution profiles of the original brine and the brine effluents from the sandstone and carbonates. This is consistent with the visual observation of the effluents. However, there is a remarkable difference in the grain size distribution profiles of the original brine/brine effluents and the chemical effluents from sandstone and carbonates as indicated by the D_{50} and D_{90} values in Figures 4.15b,c and Table 4.8. The D_{10} , D_{50} and D_{90} values for the original brine and the brine effluents from sandstone and carbonates fall within the size of the sintered glass filter used in filtering the

brine before saturation. This signifies that there was no particle release into the brine which is an indication that no reaction took place between the brine and the core samples. On the other hands, the D_{10} , D_{50} and D_{90} values for the chemical effluents from sandstone and carbonates increased significantly relative to those of brine. The increase suggests some reactions such as dissolution might have taken place between the chemicals and the core samples that led to deterioration of the grain to grain binding hence, grains detachment and release into the fluid stream. The result is consistent with earlier work (Oluyemi 2014).



(a)



(b)

(c)

Figure 4.15: Grain size distribution profiles of: (a) original brine and brine effluents from sandstone and carbonate; (b) chemical effluents from sandstone; (c) chemical effluents from carbonate.

Table 4.8: Key parameters of the grain size distributions of the original brine and the effluents from outcrop samples.

Sandstone					
Effluents	Particle Size (μm)			Classification (Folk 1966)	
	D10	D50	D90	Sorting	Description
Original brine	3	7	30	0.01	Very well sorted
SST-brine	2	22	42	0.48	Well sorted
SST-ATMP	3	150	400	0.64	Moderately well sorted
SST-betaine	2	140	400	0.81	Moderately sorted
SST-Glut 1	2	98	350	0.81	Moderately sorted
SST-Glut 2	3	100	450	0.75	Moderately sorted
Carbonate					
Original brine	3	7	30	0.01	Very well sorted
Carb-Brine	2	15	41	0.51	Moderately well sorted
Carb-ATMP	16	130	350	0.37	Well sorted
Carb-betaine	7	120	405	0.79	Moderately sorted
Carb-Glut 1	7	70	407	0.85	Moderately sorted
Carb-Glut 2	7	71	408	0.84	Moderately sorted

4.4.3 Effect of chemicals on strength and Young's Modulus

The results of the mechanical testing on the sandstone and carbonates show decrease and increase in unconfined compressive strength and Young's modulus respectively on exposure to the chemicals. Figure 4.16a shows a reduction of the uniaxial compressive strength of untreated sandstone (Leopard) from 24 ± 2 MPa to 21 ± 2 MPa; 9MPa; 8MPa; and 7MPa following treatment with brine, scale inhibitor (ATMP), corrosion inhibitor (betaine) and biocide (glutaraldehyde) respectively. The measured strength of untreated Leopard is not far from the strength of 21 ± 1 MPa declared by the supplier (Kocurek Industries). The reduction in strength of sandstone owing to treatment with brine, ATMP, betaine and glutaraldehyde is equivalent to 13%, 63%, 67% and 71% reduction respectively.

For the carbonates (Edward brown), the pre-treatment strength increased from 6 MPa to 9, 8, 10 and 13 MPa owing to treatment with brine, ATMP, betaine and glutaraldehyde respectively; see Figure 4.16b. The 33%, 25%, 40% and 60% increase in strength of carbonate post chemical treatment with brine, ATMP, betaine and glutaraldehyde suggests precipitation reaction. However, the determined strength of untreated Edward brown (6 MPa), brine, betaine and ATMP treated are outside the range of the strength (14 - 21 MPa) declared by the Kocurek Industries. This could be due to low degree of lithification (Durmekova et al. 2003).

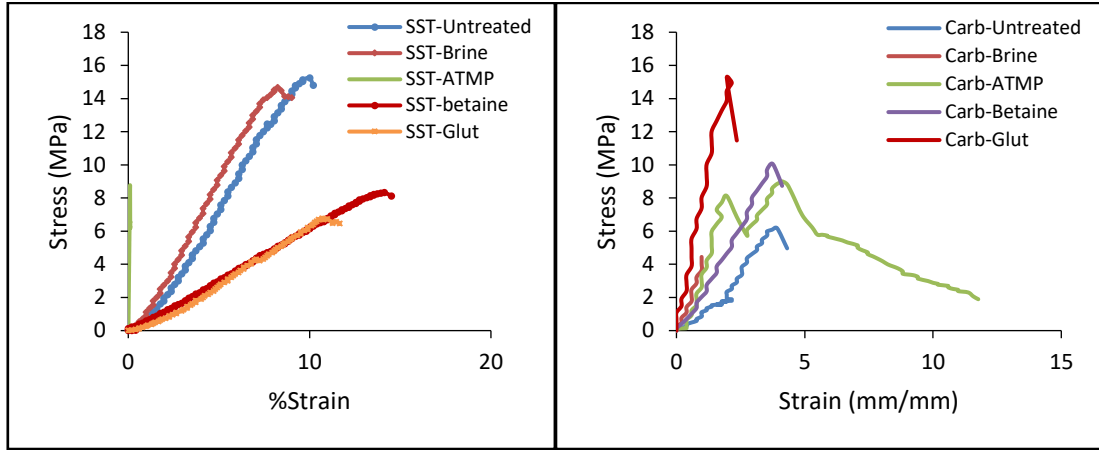
It is noteworthy that the length to diameter ratio of the cores is 1.3 which is lower than the standard ratio of 2-2.5. As such, the above strengths were corrected using the strength correction factors of 0.93 suggested by ASTM C 42-90 and 0.87 suggested by BS 1881, part 120 (Table 4.9).

These results represent approximately 13-71% reduction in strength of sandstone and 20 - 60% increase in strength of carbonate samples. This represents a remarkable alteration in the uniaxial compressive strength of the rocks post chemical treatment.

The measured Young's modulus, E , of sandstone (leopard) from the test results show a reduction in stiffness from 15 to 11GPa; 7GPa; 5GPa; and 5GPa with brine, ATMP, betaine and glutaraldehyde treatment respectively (Figure 4.16c).

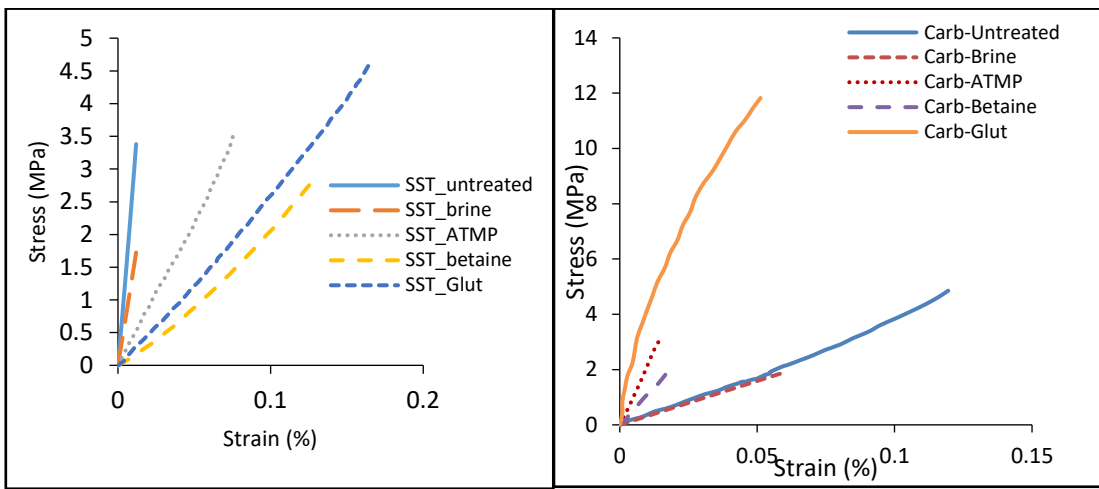
In contrast to sandstone, carbonate (Edward brown) increased from 4GPa to 10GPa; 5GPa and 8GPa following treatment with ATMP, betaine and glutaraldehyde respectively (Figure 4.16d). The value of the Young's

modulus of both rock types were affected by the chemical treatment. The reduction in the modulus of the sandstone post chemical treatment ranges from 57 to 67% relative to the corresponding value for the untreated sample; while the increment observed in the Young's modulus for the chemically treated carbonate ranges from 20 to 60% relative to the untreated sample. Betaine has the highest impact on sandstone (67%), while glutaraldehyde produced the highest impact on carbonates (60%). The measured values of the modulus for the untreated and brine treated rock samples are within the range of typical stiffness of sandstone (10 -20 GPa) and carbonates (3 – 27 GPa).



(a)

(b)



(c)

(d)

Figure 4.16: Stress-strain relationship and chemically treated: (a) sandstone with complete response to failure; (b) carbonate with complete response to failure; (c) sandstone with stress-small strain response; (d) carbonate with stress-small strain response.

Table 4.9: UCS and Young's modulus of sandstone and limestone with recommended correction factors (ASTM C42-90) and BS (1881) under static condition

Sandstone				
Sandstone	UCS (MPa)	ASTM (C42-90) Correction Factor	BP 1881-Part 120 Correction Factor	Young's Modulus (GPa)
SST-				
Untreated	24	22	21	15
SST-Brine	21	20	18	11
SST-ATMP	9	8	8	7
SST-Betaine	8	7	7	5
SST-mean Glut	6	6	5	5
Carbonates				
Carbonates	UCS (MPa)	ASTM (C42-90) Correction Factor	BP 1881-Part 120 Correction Factor	Young's Modulus (GPa)
Carb-				
Untreated	6	6	5	4
Carb-Brine	4	4	3	3
Card-mean Glut	13	12	11	8
Carb-Betaine	12	11	10	10
Carb-ATMP	10	9	8	10

4.4.4 Effect of chemicals on mineralogy

Mineral characterisation and identification play a key role in rock mechanical properties prediction (Mubiayi 2013). The strength of rock depends essentially amongst other factors on the chemical and mineralogical composition. The rate at which the strength of rock increases or decreases in response to any external force is dependent on the specific surface area of the minerals (Frigione and Marra 1976). The core samples were characterised after the treatment regime to evaluate the effect of chemicals on the element and mineral components of the core samples.

The morphology, elemental and mineralogical compositions of the chemically treated sandstone were analysed using SEM and EDX. The brine treated leopard shows the same morphology as the untreated leopard in the SEM micrograph (Figures 4.17a,b,c). The quartz, feldspar and clay

components of the brine treated leopard were confirmed by the presence of Si (31.27 wt. %), Al (2.74 wt. %), O (64.23 wt. %), Na (0.25 wt. %), K (0.44 wt.%), Fe (0.59 wt.%) in the EDX spectrum (Figure 4.16d). Other elements found in the sample are Ag (0.21 wt.%) and Cl (0.27 wt.%). The result shows little or no change in the morphology, mineralogical and elemental composition. However, few pittings were observed on the quartz grains which could have been caused by dissolution of the clay minerals.

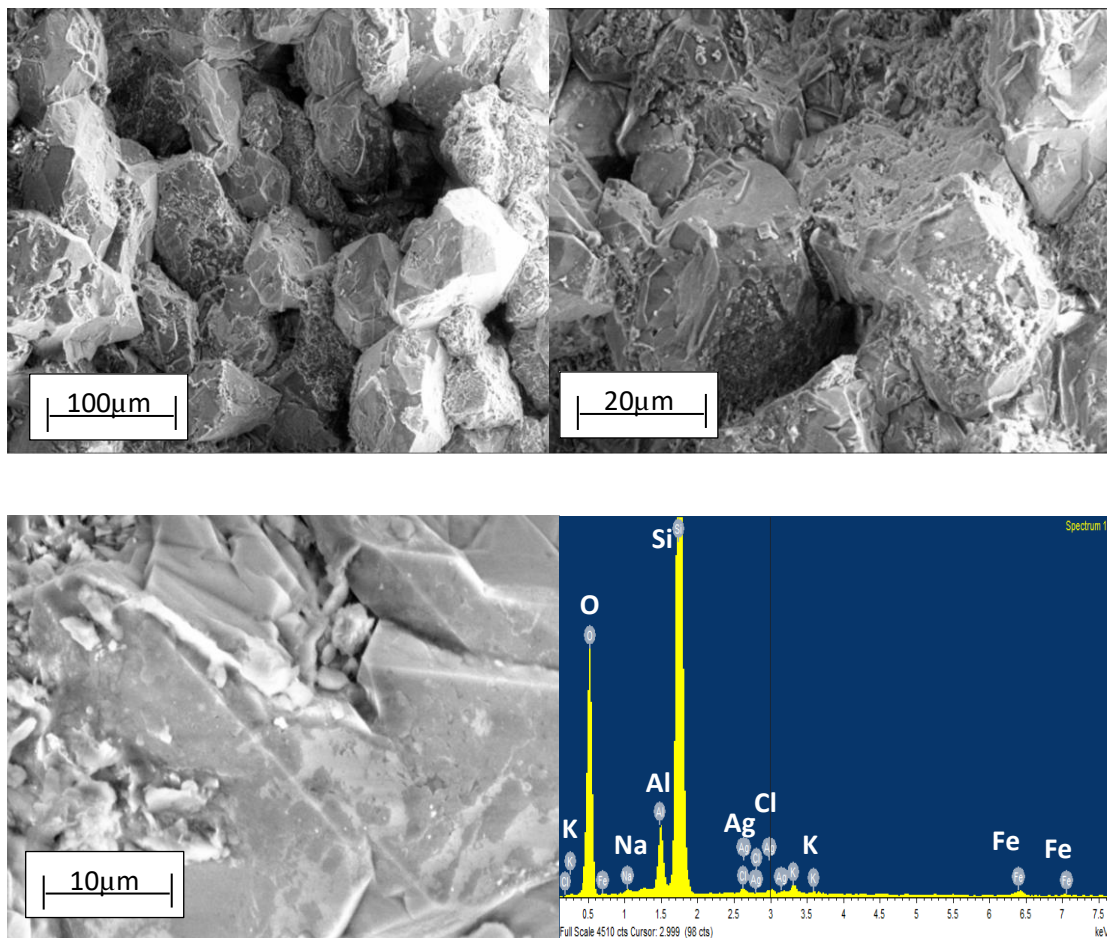


Figure 4.17: SEM micrograph and EDX scan of brine treated leopard sandstone using different magnification: (a) SEM, 250X; (b) SEM, 500X; (c) SEM, 2.00KX; (d) EDX spectrum.

SEM micrograph of the ATMP treated leopard shows same grain morphology with deviation in the elemental and invariably mineralogical composition (Figure 4.18a). The grains were pitted (Pt) with well-developed pores (P).

The degree of pitting which is a product of dissolution reaction in this sample is much higher than that observed in brine treated sample. In contrast to untreated and brine treated samples that contain Si, Al, O, Na, K, Fe, Cl and Ag as shown by EDX, ATMP treated sample was found to contain P (0.58 wt.%) and Mg (0.24 wt. %) in addition to Si (30.19 wt.%), Al (3.77 wt. %), O (62.21 wt.%), Na (0.34 wt. %), K (0.99 wt.%), Fe (1.03 wt. %), Cl (0.65 wt.%) with no trace of Ag (Figure 4.18b). Addition of the phosphorous and magnesium and depletion of silver content would have been triggered by the dissolution reaction.

Betaine treated leopard is revealed by SEM micrograph to contain well-sorted, rhombic to orthorhombic detrital quartz grains with spreading of grain particles. The grains have undergone dissolution that led to pitting (Pt) as shown in Figure 4.18c. Grains got detached due to pitting creating several pore spaces (P). The detached grains spread on unaltered quartz grains. EDX scan shows variations in the elemental content (Figure 4.18d). Unlike the untreated and brine treated leopard sandstone, the betaine treated sample is observed to contain only Si (31.94 wt.%), O (62.56 wt.%), Al (3.11), Cl (1.15 wt.%) and Ag (1.23 wt.%). The dissolution of the clay minerals and feldspar is evidenced by the disappearance of some key elements (Na and K) that make up the clay and feldspar in this sample, but were present in the untreated sample.

SEM micrograph shows glutaraldehyde treated leopard sandstone to contain detrital quartz grain coated with clay. Also observed are some pittings and enlarged pore spaces which might have been caused by dissolution of the cementing and pore lining clay (Figure 4.18e). The glutaraldehyde treated

sample is shown by EDX scan (Figure 4.18f) to consist of Si (31.42 wt.%), O (61.13 wt.%), Al (2.67 wt.%), Na (1.35 wt.%), K (0.53 wt.%), Fe (0.64 wt.%) and Cl (2.26 wt.%).

Recall that the treatment with glutaraldehyde was replicated. The SEM micrograph (Figure 4.18g) of the second glutaraldehyde leopard sandstone (LP-3) shows the same features as the first (LP-2). The elemental content of LP-3 as revealed by EDX (Figure 4.18h) are: Si (26.02 wt.%), O (66.92 wt.%), Al (2.16 wt.%), Na (0.63 wt.%), K (0.37 wt.%), Fe (0.43 wt.%), Cl (0.59 wt.%) and C (2.88 wt.%).

Comparing the results obtained from the characterised untreated leopard sandstone and chemically treated sandstone it is obvious that there is little or no change in morphology, elemental and mineralogical composition of the brine treated leopard sandstone. This is because formation brine is in equilibrium with the formation in their natural environment and only destabilises/disequilibrates in the presence of external forces. In contrast, a substantial change in elemental and mineralogical content was observed with the chemically (betaine, ATMP and glutaraldehyde) treated leopard sandstone. Looking at the results, it is obvious that the change in Si and O content from untreated to treated samples is insignificant throughout the test regime. However, variations are observed in Al, Na, Fe and K contents. In some cases, for example, betaine treated leopard sandstone, Na, Fe and K were completely lost. This is an indication that clay form part of the cementing materials for leopard sandstone. The clay dissolved leading to grain detachment and pore space enlargement. This causes weakness of

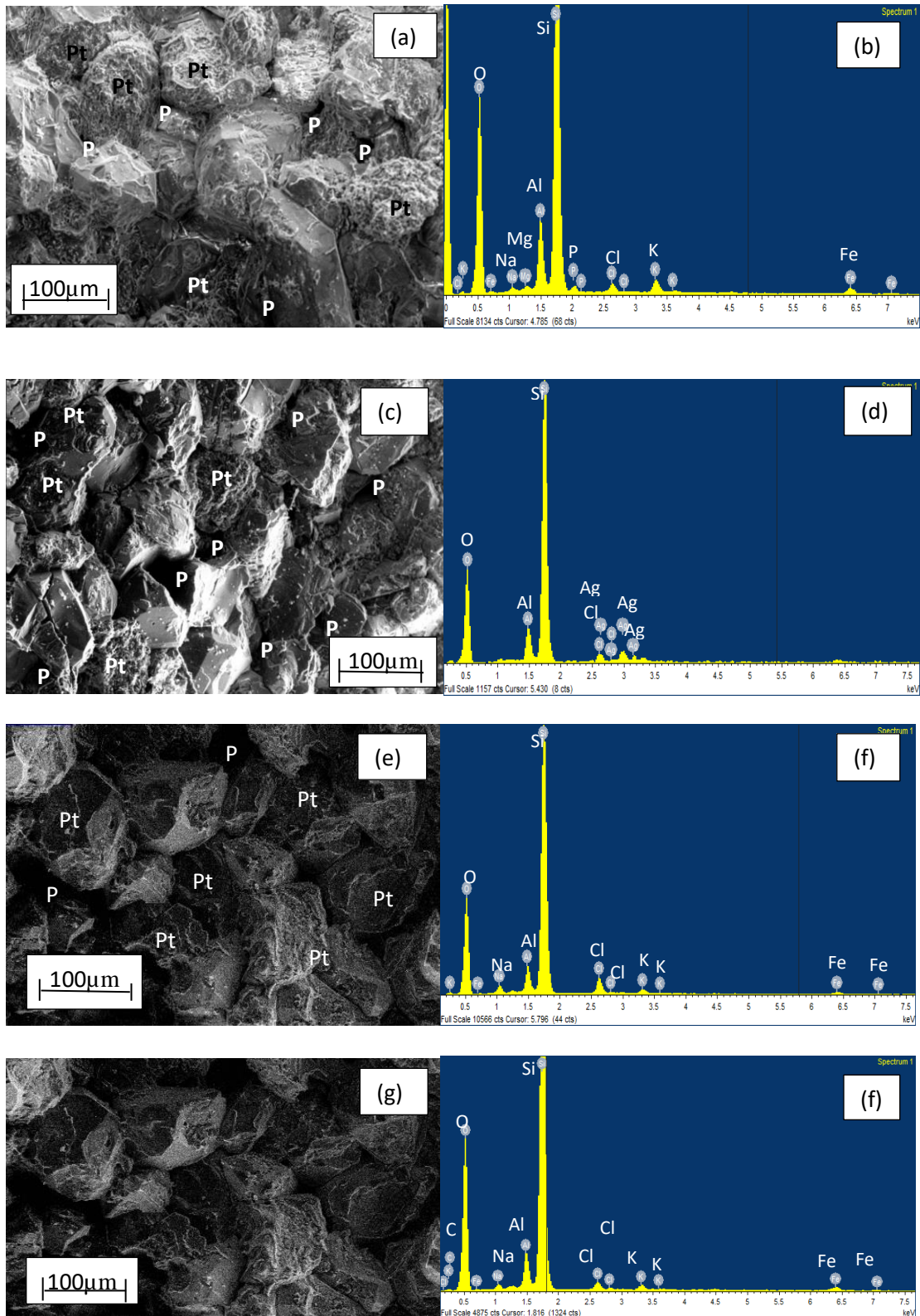


Figure 4.18: Mineralogical characterization of chemically treated leopard sandstone: (a) ATMP, SEM (Mag. 250X); (b) ATMP, EDX; (c) betaine, SEM (Mag. 250X); (d) betaine, EDX; (e) glutaraldehyde 1, SEM (Mag, 250X), (f) glutaraldehyde 1, EDX; (g) glutaraldehyde 2, SEM (Mag. 250X); (h) glutaraldehyde 2, EDX.

the grain fabrics hence, strength reduction with consequential sand failure/production.

In a similar manner, the chemically treated carbonates were characterised using SEM and EDX for the purpose of determining the morphology, elemental and mineralogical composition post chemical treatment.

SEM results of the brine treated Edward brown carbonate (Figure 4.19a,b,c) show same features as untreated Edward brown carbonate. This is an indication that brine has no negative impact on carbonates. EDX scan (Figure 4.19d) reveals the brine treated sample to contain Ca (17.09 wt.%), Mg (6.59 wt.%), C (3.95 wt.%), Na (1.20 wt.%), O (63.13 wt.%), Al (1.25 wt.%), Si (3.73 wt.%), Cl (2.02 wt.%), K (0.48 wt.%) and Fe (0.56 wt.%).

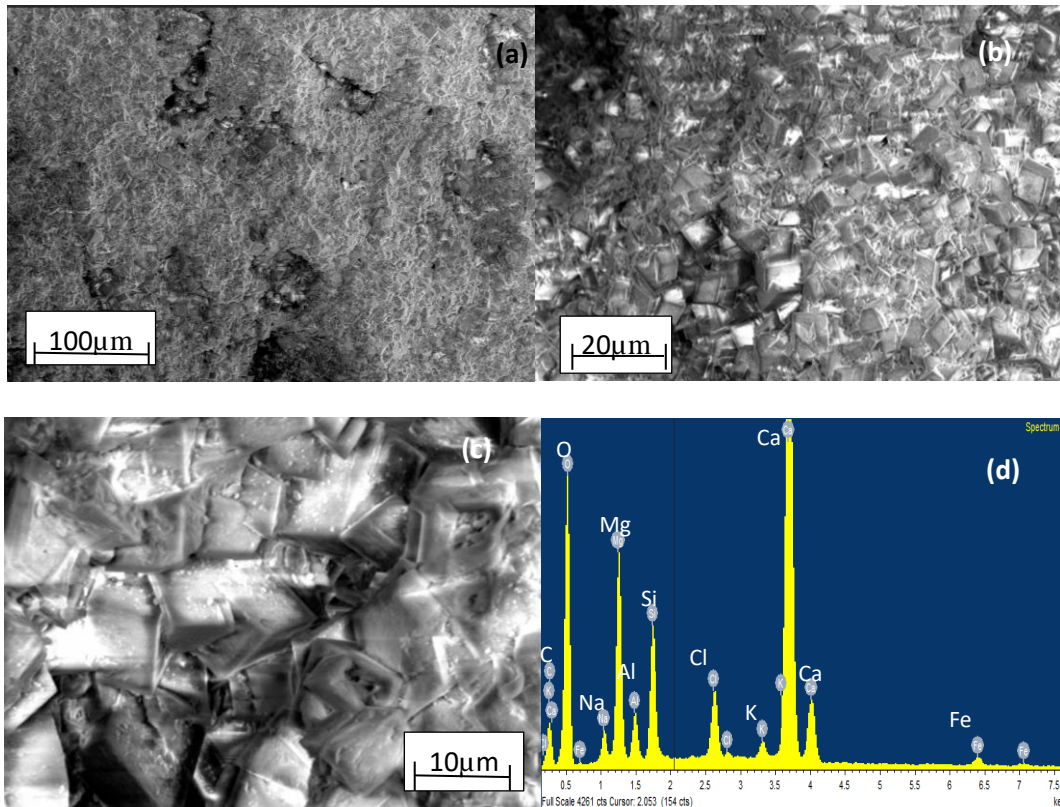


Figure 4.19: Characterisation of brine treated Edward Brown carbonate under magnification: (a) 200X; (b) 500X; (c) 2.00KX; (d) EDX scan

A cross section of Betaine treated desert pink limestone under SEM shows precipitation of calcite grain that are poorly sorted (Figure 4.20a). This sample is revealed by EDX (Figure 4.20b) to consist of Ca (22.60 wt.%), O (58.07 wt.%), C (16.56 wt.%) and Al (2.77 wt.%).

Similarly, SEM micrograph of ATMP treated desert pink limestone indicates precipitation of calcite grains (Figure 4.20c). The sample is shown to contain calcite and aluminate. Although the morphology of aluminate is not distinctive in SEM, it is identified based on the analysis of the major elements with EDX system. The EDX scan (Figure 4.20d) indicates that ATMP treated desert pink limestone contains Ca (26.63 wt.%), C (12.68 wt.%), O (60.00 wt.%), P (0.19 wt.%), Ag (0.13 wt.%) and Cl (0.37 wt.%).

Phosphorus was released by the ATMP ($\text{N}(\text{CH}_2\text{PO}_9\text{H}_2)_3$) into the fluid stream as it formed complex with calcium.

Furthermore, the two (2) glutaraldehyde treated Edward brown carbonates (ED5 and ED3) have been shown by SEM (Figure 4.20e,g) to have experienced dissolution/precipitation during the chemical-rock interaction. This is evidenced by change in morphology, pore space filling and precipitation of the calcite/dolomite grains. The dominant mineral in ED5 as revealed by SEM micrograph is calcite. Other minerals indicated by EDX analysis are quartz and clay. EDX scan (Figure 4.20f) indicates the presence of Ca (17.77 wt.%), O (65.12 wt.%), Si (0.19 wt.%), C (16.92 wt.%) in the first glutaraldehyde treated Edward brown carbonate (ED5). The ED3 on the other hands, is revealed to be dominated by dolomite mineral. Other mineral present in the sample include calcite, quartz and clay. EDX scan (Figure 4.20h) shows ED3 to contain Ca (17.16 wt.%), O (67.74 wt.%), Mg

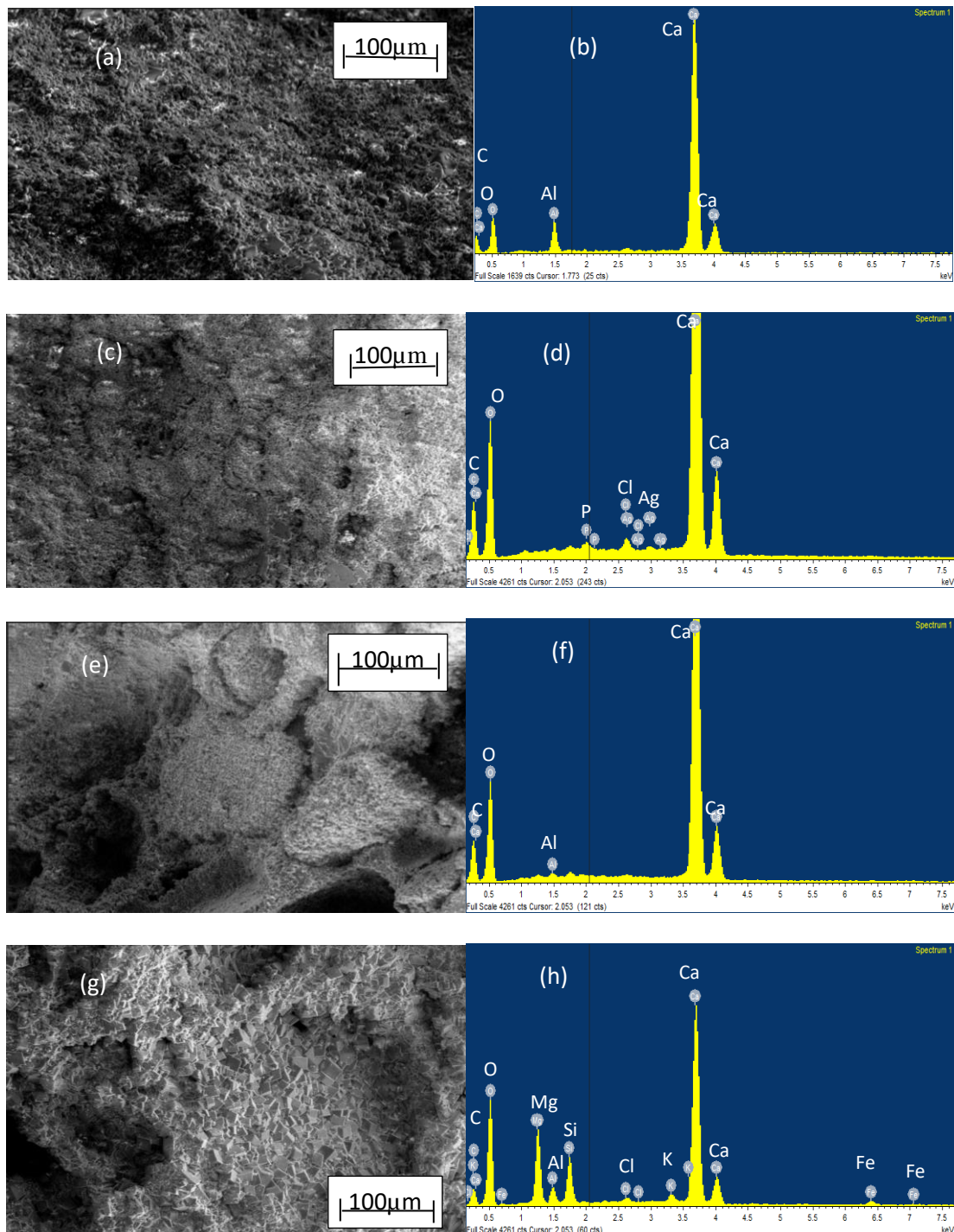


Figure 4.20: Mineralogical characterisation of chemically treated carbonates: (a) betaine-desert pink, SEM (Mag.250X, EDX); (b) betaine-desert pink, EDX; (c) ATPM-desert pink, SEM (Mag. 250X); (d) ATPM-desert pink, EDX; (e) glut-Edward brown 5, SEM (Mag. 250X); (f) glut- Edward brown 5, EDX; (g) glut-Edward brown 3, SEM (Mag.250X); (h) glut-Edward brown 3, EDX.

(6.40 wt.%), Al (1.16 wt.%), C (2.90 wt.%), Si (3.19 wt.%), K (0.54 wt.%), Fe (0.60 wt.%) and Cl (0.31 wt.%).

Again, analytical results have shown that the interaction between the brine and the carbonates does not have negative effect on the strength of the rock. However, the interaction between the oilfield chemicals and the carbonates caused precipitation of new materials that filled the pore spaces. Apart from the fact that the pore clogging can lead to formation damage, there is the danger of it causing hydrocarbon production impairment. It is worthy of note that the precipitated materials that fill the pore spaces may not have the same strength as the original cement material, thus can lead to grain fabric weakening.

4.5 Summary

Interaction between reservoir formation rocks and three chemicals (biocide, corrosion inhibitor and scale inhibitor) which are commonly used in the oilfield for remedial treatment in reservoir rock has been investigated under static condition. Clastic and carbonate reservoir and outcrop cores obtained from the Niger Delta, Nigeria and Texas, USA were used in the study. Both mechanical and analytical tests were deployed to characterize the cores prior to and after chemical treatments to analyse the interaction between the chemicals and the cores. The results suggest that chemical reactions such as adsorption, dissolution/precipitation and ionic substitution took place between the oilfield chemicals and the reservoir rocks under static condition. The interaction weakened the grain fabrics of the rocks and caused a release of disintegrated grains into the fluid streams. The deterioration of the grain fabrics caused reduction of the uniaxial compressive strength, the phenomenon that can lead to sand failure and sand production in the formation rocks. It can be observed from the results

that betaine exhibited highest interaction with both sandstone and carbonates than ATMP and glutaraldehyde with glutaraldehyde having the least interaction with both rock types.

It is imperative that field operators take into cognizance the potential for dissolution and precipitation reaction between the materials (quartz, calcite and clay) that cement the grains of sandstone and carbonate rocks and oilfield chemicals especially during shut in period following chemical placement into a well. Dissolution reaction can lead to the weakening of the rock fabric whilst precipitation may result in the formation of new materials which are weaker than the original rock materials. It is therefore recommended that the interaction between these chemicals and formation rock should be factored into the evaluation of failure and sand production potential for effective field operation especially when extensive chemical injection programme is planned for such fields.

References

ALLEN, C.C. and CONCA, J.L., 1991. Weathering of basaltic rocks under cold, arid conditions-Antarctica and Mars. In Lunar and Planetary Science Conference proceedings, 21, 711-717.

ASTM, 1992. C 42-90. Standard Test Method for Obtaining and Testing Method for obtaining and Testing Drilled cores and Sawed Beams of Concrete. 1991 Annual Book of ASTM Standards, *Concrete and Aggregates*, 4.

BALOG, A., COBIRZAN, N. and BARBU-TUDORAN, L., 2014. Evaluation of limestone with non-invasive analytical methods. *Romanian Journal of Physics*, 59(5-6), 601-607.

BYBEE, K., 2010. Two-Phase Cement/CO₂/Brine Interaction in Wellbore Environmental *Journal of Petroleum Technology*, 62(05), 78-80.

CRUNDWELL, F.K., 2017. On the mechanism of the dissolution of quartz and silica in Aqueous Solutions. *ACS Omega*, 2, 1116 -1127.

DURMEKOVÁ, T., HOLZER, R., WAGNER, P., 2003. Weak rocks in engineering practice. Conference proceedings, Geotechnical measurements and modelling, Natau, Fecker & Pimentel (eds), Swets & Zeitlinger, Lisse, 185-191.

ETIMITA, O. O., 2015. Reservoir characterization of "G900" Sandstones using wireline Logs and cores in development planning of Gabo field, Onshore Niger Delta. *IOSR Journal Application Geology and Geophysic* 3, (6) 46-52.

FOLK, R.L., 1968. A review of grain-size parameters. *Sedimentology*, 6(2), 73-93.

FRIGIONE, G. and MARRA, S., 1976. Relationship between particle size distribution and compressive strength in Portland cement. *Cement and Concrete Research*, 6, 113-128.

HAN, G. and DUSSEAULT, M., 2002. Quantitative analysis of mechanisms for water-related sand production. Paper 73737 presented at the SPE International Symposium and Exhibition on Formation Damage Control. Lafayette, Louisiana, 20-21 February.

JORDAN, M., SORBIE, K., PING, J., YUAN, M.D., TODD, A. and HOURSTON, K., 1994. Phosphonate Scale Inhibitor Adsorption/Desorption and the Potential for Formation Damage in Reconditioned Field Core. SPE Formation Damage Control Symposium. Lafayette, Louisiana, 7 – 10 Feb.

MADLAND, M., HIORTH, A., OMDAL, E. and MEGAWATI, M. 2011. Chemical alterations induced by rock–fluid interactions when injecting brines in high porosity chalks. *Transport in Porous Media*, 87(3), 679-702.

MANNHARDT, K., SCHRAMM, L.L. and NOVOSAD, J.J., 1993. Effect of rock type and brine composition on adsorption of two foam-forming surfactants. *SPE Advanced Technology Series*, 1(1), 212-218.

MARTY N., CLARET F., LASSIN A., TREMOSA J. and BLANC, P., 2015. A database of dissolution and precipitation rates for clay-rocks minerals. *Applied Geochemistry* 55, 108–118.

MUBIAYI, M.P., 2013. Characterisation of sandstones: Mineralogy and physical properties. Proceedings of the World Congress on Engineering III, 1-6.

NTON, M. and ELUEZE, A.A., 2005. Compositional characteristics and industrial assessment of sedimentary clay bodies in part of eastern Dahomey Basin, southwestern Nigeria. *Journal of Mineral and Geology*, 41(2), 175-184.

ODOH B., ONYEJI J. and UTOM A., 2012. The integrated seismic reservoir characterization (ISRC), study in Amboy field of Niger Delta oil field—Nigeria. *Geosciences* 2(3), 60–65.

OLUYEMI, G., 2014. Conceptual Physicochemical Models for Scale Inhibitor-Formation Rock Interaction. *Petroleum Science and Technology*, 32(3), 253-260.

RIJNAARTS, H., NORDE, W., BOUWER, E., LYKLEMA, J., ZEHNDER, A., 1993. Bacterial adhesion under static and dynamic conditions. *Applied and Environmental Microbiology* 59, 3255–3265.

SHAO, H., RAY, J., and JUN, Y-S., 2010. Dissolution and precipitation of clay minerals under geologic CO₂ sequestration conditions: CO₂-brine-phlogopite interactions. *Environmental Science Technology*, 44(15), 5999–6005.

SETO, M. NAG, D.K., VUTUKURI, V.S. and KATSUYAMA, K., 1997. Effect of chemical additives on the strength of sandstone. *International Journal of Rock Mechanics and Mining Sciences*, 34(3), 280. e1-280. e11

URORO, E. and IGHARO, E., 2015. Application of well log analysis in assessment of petrophysical parameters and reservoir characterization of wells in the "oth" field, Anambra Basin, southern Nigeria. *International Journal of Science and Engineering*, 8(1) 47-53.

Chapter five

5 Evaluation of the Interactions between oilfield chemicals and reservoir rocks under dynamic condition (Core flooding)

5.1 Introduction

Oilfield operational activities expose reservoir rocks to a range of oilfield chemicals. Chemical-rock interaction occurs via adsorption which is the binding of chemical to the rock (substrate) surface through Van der Waal forces. The dissolution and precipitation phenomena that take place as a result of chemical-reservoir rock interaction is capable of altering the porosity and permeability of the reservoir rock (Li and Aubertin 2003). The alteration, which could result in a decrease or an increase in these rock properties depending on the mineral composition of the rock, particle size distribution, shape of the particle and pore size, can also be a threat to the integrity of the injection schemes (Lamy-Chappuis et al. 2014) and that of the reservoir rocks.

Saturation under dynamic condition which entails chemical injection and subsequent flushing out of the chemicals (flowback) at a predetermined flowrate mimics production from the reservoir formation following chemical injection. Such dynamic test gives an opportunity to evaluate the flow of reacting fluid to and through the rock surface by diffusion and convection.

The results of interaction between oilfield chemicals and formation rocks under static condition have been discussed in Chapter Four. However, the flow effect of these chemicals was not considered. Furthermore, most previous works on the interaction between chemicals and formation rocks carried out under static (Seto et al. 1997) and dynamic (Ramachandra et al. 1999, Kan et al. 2004, 2005,

Baraka-Lokmane and Sorbie 2010, Veleso et al. 2014, Yan et al. 2015) conditions did not provide a clear understanding of the mechanism of interaction between oilfield chemicals and the formation rocks.

In this chapter, the mechanisms and effects of interaction between oilfield chemicals and formation rock on particle size distribution, porosity/permeability, mineralogy, elemental composition and UCS and CCS under dynamic condition are assessed and discussed. Outcrop samples from USA were used to carry out the study. A number of laboratory tests such as flow test, particle size distribution analysis, imaging, elemental and mineralogical tests and mechanical testing (uniaxial and triaxial compression test) were used for the investigation.

5.2 Materials & Methods

Twenty (20) outcrop sandstone and twenty (20) outcrop carbonate rocks were used for uniaxial compression test, while seven (7) outcrop sandstone and seven (7) carbonate rocks were used for triaxial compression test in this study. The geometrical parameters and locations are presented in Tables 3.2 and 3.3 of Chapter Three. Detailed description of the flow test from which porosity and permeability were determined, particle size distribution analysis, analytical test, uniaxial compression test and triaxial test under dynamic condition are presented in section 3.3 of Chapter three.

5.2.1 Data Analysis

5.2.1.1 Porosity

Results obtained from ICP-OES were analysed using Microsoft Excel and used to calculate the total volume (V_T). The V_T was determined by summing up the product of the normalised concentration (C/C_h) and sample volume (Sv) (equation 5.1).

$$V_T = \sum \left(\frac{C}{C_h} * Sv \right) \quad [5.1]$$

The dead volume (V_d) was calculated by determining the length of the inlet (1/8") and the outlet (1/16") from the pump to the space around the core i.e. inside the core holder. The sum of both inlet ($\pi r^2 L$) and outlet ($\pi r^2 L$) volume provided the dead volume. While pore volume (V_p) was obtained by subtracting the dead volume from the total volume (V_T) of the fluid that passed through core ($V_p = V_T - V_d$). Bulk volume (V_b) was determined using the dimension of the core sample; whilst the porosity (ϕ) was determined as the ratio of pore volume to bulk volume multiply by 100 (equation 5.2):

$$\phi = \frac{V_p}{V_b} * 100 \quad [5.2]$$

5.2.1.2 Permeability measurement

Core permeability was measured before and after the chemical injection using brine. This was achieved by varying the flowrates of brine in the sequence 2,6,4,3 and 2mL/min. The differential pressure was also recorded continuously. Darcy equation (Equation 5.3) was then used to calculate the permeability of the rock using the data from the measurement. Prior to the flow of fluid, parameters like core length, cross-sectional area of the core and fluid viscosity were determined. The permeability measurement was done to determine whether the interaction between the rock and the reservoir caused any substantial degradation/alteration

of the reservoir flow properties. The process was repeated after the flush out of the chemical from the core sample and the results compared.

$$K_b = \frac{Q_b \cdot \mu \cdot L}{A \cdot \Delta P} \quad [5.3]$$

where, K_b = Permeability to brine (mD), Q_b = Flow rate (cm³/sec), μ = Viscosity of brine (cP), L = Length of sample (cm), A = Cross sectional area of sample (cm²), ΔP = differential pressure (atm).

5.2.1.3 Chemical injection

A total volume ranging from 12.3 to 21 mL of each chemical (depending on the pore volume estimated for each core) was injected into each core at a flowrate of 0.25 mL/min. This low flowrate is to ensure every pore space is filled and potential high flowrate effects such as rapid pressure increase, turbulent flow etc. are avoided. The effluent (uptake) was collected for further analyses of pH, cation concentration (Ca²⁺, Fe²⁺, Mg²⁺) by ICP-OES and particle size distribution determination. The set up was left to stand for 24 hours with the inlet and outlet valves shut down to allow for longer interaction between the chemical and the core. The injected chemical was flushed out after 24 hours with filtered brine at the flowrate of 0.25 mL/min and the flow back effluent was collected for further analyses. The core was removed from the core holder after the injection, rinsed with deionized water, air and oven dried at 106°C (Verwaal and Mulder 2000; Ladd and Foott 1974) for 72 hours in preparation for mechanical tests as well as SEM, EDX and XRPD analyses. For the purpose of repeatability each chemical was injected three times into three different core samples and the mean values and standard deviation of pore volume, porosity and permeability were determined.

The procedure for the mechanical testing, SEM/EDX and XRPD analyses are described in Section 3.3 of Chapter Three.

In order to accurately inject the determined pore volume for instance, 12.3mL at 0.25mL, a conversion of both values to time was done as:

$$0.25 \text{ mL} = 1 \text{ min} \quad 12.3 \text{ mL} = x \text{ min}$$

$$x \text{ min} = \frac{12.3 \text{ mL}}{0.25 \text{ mL}} = 49 \text{ min } 2 \text{ sec.}$$

The core was flood for this length of time (49 min 2 sec) to obtain the 12.3 mL.

5.3 Results and Discussion

5.3.1 Effect of chemicals on porosity/permeability of sandstone and carbonates.

Rock materials like other natural or man-made materials display some mechanical behaviour under certain conditions that depend on their internal structure, hence an attempt is made to develop a relation between UCS and porosity; and Young's modulus and porosity for both sandstone and carbonate. Figure 5.1 shows the lithium tracer profiles from which the porosities of sandstone (a) and carbonates (b) were calculated, respectively. The striking similarities in both sandstone and carbonate differential pressure profiles (Figures 5.1 c & d) obtained from the permeability measurement during the dynamic saturation (flow) test is an indication that there was no significant differences in the macroscopic flow behaviour of both rock types. An increase in the average porosity of sandstone from $21 \pm 1.5\%$ in brine to $25 \pm 4\%$, $28 \pm 0.7\%$, and $24 \pm 5\%$ was observed after the injection of ATMP, betaine and glutaraldehyde respectively (Figure 5.1e). There was a corresponding increase in brine permeability from $76 \pm 11.5 \text{ mD}$ to 88 ± 2.8

mD; 224 ± 27.6 mD; and 92 ± 16 mD upon injection of ATMP, betaine and glutaraldehyde respectively.

In Figure 5.5f, a decrease in mean porosity of the carbonates from $28 \pm 1\%$ to 21% ; 22% and 19% was observed following injection of ATMP, betaine and glutaraldehyde respectively. Decrease in permeability from 107 ± 1 mD to 79 ± 18 mD; and 66 ± 8 mD was also observed owing to treatment with ATMP and betaine respectively. However, an increase in permeability from 107 mD to 153 ± 32.7 mD was recorded following treatment with glutaraldehyde.

The change in the porosity and permeability of the sandstone observed in the current study suggests enlargement of pore space due to dissolution of grain fabrics (Přikryl 2001; Benavente et al. 2004; Török and Vásárhelyi 2010). The increase could have emanated from the dissolution of the clay minerals that form part of the rock matrix. The main driving force that causes heterogeneous chemical reactions at the interface between the pore-fluid and the rock minerals or the materials that cement the rock grain fabrics is the pore fluid flow which carries the reactive aqueous species. The interaction between this reactive aqueous fluid and either the mineral components of the rock or the cement material causes dissolution of some minerals and precipitation of other minerals leading to alteration of initial porosity and permeability.

A decrease in porosity and permeability which signifies constriction/obstruction of pore spaces due to formation of new minerals (precipitates) is observed in carbonate treated with ATMP and betaine. The observed decrease could be as a result of precipitation of small grains between large ones within the pores (Nimmo 2014). Previous work (Xue et al. 2004) has proven that constant molar precipitation reaction can lead to porosity reductions. Precipitation of new

materials originates from the continuous interaction of the de-bonded materials with other particles. The case of glutaraldehyde's interaction with carbonates that produced a decrease in porosity and an increase in permeability can be explained by possible/observed variations in the grain size of the precipitated materials. Such observation has been reported by Nelson (1994) and Bernabé et al. (2003). Furthermore, permeability is a function of the available networks in a system and different pores give different contributions to permeability of the material according to their shape and size.

Pore space enlargement could lead to the weakening of the grain fabrics resulting in strength reduction, whilst constriction due to precipitation/release of material that may be weaker than the original material into the fluid stream leads to pore clogging with consequential low formation wellbore performance and formation damage. Of the three oilfield chemicals, betaine demonstrated most significant effect (33%) on the petrophysical properties of the sandstone core sample compared to ATMP and glutaraldehyde. On the other hand, glutaraldehyde produced the highest impact (32-43%) on the petrophysical properties of the carbonates.

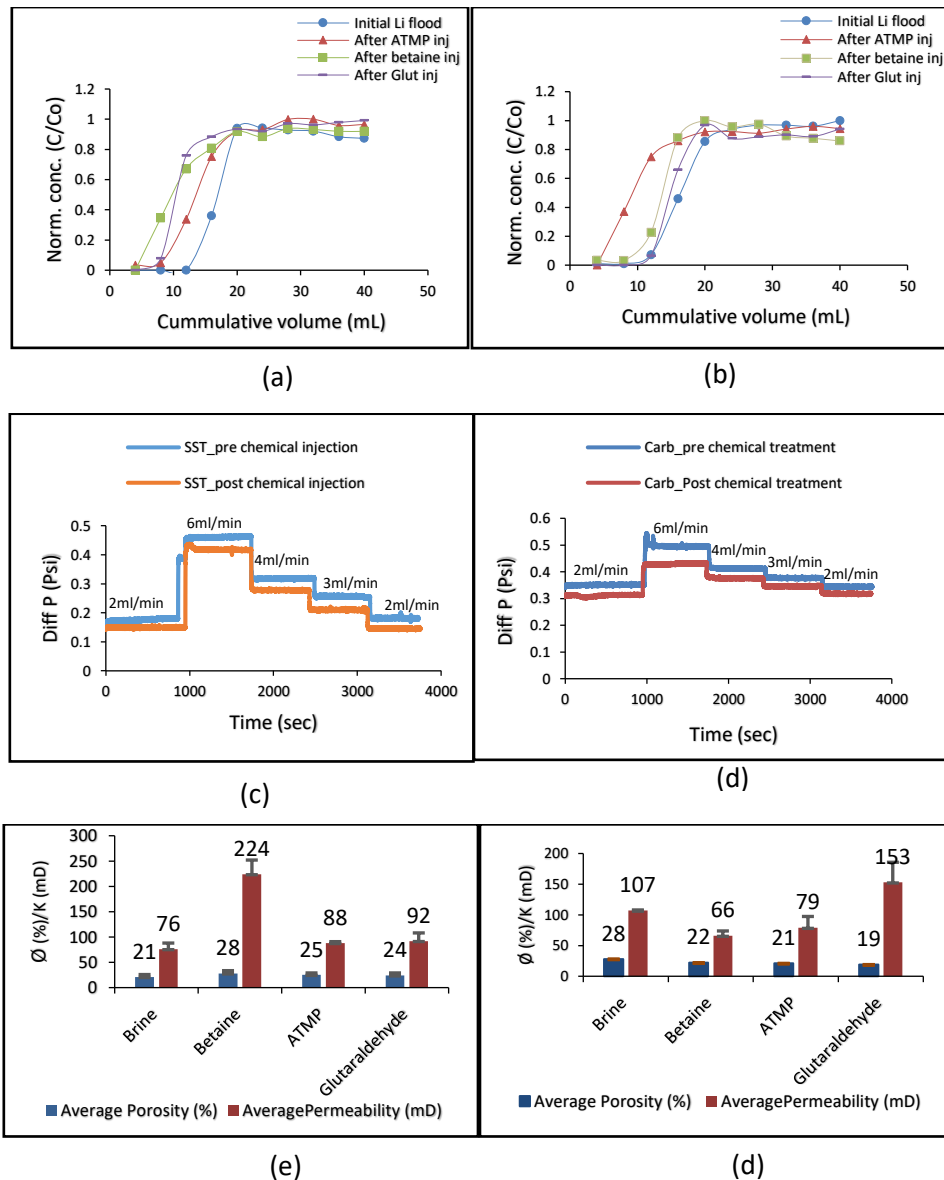


Figure 5.1: Pre and post injection petrophysical characterisation: (a) lithium tracer profile for sandstone; (b) lithium tracer profile for carbonate, where C_0 and C represent initial and final lithium concentrations; (c) differential pressure profile during sandstone permeability measurement; (d) differentials pressure profile during carbonate permeability measurement; (e) average porosity and permeability of sandstone; (f) average porosity and permeability of carbonate.

5.4 Particle/grain detachment

The grain size distribution profiles (Figure 5.2) of the sandstone and carbonate under dynamic saturation show no substantial difference in shape and value between the original brine and brine effluents. Nevertheless, there are changes in D_{10} , D_{50} and D_{90} values of the grain size distributions of the chemical uptake and flow back effluents, see Table 5.1. The slight increase in values of D_{50} and D_{90} for

the chemical flowback observed in this work may be attributed to the low flowrate used. The key grain size parameters of the brine effluents from both core samples suggest the particles originated from the fines that were less than the sintered glass filter openings can filter. Comparing these results with the mechanical and analytical test results, it is obvious that the level of deterioration with the brine-treated cores was much less than that of the chemically treated cores. This was evidenced by the release of comparatively lower amount of particles into the brine during the test. However, there is a remarkable difference in the grain size parameters between the brine effluents and the three chemical effluents (see Figure 5.2a,b and Table 5.1). In particular, the chemical effluents appear to exhibit broader grain size distribution profiles with poorer sorting (Folk 1968) in contrast to the original brine. It is evident from Figure 5.2 that there was a release of some particles into the various chemical solutions during the tests. These results indicate possible failure of the chemically treated cores due to the force generated by the superficial velocity of the fluids in the pores being greater than the formation strength can bear as simulated by the chemical flowback. This led to release of a wide range of particles into the flow streams. Increased proportion of particles in the effluent typically implies widening of the pore space and increase in porosity and permeability, possibly leading to a reduction of the uniaxial compressive strength. On the other hand, the released particles which could be weaker than the original particles could fill the pore space, reduce porosity and permeability, resulting in formation damage and low productivity. There are therefore two competing mechanisms; the macroscopic response of the core, which is the focus of the current study, will depend on the more dominant of the two mechanisms. Detailed microscopic study, for example using micro computed tomography (micro CT), would be needed to quantify the local particle transport

in the pore network of the core. The determination of the specific location of dissolution and precipitation within the core is however, not the focus of the current study.

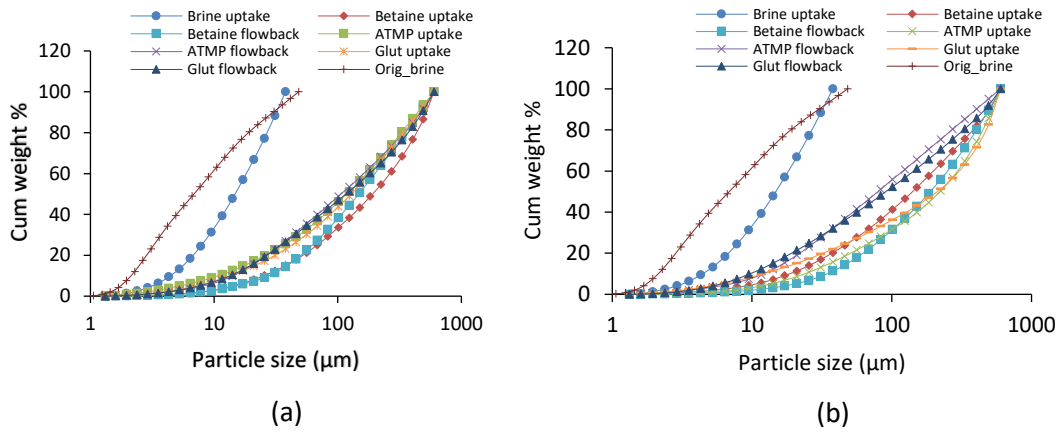


Figure 5.2: Grain size distribution profiles of original brine, brine and chemical uptake and flow back effluents under dynamic condition [(a) sandstone, and (b) carbonate].

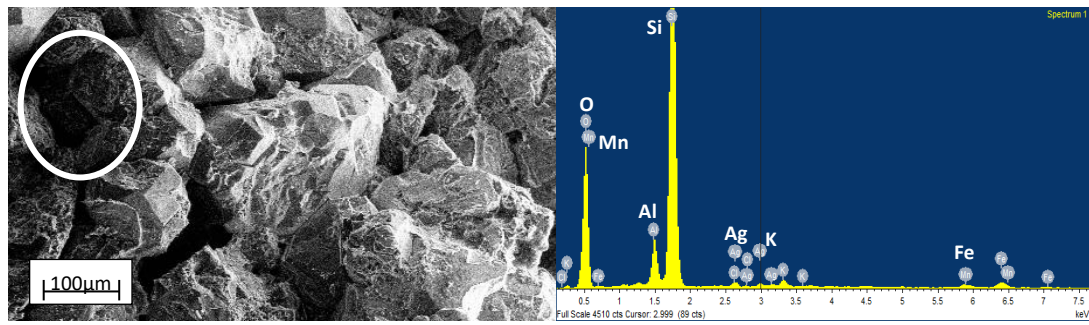
Table 5.1: D10, D50, D90 and sorting of brine, brine and chemical uptake and flowback effluents under dynamic condition (sandstone and carbonate).

Sandstone					
Effluents	D ₁₀ (μm)	D ₅₀ (μm)	D ₉₀ (μm)	Sorting (σ ₁)	(Folk 1966)
Original brine	2	7	32	0.36	Well sorted
Brine uptake	2	20	40	0.82	Moderately sorted
Betaine uptake	27	150	430	1.58	Poorly sorted
Betaine flowback	27	180	500	1.97	Poorly sorted
ATMP uptake	12	100	420	1.99	Poorly sorted
ATMP flowback	14	133	433	1.89	Poorly sorted
Glutaraldehyde uptake	14	100	430	1.99	Poorly sorted
Glutaraldehyde flowback	14	100	500	2.10	Very poorly sorted
Carbonate					
Original brine	2	7	30	0.36	Well sorted
Brine uptake	2	16	43	0.93	Moderately sorted
Betaine uptake	28	160	498	1.75	Poorly sorted
Betaine flowback	55	180	500	1.92	Poorly sorted
ATMP uptake	40	85	420	2.04	Very poorly sorted
ATMP flowback	16	220	500	1.73	Poorly sorted
Glutaraldehyde uptake	22	180	501	2.10	Very poorly sorted
Glutaraldehyde flowback	22	220	502	2.13	Very poorly sorted

5.5 Effect of chemical treatment on the mineralogy

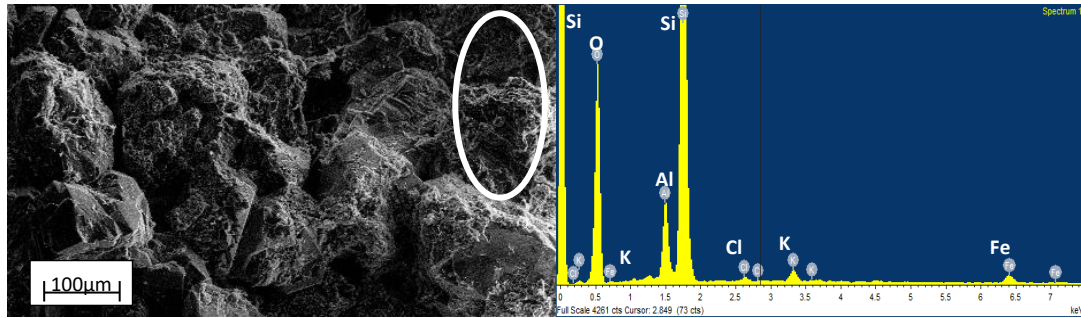
5.5.1 Sandstone

The SEM micrographs, EDX and XRPD analyses of sandstone samples post exposure to brine, betaine, ATMP and glutaraldehyde are shown in Figures 5.3 and 5.4. SEM coupled with EDX reveals variation in morphology and silicon composition in the untreated and chemically treated samples (Figure 5.3). The abundance of silica in the samples (Table 5.2) confirms that the sandstone is silica based. After chemical treatment, the SEM micrographs of the sandstone reveal pitting of the clay mineral constituents in the brine, betaine and ATMP treated sandstone without migration (circled in Figure 5.3a1,b1,c1). The pitting is believed to have resulted from dissolution of the clay minerals during chemical-rock interaction. The presence of clay minerals in the samples increased the surface area, providing an enabling environment for ion exchange. Glutaraldehyde treated sandstone shows spreading of altered clay and calcite grains on the surface of the larger unaltered quartz grains as indicated by the red arrow in Figure 5.3d1 in contrast to the untreated samples which show only unaltered quartz grains (Figure 4.1 of Chapter Four).



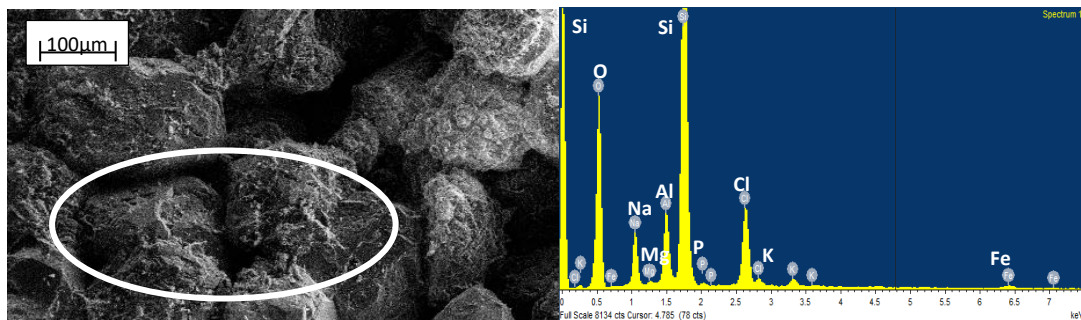
(a1)

(a2)



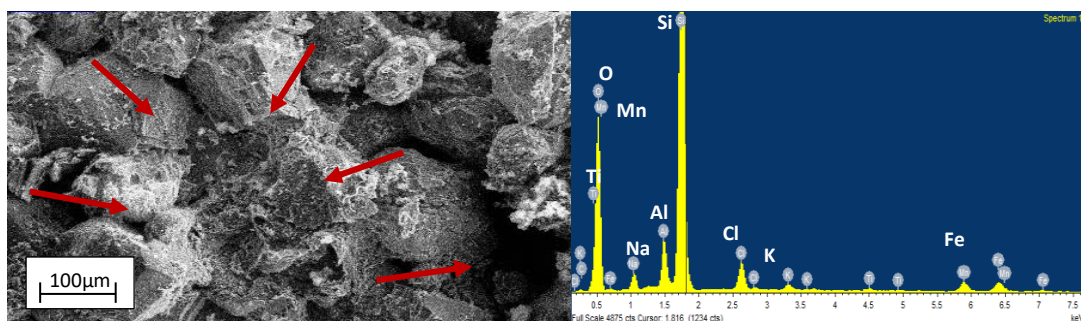
(b1)

(b2)



(c1)

(c2)



(d1)

(d2)

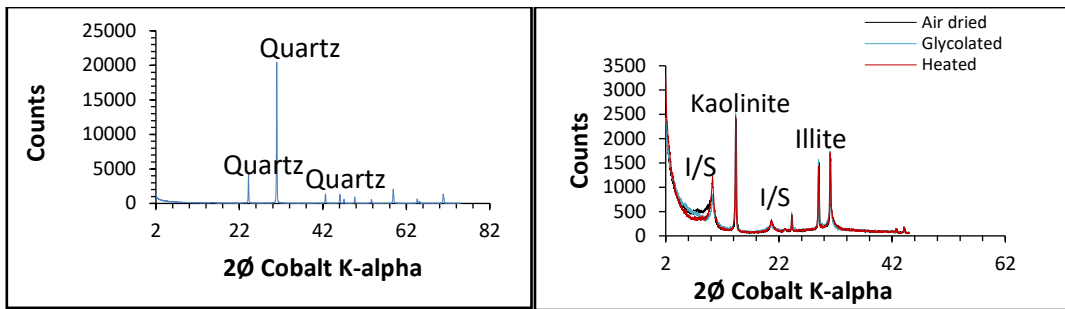
Figure 5.3: SEM micrographs and EDX spectrum of the sandstone after exposure to (a1) brine showing pitting within the white ellipse, SEM; (a2) brine, EDX; (b1) betaine showing pitting with the white ellipse, SEM; (b2) betaine; EDX, (c1) ATMP showing pitting with the white square, SEM; (c2) ATMP, EDX; (d1) glutaraldehyde showing spreading of altered clay and calcite grains on the surface of the larger unaltered quartz grains locations identified by the arrows, SEM; and (d2) glutaraldehyde, EDX.

The X-ray powder diffraction (XRPD) results of bulk mineralogical (whole rock) analysis show variations in mineralogical composition of the samples. Table 5.3 and Figure 5.4a1,b1,c1,d1 reveal high content of quartz (≥ 98.0 wt.%) in sandstone treated with brine, betaine, ATMP and glutaraldehyde respectively, with little amount of plagioclase (< 0.5 wt.%), calcite (< 0.5 wt.%), I/S-ML (< 1 wt.%) and kaolinite (< 1 wt.%). Quartz which is the dominant mineral in the sandstone core sample did not experience any observable change in the presence of the chemicals due to its non-reactive nature.

The clay minerals identified from XRPD presented in Table 5.4 and Figure 5.4a2,b2,c2,d2 include, kaolinite, illite and illite-smectite multi-layered (I/S-ML). Clay minerals analysis reveals a substantial increase of kaolinite from 14% to 23% with betaine and glutaraldehyde treated samples; 19% and 17% with brine and ATMP treated samples respectively. A reduction of illite from 35% to 19%, 12%, 15% and 13% was observed with brine, betaine, ATMP and glutaraldehyde treated samples respectively. However, an increase in illite/smectite mixed layer (I/S-ML) from 51% to 62%, 65%, 68% and 64% was observed with brine, betaine, ATMP and glutaraldehyde treated samples respectively. It is noteworthy that clay minerals are very reactive in nature due to their large surface area; as such they possess high adsorption capacity to chemicals (Jordan et al. 1994). This suggests that the interaction of the chemicals with the sandstone resulted in illite dissolution and kaolinite precipitation. The impact of interaction is more

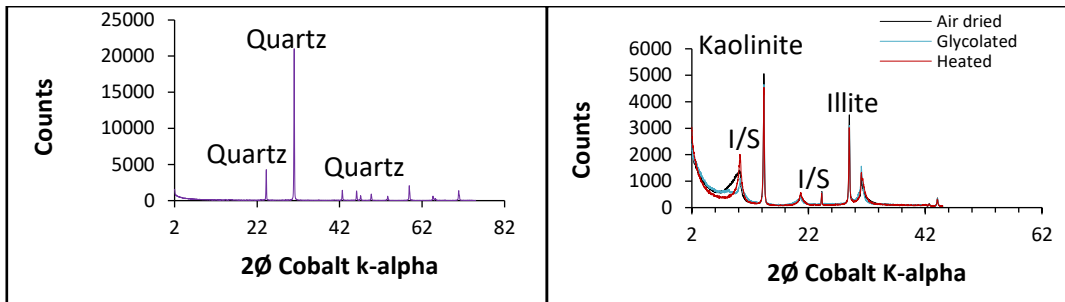
significant with betaine and glutaraldehyde, whilst, ATMP had more impact on I/S-ML.

Further analysis of the effluents from treated sandstone using ICP-OES to determine the concentrations of Na^+ , Ca^{2+} and Mg^{2+} showed insignificant difference between the uptake and flowback elemental concentrations (t-test, $p \geq 0.05$). However, there was a significant decrease (47%, 45% and 57%) in Na^+ concentration on being treated with betaine, ATMP and glutaraldehyde, respectively. Brine and ATMP effluents showed 7% increase in Ca^{2+} concentration; whilst a 16% and 25% decrease in Ca^{2+} was observed with betaine and glutaraldehyde effluents respectively. Mg^{2+} concentration increased by 21%, 2% and 8% in brine, betaine and ATMP effluents respectively, but decreased by 10% in glutaraldehyde effluent. The percentage changes in the cations concentrations in betaine, ATMP and glutaraldehyde could be attributed to the fact that sorption had taken place, while a decrease in cations concentration in the effluents is an indication that some cations were taken up by the rock (adsorption) leading to concentration reduction in the effluents. This result is consistent with the description of adsorption by Bolt et al. (1976).



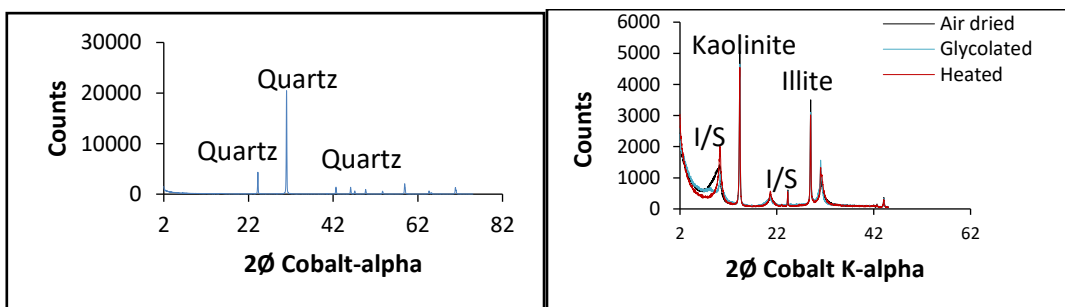
(a1)

(a2)



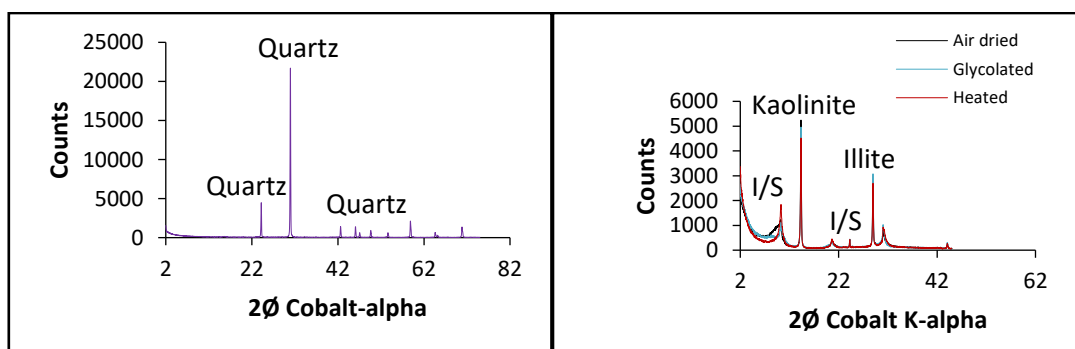
(b1)

(b2)



(c1)

(c2)



(d1)

(d2)

Figure 5.4: Bulk mineralogy of clay fraction characterisation of treated sandstone with: (a1) Brine, XRPD; (a2) Brine, Clay fraction; (b1) Betaine, XRPD; (b2) Betaine, Clay fraction; (c1) ATMP, XRPD; (c2) ATMP, Clay fraction; (d1) Glutaraldehyde, XRPD; (d2) Glutaraldehyde, Clay fraction.

Table 5.2: Elemental composition of sandstone and carbonate cores pre and post chemical treatment.

Sandstone					
Elements	Untreated (wt%)	Brine (wt%)	Betaine (wt%)	ATMP (wt%)	Glutaraldehyde (wt%)
O	64.2	62.9	64.2	63.9	58.0
Na	0.43	ND	ND	4.43	1.74
Al	3.00	3.24	2.15	3.11	3.00
Si	30.38	31.1	32.6	23.1	29.7
Cl	0.30	0.41	0.15	4.44	2.42
K	0.87	0.57	0.32	0.36	0.47
Fe	0.50	1.11	0.47	0.28	1.51
Ag	0.29	0.21	ND	ND	ND
Ti	ND	ND	0.18	ND	0.22
Mg	ND	ND	ND	0.19	ND
P	ND	ND	ND	0.19	ND
C	ND	ND	ND	ND	1.5
Mn	ND	0.48	ND	ND	1.44
Total	100	100	100	100	100
Carbonate					
Elements	Untreated (wt%)	Brine (wt%)	Betaine (wt%)	ATMP (wt%)	Glutaraldehyde (wt %)
C	5.16	2.76	2.07	5.69	5.76
O	70.2	70.7	66.8	70.9	69.7
Mg	5.79	6.46	7.33	6.43	6.57
Al	2.2	1.79	2.18	1.36	1.26
Si	4.3	5.47	4.73	3.21	2.97
Cl	0.44	0.27	0.73	0.18	1.16
K	0.65	0.61	0.52	0.34	0.33
Ca	10.9	16.4	18.7	11.2	10.6
Fe	0.38	0.86	0.92	0.43	0.3
Na	ND	ND	ND	ND	1.36
P	ND	ND	ND	0.3	ND
Ag	ND	0.2	0.19	ND	ND
Total	100	100	100	100	100
ND = Not detected					

Table 5.3: XRPD Bulk Mineralogy (wt %) based on reference intensity ratio (RIR) Method.

Sample ID	Quartz	Plagioclas	K-feldspar	Calcite	Dolomite	Pyrite	Halite	I-/S-ML	Kaolinite	Total
LP-Untreated	98.4	0.2	0.0	0.4	0.0	0.0	0.2	0.8	trace	100.0
LP-Brine	98.5	0.3	0.0	0.1	0.0	0.0	0.2	0.9	trace	100.0
LP-Betaine	98.0	0.2	0.0	0.1	0.0	0.0	0.1	0.8	0.8	100.0
LP-ATMP	98.4	0.4	trace	0.2	0.0	0.0	0.1	0.8	0.1	100.0
LP-Glut	98.0	0.4	0.0	0.4	0.0	0.0	0.2	0.4	0.6	100.0
ED-Untreated	3.7	0.0	0.0	21.2	73.8	0.2	0.2	0.9	0.0	100.0
ED-Brine	4.0	0.0	0.0	2.3	92.6	0.0	0.8	0.3	0.0	100.0
ED-Betaine	4.2	0.0	0.0	2.2	93.0	0.0	0.3	0.3	0.0	100.0
ED-ATMP	3.8	0.0	0.0	1.6	93.6	0.1	0.7	0.2	0.0	100.0
ED-Glut	2.8	0.0	0.0	1.6	95.1	0.0	0.3	0.2	0.0	100.0

LP = Leopard (Sandstone); ED = Edward brown (Carbonate); ATMP = Aminotri(methylenephosphonic acid; Glut = Glutaraldehyde

Table 5.4: Relative percentage of clay minerals in the <2 μ m clay size fraction.

Sample ID	Kaolinite	Illite	I/S-ML
LP-Untreated	14	35	51
LP-Brine	19	19	62
LP-Betaine	23	12	65
LP-ATMP	17	15	68
LP-Glut	23	13	64
ED-Untreated	7	7	86
ED-Brine	10	6	84
ED-Betaine	10	4	84
ED-ATMP	9	5	86
ED-Glut	8	6	86

LP = Leopard (sandstone); ED = Edward brown (carbonate); ATMP = Aminotri(methylenephosphonic acid; Glut = Glutaraldehyde

5.5.2 Carbonate

The SEM micrograph shows some altered, pitted, disengaged grains and spreading of altered grains over unaltered grains in brine, betaine, ATMP and glutaraldehyde treated carbonate respectively (Figure 5.5a1,b1,c1,d1). EDX result shows abundance of calcium, magnesium, carbon and oxygen elements typical of dolomite (Figure 5.5a2,b2,c2,d2 and Table 5.2). In this work, and other EDX

spectra (Welton 1984), the peak height of magnesium relative to that of calcium for the untreated (Figure 4.2) was reduced after chemical treatment (Figure 5.5) possibly due to rarefaction of magnesium in the EDX system.

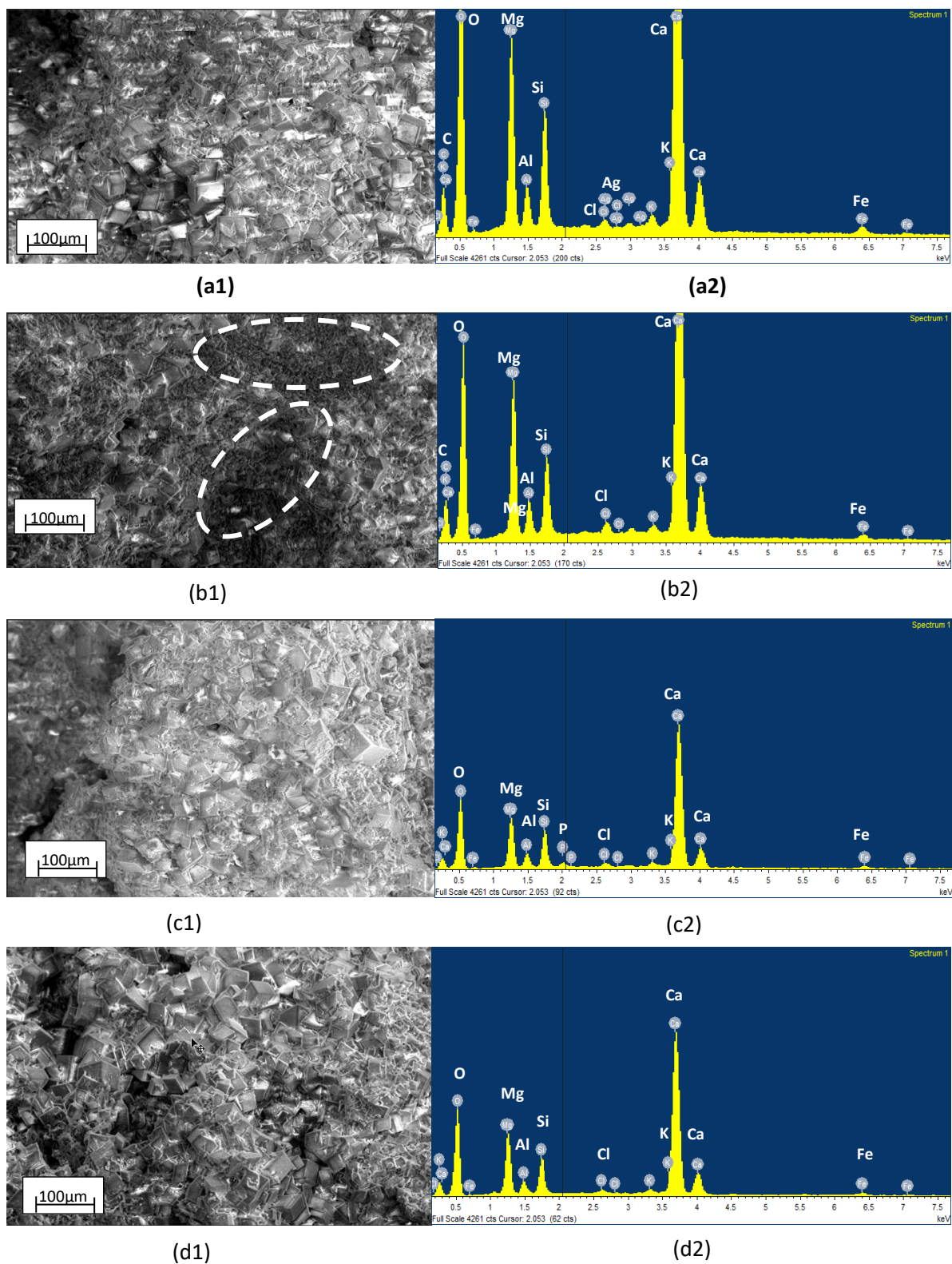


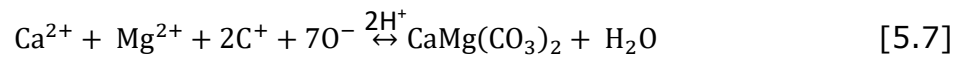
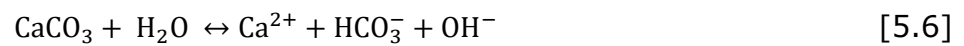
Figure 5.5: Carbonate post chemical treatment SEM micrograph showing filled pore spaces and EDX: (a1) brine, SEM; (a2) Brine, EDX; (b1) betaine SEM; (b2) Betaine, EDX;(c1) ATMP, SEM; (c2) ATMP, EDX; (d1) glutaraldehyde, SEM and (d) glutaraldehyde, EDX.

The XRPD of whole rock analysis reveals that the carbonate contains majorly dolomite (Figures 5.6a1,b1,c1,d1) which increased in weight percent (wt.%) from

73.8 to 92.6, 93.0, 93.6 and 95.1 after treatment with brine, betaine, ATMP and glutaraldehyde respectively (Table 5.3). The concentration of calcite reduced in weight percent (wt.%) from 21.2 to 2.3, 2.2 and 1.6 in the presence of brine, betaine, ATMP and glutaraldehyde respectively. A slight increase in quartz content from 3.7 to 4.0 and 4.2 wt.% was observed in brine and betaine treated carbonate respectively, while there was little or no change in ATMP treated carbonate (3.8 wt.%) and a decrease to 2.8 wt. % is observed in glutaraldehyde treated carbonate. The change in weight percent of calcite and dolomite supports the view of dissolution/precipitation reaction as discussed earlier. Oluyemi (2014) had suggested that ionic substitution reaction between the chemical species and the brine could lead to the formation and deposition of new materials in the pores. However, precipitation reaction dominates in the interaction between carbonate rocks and the chemicals as evidenced by the consumption of calcite to produce dolomitic minerals. ATMP-carbonate interaction influenced a change in pH from 1 to 5 which changed the Ca^{2+} release into the effluent from 270 mg/L at pH 1 to 347 mg/L (uptake) and 319 mg/L (flow back) at pH 5.

Again, changes in concentrations of Na^+ , Ca^{2+} and Mg^{2+} were also observed in chemically treated carbonate. Brine effluent showed 72% increase in Na^+ concentration; whilst betaine, ATMP and glutaraldehyde effluents showed 40%, 61% and 65% decrease in Na^+ concentration respectively. Similarly, betaine and glutaraldehyde effluents showed 24% and 35% decrease in Ca^{2+} concentration; whilst brine and ATMP showed 6% and 23% increase respectively. No change was observed with Mg^{2+} concentration in betaine effluent. However, 25, 24 and 19% increase of Mg^{2+} concentration was observed in the brine, ATMP and glutaraldehyde effluents respectively. This result suggests that while Na^+ and Ca^{2+} were being adsorbed by the rock, Mg^{2+} was released into the effluent.

Three simultaneous reaction mechanisms are possible with calcite dissolution process (Plummer et al. 1978). In the current study, the likely reaction involving the ionic exchange during calcite dissolution and dolomite precipitation when the carbonate rock was exposed to the chemicals are presented in Equations 5.4 – 5.7:



The XRPD analysis of clay minerals shows an increase in kaolinite composition from 7 to 10% owing to brine and betaine treatment; 9% due to ATMP treatment with marginal change (8%) in glutaraldehyde treated limestone (Figures 5.6a2,b2,c2,d2 and Table 5.6). Illite reduced from 7 to 4 and 5% in the presence of betaine and ATMP with little reduction (6%) in the presence of brine and glutaraldehyde. Again, illite dissolved to precipitate kaolinite as evidenced by the reduction in the relative contents of illite in the presence of the chemicals. High content (86%) of illite/smectite mixed layer (I/S-ML) was obtained which remained constant in the presence of the chemicals. Some clay minerals such as smectite, illite and I/S-ML are well known for expandability which causes constriction of pore throat. This accounts for reduced pore volume/porosity and permeability discussed in section 5.2. This research has indicated the possibility of the inhibitors, especially ATMP and betaine forming complexes with the divalent cations (Ca^{2+} , Mg^{2+}) that eventually precipitate. This has been previously reported by Tantayakom et al. (2004). In addition, the research has indicated that pore

constriction can still take place irrespective of the initial pH of the injected chemicals; this agrees with Singurindy and Berkowitz (2003) findings.

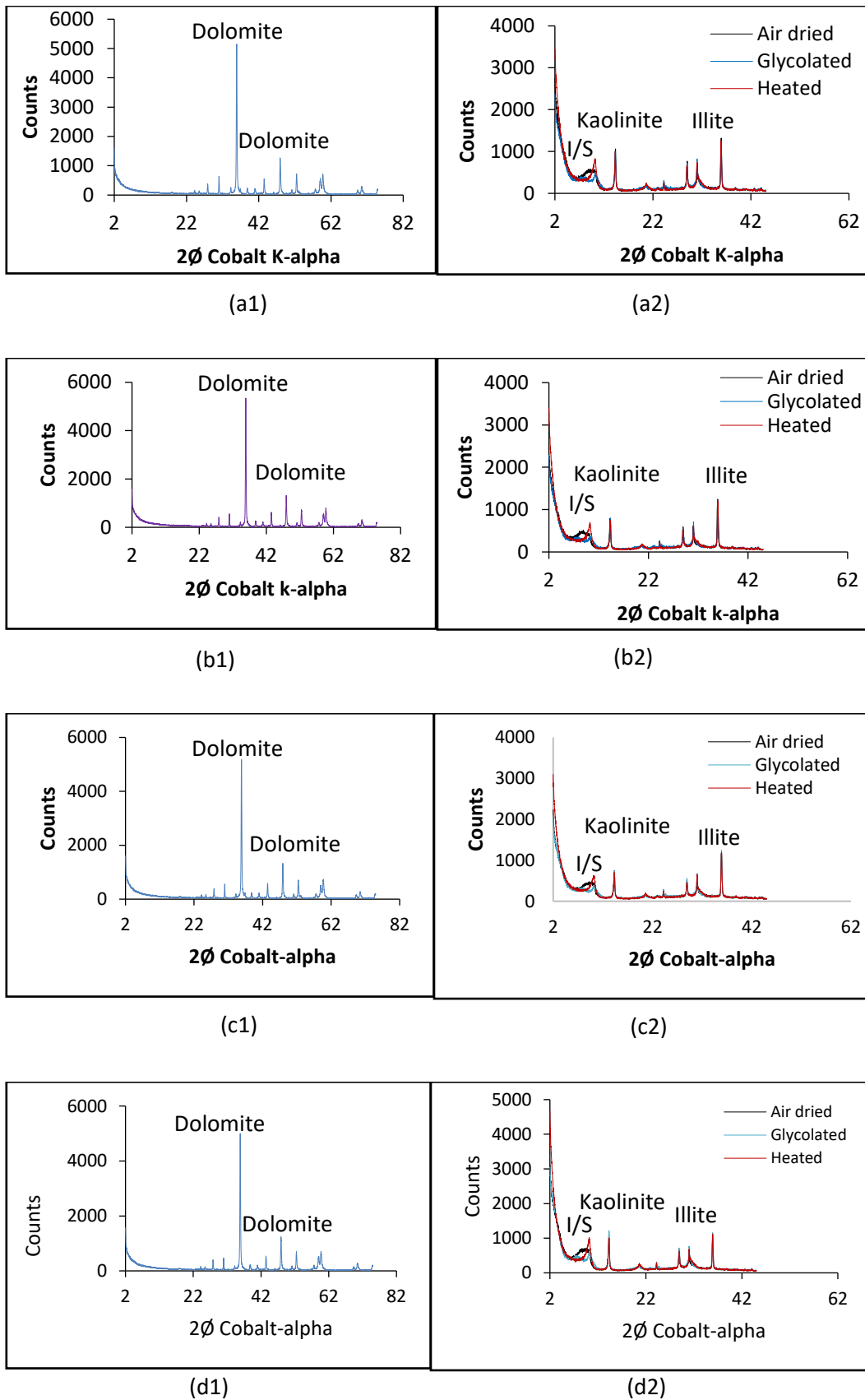


Figure 5.6: Bulk mineralogy (weight %) and clay fraction characterisation of treated carbonate: (a1) Brine, XRPD; (a2) Brine, clay fraction; (b1) Betaine, XRPD; (b2) Betaine, clay fraction; (c1) ATMP, XRPD; (c2) ATMP, Clay fraction; (d1) Glutaraldehyde (XRPD); (d2) Glutaraldehyde, Clay fraction.

5.6 Effect of chemicals on Unconfined Compressive Strength and Young's modulus

Figure 5.7 shows the pre and post chemical treatment uniaxial stress-strain responses for both sandstone and carbonate samples. The stress-strain curves for untreated and chemically treated sandstone (Figure 5.7a) and carbonates (Figure 5.7b) reveal linearly increased axial strain with increasing applied load until the sample yielded or failed. UCS results indicate a change in the unconfined compressive strength of the chemically treated sandstone and carbonate. Reduction in the mean strength of sandstone from 24 ± 2.0 MPa to 21 ± 2.0 MPa; 14 ± 3.4 MPa; 12 ± 0.6 MPa; 13 ± 0.7 MPa and an increase in mean strength of carbonate from 6 ± 0.6 MPa to 11MPa; 13 ± 2.8 MPa; 12 ± 2.1 MPa; and 9 ± 1.5 MPa were recorded owing to treatment with brine, ATMP, betaine and glutaraldehyde respectively (Table 5.5). Recall that the length/diameter (L/D) ratio of the core samples is 1.3 and recognising that rock strength is influenced by sample dimensions, an ASTM standard correction factor of 0.93 (ASTM 1992) was used to correct the measured strength of core samples as presented in Table 5.5.

The measured UCS of untreated and brine treated sandstone (leopard) of 24 ± 2 MPa is within the range of strength (21 - 26 MPa) declared by the supplier, Kocurek Industries Ltd. On the other hand, the measured UCS of untreated carbonates (Edward brown) of 6 ± 0.6 MPa falls below the range 14 - 21 MPa declared by Kocurek Industries Ltd. Although increase in strength was observed with the chemically treated carbonates, the observed strengths still fall below the stipulated range. The low strength of the carbonate could be explained by the fact that the carbonates have less favourable mechanical properties due to low degree of lithification (Durmekova et al. 2003). The low strength observed in the untreated carbonate samples could also be attributed to the effect of humidity

considering the length of time the samples were kept in the laboratory 'as supplied' before the test was carried out. The percentage reduction (18, 44 and 55%) in the UCS of sandstone samples from Niger Delta, Nigeria exposed to ATMP, betaine and glutaraldehyde respectively has been reported in section 4.2.2 of Chapter Four. When limestone samples from the Sokoto and Anambra Basins, Nigeria were exposed to these chemicals under static condition, a 29 and 41% reduction in UCS was recorded in betaine and glutaraldehyde respectively, whilst the ATMP treated limestone failed before the UCS was measured.

The stress-small strain response for both rocks is shown in Figure 5.8a,b; the strain in this case was measured using a strain gauge attached to the surface of the core. As expected, the stress versus small strain relationship was linear. The Young's modulus of sandstone reduced from 19 GPa to 13 ± 2.8 GPa; 10 ± 3.4 GPa; 9.5 ± 0.7 GPa; 11 ± 4 GPa whilst, that of the carbonate increased from 6 GPa to 16 ± 2.8 GPa; 10 ± 2.8 GPa; 8 ± 4.0 GPa and 10 ± 3.5 GPa when exposed to brine, ATMP, betaine and glutaraldehyde respectively (Table 5.5). Sandstone experienced a range of 32 to 50% reduction in Young modulus in the presence of the chemicals; while, carbonate exhibits 33 to 167% increase in Young modulus in the presence of the chemicals.

Rock strength and modulus are strongly influenced by mineral composition, grain size distribution (grain detachment) and porosity. The observed effect of the oilfield chemicals on the strength of sandstone is attributed to deterioration of the grain to grain binding, while the effect on the carbonate as observed is attributed to pore clogging. The result on the effect of oilfield chemicals on sandstone is consistent with previous work reported by Kahraman et al. (2008). A change in the grain to grain binding due to chemical influence leads to change in porosity

and permeability leading to a reduction in the unconfined compressive strength of the cores under study.

Apart from Young modulus of betaine treated sandstone that fell below the range, all other determined Young's modulus values for sandstone and carbonates were within the typical range of 10 – 20 GPa for sandstone and 3 – 27 GPa for carbonates.

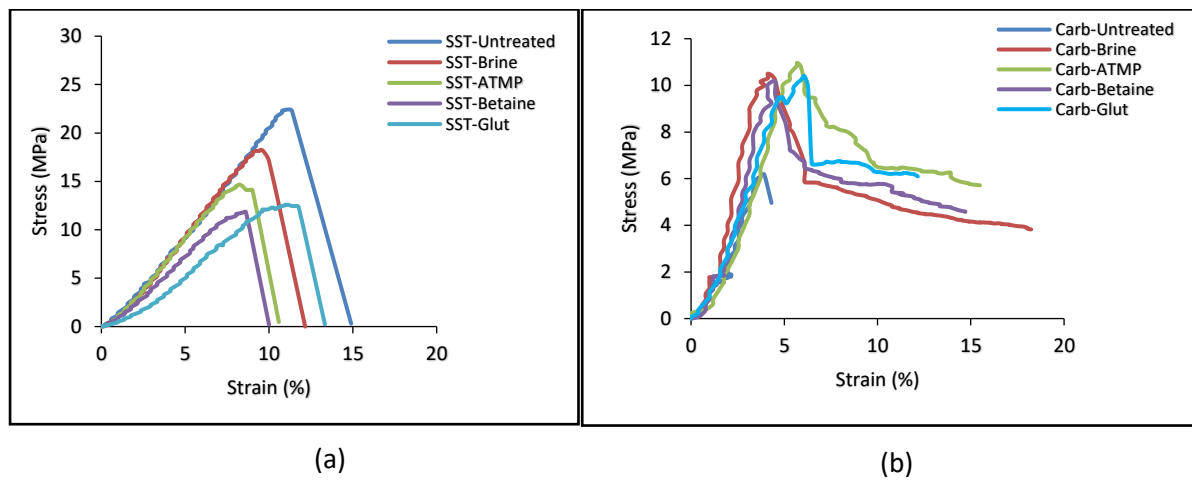


Figure 5.7: Stress-strain curve for untreated and chemically treated samples under dynamic condition: (a) sandstone and (b) carbonate.

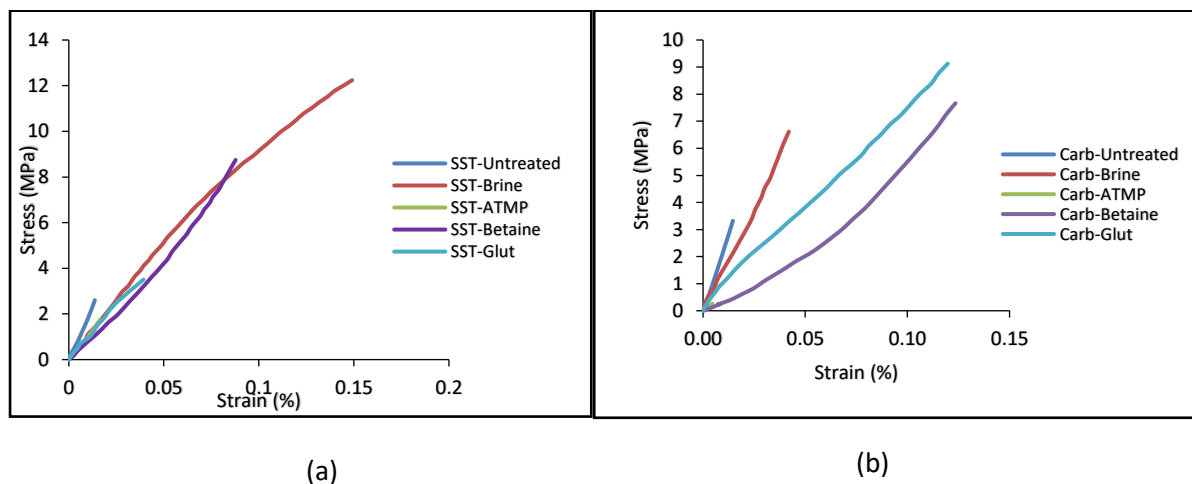


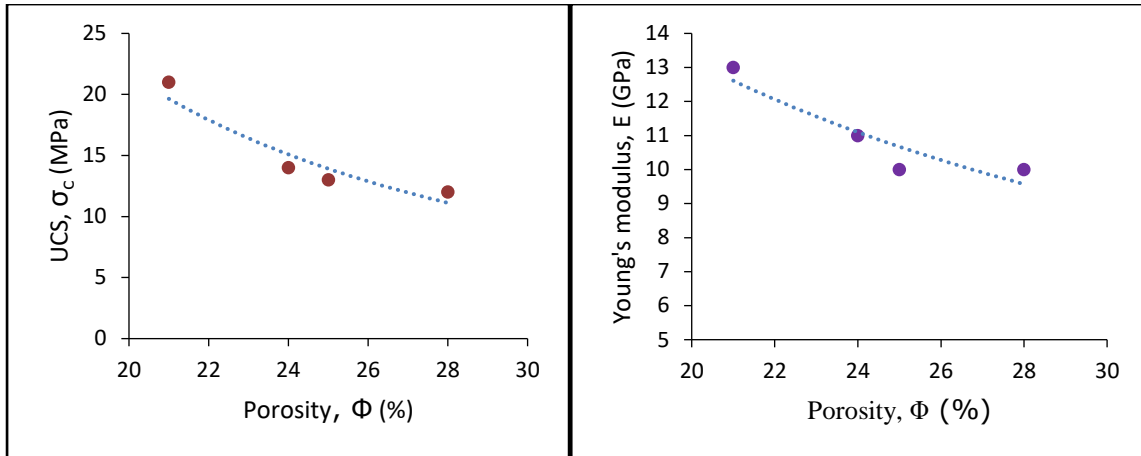
Figure 5.8: Stress-small strain response for untreated and chemically treated samples under dynamic condition: (c) sandstone, and (d) carbonate.

Table 5.5: UCS and Young's modulus of treated and untreated sandstone and carbonate samples (n=3) with recommended size correction factor under dynamic saturation.

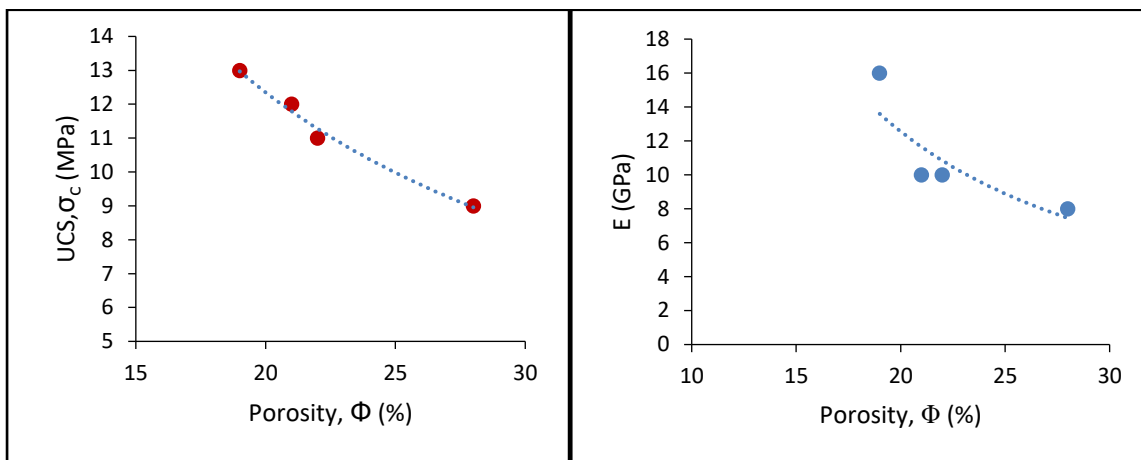
Sandstone				
	UCS (MPa)	Corrected UCS (MPa)	Length/Diameter (L/D) ratio	Young's Modulus (GPa)
SST-Untreated	24±2.0	22±1.8	1.3	19
SST-Brine	21±4.0	20±3.7	1.3	13±2.8
SST-ATMP	14±3.6	13±3.3	1.3	10±3.8
SST-Betaine	12±0.6	11±0.6	1.3	10±0.7
SST-Glut	13±0.7	12±0.7	1.3	11±4.0
Carbonate				
Carb-Untreated	6±0.6	6±0.6	1.3	6
Carb-Brine	13±2.8	12±2.6	1.3	16±2.8
Carb-ATMP	11±0.1	10±0.1	1.3	10±2.8
Carb-Betaine	10±3.0	9±2.8	1.3	8±4.0
Carb-Glut	9±1.5	8±1.3	1.3	10±3.5
SST =Sandstone; Carb = Carbonate; Glut = Glutaraldehyde				
Note: The correction was based on the ASTM C42-90 correction factor of 0.93				

Various models for example, power law, linear, logarithmic, exponential and second – order polynomial were used to correlate porosity and UCS of sandstone and carbonates to see which one fits the data best (Figure 5.9). Statistically significant ($p < 0.05$) inverse relationships between uniaxial compressive strength and Young's modulus with porosity were established which can be described by any of the five laws. The sandstone and carbonate UCS-porosity data fits best into the second – order polynomial model ($R^2 = 0.9991$; 0.9892 respectively). Similarly, relationship exists between porosity and the Young's modulus of sandstone and carbonates as presented in Table 5.6. Palchik (1999) has also established such relationship (Linear, Log, Power, Exponential and Polynomial) between porosity and UCS for sandstone in brine. These empirical relationships - suggests that porosity (Φ) can be used to predict UCS and Young's Modulus of sandstone and carbonate rocks within the range $20\% \leq \Phi \leq 30\%$. Despite the limited data points ($n = 4$) in this study, the UCS – porosity relationship from the current work was consistent with that for sandstone and carbonates with wide range of petrophysical properties, mineralogical and heterogeneity as shown in Figure 5.10

(Reyer and Philipp 2014; Sabatakakis et al. 2008; Chang et al. 2006; Palchik 1999) for sandstone (Figure 5.10a) and carbonates (Figure 5.10b). However, a cautious approach is advised when utilising such empirical relationships to estimate UCS which has also been noted by Chang et al. (2006) where they indicated that porosity alone is not a good indicator of UCS in low porosity (<5%) sandstone and carbonates. It is worth noting the wide range of data reported for both rock types which could also be linked to the measurement approach e.g. on dry or saturated cores, static or dynamic measurements or even differences in diagenetic processes in the formations.



(a)



(b)

Figure 5.9: Relationship between porosity, UCS and Young's Modulus of: (a) Sandstone; (b) Carbonate. The dot-dot line is the second order polynomial best fit to the experimental data.

Table 5.6: Summary of different models used to describe UCS-porosity relationship

Sandstone		
	Equation	Regression coefficient (R ²)
UCS, MPa	$\sigma = -31.79\ln(\Phi) + 116.52$	0.855
	$\sigma = -1.28\Phi + 46.36$	0.819
	$\sigma = 103.46e^{-0.08\Phi}$	0.857
	$\sigma = 8072.9\Phi^{-1.977}$	0.891
	$\sigma = 0.25\Phi^2 - 13.53\Phi + 194.86$	0.999
E, GPa	$E = -0.44\Phi + 21.78$	0.807
	$E = 232.87\Phi^{-0.958}$	0.845
	$E = 28.18e^{-0.039\Phi}$	0.812
	$E = -10.92\ln(\Phi) + 45.868$	0.841
	$E = 0.0833\Phi^2 - 4.5233\Phi + 71.28$	0.973
Carbonates		
UCS, MPa	$\sigma = -0.4333\Phi + 21$	0.966
	$\sigma = 215.79\Phi^{-0.955}$	0.987
	$\sigma = 27.679e^{-0.04\Phi}$	0.979
	$\sigma = -10.27\ln(\Phi) + 43.108$	0.978
	$\sigma = 0.0287\Phi^2 - 1.8008\Phi + 36.922$	0.989
E, GPa	$E = 0.711\Phi + 27$	0.632
	$E = 1293.3\Phi^{-1.547}$	0.761
	$E = 44.721e^{-0.064\Phi}$	0.717
	$E = -17.36\ln(\Phi) + 64.857$	0.679
	$E = 0.2186\Phi^2 - 11.13\Phi + 148.31$	0.956

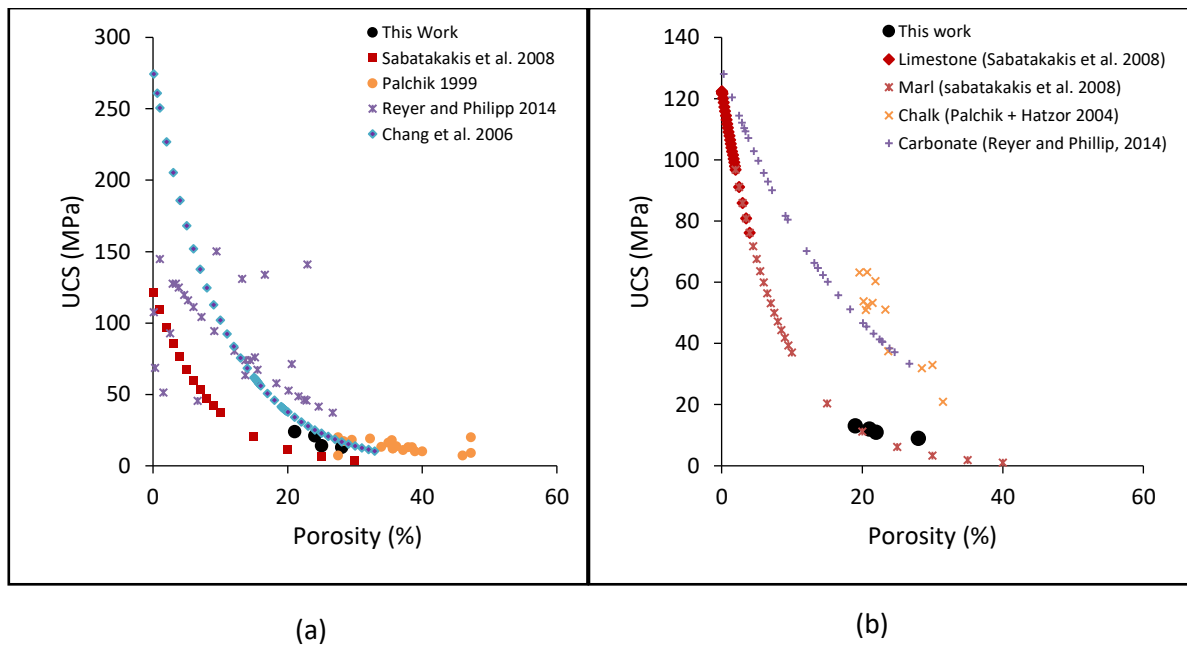


Figure 5.10: Comparison of the porosity – unconstrained compressive strength (UCS) relationship with existing correlations for (a) sandstone; and (b) carbonates.

The results show that the strength (UCS) of sandstone decreases with increase in porosity and grain size distribution (D_{50} and sorting) following exposure to the chemicals used in the study (Table 5.7). XRPD has shown clearly that clay minerals form the major cementing materials of the sandstone. The changes in the clay content following chemical treatment suggest dissolution/precipitation reaction within the sandstone. It is established that porosity is the bridge that links both particle size distribution and other properties of materials (Wang et al. 1999). As such, the relationship between other parameters (particle size distribution, sorting and mineralogy) and UCS has been revealed through the inverse relationship between the porosity and the UCS (Figure 5.9a). The changes in the cementing materials due to chemical treatment created voids in the sandstone samples leading to porosity increase, hence decrease in UCS as a result of weakened grain fabrics.

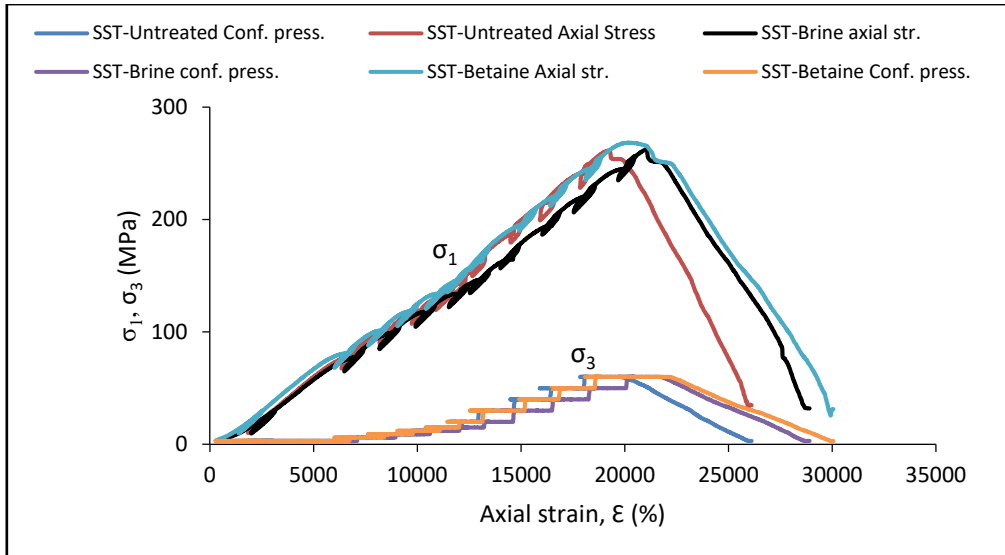
In a similar manner, the results show that the UCS of the carbonates increases with a decrease in porosity and increase in grain size distribution (D_{50} and sorting) following chemical treatment (Table 5.7). The change might have been caused by dissolution/precipitation reaction following treatment with betaine, ATMP and glutaraldehyde. The filling of the pore space by these precipitates likely led to a decrease in porosity and a subsequent increase in the UCS of the carbonates.

Table 5.7: Summary of the effects of chemicals on particle size distribution, porosity, mineralogy and UCS of sandstone and carbonates.

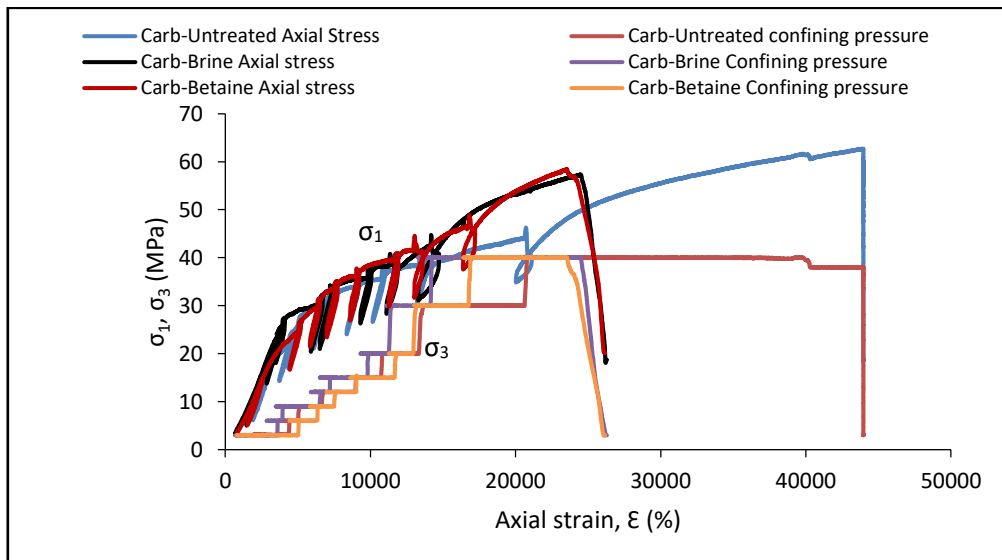
Sandstone									
Sample ID	Mean D ₅₀ (µm)	Porosity (%)	Mineralogy						UCS (MPa)
			Quartz (wt.%)	Dolomite (wt.%)	Calcite (wt.%)	Kaolinite (%)	Illite (%)	I/S-ML (%)	
SST-Untreated	N/A	N/A	98.4	N/A	0.4	14	35	51	22
SST-Brine	20	21	98.5	N/A	0.1	19	19	62	20
SST-Betaine	165	28	98.0	N/A	0.1	23	12	68	11
SST-ATMP	117	25	98.4	N/A	0.2	17	15	65	13
SST-Glut	100	24	98.0	N/A	0.4	23	13	64	12
Carbonate									
Carb-Untreated	N/A	N/A	3.7	73.8	21.2	7	7	86	6
Carb-Brine	16	28	4.0	92.6	2.3	10	6	84	12
Carb-Betaine	170	22	4.2	93.0	2.2	10	4	84	9
Carb-ATMP	153	21	3.8	93.6	1.6	9	5	86	10
Carb-Glut	200	19	2.8	95.1	1.6	8	6	86	8

5.7 Effect of chemicals on Confined Compressive Strength and Young's modulus

To determine the confined compressive strength of sandstone and carbonates a multi-stage triaxial test which is a non-zero confining pressure test was performed on the sandstone and carbonate under compression. The multi-stage triaxial test was used to obtain multiple failure states with one sample instead of the conventional single-stage triaxial test that requires one sample per test. The obtained data was used to determine the peak strength envelope, angle of internal friction, apparent cohesion or shear strength, and Young's modulus under compression. Figure 5.11 shows the multiple failures at different confining pressure. These plots were used to determine the Young's modulus for both sandstone and carbonate. The dimensions and densities of sandstone and carbonate are presented in Table 5.8.



(a)



(b)

Figure 5.11: Stress-strain response during multiple failures at different confining pressure for: (a) Sandstone; (b) Carbonate.

Table 5.8: The dimensions and densities of sandstone and carbonate

Sandstone							
Sample identifier	Height (mm)	Top Diameter (mm)	Middle Diameter (mm)	Bottom diameter (mm)	Mean Diameter (mm)	Mass (g)	Specific Density
LP4	101.16	50.55	50.55	50.54	50.55	428.91	2.11
LP7	101.29	50.63	50.63	50.63	50.63	427.29	2.10
LP10	101.33	50.61	50.64	50.66	50.64	427.46	2.09
LP13	101.36	50.63	50.64	50.66	50.64	429.06	2.10
LP14	101.26	50.55	50.54	50.51	50.53	428.74	2.11
LP29	101.33	50.54	50.54	50.53	50.54	429.27	2.11
LP34	101.24	50.67	50.69	50.70	50.69	431.8	2.11
Carbonate							
ED7	101.74	49.85	49.95	49.98	49.93	334.67	1.68
ED8	101.84	50.45	50.45	50.44	50.45	329.72	1.62
ED10	101.66	50.02	50.24	50.21	50.16	337.35	1.68
ED14	101.44	50.10	50.28	50.26	50.21	355.16	1.77
ED24	101.46	50.51	50.47	50.48	50.49	346.06	1.70
ED33	101.43	50.17	50.17	50.30	50.21	349.84	1.74
ED36	101.32	50.39	50.35	49.96	50.23	337.46	1.68

LP = Leopard (sandstone); ED = Edward brown (Carbonate)

Three types of plots are available to present failure data, namely; the principal stress plots ($\sigma_1 - \sigma_3$), the shear versus normal stress plots ($\sigma_s - \sigma_n$); and the shear stress versus effective mean stress ($q - p$) plots. 'p' is the effective stress, which represents the normal compressive stress (Equations 5.8 and 5.10), and 'q' is the effective differential stress that represents the shear stress (Equations 5.9 and 5.11). The magnitudes of both stresses were calculated from the principal stresses as follows (even though the principal stresses are normal stresses and not shear stresses). Note that $\sigma_1 > \sigma_2 > \sigma_3$ where σ_1 is the major, σ_2 is the intermediate and σ_3 is the minor principal stresses:

$$p = \frac{1}{3}(\sigma_1 + \sigma_2 + \sigma_3) \quad [5.8]$$

$$q^2 = \frac{1}{2}[(\sigma_1 - \sigma_2)^2 + (\sigma_2 - \sigma_3)^2 + (\sigma_1 - \sigma_3)^2] \quad [5.9]$$

In the triaxial tests carried out in this study $\sigma_2 = \sigma_3$, hence:

$$p = \frac{1}{3}(\sigma_1 + 2\sigma_3) \quad [5.10]$$

$$q = (\sigma_1 - \sigma_3) \quad [5.11]$$

In this work the principal stress plots ($\sigma_1 - \sigma_3$) with the corresponding q-p plots are employed for the presentation of the failure data. The principal stress plots have been recommended by Zoback (2007) for the determination of the unconfined compressive strength. There is also a general knowledge that principal stress plot is capable of mapping the entire failure surface that includes all types of failure. In this study, bilinear Mohr-Coulomb was implemented in describing the failure envelopes because the data fits into them. The bilinearity of the yield surface accounts for the dependency property of friction angle on pressure (Nouri et al. 2009). The q-p plot became necessary because both sandstone and carbonate are porous and have the tendency to develop shear-enhanced compaction induced by the triaxial compressive stresses.

Sandstone and carbonate exhibit strain softening at Low Effective Confining Stress (LECS) and strain hardening at High Effective Confining Stress (HECS). The strain hardening which expands and strain softening which contracts are used to formulate the yield surface as a function of the plastic deformations. Therefore, two sets of material properties were given for two ranges of confining pressures (Table 5.9). According to Nouri et al. (2009), the peak states obtained at LECS are described as the friction-hardening phase and at HECS as the cohesion-softening phase. Two models were explored to explain rock plastic behaviour at the two regimes (LECS and HECS) for both sandstone and carbonate (Table 5.10).

The onset of plastic deformation at any point in the medium is said to take place when the stress path attains the initial yield envelope (Figure 5.11).

Table 5.9: Summary of triaxial test results for sandstone and carbonate.

Sandstone					
Sample (n = 2)	Peak states	UCS, Co (MPa)	Angle of Internal Friction, ϕ (Degree)	Apparent Cohesion (MPa)	Range of Confining Pressure (MPa)
SST-Untreated	LECS	68	46	13	$0 \leq \sigma_3 \leq 12$
	HECS	105	28	31	$12 < \sigma_3 \leq 60$
SST-Brine	LECS	64	47	12	$0 \leq \sigma_3 \leq 12$
	HECS	114	28	33	$12 < \sigma_3 \leq 60$
SST-Betaine	LECS	65	46	14	$0 \leq \sigma_3 \leq 12$
	HECS	96	30	30	$12 < \sigma_3 \leq 60$
Carbonate					
Carb-Untreated	LECS	18	9	8	$0 \leq \sigma_3 \leq 15$
	HECS	28	-	22	$15 < \sigma_3 \leq 60$
Carb-Brine	LECS	20	3	10	$0 \leq \sigma_3 \leq 15$
	HECS	30	-	26	$15 < \sigma_3 \leq 60$
Carb-Betaine	LECS	22	5	10	$0 \leq \sigma_3 \leq 15$
	HECS	34	-	23	$15 < \sigma_3 \leq 60$

LECS = Low Effective Confining Stress; HECS = High Effective Confining Stress

Table 5.10: Summary of the models obtained at the two peaks to describe shear strength.

Sandstone		
	Peak state	Models
SST-Untreated	LECS	$\sigma_s = 5.3233\sigma_n + 67.51$
	HECS	$\sigma_s = 2.6779\sigma_n + 105.50$
SST-Brine	LECS	$\sigma_s = 5.7400\sigma_n + 63.60$
	HECS	$\sigma_s = 2.5809\sigma_n + 113.18$
SST-Betaine	LECS	$\sigma_s = 5.8633\sigma_n + 64.95$
	HECS	$\sigma_s = 2.7933\sigma_n + 105.67$
Carbonate		
Carb-Untreated	LECS	$\sigma_s = 1.3567\sigma_n + 17.70$
	HECS	$\sigma_s = 0.5138\sigma_n + 27.75$
Carb-Brine	LECS	$\sigma_s = 1.0800\sigma_n + 19.90$
	HECS	$\sigma_s = 0.4018\sigma_n + 29.96$
Carb-Betaine	LECS	$\sigma_s = 1.2367\sigma_n + 21.55$
	HECS	$\sigma_s = 0.3861\sigma_n + 33.90$

5.7.1 Sandstone

It can be observed that the intact sandstone samples experienced shear failure in response to the high shear stress along the plane (Figures 5.12 a, c, e). The nature of the deformation displayed by the sandstone samples suggests development of fault zone along the failure plane which made the two sides of the plane to move relative to one another in a frictional process (Figures 5.12 b, d, f).

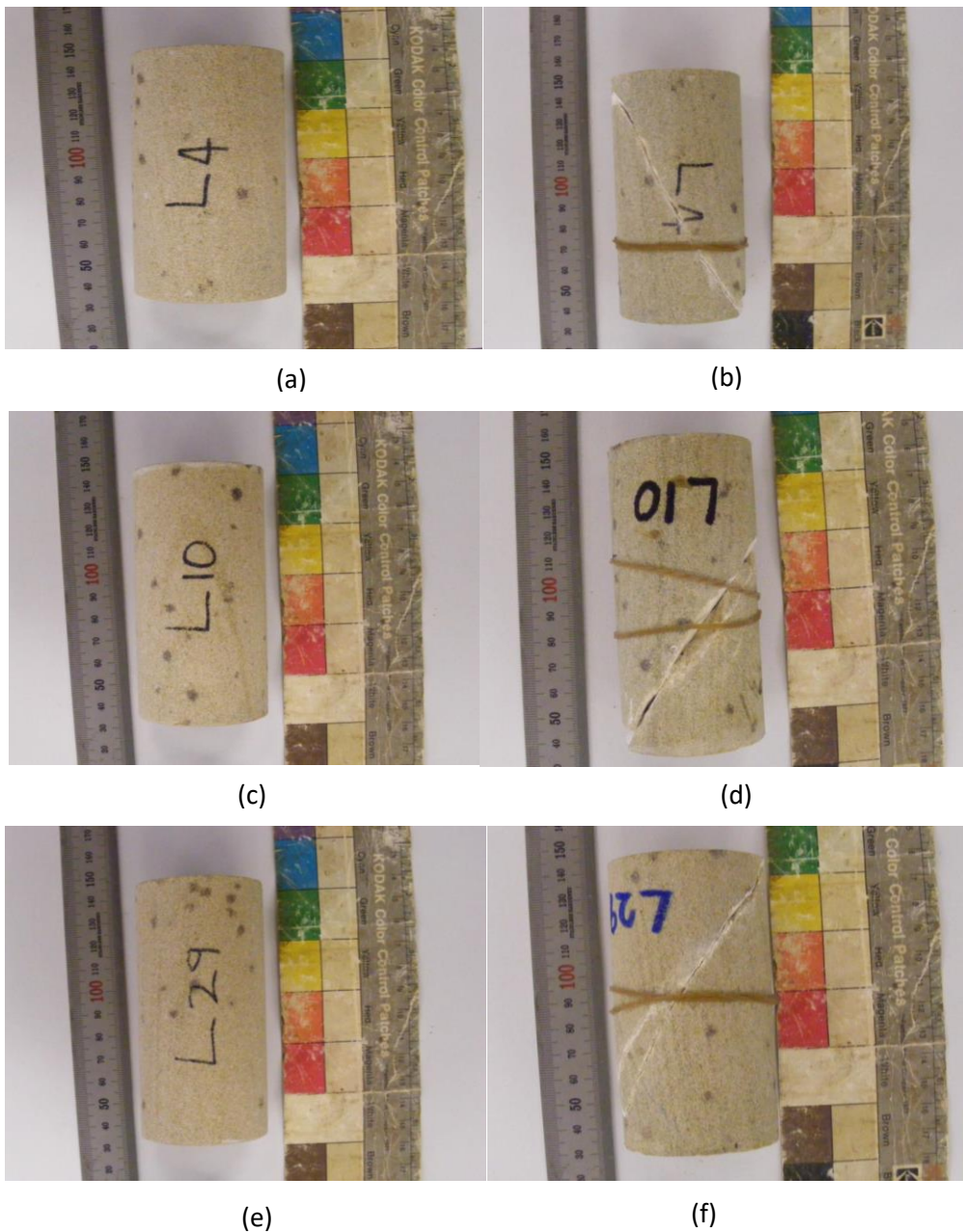


Figure 5.12: Sandstone samples before test: (a, c & e) and after test (b, d & f).

At the LECS phase the mean compressive strength, C_0 , of the untreated sandstone, apparent cohesion, S_0 (the real cohesion), angle of internal friction, ϕ , and Young's modulus, E calculated are 68 MPa, 14 MPa, 46° , 1 and 21 GPa respectively. It was observed (Figure 5.13) that micro-cracking did not form during the LECS regime. This implies that tension cut-off was constant up to the peak of mobilized friction angle (Nouri et al. 2009). A higher C_0 (106 MPa), S_0 (31 MPa) and a lower angle of internal friction (29°) were obtained at HECS regime from the same untreated sandstone sample. This may be attributed to the fact that tension cut-off is not constant during the motion of yield surface at this regime. Besides, at this phase a gradual transition to a material with decreased stiffness, but still having the ability to withstand load as the strain increases was observed. At the LECS phase, the sandstone experienced a slight strength reduction from 68 MPa to 64 and 65 MPa following treatment with the brine and betaine respectively. Similarly, at HECS phase, the sandstone strength reduced from 106 MPa to 96 MPa owing to treatment with betaine. On the other hand, the strength increased from 106 MPa to 114 MPa in the presence of brine. This constitutes 4 - 6% and 8 - 9% changes at LECS and HECS phases respectively. The result suggests that the interaction between the chemical and the core has little effect on the UCS of sandstone under confined condition.

Little or no change was observed with the cohesion, S_0 at LECS and HECS phases. The cohesion at LECS measures the bonding of materials and its softening with plastic shear deformations which is associated with the development of micro-cracks and loss of cohesive strength. The cohesion at HECS is known to decline at a slower pace than the cohesion at LECS. The reason for this could be attributed to the higher ductile nature of the materials at higher effective confining stresses.

Again, there is little or no change of the angle of internal friction at LECS and HECS phases in the presence of brine and betaine (Table 5.9). The obtained values of angle of internal friction ($\varphi \geq 0$) indicates that the materials were positively dilatant (Fjaer et al. 2008). The shear stress has an inverse relationship with the normal stress at both LECS and HECS phases as summarised in Table 5.10.

There was no remarkable change in the Young's modulus (20 to 19 GPa) owing to treatment with brine and betaine. Elastic failure is experienced at LECS phase whilst plastic deformation was obtained at HECS phase for both untreated and chemically treated sandstone samples. A gradual transition took place between LECS and HECS when the material stiffness decreased slightly, yet it exhibits the ability to carry the load as the strain increases.

Comparing the Young modulus result obtained from uniaxial compression test (32% - 50% reduction) result and that of triaxial compression test (5%), it is obvious that the percentage change is very minimal under the triaxial compression test.

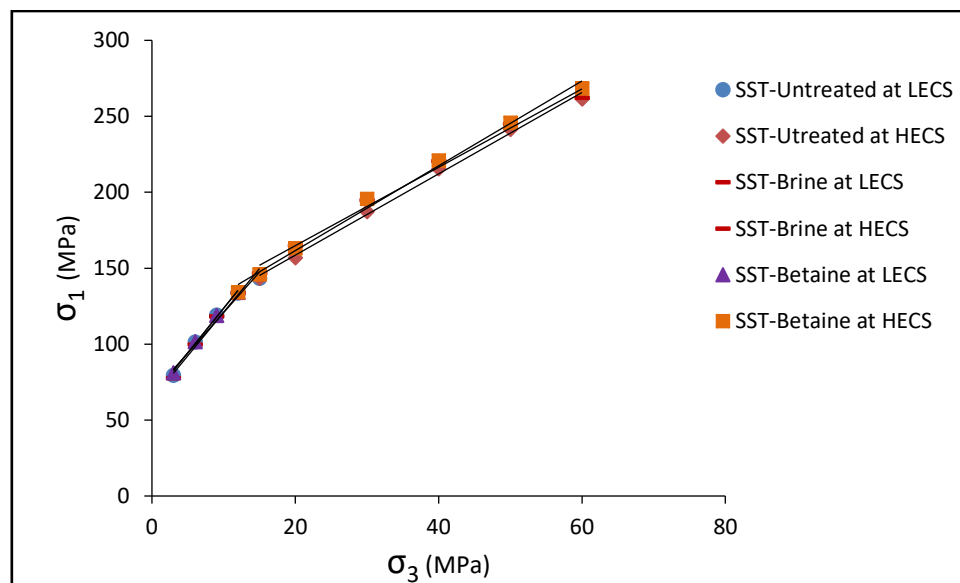


Figure 5.13: Failure envelope for untreated, brine treated and betaine treated sandstone.

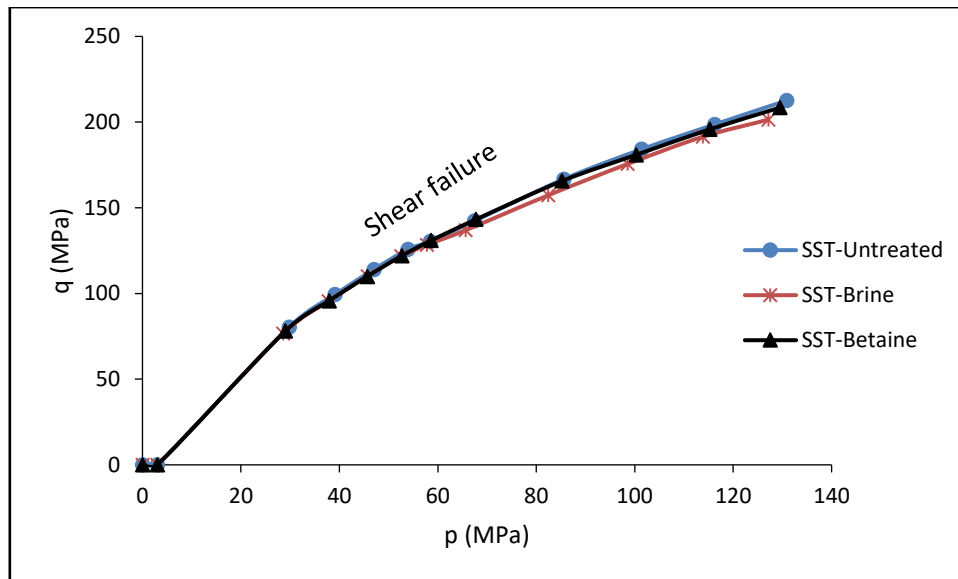


Figure 5.14: q-p curves indicating shear failure mode devoid of compaction for sandstone. Comparing the UCS results obtained from triaxial test with those obtained from uniaxial test (Figure 5.15), it is obvious that there was insignificant change in strength due to chemical treatment under confined pressure. The strength reduction under uniaxial compression test is in the ranges of 13 to 50%; whilst that of triaxial test is 4 to 6%. Besides, the values uniaxial compressive strength obtained under confined condition was much higher than those obtained under unconfined condition. The disparity in obtained values can be explained by the fact that in confinement supports sandstone strength and prevent it from brittle collapse; whilst under unconfined condition the sandstone failed due to early crack initiation.

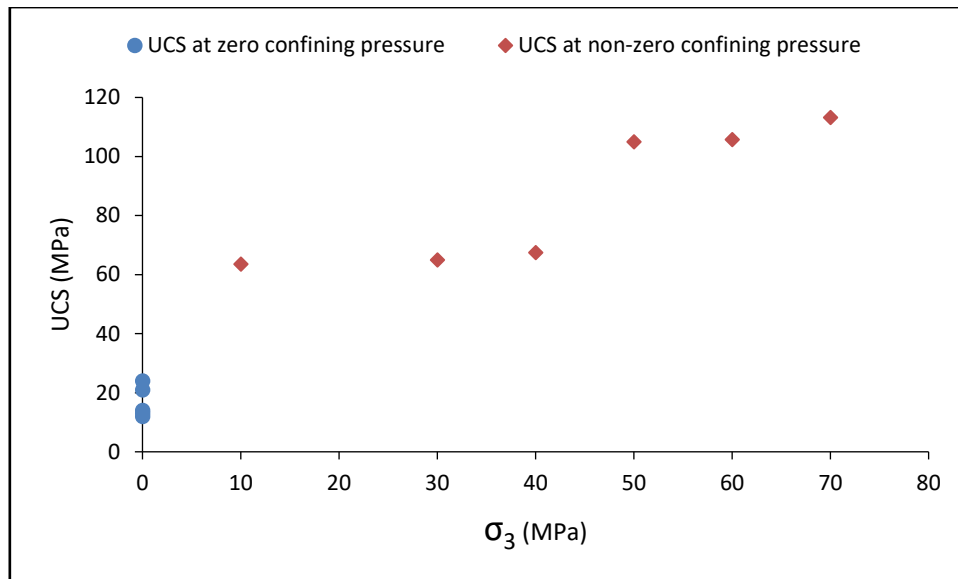


Figure 5.15: Comparison between the UCS at zero confining pressure and non-zero confining pressure.

5.7.2 Carbonate

Similarly, the bilinear Mohr-Coulomb envelopes (Figure 5.16) shows a slight increase in the UCS of the carbonate under confined condition following treatment with brine at LECS (from 18 to 20 MPa); HECS (from 28 to 30 MPa) and betaine at LECS (from 18 to 22 MPa); HECS (from 28 to 34 MPa). Also observed is a slight change in cohesion from 8 to 10 MPa at LECS phase for brine and betaine treated sample; and from 22 to 26 MPa at HECS phase in the presence of brine, no change was observed at HECS in the presence of betaine. The angle of internal friction changed from 9° to 3° and 5° at LECS due to treatment with brine and betaine respectively (Table 5.9). Unfortunately, no measurement was taken for angle of internal friction at HECS because at this phase, the samples suffered compaction leading to termination of the tests. The compaction is plainly evident from the q - p plots and post-test photograph (Figure 5.17 and 5.18). A 22% and 21% increase in CCS was observed with the betaine treated carbonate at LECS and HECS phases respectively. No remarkable change (11% increase) was noticed with the brine treated carbonate at both phases, (see Table 5.7).

Unlike the sandstone, the carbonates were of low density, thus there was a likelihood of shear-enhanced compaction induced by the triaxial compressive stresses which might complicate the Mohr-Coulomb strength envelopes interpretation. As such q-p curves (Figure 5.17) were plotted in addition to the principal stress curves (Mohr-Coulomb envelopes) to investigate the compaction tendency of the rocks' strength.

The mean Young's modulus calculated from the stress-strain (micro-strain) plot for untreated, brine and betaine treated carbonate under confined condition are 10, 11 and 10 GPa respectively. This means that the chemical interaction had no effect on the Young's modulus. Similarly, little or no change in Young's modulus (ranging between 6 - 8 GPa) was observed with the betaine treated carbonate under unconfined condition.

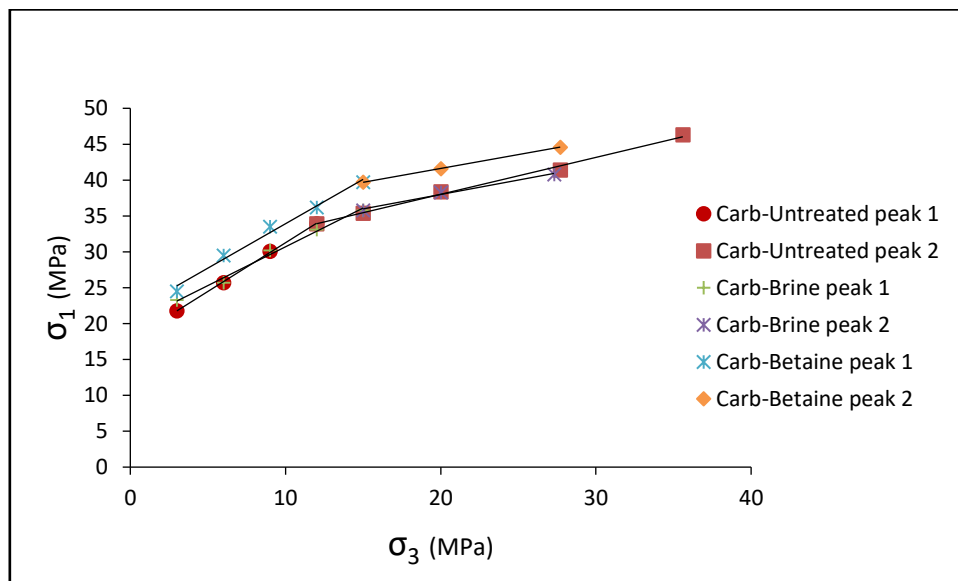


Figure 5.16: Bilinear yield surface of carbonate at peak states.

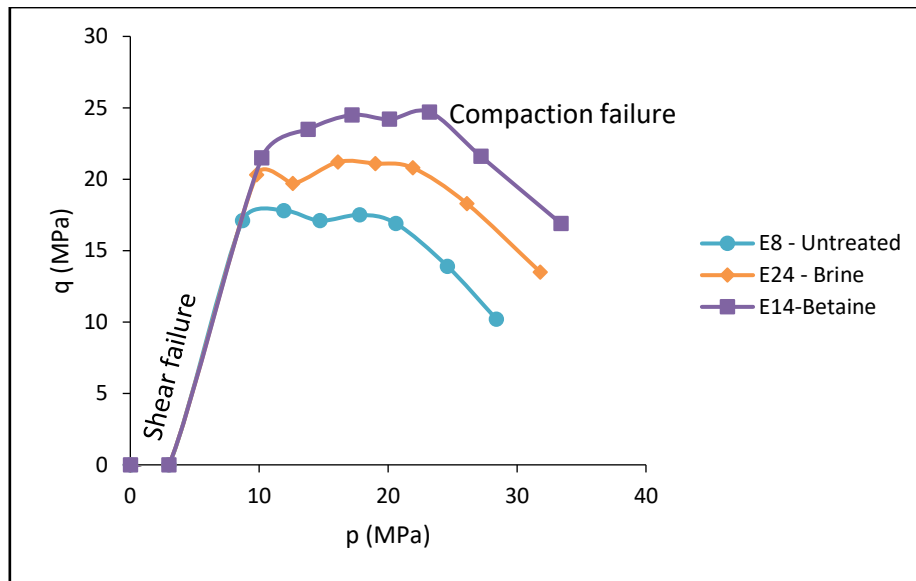


Figure 5.17: q-p curves indicating various failure modes for carbonate

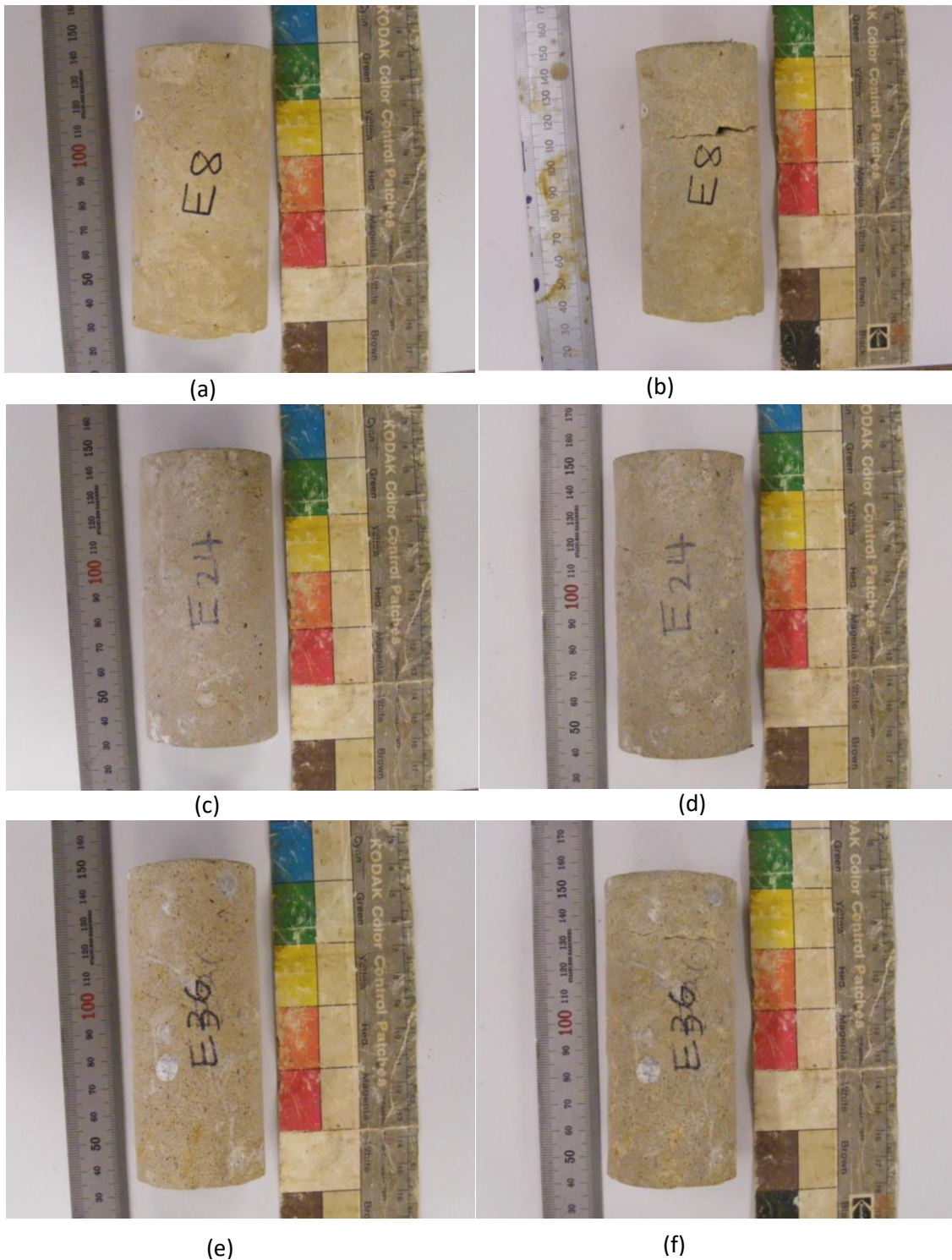


Figure 5.18: Carbonate samples before test: (a, c & e) and after test (b, d & f).

Both uniaxial and triaxial tests have shown an increase (to varying degrees) in strength of carbonate in the presence of chemicals. Under unconfined compression test 67% and 100% strength increases were observed owing to treatment with betaine and brine respectively. While, under confined compression test 22% and

21% strength increases were observed following treatment with betaine at LECS and HECS phases respectively. Only 11% increase was observed with brine. The results suggest that little precipitation reaction took place in the presence of betaine under confined condition, hence the effect on the UCS and hydrocarbon production may be insignificant. Again, these results have shown that the reservoir rock is able to withstand the presence of the oilfield chemical especially betaine at depth.

The two distinct stages involved in sand production in the reservoir rocks include mechanical degradation of intact rock to loose particles through stress concentration around the wellbore; secondly, by hydrodynamic forces to the wellbore (Nouri et al. 2009). The mechanical degradation occurs at the development of micro-cracks as failure concentrates in narrow band at post-peak strength. This phenomenon seems to be the case with the results obtained at zero confined pressure; whilst the results obtained under confined pressure is devoid of it.

5.8 Summary

The interaction between reservoir formation rocks and three commonly used oilfield chemicals (biocide, corrosion inhibitor and scale inhibitor) has been evaluated under dynamic condition. Clastic and carbonate cores obtained from Texas, USA through Kocurek Industries were used in the study. Both mechanical and analytical tests were deployed to characterise the cores pre and post chemical treatments and analyse the interaction between the chemicals and the rocks. The results suggest that chemical interactions in form of adsorption, dissolution, precipitation and ionic substitution took place between the oilfield chemicals and the rocks. The dissolution reaction caused deterioration of the rocks grain to grain

binding, leading to release of disintegrated grains into the fluid streams. The release of the grains caused porosity increase and reduction of unconfined compressive strength of sandstone at zero confining pressure with a consequence of sand failure and production in formation rocks. However, the precipitated particles under zero confining pressure filled the pore space leading to porosity and permeability reduction as observed with the carbonate. Such pore constriction potentially leads to formation damage and hydrocarbon production impairment. On the other hand, the triaxial test results shows that the dissolution and precipitation reactions under non-zero confined pressure in the presence of oilfield chemical (betaine) have no negative effect on the geomechanical strength of the reservoir rock. This could be attributed to the fact that investigation was not conducted under the under the reservoir conditions.

References

- ASTM, 1992. Standard Test Method for Obtaining and Testing Method for obtaining and Testing Drilled cores and Sawed Beams of Concrete. 1991 Annual Book of ASTM Standards, *Concrete and Aggregates*, vol 4, C 42-90.
- BARAKA-LOKMANE, S., SORBIE, K.S. 2010. Effect of pH and scale inhibitor concentration on phosphonate-carbonate interaction. *Journal of Petroleum Science and Engineering*. 70, 10–27.
- BENAVENTE, D., MAG DEL CURA, FORT, R., ORDONEZ, S. 2004. Durability estimation of porous building stones from pore structure and strength. *Engineering Geology*, 74(1), 113-127.
- BERNABÉ, Y., MOK, U., EVANS, B., 2003. Permeability-porosity relationships in rocks subjected to various evolution processes. *Pure and Applied Geophysics*, 160(5), 937-960.
- BOLT G., BRUGGENWERT M. and KAMPHORST A. 1976. Adsorption of cations by soils. In Soil Chemistry. A. *Basic Elements* (eds. G. H. Bolt and M. G. M. Bruggenwert)
- CHANG, C., ZOBACK, M.D., KHAKSAR, A., 2006. Empirical relations between rock strength and physical properties in sedimentary rocks. *Journal of Petroleum Technology* 51, 223-237.
- DURMEKOVÁ, T., HOLZER, R., WAGNER, P., 2003. Weak rocks in engineering practice. Conference proceedings, Geotechnical measurements and modelling, Natau, Fecker & Pimentel (eds), Swets & Zeitlinger, Lisse, 185-191.
- FJAER, E., HOLT, R.M., HORSRUD, P., RAAEN, A.M., RISNES, R., 2008. *Developments in Petroleum Science* 53, 55-102.
- FOLK, R.L., 1968. A review of grain-size parameters. *Sedimentology* 6(2), 73-93.

JORDAN, M., SORBIE, K., JIANG, P., YUAN, M. AND TODD, A., 1994. TK" Mineralogical controls on inhibitor adsorption/desorption in Brent Group sandstone and their importance in predicting and extending field squeeze lifetimes. *Proceedings, European Production Operations Conference and Exhibition*, Aberdeen, UK.

KAHRAMAN, S., GUNAYDIN, O., FENER, M., 2008. The effect of water saturation on the strength of marbles. ISRM International Symposium-5th Asian Rock Mechanics Symposium. Tehran, Iran, 24 – 26 November.

KAN, A.T., FU, G., TOMSON, M.B., AL-THUBAITI, M., XIAO, A. J. 2004. Factors affecting scale inhibitor retention in carbonate-rich formation during squeeze treatment, *SPE Journal* 9(3): 280–289. SPE80230-PA.

KAN, A.T., FU, G.M., TOMSON, M.B. 2005. Adsorption and precipitation of an aminoalkylphosphonate onto calcite. *Journal of Colloid and Interface Science*, 281(2), 275–284.

LADD, C.C. and FOOTT, R., 1974. New design procedure for stability of soft clays: 10F, 3T, 39R. *Journal Geotechnics Engineering Division* V100, N. GT7, JULY 1974, P763–786. *International Journal of Rock Mechanics and Mining Sciences & Geomechanics Abstracts*. Pergamon. A220.

LAMY-CHAPPUIS, B., ANGUS, D., FISHER, Q., GRATTONI, C. and YARDLEY, B., 2014. Rapid porosity and permeability changes of calcareous sandstone due to CO₂-enriched brine injection. *Geophysical Research Letters*, 41(2), 399-406.

LI, L. and AUBERTIN, M., 2003. A general relationship between porosity and uniaxial strength of engineering materials. *Canadian Journal of Civil Engineering*, 30(4), 644-658.

NIMMO, J., 2004. Porosity and pore size distribution. *Encyclopaedia of Soils in the Environment*, 3, 295-303.

NELSON, P. H., 1994. Permeability-porosity relationships in sedimentary rocks. *The Log Analyst*, 35, 38-62.

NOURI, A., KURU, E., VAZIRI, H., 2009. Elastoplastic modelling of sand production using fracture energy regularization method. *Journal of Canadian Petroleum Technology* 48 (4), 64-71.

OLUYEMI, G., 2014. Conceptual Physicochemical Models for Scale Inhibitor-Formation Rock Interaction. *Petroleum Science and Technology*, 32(3), 253-260.

OLUYEMI, G.F., OYENEYIN, B.M. and MACLEOD, C., 2010. UCS neural network model for real time sand prediction. *International Journal Engineering Resource in Africa* 2, 1-13.

PALCHIK, V., HATZOR, Y., 2004. The Influence of Porosity on Tensile and Compressive Strength of Porous Chalks. *Rock Mechanics Rock Engineering* 37 (4): 331-341.

PALCHIK, V., 1999. Technical note: influence of porosity and elastic modulus on uni-axial compressive strength in soft brittle porous sandstones. *Rock Mechanics Rock Engineering* 32 (4), 303-309.

PLUMMER, L., WIGLEY, T. and PARKHURST, D., 1978. The kinetics of calcite dissolution in CO₂-water systems at 5 degrees to 60 degrees C and 0.0 to 1.0 atm CO₂. *American Journal of Science*, 278(2), 179-216.

PŘIKRYL, R., 2001. Some microstructural aspects of strength variation in rocks. *International Journal of Rock Mechanics and Mining Sciences*, 38(5), 671-682.

RAMACHANDRAN, S., JOVANCICEVIC, V. and WARD, M.B., 1999. Understanding interactions between corrosion inhibitors & iron carbonate films using molecular modelling, Houston, NACE International, paper no. 7).

REYER, D., PHILIPP, S. 2014. Empirical relations of rock properties of outcrop and core samples from the Northwest German Basin for geothermal drilling. *Geothermal Energy Sciences*, 2, 21-37.

SABATAKAKIS N., KOUKIS G., TSIAMBAOS G., PAPANAKLI S., 2008. Index properties and strength variation controlled by microstructure for sedimentary rocks. *Engineering Geology* 97 (1), 80–90.

SETO, M. NAG, D.K., VUTUKURI, V.S. and KATSUYAMA, K., 1997. Effect of chemical additives on the strength of sandstone. *International Journal of Rock Mechanics and Mining Science*, 34:3-4.

SINGURINDY, O., BERKOWITZ, B., 2003. Flow, dissolution, and precipitation in dolomite. *Water Resources Research*, 39(6).

TANTAYAKOM, V., FOGLER, H., DE MORAES, F., BUALUANG, M., CHAVADEJ, S., MALAKUL, P., 2004. Study of Ca-ATMP precipitation in the presence of magnesium ion. *Langmuir* 20 (6), 2220-2226.

TÖRÖK, Á., and VÁSÁRHELYI, B., 2010. The influence of fabric and water content on selected rock mechanical parameters of travertine, examples from Hungary. *Engineering Geology* 115(3), 237-245.

VELOSO, C.B., SILVA, N. A., WATANABE T. G., PAES, B. C., DE LUNA, F.T. and CAVALCANTE, Jr, C.L. 2014. Scale inhibitor adsorption studies in rock sandstone type. *Adsorption*, 20(8), 977–985.

VERWALL, W. and MULDER, A., 2000. Rock and aggregate test procedures. *Rock and aggregate laboratory manual*, 13, p.14.

WANG, A., ZHANG, C., ZHANG, N., (1999). The theoretic analysis of the influence of the particle size distribution of cement system on the property of cement. *Cement and Concrete Research* 29, 1721-1726.

WELTON, J., 1984. SEM Petrology Atlas. Methods in Exploration Series No.4, The American Association of petroleum Geologists.

XUE, T., XIANG, Y., GUO, F., 2004. Numerical method to determine mechanical parameters of engineering design in rock masses. *Journal Zhejiang University Science* 5(7), 884-889.

YAN, F., BHANDRI, N., WANG, L., DAI, Z., ZHANG, Z., BOLANOS, V., KAN, A. and TOMSON, M., 2015. Interaction between scale inhibitors and shale and sandstone formations. Presented at International symposium on oilfield chemistry, The Woodlands, TX, USA, 13 – 15 April.

ZOBACK, M.D., 2007. Reservoir Geomechanics. Cambridge University Press, New York, NY, USA, 84-94.

Chapter Six

6 Numerical modelling of oilfield chemical interaction with the porous medium

6.1 Introduction

Injection of reactive fluids into the reservoir rocks may cause chemical disequilibrium as well as initiate various chemical reactions that can cause deleterious effect on the rock strength (Czernichowski-Lauriol et al. 2006). Understanding the processes like flow, heat transfer, multi-species transport, and chemical reactions is required to predict the amount of precipitation or dissolution over the entire period of interaction (Bartels et al. 2002).

Several models exist (Appelo and Postma 2005, Anderson et al. 2012, Liu et al. 1997) to describe the effects of interaction between fluids and porous medium numerically. Nevertheless, none of these models has considered the deleterious effect of oilfield chemicals that are used routinely for one treatment or the other in the oil field.

In this chapter, the numerical simulation of oilfield chemical-rock interaction through coupling of fluid flow, transport and chemical reaction in the porous media using COMSOL Multiphysics® software is undertaken and discussed. It is worthy of note that this is a feasibility study since COMSOL Multiphysics has inbuilt equations that were used with the user defined equations to generate data.

The motivation behind the simulation is to develop a model that accounts for the weakening effects of oilfield chemicals in sand production prediction as explored in Chapters Four and Five. In addition, the simulation enables comprehension of

the fundamental mechanisms involved in oilfield chemical-reservoir rock interaction.

6.2 Geochemical modelling Approach

To model the interaction between fluid and mineral phases during oil and gas production, a number of steps were taken to account for the flow of fluid, chemical reaction between the injected fluids and the in situ reservoir minerals and transport of the dissolved materials in the porous medium. The processes involved in the entire model are described by a two dimensional (2D) medium with a geometry of 20m long and 10m wide and extremely fine mesh (Figure 6.1).

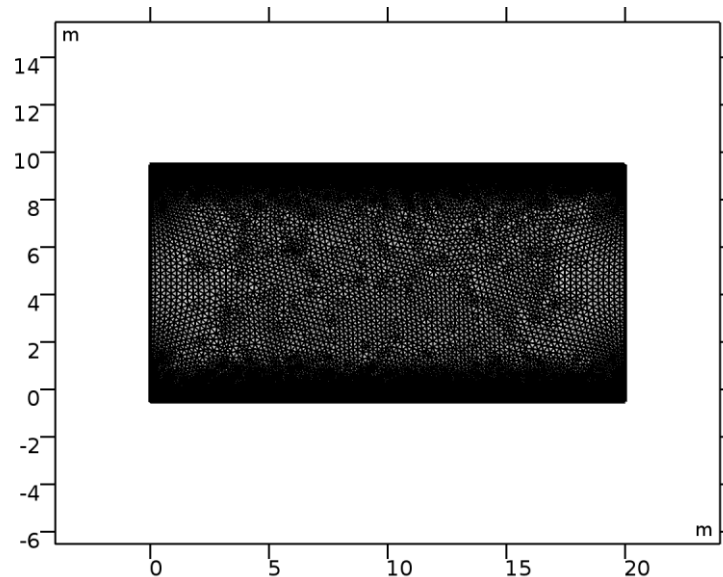


Figure 6.1: Model geometry and mesh arrangements

6.2.1 Fluid flow modelling

Darcy's law is generally used for the description of fluid flow in porous media. However, it has some limitations in the sense that it cannot handle particles in the fluid and cannot account for viscous effects that arise from the free fluid flow (Liu et al. 1997). As such the Brinkman equation (Equation 6.1) which extends Darcy's law to account for viscous transport, in the momentum balance, and also introduces velocities as dependent variables, was employed in this work. This

model handles free flow in porous media where momentum transport by shear stresses in the fluid is considered important. Solution of the momentum balance equations in the direction of x, y and z in combination with continuity equation is used to determine flow field.

$$\rho \frac{\partial u}{\partial t} - \nabla * \eta(\vec{u} + (\vec{u})^T) + \left(\frac{\eta}{k} u + \nabla P - F \right) = 0 \quad [6.1]$$

$$\nabla \cdot u = 0$$

Where ρ denotes fluid density (kg/m³), \vec{u} the velocity vector (m/s), η the dynamic viscosity (pa.s), k the permeability of the porous structure (m²), P the pressure (Pa), T is tortuosity and F the force that accounts for the influence of small compressibility effect where required (N/m²).

The boundary conditions for the modelling was applied such that fluid flow into the porous medium with a uniform velocity at the inlet ($n \cdot u = u_0$) and flow out under pressure at the outlet ($P = P_0$). The wall was made impervious (no slip – $u = 0$). Therefore:

Inlet/Outlet	$u \cdot n = u_0$
Outlet/Pressure	$P = P_0$
No Slip	$u = 0$

6.2.2 Model definition

The model domain and notations for the boundary conditions are depicted in (Figure 6.2).

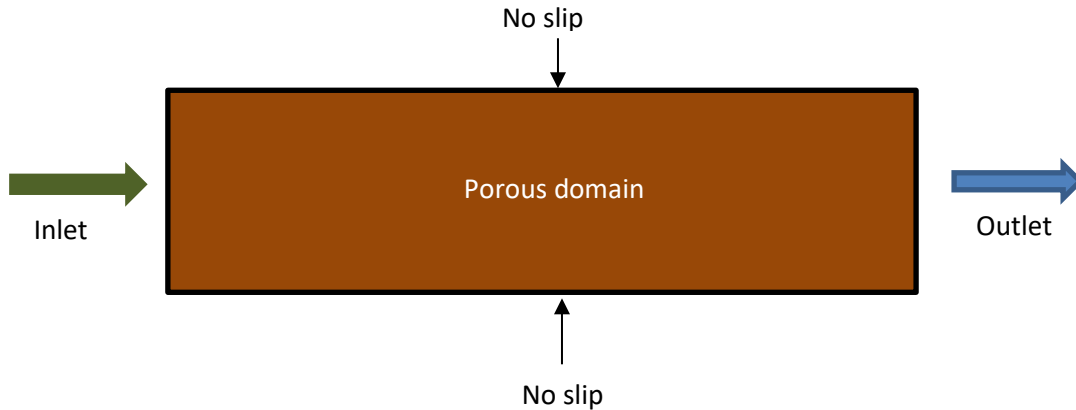


Figure 6.2: Sketch of Modelled domain and boundary notations

Whilst, flow in the free channel is described by Navier-Stokes equations, flow in the porous domain when $F = 0$ is described by the Brinkman equations (Equation 6.1)

6.2.3 Mass Transport

The transport process in a porous medium is described by a two dimensional (2D) advection-diffusion equation. The transport of diluted species in porous media models the process of heterogeneous reaction where a reactant injected into the porous medium interacts with the components of the porous medium and causes it to dissolve leading to mass transport/transfer to the point of precipitation.

The transport of the diluted species in porous media model was opened from the model library located under the Chemical Reaction Engineering Module of COMSOL. The governing equation (Equation 6.2) that defines the model is:

$$\frac{\partial c}{\partial t} = u\nabla C - D\nabla^2 C = 0 \quad [6.2]$$

Where $\frac{\partial c}{\partial t}$ is the concentration gradient, C is the fluid concentration (mol/m^3), D is the diffusion coefficient (m^2/s) and u is fluid velocity (m/s).

A model parameter was created for the concentration throughout the model and two variables were created in the variables table for the reaction rate and reaction quotient to be used later in the model. The materials used include: sodium chloride (liquid) and carbonate (solid).

6.2.4 Modelling Reacting flow in porous media

The model considered the following transport phenomena properties: the fluid and matrix modelled with Brinkman equations and the porous media (mass) transport properties modelled through diffusion and convection with chemical reaction kinetics.

The porous media flow was simulated by the Chemical Reaction Engineering Module using the physics interface "Reacting Flow in Porous Media" which support both free-flow and porous-media domains.

The fluid flow was defined by the Transport Properties throughout the model. It uses the Brinkman equations, to account for the flow properties that are required inputs for the inlet velocity, pressure, density and viscosity.

Through diffusion and convection, the mass properties were defined in the Transport Properties node. This also requires inputs for the reaction quotient variable defined earlier in the Variables table as 'Q' for the concentrations which was defined in the inflow nodes, and for the diffusivity which was defined in the Transport Properties node.

The flow of the fluid throughout the media was defined by the 'Porous Matrix Properties' using the Brinkman equation. The porosity (ϕ) and permeability of the porous media were included in the Brinkman equation.

The adsorption/consumption of the chemical species to the porous media was accounted for by the 'Reactions' node. This was done using the reaction rate variable earlier defined, and the concentration of the chemical species.

6.2.5 Chemical Reaction

Porous media-chemical interaction was modelled using the chemical mass balance equation and rate law. Initially, the reaction between ATMP ($C_3H_{12}NO_9P_3$) and the rock (carbonate – $CaCO_3$) was denoted as A and used in the reaction rate equation (Equation 6.3).

The rate of reaction r , is given as:

$$r = -\frac{d[A]}{dt} = k[A] \quad [6.3]$$

Where k = rate constant (1/s)

6.2.6 Modelling dissolution/precipitation

An interface called Domain ordinary differential equation (ODE) was added to the model tree from Mathematics branch to compute the time-dependent change in $CaCO_3$ content, and the evolution of porosity as specific surface area (SSA) of the mineral grain. The rate equation was included as a user-defined expression in a Reaction domain condition, within a Transport of Diluted Species interface. The reaction rate provided a source term for the porosity, as the rock material is broken up. Another set of variable (variable 2) was created in the Variable table to define the permeability and the specific surface area. The source term which gives the rate of change of the unitless variables and the sink term were defined.

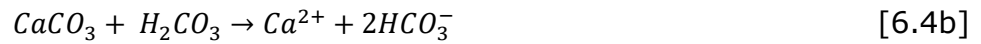
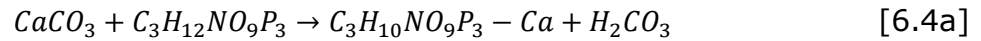
6.3 Results and Discussion

6.3.1 Chemical interaction with the porous media

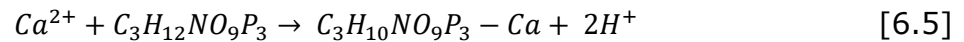
In modelling the interaction between the porous rock and the chemical species calcite which is one of the dominant minerals in the carbonate was selected, thus the modelling initially focuses on it, with a plan to include other dominant minerals like dolomite in the future for further investigation. The concentrations of ATMP, bicarbonate and ATMP-Ca complex obtained from the experiment (Chapter 5) were included in the model.

6.3.2 Reaction mechanisms

The chemical reactions for ATMP and calcite during oilfield chemical-carbonate interaction included in the model based on Plummer et al. (1978) and at ambient temperature are:



The first reaction (Equation 6.4a) took place at pH = 1 which reflects the dominating effect of the ATMP, the second reaction (Equation 6.4b) reflects the effect of carbonic acid at pH = 5. The backward precipitation (Equation 6.5) was then added.



Based on equation 6.4a,b the rate equation (6.6) that covers both dissolution and precipitation was formulated as:

$$r = \underbrace{k_1[C_3H_{12}NO_9P_3] + k_2[H_2CO_3]}_{r_{fw}} - \underbrace{k_3[C_3H_{10}NO_9P_3 - Ca][2HCO_3^-]}_{r_b} \quad [6.6]$$

where r is the specific rate of calcite dissolution ($\text{mol}/\text{m}^3/\text{s}$), separated in a forward rate r_{fw} and precipitation in a backward rate r_b and k_1 , k_2 and k_3 are the rate constants.

6.3.3 Model formulation

The simulator used in this modelling is based on the model that consists of mass and momentum conservation equations (mass balance and fluid flow). The reaction rates and sink/source terms that depict injection/production wells augments the mass conservation equations (Liu et al. 1997). Porosity-permeability relations are also part of the model formulation. The models were developed based on the parameters presented in Table 6.1. The variables for the reaction rates and the porous matrix, are presented in Tables 6.2 and 6.3, respectively.

Table 6.1: Model Parameters

Name	Expression	Value	Description
q	2.5[cm ³ /s]	2.5E-6 m ³ /s	Volume flow rate
area	0.002042[m ²]	0.002042 m ²	Porous media area
V0	q/area	0.0012243 m/s	Velocity
D_ATM	1.69E-6[m ² /s]	1.69E-6 m ² /s	Diffusion coefficient of ATMP
c0_ATM	1.3917[mol/L]	1391.7 mol/m ³	Concentration of ATMP
c0_ATM_Ca	0.195[mol/L]	195 mol/m ³	Concentration of ATM_Ca complex
c0_H2CO3	0.195[mol/L]	195 mol/m ³	Concentration of Carbonic acid
Ar	1E06[mol/(m ³ /s)]	1E6 s·mol/m ³	Frequency factor
Ea	55.25[kJ/mol]	55250 J/mol	Activation energy
T_iso	298[K]	298 K	Temperature
r_const	8.314[J/mol/K]	8.314 J/(mol·K)	Rate constant
A	1[mol/m ² /s]	1 mol/(m ² ·s)	Pre-exponential factor
k_Cal	2.0669E-10[mol/m ² /s]	2.0669E-10 mol/(m ² ·s)	Rate constant
Ps	2.71[g/cm ³]	2710 kg/m ³	Density of solid
N ₀	20.79[mol]	20.79 mol	Initial mole of solid
K	3.177E-2[mol/L]	31.77 mol/m ³	Solubility Product Constant
SSA0	1.98e+05[m ⁻¹]	1.98E5 1/m	Specific Surface Area
c0_Cal	16.67[mol/L]	16670 mol/m ³	Calcite concentration
D_ATMP_Ca	9.61E-08[m ² /s]	9.61E-8 m ² /s	
M_CaCO3	100.087[g/mol]	0.10009 kg/mol	Rel. Molecular Mass, calcite
rho_CaCO3	2.71[g/cm ³]	2710 kg/m ³	Density, calcite
poro0	0.3	0.3	porosity, initial
eps0_CaCO3	1 - poro0	0.7	Volumetric fraction of calcite, initial
perm0	1.056E-13[m ²]	1.056E-13 m ²	Permeability, initial
p0	0.67	0.67	

Table 6.2: Variables for Reaction Rate

Name	Expression	Unit	Description
Q	c_ATM_Ca*c_H2CO3/c_ATM	mol/m ³	Reaction quotient
R_Cal	(SSA)*(k_Cal)*(1 - (Q/K))	mol/(m ³ ·s)	Rate of reaction
R_CaCO3	-R_Cal*(M_CaCO3/rho_CaCO3)	1/s	Rate of relative volume change, CaCO3
R_poro	-R_CaCO3	1/s	Rate of porosity change

Table 6.3: Variables for Porous Matrix

Name	Expression	Unit	Description
perm	perm0	m ²	Permeability
SSA	SSA0*(eps_CaCO3/eps0_CaCO3)^p0	1/m	Specific surface area

6.3.4 Fluid and Matrix

The Brinkman equations (equation 6.7) take into consideration momentum transport through the kinetic potential from fluid velocity, pressure, and gravity in porous media. The fluid velocity and pressure were defined at the inlet and outlet boundaries, respectively. In effect, the Brinkman equation is considered as an extension of Darcy's law to delineate the kinetic energy dissipation by viscous shear. Figure 6.1 shows the mesh arrangements of the porous matrix; in order to obtain accurate solutions extremely fine mesh was chosen. The mesh consists of triangular and quadrilateral elements with cells of 21160 and 1196 respectively, see Table 6.4. The flow through the 2D cross-section of a 20m x 10m rectangular porous medium exhibits uniform velocity profile that developed throughout the length of the porous medium (Figure 6.3a). The smooth contours (Figure 6.3b) is a reflection of constant pressure at the outlet. The boundary conditions associated with the flow are No-slip at the wall (equation 6.8a), inlet with velocity (equation 6.8b) and outlet with pressure (equation 6.8c). CaCO₃ is the immobile species, while ATMP, ATMP-Ca and H₂CO₃ are the mobile phases. The influence of the immobile species depends on the variation in mineral content as described by the ratio of the factor that accounts for the changes in the reactive sites during dissolution/precipitation, N/N₀. The ratio N/N₀ was assumed to be approximately 1 at the initial stage to model flow and transport with the mobile species. The mobile species concentrations were denoted cATMP, cATMPCa and cH₂CO₃.

$$\nabla \cdot \left[-pI + \mu \frac{1}{\epsilon_p} (\vec{u} + (\vec{u})^T) \right] - \left(\mu k^{-1} + |u| + \frac{Q_{br}}{\epsilon_p^2} \right) u + F = 0 \quad [6.7]$$

$$Q_{br} = \rho \nabla \cdot (u)$$

Boundary conditions

$$u = 0 \quad [6.8a]$$

$$u = -u_0 n \quad [6.8b]$$

$$\left[-pI + \eta \frac{1}{\epsilon_p} (\nabla u + (\nabla u)^T) \right] n = -\hat{p}_0 n \quad [6.8c]$$

$$\hat{p}_0 \leq p_0$$

where p is the fluid pressure (Pa), ϵ_p is the matrix porosity, η is the fluid dynamic viscosity (pa.s), I is the identity matrix, T is tortuosity, n is the number of released particles, F is the external force (N/m²), u is the fluid velocity (m/s), k is the permeability of the matrix (m²).

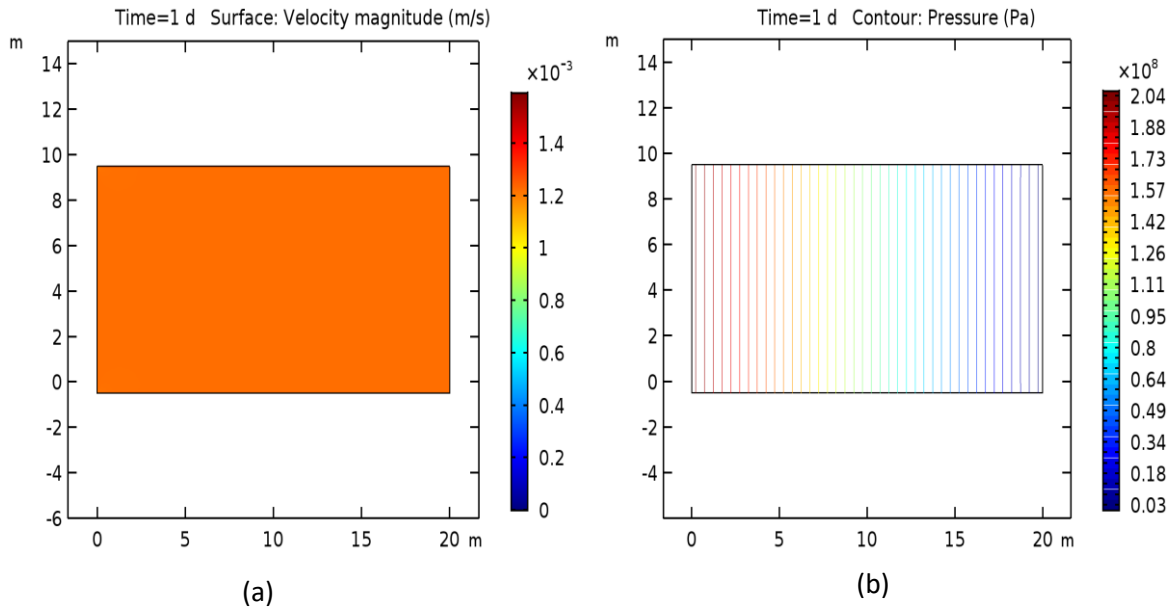


Figure 6.3: Model domain with (a) Velocity profile; and (b) Pressure distribution contour.

Table 6.4: Mesh statistics

Description	Value
Minimum element quality	0.3639
Average element quality	0.9211
Triangular elements	21160
Quadrilateral elements	1196
Edge elements	732
Vertex elements	4

6.3.5 Mass Transfer in porous media

In order to account for the advective and diffusive forces associated with the chemical species in the pore space, the concentration of the chemical species denoted as C_i was considered. Fick's first law (Equation 6.9) gives the flux due to diffusion in dilute species transport which depends solely on the solute's interaction with the solvent, thus establishing the diffusion coefficient. The boundary conditions include no flux (Equation 6.10a), inflow (Equation 6.10b), outflow (Equation 6.10c) and reactions (Equation 6.10d).

$$\nabla \cdot \Gamma_i + u \cdot \nabla c_i = R_i + S_i \quad [6.9]$$

$$N_i = \Gamma_i + uc_i = -D_{ej} \nabla c_i + uc_i$$

Boundary conditions

$$-n \cdot N_i = 0 \quad [6.10a]$$

$$c_i = c_{oj} \quad [6.10b]$$

$$-n \cdot D_i \nabla c_i = 0 \quad [6.10c]$$

$$\nabla \cdot (-D_i \nabla c_i) + u \cdot \nabla c_i = R_i \quad [6.10d]$$

where Γ_i is the diffusive flux ($\text{mol}/\text{m}^2/\text{s}^2$), c_i is the concentration of the species (mol/m^3), R_i is the reaction rate expression for the species ($\text{mol}/(\text{m}^3 \cdot \text{s})$), S_i is the source/sink term and u is the velocity vector (m/s), N_i is the flux vector

(mol/(m².s)) and it is associated with the mass balance equation (Equation 6.10d). N is used in boundary conditions and flux computation. Where diffusion and convection are the only transport mechanism the flux vector N_i takes the form:

$$N_i = DVc_i + uc_i \quad [6.11]$$

For the mass balance, $\nabla \cdot (-DVc_i)$ accounts for diffusive transport responsible for the interaction between the diluted species and solvent; whilst the convective transport due to a velocity field u is described by $u \cdot \nabla c_i$.

The transport in saturated porous medium when the pore space is filled with the fluid and volume fraction is equal to porosity ($\theta = \phi$) is described by the equation for concentrations, c_i as:

$$\begin{aligned} (\epsilon_p + \rho_b k_{p,i}) \frac{\partial c_i}{\partial t} (c_i - \rho_p c_{p,i}) + \frac{\partial \phi}{\partial t} (\rho_b c_{p,i}) + u \cdot \nabla c_i = \nabla \cdot [(D_{D,i} + \\ \theta \tau_{F,i} D_{F,i}) \nabla c_i] + R_i + S_i \end{aligned} \quad [6.12]$$

where C_i is the concentration of species i in the liquid (mol/m³), c_{p, I} is the amount of adsorbed to (or desorbed from) solid particles (mol/weight of solid), ρ_b is the bulk density of the porous medium (kg/m³), D_D is the tensor (m²/s) and D_F is the effective diffusion (m²/s).

The first two terms on the left hand side of Equation 6.12 represent species accumulation within the fluids and solid phases respectively, while the third term corresponds to convection due to the velocity field u. Whilst, on the right hand side the first term describes the spreading of species by diffusion and the last two terms represent production and consumption of the species.

The mass transport equation balances throughout the porous medium utilising the volume fraction θ, the porosity φ, the solid phase density ρ (kg/m³) and the bulk

density ρ_b , but $\rho_b = (1 - \phi)\rho$. The movement of the species with the bulk fluid velocity is described by convection. The velocity field u represents a superficial volume average over a unit volume of the porous medium (pores and matrix). This velocity can be defined as volume flow rates per unit cross section of the medium. To estimate the velocity within the pores an average linear velocity u_F was solved as:

$$u_F = \frac{u}{\phi} \quad [6.13]$$

The effective diffusion D_e in porous medium is a function of the structure of the porous materials and the phases involved. The effective diffusivity occurs in free flow and saturated porous media taking the form:

$$D_{ej} = \frac{\phi}{\tau_{Fj}} D_{Fj} \quad [6.14]$$

where D_{Fj} denotes single-phase diffusion coefficient for the species diluted in pure liquid phase (m^2/s), and τ_{Fj} is the dimensionless tortuosity factor which accounts for the reduced diffusivity due to the fact that solid grains impede Brownian motion (Rosner 1986).

Species transport in the porous media is influenced by chemical reactions which correspond to change in concentration of species per porous media unit volume per time. Figure 6.4 shows variations in the concentration of the reactant (ATMP) and product (ATMP-Ca). Figure 6.4a shows high concentration of the ATMP at the inlet but diminishes as it is being consumed (Figure 6.4b) through diffusion and convection and fizzles out completely before reaching the outlet. On the other hand, Figures 6.4c,d show concentration of the ATMP-Ca complex as it is being produced at/or near the outlet with zero concentration at the inlet. The variation

in the concentrations of the chemical at the inlet (reactant) and outlet (products) can be explained by the source/sink and production phenomena. The chemical species was consumed by the porous medium near the inlet through reaction to produce the ATMP-Ca complex at/or near the outlet after 24 hours.

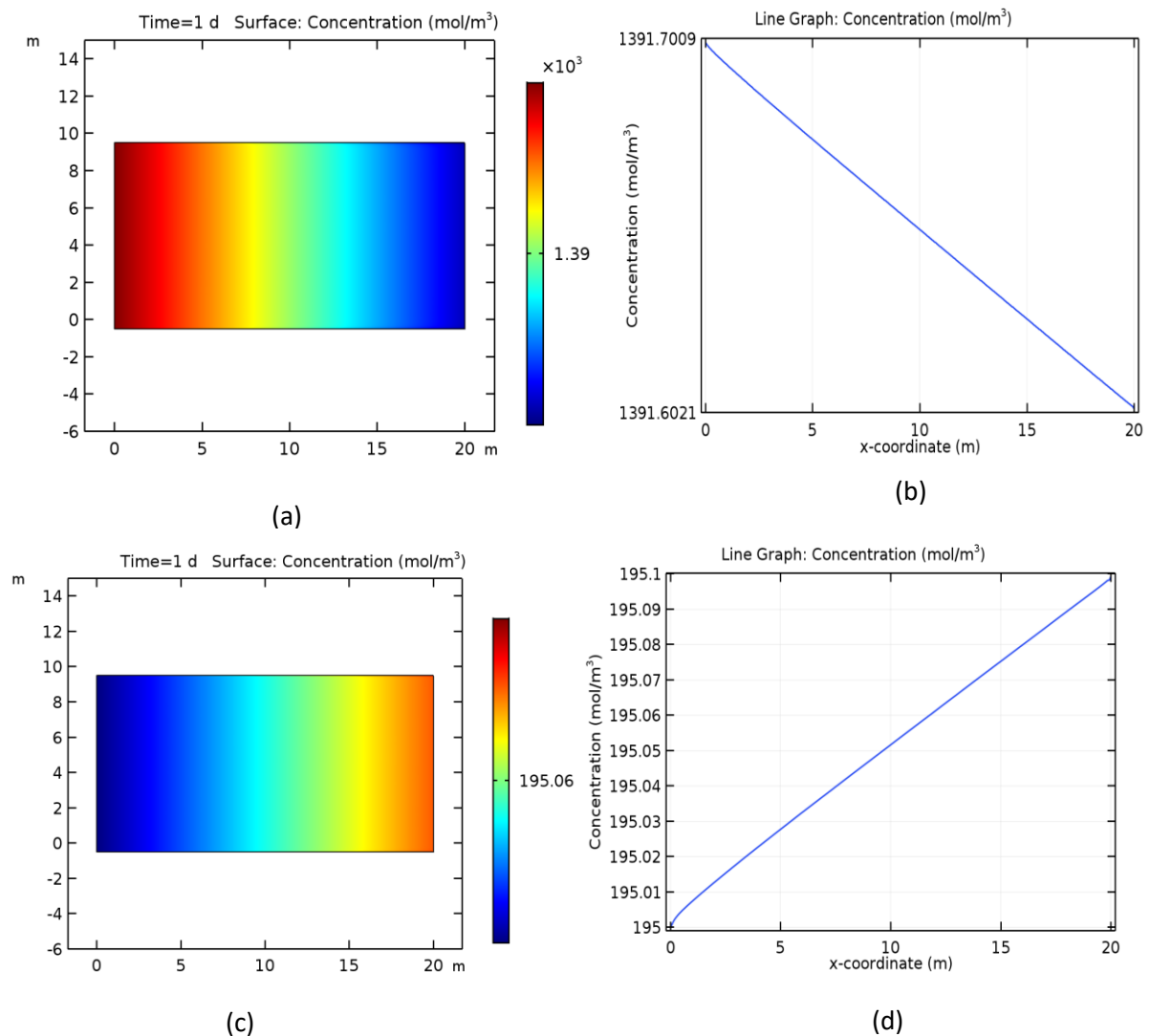


Figure 6.4: Change in concentrations of reactant and product (a) ATMP (reactant); (b) consumed ATMP (reactant) (c) ATMP-Ca complex (product); and (d) produced ATMP-Ca complex (product) during chemical-rock interaction.

6.3.6 Reactions and Rate laws

The rate equations associated with the ATMP-rock interaction, as described by the change in solute concentration due to mineral dissolution/precipitation process

were obtained by following an approach similar to that of Appelo and Postma (2005) and Bunney et al. (1996) in the form:

$$R = k \frac{A_0}{V} \left(\frac{N}{N_0} \right)^{p^0} (1 - \Omega) \quad [6.15]$$

where R is the overall reaction rate (mol/m³/s), k is the rate constant (mol/m²/s), A₀ is the initial surface area of the mineral (m²), V is the Volume of fluid in contact with mineral (m³), Ω is saturation state, N₀ is the initial moles of mineral and N is the mole of mineral at a given time. The factor (N/N₀)^{p⁰} accounts for the changes in the surface area (reactive sites) during dissolution. These changes could be caused amongst others by changes in the size distribution of the particle population. According to Appelo and Postman (2005), p⁰ = 2/3 for a monodisperse population of uniformly dissolving spheres and cubes because N is proportional to the volume, or r³ while the surface area is proportional to r². However, for polydispersed crystal populations, the finest crystals dissolves selectively modifying the size distribution, thus p⁰ becomes 3.4 (Dixon and Hendix 1993). However, the saturation state, Ω, is given by:

$$\Omega = \frac{IAP}{K} \quad [6.16a]$$

$$IAP = Q \quad [6.16b]$$

where Q is activity product (Equation 6.19) and K is solubility product (Equation 6.20).

$$R_{i=k_{cal}} = \frac{A_0}{V} \left(\frac{N}{N_0} \right)^{p^0} \left(1 - \frac{Q}{K} \right) \quad [6.17a]$$

$$\frac{A_0}{V} = SSA$$

where R_i is the reaction rate ($\text{mol}/\text{m}^3\cdot\text{s}$), k_i is the rate constant of calcite ($2.0669 \times 10^{-10} \text{ mol}/\text{m}^2/\text{s}$) A_0 is the surface area of calcite (m^2), V is the volume (m^3) and SSA is the specific surface area (m^{-1}). Hence,

$$R_i = k_i * \left(1 - Q/K\right) * SSA * \left(\frac{N}{N_0}\right)^{p_0} \quad [6.17b]$$

$$\text{Rate constant } k_i = A. \exp\left(-E_a/RT\right) \quad [6.18]$$

where, A is the pre-exponential factor (same unit as k_i), E_a is the activation energy ($55.25\text{kJ}/\text{mol}$), R = gas constant ($8.314\text{J}/\text{mol}/\text{m}^2\cdot\text{s}$) and T is the absolute temperature at 25°C (298K).

$$Q_i = \frac{[C_3H_{10}NO_9P_3-Ca][2HCO_3^-]}{[C_3H_{10}NO_9P_3][H_2CO_3]} \quad [6.19]$$

$$K_i = \frac{[C_3H_{10}NO_9P_3-Ca][2HCO_3^-]}{[C_3H_{12}NO_9P_3][H_2CO_3]} \quad [6.20]$$

The initial specific surface area (SSA_0) for the calcium carbonate was obtained using Avogadro's law based on Inks and Hahn (1967):

$$SSA_0 = \frac{(X)(S)}{(100-X)(W)} \quad [6.21]$$

where X is the %calcium -45 exchanged, S is the grams of calcium in solution, w is the weight of sample and d is the specific gravity (density) of calcium carbonate.

The number of atoms of calcium on the surface per gram of CaCO_3 is:

$$N = \frac{(1)(6.02)(10^{23})}{\text{atomic wt of calcium}} \quad [6.22]$$

Volume occupied by one molecule of CaCO_3 is:

$$V = \frac{\text{Molecular weight of CaCO}_3}{(d)(6.02)(10^{23})} \quad [6.23]$$

Area represented by one side of a molecule assuming a cubic lattice is:

$$A = \left(\frac{\text{Mol wt of CaCO}_3}{(d)(6.02)(10^{23})} \right)^{2/3} \quad [6.24]$$

6.3.7 Dissolution/Precipitation reaction

Mineral precipitation/dissolution goes through a chain of processes such as solutes transport between the bulk solution and mineral surface, adsorption and desorption of solutes at the surface, hydration and dehydration of ions and surface migration (Appelo and Postma 2005). Mineral reaction that leads to the precipitation of mineral obeyed first and second derivatives and takes the form:

$$e_a \frac{\partial^2 u}{\partial t^2} + d_a \frac{\partial u}{\partial t} = S_i \quad [6.25]$$

$$u = [\phi, \theta]^\tau$$

Substituting the u in equation 6.25 with $[\phi, \theta]^\tau$, we have:

$$e_a \frac{\partial^2 (\phi)^\tau}{\partial t^2} + d_a \frac{\partial (\phi)^\tau}{\partial t} = S_i \quad [6.26]$$

$$e_a \frac{\partial^2 (\theta)^\tau}{\partial t^2} + d_a \frac{\partial (\theta)^\tau}{\partial t} = S_i \quad [6.27]$$

where ϕ is porosity change and θ is the volume fraction within the microscopic volume of porous material or change in calcite content with time, d_a and e_a are the mass transfer coefficient and S_i is the source/sink term. The Source Terms for the ordinary differential equation (ODE) gives the rates of change of the unitless variables; but e_a is zero and d_a is equal to 1. The tortuosity factor τ is according to Millington and Quirk model (1961) (6.26 and 6.27) in saturated porous media:

$$\tau_{Fj} = \phi^{-1/3} \quad [6.28]$$

Taking the values of d_a and e_a into consideration the first term in equation 6.26 and Equation 6.27 becomes zero and the two equations reduce to:

$$d_a \frac{\partial(\phi)^\tau}{\partial t} = S_i \quad [6.29]$$

$$d_a \frac{\partial(\theta)^\tau}{\partial t} = S_i \quad [6.30]$$

But $d_a = 1$, hence Equation 6.29 and Equation 6.30 reduce to:

$$\frac{\partial(\phi)^\tau}{\partial t} = S_i \quad [6.31]$$

$$\frac{\partial(\theta)^\tau}{\partial t} = S_i \quad [6.32]$$

Length = 20m, $\tau = 0.3686$, $\theta = -1.82 * 10^{-5}$, $\phi = 1.82 * 10^{-5}$

The source/sink term S_i is equal to ± 0.02 . Figures 6.5 and 6.6 show the precipitation of calcite and reduction of porosity with time as the oilfield chemical which is a reacting fluid was injected into and transported through the porous medium.

Rate of relative mineral volume change R_θ due to precipitation/dissolution is given as:

$$R_\theta = R_i * \left(\frac{M_i}{\rho_i} \right) \quad [6.33]$$

Where M and ρ are the relative molecular mass and density of the mineral i , respectively and R_i is the rate of reaction. When it is precipitation R_θ becomes negative and positive when it is dissolution. Conversely, when it is precipitation, R_ϕ bears a positive sign and negative sign when it is dissolution. The rate of dissolution/precipitation is a function of the rate of mineral volume change R_θ and the rate of porosity change R_ϕ .

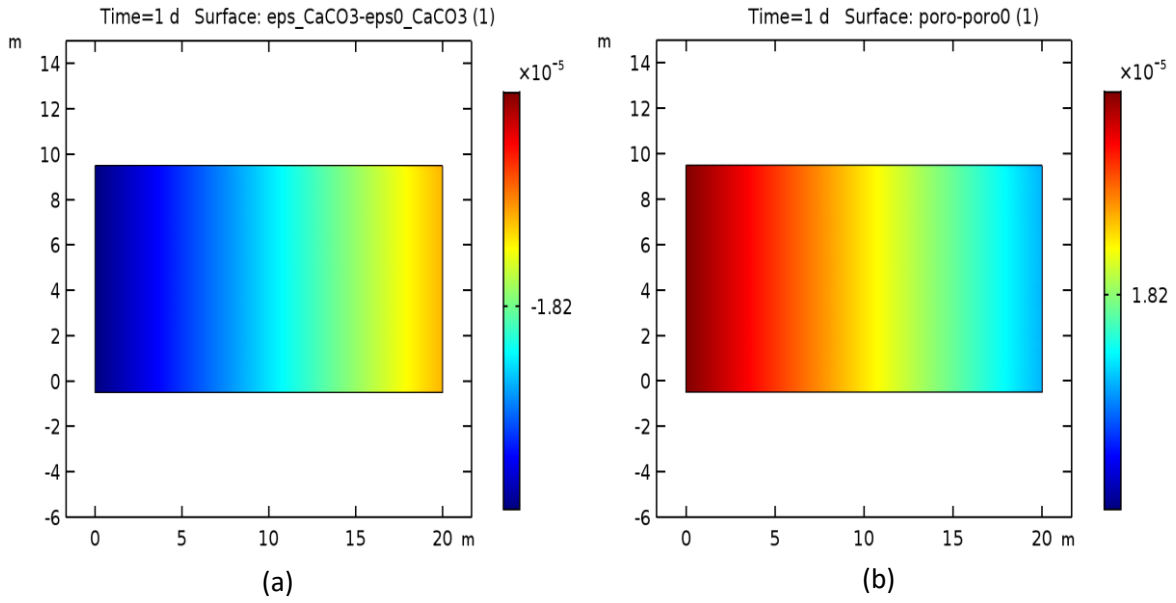


Figure 6.5: Precipitation of calcite (a) and reduction of porosity (b) over 24 hours.

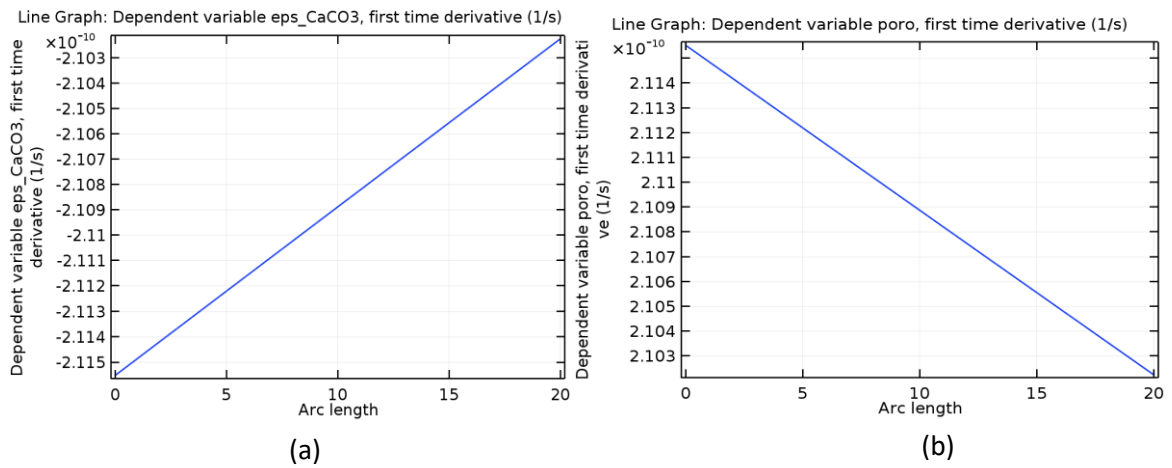


Figure 6.6: Time dependent change in (a) Calcite content; and (b) Porosity.

The results have shown that mineral precipitation takes place in the presence of oilfield chemicals at $R_{\theta} \leq -1.33e-14 \leq \phi \leq 1.33e-14$ per second leading to core pore clogging; whilst dissolution takes place at $R_{\theta} \leq 1.33e-14 \leq \phi \leq -1.33e-14$ per second leading to weakening of rock fabric and eventual sand failure. Thus, a positive value of R_{θ} denotes mineral dissolution while a negative value stands for mineral precipitation. This implies that mineral precipitation/dissolution in the presence of oilfield can be predicted using the rate of mineral volumetric change as well as the rate of porosity change. The result is consistent with a previous study by Liu et al. (1997).

Demonstration of the model was conducted by flooding the porous rock (carbonate) with aminotrimethylene phosphonic acid-ATMP. It was found that the model could explain the steady state effluent concentration resulting from the combined effect of transport and dissolution/precipitation. Like the experimental results, the numerical modelling revealed that the porous medium porosity decreased and precipitation reaction took place; hence depicting pore clogging. Depending on the state of the precipitated materials, low geomechanical strength could be obtained due to the fact that the precipitated material may be weaker than the original material that eroded. This episode can lead to sand production. On the other hand, high geomechanical strength could be observed due to filling of the pores arising from mineral precipitation which may cause formation damage. The fact that the precipitates filled the pores and increased the uniaxial compressive strength does not preclude sand failure as the strength increase may be transient which can dissipate after some time.

6.4 Summary

The interaction between the oilfield chemical and the reservoir rock has been simulated using COMSOL Multiphysics 5.3. Fluid flow, mass transport and chemical reaction were coupled to study the dissolution/precipitation characteristics of the mineral in the presence of the chemical. Results clearly show that the dissolution/precipitation of minerals is a function of the change in the volume fraction of the mineral and porosity. If the rate of change of the relative mineral volume is positive with negative rate of change of porosity, dissolution takes place; whilst negative rate of change of relative mineral volume with positive change in porosity is an indication of precipitation reaction. The model can be integrated into the existing sand failure and production prediction models.

Lastly, the simulation has provided a clear understanding of the basic mechanisms involved in the oilfield chemical-rock interaction.

Integrating the model developed in this work with sand prediction model will help to optimise the field operation and in the process save money.

References

- ANDERSEN, P.Ø., EVJE, S., MADLAND, M.V., HIORTH, A., 2012 A geochemical model for interpretation of chalk core flooding experiments. *Chemical Engineering Science* 84, 218–241.
- APPELO, C. and POSTMA, D., 2005. *Geochemistry, Groundwater and Pollution*. Second edition, AA Balkema, Rotterdam.
- BARTELS, J., KÜHN, M., SCHNEIDER, W., CLAUSER, C., PAPE, H., MEYN, V., LAJCSAK, I., 2002. Core flooding laboratory experiment validates numerical simulation of induced permeability change in reservoir sandstone. *Geophysical Research Letters*, 29 (9), 1320.
- BRINKMAN, H.C., 1946. A calculation of the viscous forces exerted by a flowing fluid of a dense swarm of particles. *Applied Science Resources*, 27-34.
- BUNNEY, J.R., SORBIE, K.S., JORDAN, M.M., 1996. Assessment of chemical disequilibria in oil reservoirs: implications for production and diagenetic timescale geochemical modelling. AAPG Annual Convention, San Diego, LA.
- CZERNICHOWSKI-LAURIOL, I., ROCHELLE, C.A., GAUS, I., AZAROUAL, M., PEARCE, J., DURST, P., 2006. Geochemical interactions between CO₂, pore-waters and reservoir rocks: lessons learned from laboratory experiments, field studies and computer simulations. In: *Advances in the Geological Storage of Carbon Dioxide*. NATO Science Series IV, 157–174.
- DIXON, D.G. and HENDRIX, J.L., 1993. Theoretical basis for variable order assumption in the kinetics of leaching of discrete grains. *AIChE Journal* 39, 904–907.

INKS, C.G., HAHN, R.B., 1967. Determination of surface area of calcium carbonate by isotopic exchange. *Analytical Chemistry* 39 (6), 625–628.

LIU, X., ORMOND, A., BARTKO, K., LI, Y., ORTOLEVA, P., 1997. A geochemical reaction-transport simulator for matrix acidizing analysis and design. *Journal of petroleum Science and Engineering* 17, 181-196.

MILLINGTON, R.J., AND QUIRK, J.M., 1961. Permeability of Porous Solids, *Transactions of the Faraday Society*, vol. 57, 1200–1207.

PLUMMER, L. N., WIGLEY, T. M. L. and PARKHURST, D. L., 1978. The kinetics of calcite dissolution in CO₂-water systems at 5 degrees to 60 degrees C and 0.0 to 1.0 atm CO₂. *American Journal of Science*, 278(2), 179–216.

ROSNER, D.E., 1986. Transport Processes in Chemically Reacting Flow Systems, ISBN-13:978-1483130262, Butterworth-Heinemann.

Chapter Seven

7 Conclusion and Recommendations for Future work

7.1 Conclusion

The effect of interaction between the oilfield chemicals and the reservoir rock on the geomechanical strength of the reservoir has been investigated using experimental and numerical approaches. The experimental investigation was performed under static and dynamic conditions. The purpose of conducting the experiment under the two conditions was to simulate shut-in and production from the reservoir formation after chemical stimulation. The rock properties investigated in the laboratory include porosity, permeability, mineralogy, compressive strength (unconfined and confined) and particle size distribution with sorting. On the other hand, the numerical simulation took into consideration physics like fluid flow using the Brinkman equation, mass transport through the porous media using mass balance equation and chemical reaction that encompassed rate of reaction for dissolution and precipitation. The following important conclusions have been drawn from the current work:

An expanded literature review on effect of fluid-rock interaction on the geomechanical strength of the reservoir rock in Chapter two revealed that the weakening effect of the oilfield chemicals that are used day to day in oil and gas industry has not been accounted for in currently existing and used sand prediction models. Furthermore, the mechanisms of interaction between the oilfield chemicals and the reservoir rocks have been identified. These mechanisms include adsorption, dissolution, precipitation and ionic substitution reactions.

The weakening effect of the selected oilfield chemicals - ATMP, glutaraldehyde, and betaine on the mechanical, physical and petrophysical properties of the reservoir rocks (carbonates and sandstone) were studied in Chapter four under static condition and in Chapter five under dynamic condition. This work revealed that the interaction of oilfield chemicals with reservoir rocks results in more negative impact on the unconfined compressive strength than confined compressive strength. Strong correlations between porosity and UCS; porosity and Young's modulus as it relates to sand production have been established. These relationships have been used in this thesis to predict the response of geomechanical strength of the reservoir as a function of porosity in the presence of oilfield chemicals. Surprisingly the effect of the oilfield chemicals-rock interaction on the uniaxial compressive strength is higher under static condition than that obtained under dynamic saturations despite that the transport under static condition is by diffusion only; whilst the transport under dynamic condition is by diffusion and convection.

In Chapter six, the volumetric transformation/changes of the mineral constituent of the reservoir rocks due to geochemical reaction in space and time have been evaluated via the mineral volume fraction, porosity and geomechanical strength. The results show that the change in mineral volume fraction and porosity are functions of dissolution and precipitation of the minerals which in turn are functions of the type of minerals in the rocks. A model of oilfield chemicals interaction with carbonate reservoir rock suitable for the prediction of the sand failure/ production has been developed. The sanding potential is predicted through changes in mineral volume, porosity and geomechanical strength. The results obtained from the numerical modelling are consistent with the experimental results.

Having identified the effect of the selected oilfield chemicals on the geomechanical strength of the reservoir in the current work, it is imperative for the field operators to take into cognizance the potential for dissolution and precipitation reaction between the materials (quartz and calcite) that cement the grains of sandstone and limestone and oilfield chemicals. Dissolution reaction can lead to the weakening of the rock fabric whilst precipitation may result in the formation of new materials which are weaker than the original rock materials. It is therefore important to factor the interaction between these chemicals and formation rock into the evaluation of failure and sand production potential for field operation especially when extensive chemical injection programme is planned for such fields.

7.2 Recommendations for future work

The following recommendations have been made from the present study for future research:

1. In the current study only three oilfield chemicals have been explored. The possibility of the weakening effect of these chemicals have been inferred by the results in the current work. It will be more appropriate to extend the investigation to other commonly used oilfield chemicals to ascertain the effects of these chemicals on the geomechanical properties/strength of the reservoir rock. The basis for further investigation has been provided by the findings in the current study.
2. The current study focused on the macroscopic response of the core using SEM/EDX, XRPD, UCT, etc., however detailed microscopic study would be needed to quantify the local particle transport in the pore network of the core. Thus, it is expedient to carry out micro CT analysis for this purpose

and also for the purpose of determining the specific location of dissolution and precipitation within the core in future.

3. Both dynamic and static experiments were conducted under ambient temperature and atmospheric pressure which revealed that the oilfield chemicals have deleterious effect on the reservoir strength under such conditions. It is noteworthy that high temperature speeds up chemical reaction, thus repeating the experiments in the future studies using the reservoir temperature and pressure conditions to see if there will be any change in response to high temperature and pressure should be encouraged. The result could provide more information on the role of these parameters (temperature and pressure) in the interaction between the oilfield chemicals and the reservoir rocks in real scenario.
4. In this current work, only one of the chemicals (betaine) was used to investigate the effect of the chemical-rocks interaction on the confined compressive strength. To effectively account for the effect of the other two chemicals (ATMP and glutaraldehyde) on the confined compressive strength it will be necessary to conduct triaxial test on the samples that have been exposed to the remaining two chemicals.
5. The effect of concentration and pH of the chemicals on the geomechanical properties as well as strength was not focused on in the current work. As such changes in the two parameters were not monitored during the laboratory experiment. Determining the effect of change of these parameters during the experiment is imperative to be able to account effectively for the role they play in the dissolution and precipitation reactions.

6. It is expected that weight would be lost due to particle detachment arising from the interaction of the chemicals with the formation rocks, however, like the existing literatures, weight loss was not considered in this research. It is important that weight loss be considered in future work.
7. The simulation was demonstrated using a combination of some of the data obtained from the oilfield chemical interaction with the carbonates and data in the software, it will be appropriate to consider modelling the effect of interaction between the oilfield chemicals and sandstone in the future studies.
8. In the current work, it is only the geochemical modelling that was covered numerically; this does not provide the complete information on the effect of the chemical-rock interaction numerically. Therefore, geomechanical modelling should be considered in the future studies.
9. The coupling of this nature should have generated non-linear graphs, however, due to limitations of the COMSOL Multiphysics, the generated mesh produced linear graphs. It is imperative that other softwares like Toughreact or Phreeqc be used to model the rate of dissolution/precipitation reaction.

Appendices

Appendix A: Linear variable differential transformer (LVDT) calibration

LVDT and the micrometre were connected to RDP transducer indicator which was powered. The LVDT was turned twice (2 turn) to give 1mm and the RDP was recorded in voltage while the micrometre was recorded in mm. Both the positive and negative readings of up to 25, i.e -25 to +25 were recorded. At each reading whether positive or negative the LVDT was returned to zero.

Balancing the Wheatstone bridge:

$$1 \text{ step} \longrightarrow +1903 \mu\epsilon = 0.209 \text{ V}$$

$$-1901 \mu\epsilon = -0.208 \text{ V}$$

Converting the voltage to microstrain, $0.209 - (-0.208) \text{ v} = 1903 - (-1901) \mu\epsilon$

$$0.417 \text{ v} = 3804 \mu\epsilon$$

$$1 \text{ v} = X \mu\epsilon$$

$$X \mu\epsilon = 3804 / 0.417 = 9122 \mu\epsilon$$

Each value of strain in volt was multiplied by 9122 and 10^{-6} to convert to strain values.

The load line out for instron is ± 10 volt full scale

$$10 \text{ v} = 150 \text{ kN}$$

$$1 \text{ v} = X \text{ kN}$$

$$X = (1 \times 150) / 10$$

$$15 \text{ kN}$$

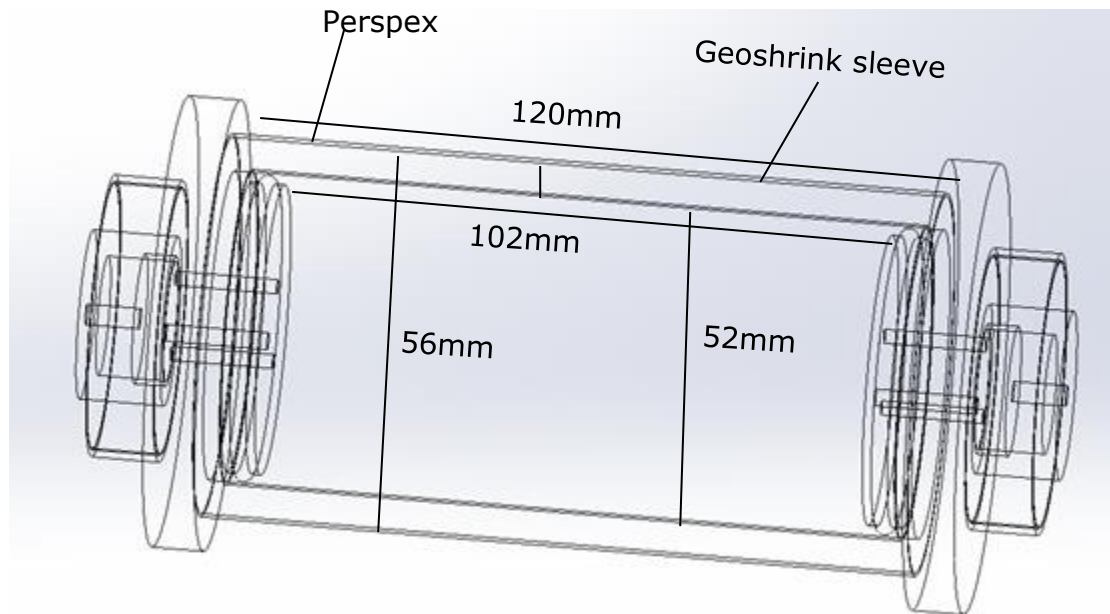


A1: Picture of LVDT calibration

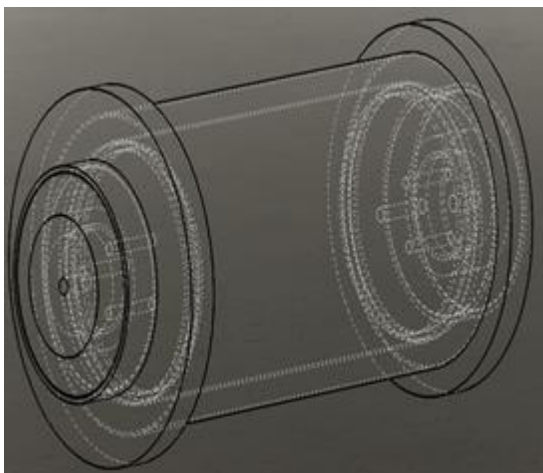
Table A-D1: Showing LVDT calibration

RDP	Voltage
-25.07	-2.464
-24.09	-2.367
-23.08	-2.268
-22.06	-2.168
-21.04	-2.068
-20.03	-1.968
-19.02	-1.869
-18.01	-1.771
-17.01	-1.671
-16	-1.573
-15	-1.475
-14	-1.376
-13	-1.278
-12	-1.18
-11	-1.082
-10	-0.984
-9	-0.886
-8	-0.788
-7.01	-0.69
-6.01	-0.592
-5.01	-0.494
-4.01	-0.396
-3.01	-0.298
-2.01	-0.199
-1	-0.1
0	-0.002
1	0.097
2.01	0.196
3.03	0.297
4.04	0.395
5.05	0.494
6.05	0.593
7.05	0.691
8.05	0.789
9.04	0.886
10.04	0.984
11.03	1.082
12.01	1.177
13	1.274
13.98	1.371
14.97	1.468
15.97	1.566
16.98	1.664

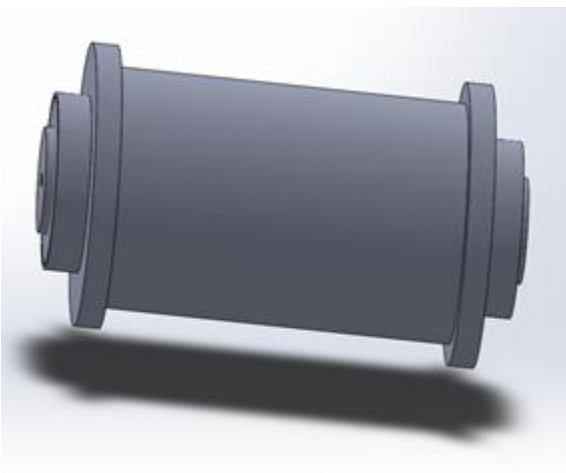
Appendix B: Design and Engineering drawing for Perspex core holder



(a)

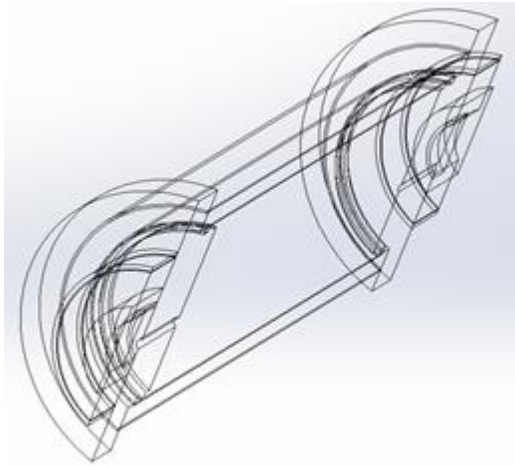


(b)

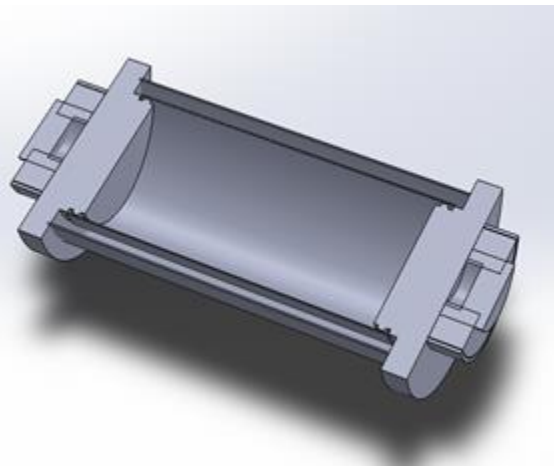


(c)

B1 (a) – (c): Perspex core holder full assemblage

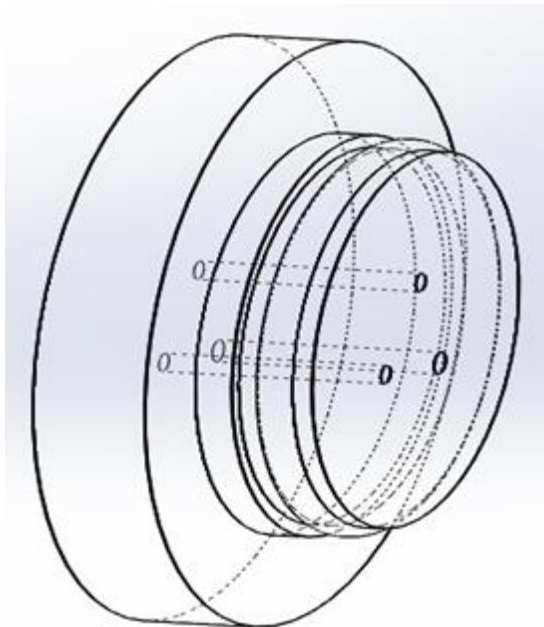


(d)

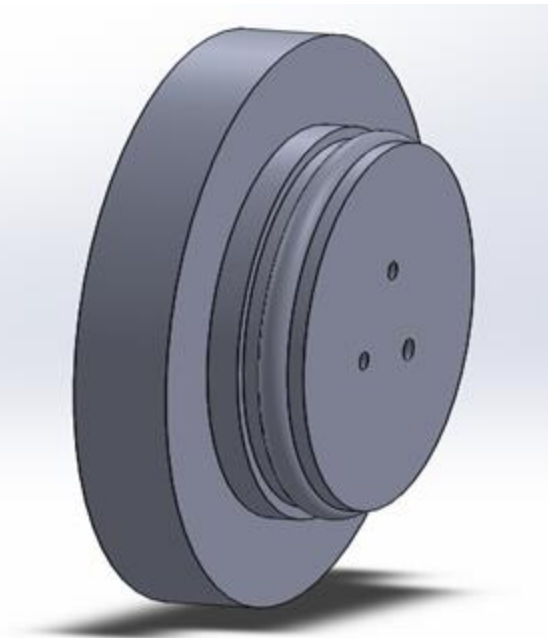


(e)

B1 (d) – (e): Cross section of Perpex core holder



(f)

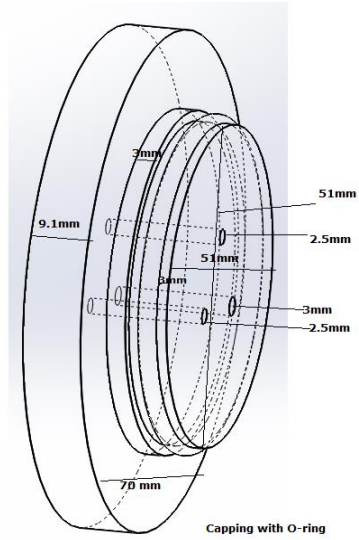


(g)

B1 (f) – (g): Core holder capping

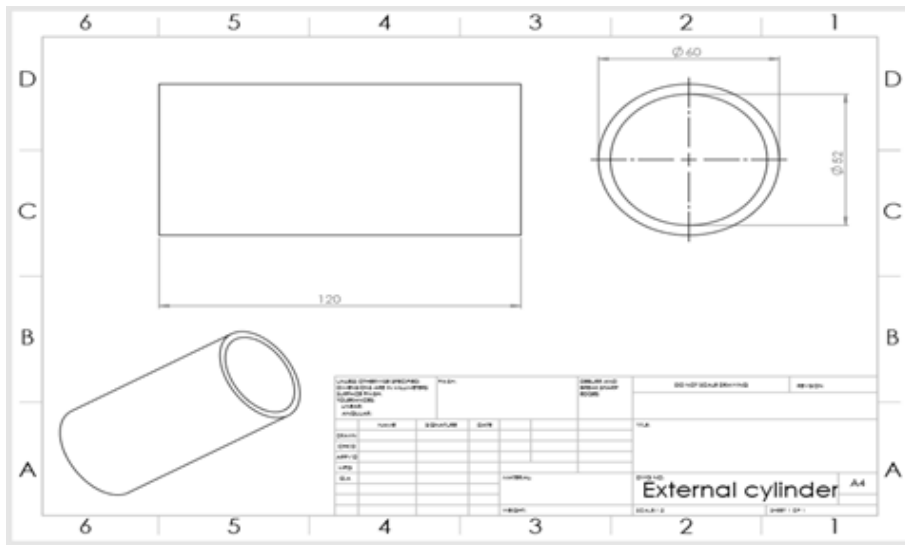


(h)

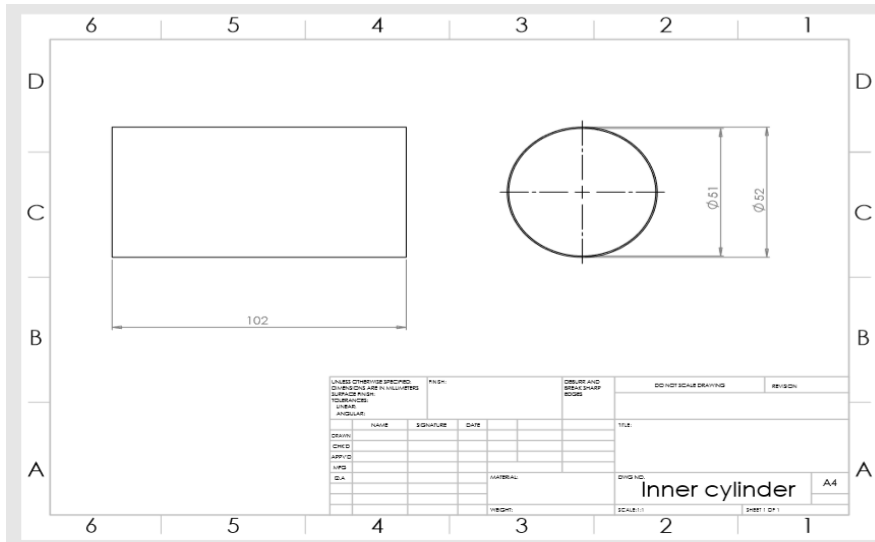


(i)

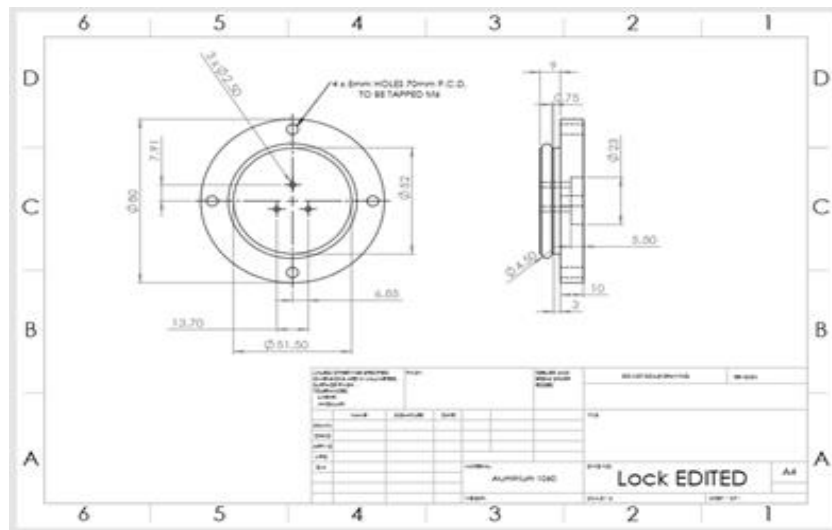
B1: Designed Perplex core holder showing: (i) O-ring; (j) capping with O-ring.



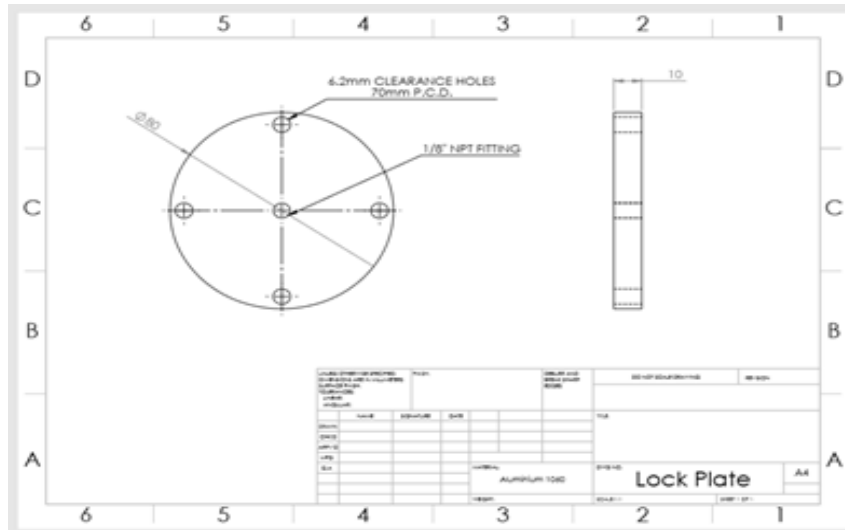
B2: External Cylinder of the core holder



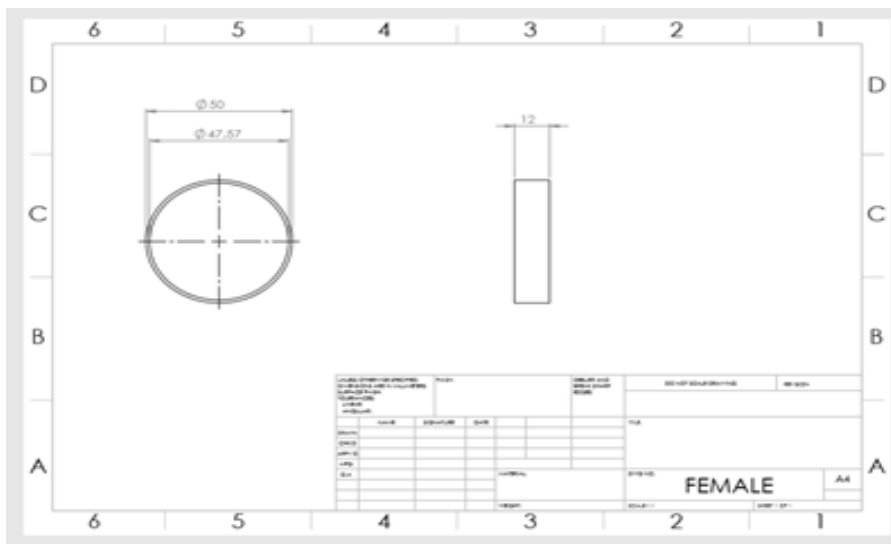
B3: Inner Cylinder of the core holder



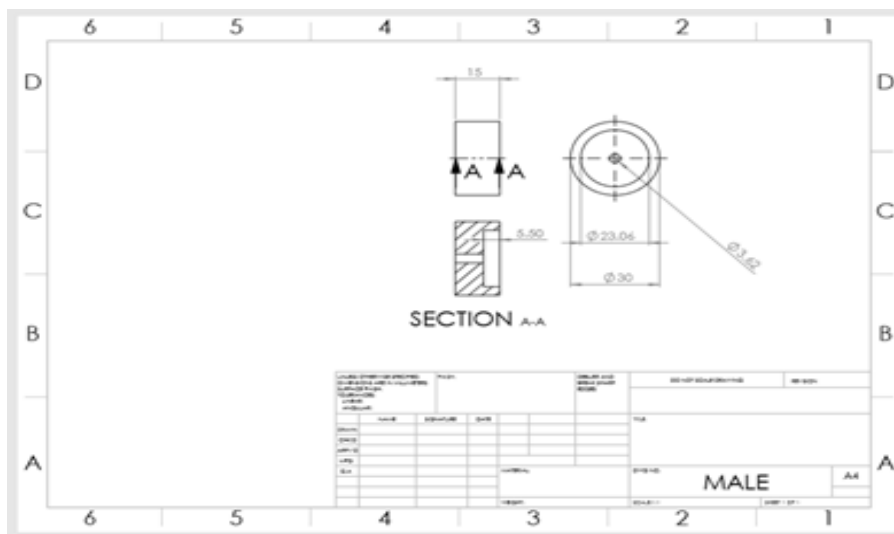
B4: Core holder capping



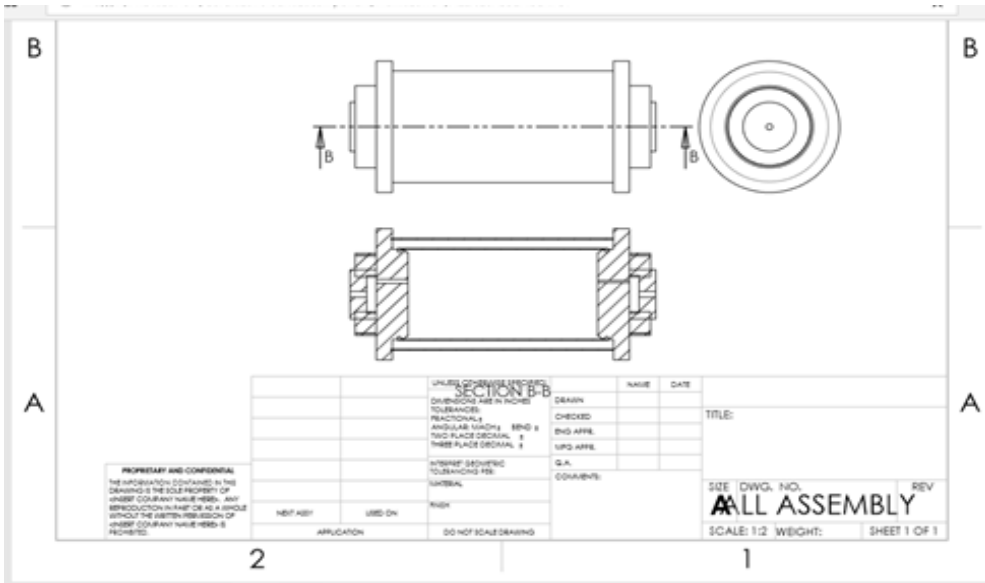
B5: Lock Plate



B6: Female Lock



B7: Male Fitting



B8: All Assembly

Appendix C: Procedure for determination of pore volume, dead volume and porosity

- I. Results obtained from ICP-OES were analysed using Microsoft Excel and used to calculate the total volume.
- II. The total volume (V_T) was determined by summing up the product of the normalised concentration (C/C_h) and sample volume (Sv).

$$V_T = \sum \left(\frac{C}{C_h} * Sv \right) \quad [C-1]$$

- III. The dead volume (V_d) was calculated by determining the length of the inlet (1/8") and the outlet (1/16") from the pump to the space around the core i.e. inside the core holder. Summing up the volume of both inlet ($\pi r^2 L$) and outlet ($\pi r^2 L$) to obtain the dead volume.

$$\text{Inlet} = 1/8" = \pi r^2 L \quad [C-2]$$

$$\text{Outlet} = 1/16" = \pi r^2 L \quad [C-3]$$

$$\text{Dead Volume} = 1/8" + 1/16"$$

- IV. The pore volume (V_p) was obtained by subtracting the dead volume from the total volume (V_T) of the fluid that passed through core. i.e.

$$V_p = V_T - V_d \quad [C-4]$$

- V. Determined the bulk volume (V_b) using the dimension of the core sample i.e.

$$V_b = \pi r^2 h \quad [C-5]$$

- VI. Finally, determined the porosity (Φ) as the ratio of pore volume (V_p) to bulk volume (V_b).

$$\Phi = \frac{V_p}{V_b} * 100 \quad [C-6]$$